Contenido de esta memoria adicional. Los documentos que se han recopilado están en el siguiente orden:

A Morphological Cellular Automata based on Morphological Independence

Neurocognitive disorder detection based on Feature Vectors extracted from VBM analysis of structural MRI

A Comparison of VBM Results by SPM, ICA
and LICA

Hybrid Dendritic Computing with Kernel-LICA applied to Alzheimer's Disease detection in MRI

On the Use of Morphometry Based Features for Alzheimer's Disease Detection on MRI

An adaptive field rule for non-parametric MRI intensity inhomogeneity estimation algorithm

Robustness of an adaptive MRI segmentation algorithm parametric intensity inhomogeneity modeling

Neuroimage Experimental Data Base Resources

Machine Learning approach for Myotonic Dystrophy diagnostic support from MRI

Lattice Independent Component Analysis for fMRI

Results of an Adaboost Approach on Alzheimer's Disease Detection on MRI

Classification Results of Artificial Neural Networks for Alzheimer's Disease Detection

Neural classifiers for schizophrenia diagnostic support on diffusion imaging data

Analisis preliminares para portar SPM v8 desde Matlab a Scilab

A Morphological Cellular Automata based on Morphological Independence

Josune Gallego, Carmen Hernandez, Manuel Graña

January 3, 2011

Computational Intelligence Group, UPV/EHU, www.ehu.es/ccwintco

Abstract

We discuss a definition of Morphological Cellular Neural Networks (MCNN) where the state change operator are Auto-associative Morphological Memories (AMM). The fast convergence properties of AMM and the shape of its fixed point set make the MCNN dynamics trivial. However, segmentation results are poor. We propose a Morphological Cellular Automata (MCA) with assured convergence to a state characterized by morphological dependences and independences between neighbouring cell states. Cell dynamic rules test morphological dependence among neighbouring cell's states. When neighbouring cell states are morphological dependent in the erosive or dilative sense, the morphologically dominant state colonizes the neighbour with morphological dependent state. The resulting configuration of cell states is composed of homogeneous regions whose boundaries are defined by the morphological independence relation. Results are given on image segmentation, where MCA cells correspond to image pixels.

1 Introduction

Massively parallel neural networks have been applied to solve NP-complete problems, such as the satisfiability problem [5, 7] in propositional logic. Cellular Neural Networks (CNN) have been applied to image processing and segmentation [1, 2, 3], however they are mostly restricted to one channel images. We look for an extension of this elegant approach to multispectral images. We propose the application of morphological operators and properties arising from the work on Associative Morphological Memories (AMM) [17, 13, 16] which lately have become Lattice Associative Memories [14, 15]. AMM's are constructed as lattice correlation matrices. Dual AMM constructions can be made using the dual min and max operators. Morphological Cellular Neural Network (MCNN) provide a formal morphological extension to the CNN, consisting in using the AMM

as the synaptic operators between neighbouring cells. Though theoretically appealing, and possessing a really fast convergence, segmentation results are poor in practice, until further theoretical developments allow to identify regions of lattice dependent pixels.

The AMM are selectively sensitive to specific types of noise (erosive and dilative noise). The notion of morphological independence and morphological strong independence was introduced in [16] to study the construction of AMM robust to general noise. It was established that AMM are able to robustly store and recall sets of morphologically strongly independent patterns. That leads us to the idea of considering morphological dependence as a kind of equivalence relation. Pixel regions could be identified by being morphologically dependent on a given morphologically dominant, some kind of morphological region representative vector which can be found in the image. For the visual identification of the region, we can substitute all the morphologically dependent pixels by the morphologically dominant one. This in essence the working of the Morphological Cellular Automata (MCA) proposed and tested in this paper. The work in this paper is an hybridization [4, 18] of CNN and morphological neural network approaches.

The structure of the paper is as follows. Section 2 reviews the definition and basic results of Cellular Neural Networks. Section 3 reviews the definitions of Associative Morphological Memories and Morphological Independence. Section 4 introduces the MCNN. Section 5 introduces the MCA. Section 6 gives results on image segmentation of MCNN and MCA. Finally, section 7 gives our conclusions.

2 Cellular Neural Networks

Cellular Neural Networks (CNN) have been introduced in [1, 2, 3] as a powerful distributed computational model. A *standard CNN architecture* consists of an $M \times N$ rectangular array of cells $C(i,j)$ where (i,j) are the cell Cartesian coordinates on a grid, $i = 1,2,\ldots,M$, $j = 1,2,\ldots,N$. The sphere of influence $S_r(i,j)$ of radius r of the cell $C(i,j)$ is the set of cells in grid site coordinates whose Manhattan distance is less than the radius: $S_r(i,j) = \left\{ C(k,l) \left| \max_{1 \le k \le M, 1 \le l \le N} \{|k-i|, |l-j|\} \le r \right. \right\}$, where r is a positive integer.

A $M \times N$ *standard CNN* is defined by a rectangular grid of cells $C(i,j)$, each defined mathematically by its state and output equations:

$$\dot{x}_{ij} = -x_{ij} + \sum_{S_r(i,j)} A(i,j;k,l)\, y_{kl} + \sum_{S_r(i,j)} B(i,j;k,l)\, u_{kl} + z_{ij} \tag{1}$$

$$y_{ij} = f(x_{ij}) \tag{2}$$

where $x_{ij} \in \mathbb{R}$, $y_{ij} \in \mathbb{R}$, $u_{ij} \in \mathbb{R}$, and $z_{ij} \in \mathbb{R}$ are the state, output, input signal and threshold of cell $C(i,j)$, respectively. The output function is a non-linear function, corresponding to the activation function of conventional

Artificial Neural Networks. The simplest one is the standard nonlinearity [1]: $f(x_{ij}) = \frac{1}{2}|x_{ij}-1| + \frac{1}{2}|x_{ij}-1|$. The evolution of the CNN cell states starts from an initial condition $x_{ij}(0)$, $i = 1, 2, \ldots, M$, $j = 1, 2, \ldots, N$. The synaptic connections $A(i,j;k,l)$ and $B(i,j;k,l)$ can be non-linear operators, denoted $A(i,j;k,l) \circ y_{kl}$ and $B(i,j;k,l) \circ u_{kl}$. They can be time variant, though usually they are assumed time invariant. If the synaptic connections are space invariant they are denote $A(k,l)$ and $B(k,l)$.

The CNN effectively implements a system of ordinary differential equations. The existence and uniqueness of solutions are guaranteed in the case of linear synaptic operators and continuous input signal, threshold and Lipschitz continuous non-linearity $f(x)$. If the initial state, input signal and threshold are bounded then the solution of the standard CNN is bounded.

The time and space invariant CNN with a linear output function implements a linear system that performs linear filtering of the input signal, usually an image. Therefore they can be designed to perform edge detection, smoothing, contrast boosting and other linear filtering operations on the input image [1]. Synaptic connections may have delays, so that they are systems with memory and inner states. The inclusion of delays allows to work on image sequences, performing temporal filtering for motion detection and other time based operations. Morphological image operators, such as erosion and dilation, can be approximated with appropriate nonlinearities.

3 Associative Morphological Memories and morphological independence

One of the most outstanding areas of Lattice Computing [6], the work on Associative Morphological Memories (AMM) stems from the consideration of the partially ordered ring $(\mathbb{R}, \vee, \wedge, +)$ instead of the algebraic ring $(\mathbb{R}, +, \cdot)$ as the computational framework for the definition of Neural Networks algorithms [17, 13]. The operators $\vee$ and $\wedge$ denote, respectively, the max and min operators. The AMM are the morphological counterpart of the well known Hopfield Associative Memories [11]. Given a set of input/output pairs of pattern $(X,Y) = \left\{\left(\mathbf{x}^{\xi}, \mathbf{y}^{\xi}\right); \xi = 1, .., k\right\}$, an heteroassociative memory based on the pattern's cross correlation [11] is built up as $W = \sum_{\xi} \mathbf{y}^{\xi} \cdot \left(\mathbf{x}^{\xi}\right)'$. Mimicking this construction procedure [17, 13] propose the following dual constructions of Heteroassociative Morphological Memories (HMM's), the erosive HMM: $W_{XY} = \bigwedge_{\xi=1}^{k} \left[\mathbf{y}^{\xi} \times \left(-\mathbf{x}^{\xi}\right)'\right]$ and the dilative HMM $M_{XY} = \bigvee_{\xi=1}^{k} \left[\mathbf{y}^{\xi} \times \left(-\mathbf{x}^{\xi}\right)'\right]$where $\times$ can be the $\boxtimes$ or $\boxtimes$ operators. Here $\boxtimes$ and $\boxtimes$ denote the max and min matrix product, respectively defined as follows:

$$C = A \boxtimes B = [c_{ij}] \Leftrightarrow c_{ij} = \bigvee_{k=1..n} \{a_{ik} + b_{kj}\}, \tag{3}$$

$$C = A \boxtimes B = [c_{ij}] \Leftrightarrow c_{ij} = \bigwedge_{k=1..n} \{a_{ik} + b_{kj}\}. \tag{4}$$

If $X = Y$ then the HMM memories are Autoassociative Morphological Memories (AMM). Memory recall is the response obtained from the HMM or AMM when presented with a pattern. Pattern presentation consists in the max or min matrix product with the W or M memory, respectively. For HMM memory recall is equivalent to realization of an input/output map. For the AMM it is equivalent to recalling an stored pattern. The interest of associative memories lies in its ability to recover stored patterns when presented with incomplete or distorted patterns.

In the continuous case, the AMM's are able to store and recall any set of patterns, that is, $W_{XX} \boxtimes \mathbf{x} = \mathbf{x} = M_{XX} \boxtimes \mathbf{x}$, $\forall \mathbf{x} \in X$, which can be stated in compact form as follows $W_{XX} \boxtimes X = X = M_{XX} \boxtimes X$, for any X. That is, AMMs possess *perfect recall* for noiseless patterns [17, 13]. It is also interesting to note that if we iterate the memory recall we obtain a fixed point very fast, in fact it is obtained at the second iteration:

$$W_{XX} \boxtimes \mathbf{z} = \mathbf{v} \Rightarrow W_{XX} \boxtimes \mathbf{v} = \mathbf{v}, \tag{5}$$

$$M_{XX} \boxtimes \mathbf{z} = \mathbf{u} \Rightarrow M_{XX} \boxtimes \mathbf{u} = \mathbf{u}. \tag{6}$$

The set of fixed points $F(X)$ of the morphological memories constructed from the set of patterns X is the same for both types of AMM: $F(X) = \{\mathbf{x} \,|W_{XX} \boxtimes \mathbf{x} = \mathbf{x}\} = \{\mathbf{x} \,|M_{XX} \boxtimes \mathbf{x} = \mathbf{x}\}$. They are the set of vectors lattice dependent on X.

Let it be $\widetilde{\mathbf{x}}^\gamma$ a noisy version of $\mathbf{x}^\gamma$. If $\widetilde{\mathbf{x}}^\gamma \leq \mathbf{x}^\gamma$ then $\widetilde{\mathbf{x}}^\gamma$ is the result of applying *erosive noise* to $\mathbf{x}^\gamma$. If $\widetilde{\mathbf{x}}^\gamma \geq \mathbf{x}^\gamma$ then $\widetilde{\mathbf{x}}^\gamma$ is the result of applying *dilative noise* to $\mathbf{x}^\gamma$. Morphological memories are selectively sensitive to erosive and dilative noise. The conditions of *robust* perfect recall (i.e. perfect recall from noisy patterns) are the following ones[17, 13]. Given a set of patterns X, the equality

$$W_{XX} \boxtimes \widetilde{\mathbf{x}}^\gamma = \mathbf{x}^\gamma,\ \mathbf{x}^\gamma \in X \tag{7}$$

holds when the noise affecting the pattern is erosive $\widetilde{\mathbf{x}}^\gamma \leq \mathbf{x}^\gamma$ and the following relation holds:

$$\forall i \exists j_i; \widetilde{x}_{j_i}^\gamma = x_{j_i}^\gamma \vee \left(\bigvee_{\xi \neq \gamma} \left(x_i^\gamma - x_i^\xi + x_{j_i}^\xi \right) \right). \tag{8}$$

Similarly, the equality

$$M_{XX} \boxtimes \widetilde{\mathbf{x}}^\gamma = \mathbf{x}^\gamma \tag{9}$$

holds when the noise affecting the pattern is dilative $\widetilde{\mathbf{x}}^\gamma \geq \mathbf{x}^\gamma$ and the following relation holds:

$$\forall i \exists j_i; \widetilde{x}_{j_i}^\gamma = x_{j_i}^\gamma \wedge \left(\bigwedge_{\xi \neq \gamma} \left(x_i^\gamma - x_i^\xi + x_{j_i}^\xi \right) \right). \tag{10}$$

The recall with both dual AMM will fail to recover the stored pattern if it is affected by a mixture of erosive and dilative noise.

To obtain general noise robustness [12] some works proposed the kernel method and some enhancements [13, 16]. In the formalization of the kernel construction, [16] introduced the notion of morphological independence. Here we distinguish erosive and dilative versions of this definition. Given vectors $\mathbf{x}, \mathbf{y} \in \mathbb{R}^d$, $\mathbf{y}$ is morphologically *dependent* in the *erosive* sense of $\mathbf{x}$ if $\mathbf{y} \leq \mathbf{x}$, $\mathbf{y}$ is morphologically *dependent* in the *dilative* sense of $\mathbf{x}$ if $\mathbf{y} \geq \mathbf{x}$. In both cases, we say that $\mathbf{x}$ is dominant. Given a set of vectors $X = \left(\mathbf{x}^1, \mathbf{x}^2, \ldots, \mathbf{x}^k\right)$, a vector of the same dimensionality $\mathbf{y}$ is said to be morphologically independent of X in the *erosive* sense if $\mathbf{y} \not\leq \mathbf{x}^\gamma; \gamma = \{1, .., k\}$, and morphologically independent of X in the *dilative* sense if $\mathbf{y} \not\geq \mathbf{x}^\gamma; \gamma = \{1, .., k\}$. The set of vectors X is said to be morphologically independent in either sense when all the patterns are morphologically independent of the remaining patterns in the set. Given the erosive W_{XX} and dilative M_{XX} memories constructed from X, if a test pattern $\mathbf{y} \notin X$ is morphologically independent of X in the erosive sense, then $W_{XX} \boxtimes \mathbf{y} \notin X$. Also, if $\mathbf{y}$ is morphologically independent of X in the dilative sense, then $M_{XX} \boxtimes \mathbf{y} \notin X$. Morphological independence has been generalized to lattice independence in recent works [14, 15] establishing its relation with affine independence. This equivalence is very useful for the induction of endmembers from data for linear unmixing processes [10, 9].

4 The Morphological Cellular Neural Network (MCNN)

The aim of Morphological Cellular Neural Network (MCNN) is to perform the segmentation of images with multidimensional range, such as colour, multispectral or hyperspectral images, on the basis of the morphological properties of the pixel values. First we consider the definition of MCNN along the lines of the conventional CNN described in section 2. Let us consider that cells $C(i, j)$ have a multidimensional state $\mathbf{x}_{ij} \in \mathbb{R}^d$. Let us denote $Y_{ij}(t)$ the set of the states of the neighbouring cells in $S_r(i, j)$ at time t. The MCNN synaptic operators will be based on the erosive and dilative memories: W_{YY} and M_{YY}, respectively, built from $Y_{ij}(t)$[1]. According to the kind of the AMM, we can define dual MCNN dynamics. The erosive MCNN

$$\mathbf{x}_{ij}(t+1) = W_{YY} \boxtimes \mathbf{x}_{ij}(t), \tag{11}$$

and the dilative MCNN. The dynamics of the MCNN can be defined formally as follows:

$$\mathbf{x}_{ij}(t+1) = M_{YY} \boxtimes \mathbf{x}_{ij}(t). \tag{12}$$

The convergence of the MCNN dynamics is related to the properties of AMM fixed points. Although both memories share the same fixed point set they do

[1] (We have taken a notation liberty: $Y_{ij}(t) \equiv Y$)

not obtain the same result for non-fixed point vectors, therefore dynamics of equations (11) and (12) will produce divergent behaviours starting from the same initial conditions.

Will the MCNN converge to a fixed point global state in finite time?. If $\mathbf{x}_{ij}(t+1) \neq \mathbf{x}_{ij}(t)$ and the neighbouring cells do not change $Y_{ij}(t) = Y_{ij}(t+1)$, then $\mathbf{x}_{ij}(t+2) = \mathbf{x}_{ij}(t+1)$ by equation (5) or (6), depending on the MCNN type. If there is a change in the neighbouring cells, i.e. $Y_{ij}(t) \neq Y_{ij}(t+1)$, there will be a finite number of state changes before the cell's state reaches a fixed point even if all the neighbouring cells change their states. However, there is not guarantee that no indefinite cycling behaviours may appear. The process may only be proved to converge if it is possible to prove that the sequences of fixed points $F(Y_{ij})$ and $F(Y_{kl})$ are ordered and have a limit value. To our knowledge, this is an open question.

In the stationary configuration we have that each cell state is a fixed point of the AMM constructed with its corresponding neighbouring cell states:

$$\mathbf{x}_{ij} = W_{Y_{ij}Y_{ij}} \boxtimes \mathbf{x}_{ij},\ i = 1, 2, \ldots, N; j = 1, 2, \ldots, M.$$

From the review of the section 3, this condition holds when some of the following situations arise:

- $\mathbf{x}_{ij} = \mathbf{x}_{kl}$ for at least one $(k, l) \in S_r(i, j)$. If all the neighbouring cells have the same state, then the cell is in the middle of an homogenous region of the MCNN configuration. If some of the neighbouring cells have different states, then it is in the boundary between regions.

- $\mathbf{x}_{ij}$ is lattice dependent of Y_{ij}. That means that stationary regions can be composed of cell states which are different, but mutually lattice dependent. This is a drawback from the image segmentation point of view, unless some kind of equivalence relation can be defined allowing to identify the same region.

5 The Morphological Cellular Automata (MCA)

We look for the detection of homogeneous image regions. The MCNN converge to a segmentation of the image into regions of lattice dependent states, which are not visually identified as an homogenous region. Therefore, we return to the concept of morphological independence. Our aim is to obtain as boundaries morphological independent neighbours, while using morphological dependence to "assimilate" neighbouring pixels. This Morphological Cellular Automata (MCA) is summarized in Algorithm 1.

Let us define $\left\{\mathbf{f}(i, j) \in \mathbb{R}^d; i = 1, .., N; j = 1, .., M\right\}$ the RGB, multispectral or hyperspectral image, $\boldsymbol{\mu}$ and $\boldsymbol{\sigma}$ the vectors of the mean and standard deviations of each band computed over the image, α the band-wise equivalence interval factor. The addition and subtraction of $\alpha\boldsymbol{\sigma}$ to each state vector allows

Algorithm 1 Morphological Cellular Automata dynamics

1. Initialize the MCNN state to the image pixel values: $X(0) = \{\mathbf{x}_{ij}(0) = \mathbf{f}^c(i,j)\}$.
2. Repeat until convergence $X(t) = X(t+1)$, for increasing t:
   (a) For each pair of neighbouring cells (i,j), $(k,l) \in S_1(i,j)$:
      i. compute the upper and lower bounds of the interval defined assuming independent Gaussian noise sources $\mathbf{x}_{ij}^- = \mathbf{x}_{ij}(t) - \alpha\boldsymbol{\sigma}$ and $\mathbf{x}_{ij}^+ = \mathbf{x}_{ij}(t) + \alpha\boldsymbol{\sigma}$
      ii. if $(\mathbf{x}_{ij}^- < \mathbf{x}_{kl}(t) < \mathbf{x}_{ij}^+$ and $\|\mathbf{x}_{ij}(t)\| < \|\mathbf{x}_{kl}(t)\|$) or $\left(\mathbf{x}_{ij}^- \leq \mathbf{x}_{kl}(t)\right)$ or $\left(\mathbf{x}_{kl}(t) \geq \mathbf{x}_{ij}^+\right)$
         - then $\mathbf{x}_{ij}(t+1) = \mathbf{x}_{kl}(t+1) = \mathbf{x}_{kl}(t)$,
         - else $\mathbf{x}_{ij}(t+1) = \mathbf{x}_{ij}(t)$; $\mathbf{x}_{kl}(t+1) = \mathbf{x}_{kl}(t)$

to define an interval of equivalence between cell states intended to overcome over-segmentation when morphological independence is due to noise conditions. The image is preprocessed as in the previous algorithm so that each pixel is a zero mean vector $\{\mathbf{f}^c(i,j) = \mathbf{f}(i,j) - \boldsymbol{\mu};\ i = 1,..,N; j = 1,..,M\}$. Algorithm 1 is initialized with this centred image. It repeats the computation of the new configuration $X(t)$ until convergence is reached. Convergence consists in the absence of changes. Cells are considered in pairs, and their state is changed according to the following reasoning: If there is morphological dependence (either erosive or dilative) the dominant cell assimilates the dependent cell. Previously, we consider the existence of an equivalence interval defined on the basis of the band-wise variance. If the neighbouring cell falls in this interval, then the one with the greatest norm dominates, regardless of morphological independence/dependence relation.

6 Results on image segmentation

The experimental image is the well known "lena" image. To reduce the computational burden, we have down sampled it to a 64×64 size. The actual image used in the experiments is shown in figure 1a. The segmentation obtained with the algorithm of the MCA without equivalence interval ($\alpha = 0$) is shown in figure 1b. This segmentation is obtained when the algorithm reaches an invariant state. The colours shown correspond to the morphologically independent colours that have propagated from their original pixel sites, absorbing morphologically dependent pixel sites. The main features of the image can be distinguished in this segmentation. Observe that some regions of similar colour are not identified because they are separated by connected regions of an morphologically independent colour. For comparison we show in figure 2 the results

(a) (b)

Figure 1: (a) Original Lena image. (b) Segmentation of the lena image obtained without noise parameter

(a) (b)

Figure 2: colour quantization into 8 colours (a) and 32 colours (b).

of the identification of colour regions performed by standard colour Quantization algorithms based on the minimization of the quantization distortion. The activation of the noise related equivalence interval has the effect of allowing the fusion of regions of morphologically independent colours. As can be appreciated in figure 3, increasing α decreases the number of identified regions until all detail is lost. This mechanism may allow to obtain segmentations at diverse resolutions.

7 Conclusions

We have first proposed a MCNN based on the application of AMM as synaptic operators. The approach has a very fast convergence but introduces little changes in the image and does not detect homogenous regions for segmentation. Therefore, we have introduced a MCA based on the morphological dependence and independence notions to obtain homogeneous regions from morphological dependent pixels, with the boundary of such regions defined by the morphological independence between neighbouring pixels. We have shown that the

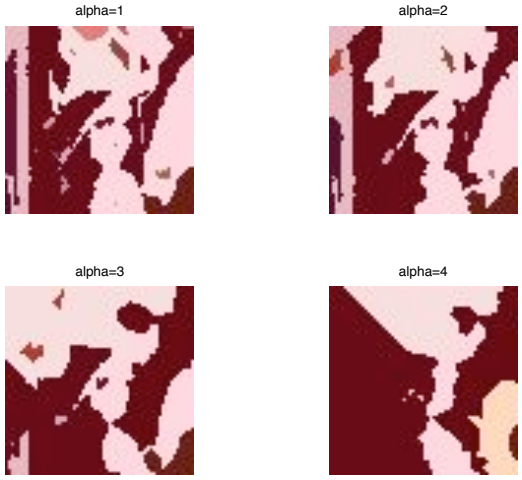

Figure 3: Evolution of the segmentation obtained increasing the parameter α

approach produces consistent connected regions of homogeneous colours. Besides, we introduce a colour equivalence parameter α controlling the size of an equivalence interval defined on the colour component variances which allows to control the resolution of the segmentation. We look forward to the application of these works in practical devices such as intelligent blackboards [8].

References

[1] L. O. Chua and T. Roska. *Cellular neural networks and visual computing: foundation and applications*. Cambridge University Press, June 2002.

[2] L.O. Chua and L. Yang. Cellular neural networks: applications. *Circuits and Systems, IEEE Transactions on*, 35(10):1273–1290, 1988.

[3] L.O. Chua and L. Yang. Cellular neural networks: theory. *Circuits and Systems, IEEE Transactions on*, 35(10):1257–1272, 1988.

[4] E. Corchado, A. Abraham, and A.C. Ponce. Hybrid intelligent algorithms and applications. *Information Science*, 180(14):2633–2634, 2010.

[5] A. d'Anjou, M. Graña, F. J. Torrealdea, and M. Hernandez. Solving satisfiability via boltzmann machines. *IEEE Transactions on pattern analysis and machine intelligence*, 15:514–521, 1993.

[6] M. Graña. A brief review of lattice computing. In *Proc. WCCI 2008*, pages 1777–1781, 2008.

[7] M. Graña, A. d'Anjou, F.X. Albizuri, M. Hernandez, F. J. Torrealdea, and A.I. Gonzalez. Experiments of fast learning with high order boltzmann machines. *Applied Intelligence*, 7(4):287–303, 1997.

[8] M. Graña, A. d'Anjou, and F. J. Torrealdea. User expectations for the intelligent blackboard. *Displays*, 17 (3-4):143–146, 1997.

[9] M. Graña, A. Manhaes-Savio, M. García-Sebastián, and E. Fernandez. A lattice computing approach for on-line fmri analysis. *Image and Vision Computing*, 28(7):1155–1161, 2010.

[10] M. Graña, I. Villaverde, J.O. Maldonado, and C. Hernandez. Two lattice computing approaches for the unsupervised segmentation of hyperspectral images. *Neurocomputing*, 72(10-12):2111–2120, 2009.

[11] Hopfield J.J. Neural networks and physical systems with emergent collective computational abilities. *Proc. Nat. Acad. Sciences*, 79(2554-2558), 1982.

[12] Bogdan Raducanu, Manuel Graña, and F. Xabier Albizuri. Morphological scale spaces and associative morphological memories: Results on robustness and practical applications. *J. Math. Imaging Vis.*, 19(2):113–131, 2003.

[13] G. X. Ritter, J. L. Diaz de Leon, and P. Sussner. Morphological bidirectional associative memories. *Neural Networks*, 12(6):851 – 867, 1999.

[14] Gerhard Ritter and Paul Gader. Fixed points of lattice transforms and lattice associative memories. volume 144 of *Advances in Imaging and Electron Physics*, pages 165 – 242. Elsevier, 2006.

[15] Gerhard X. Ritter and Gonzalo Urcid. Lattice algebra approach to endmember determination in hyperspectral imagery. volume 160 of *Advances in Imaging and Electron Physics*, pages 113 – 169. Elsevier, 2010.

[16] Gerhard X. Ritter, Gonzalo Urcid, and Laurentiu Iancu. Reconstruction of patterns from noisy inputs using morphological associative memories. *Journal of Mathematical Imaging and Vision*, 19:95–111, 2003. 10.1023/A:1024773330134.

[17] G.X. Ritter, P. Sussner, and J.L. Diaz-de Leon. Morphological associative memories. *Neural Networks, IEEE Transactions on*, 9(2):281 –293, mar. 1998.

[18] Michal Wozniak and Marcin Zmyslony. Designing fusers on the basis of discriminants - evolutionary and neural methods of training. In E. Corchado, M. Graña, and A. Savio, editors, *HAIS 2010*, LNAI, pages 590–597. Springer, 2010.

Neurocognitive disorder detection based on Feature Vectors extracted from VBM analysis of structural MRI

A. Savio[1], M.T. García-Sebastián[1], D. Chyzyk[1], C. Hernandez[1], M. Graña[1], A. Sistiaga[3,5,6], A. López de Munain[4,5,6], J. Villanúa[2]

May 11, 2011

[1]Grupo de Inteligencia Computacional, www.ehu.es/ccwintco
[2]Osatek S.A., Hospital Donostia San Sebastián, Spain.
[3]Neuroscience Department, Universidad del Pais Vasco UPV-EHU, San Sebastian, Spain
[4]Neurology Service, Donostia Hospital, San Sebastian, Spain
[5]Area de Neurociencias, Instituto Biodonostia
[6]Centro de Investigación Biomédica en Red sobre Enfermedades Neurodegenerativas (CIBERNED), Instituto Carlos III, Spain

Abstract

Dementia is a growing concern due to the aging process of the western societies. Non-invasive detection is therefore a high priority research endeavor. In this paper we report results of classification systems applied to the feature vectors obtained by a feature extraction method computed on Structural Magnetic Resonance Imaging (sMRI) volumes for the detection of two neurological disorders with cognitive impairment: Myotonic Dystrophy of type 1 (MD1) and Alzheimer Disease (AD). The feature extraction process is based on the voxel clusters detected by Voxel Based Morphometry (VBM) analysis of sMRI upon a set of patient and control subjects. This feature extraction process is specific for each kind of disease and is grounded on the findings obtained by medical experts. The 10-fold cross-validation results of several statistical and neural network based classification algorithms trained and tested on these features show high specificity and moderate sensitivity of the classifiers, suggesting that the approach is better suited for rejecting than for detecting early stages of the diseases.

1 Introduction

Nowadays, there is much research effort devoted to the development of ways to provide automatized diagnostic support tools that may help the clinicians

to perform their work faster with additional assesment data, to meet the ever increasing demands of primary attention of a rising population of patients with neurological disorders. The present paper will be focused on the application of statistical and Computational Intelligence algorithms for the automatic detection of two very specific pathologies, Alzheimer's Disease (AD) and Myotonic Dystrophy of type 1 (MD1), from the analysis of structural (T1 weighted) Magnetic Resonance Imaging (sMRI) data. The AD is a primary dementia while MD1 is a muscular dystrophy, but both of them show cognitive impairment. The prevalence of MD1 in our local region of Gipuzkoa (Spain) is high[17, 18]. We describe a feature extraction method based on Voxel Based Morphometry (VBM). These features will be the input for several Artificial Neural Network (ANN) and Support Vector Machine (SVM) classification systems.

We have found in the literature several sMRI feature extraction proposals for classification: some based on morphometric methods [16, 20, 37, 65], some based on ROIs/VOIs (regions-of-interest/volumes-of-interest) [45, 43, 24], and some on gray matter (GM) voxels in automated segmentation images [39]. There are also studies aiming to explore the improvement obtained in the SVM classifier by adding covariates such as demographic or genotype information [64]. Work has also been reported on the selection of the most informative features for classification, such as the SVM-Recursive Feature Elimination [20], the selection based on statistical tests [45, 53] or the wavelet decomposition of the RAVENS maps [43], among others.

Our approach uses the VBM detected clusters as a mask to select the potentially most discriminating voxels on the Grey Matter (GM) segmentation volumes. Feature vectors for classification are either the GM segmentation voxel values or some summary statistics of each cluster. We both consider the feature vector computed from all the VBM clusters and the combination of the individual classifiers built from the clusters independently. We test classification systems built using the standard SVM, with linear and non-linear (RBF) kernels, and some ANN architectures: Learned Vector Quantization (LVQ), Multi-Layer Perceptron (MLP), Radial Basis Function (RBF), Probabilistic Neural Networks (PNN). We have also tested combinations of SVM classifiers trained on independent VBM clusters and an Adaptive Boosting (AdaBoost) strategy tailored to the SVM [44]. As a general result, the diverse systems showed a moderate accuracy due to a moderate sensitivity, and high specificity. Best results we obtained with an LVQ approach and an AdaBoost on SVM classifiers. Some of the results have been published separately in conference proceedings [25, 56, 55].

Section 2 gives some background medical information on the studied dementia. Section 3 gives a description of the subjects selected for the study, the image processing and in Section 4 we describe feature extraction details and the classifier systems. Section 5 gives classification performance results obtained in the diverse computational experiments performed on the data. Finally, section 6 gives the conclusions of this work and suggestions for further research .

2 Medical background

2.1 Alzheimer's Disease

Alzheimer's Disease (AD) is a neurodegenerative disorder, which is one of the most common cause of dementia in old people. Due to the socioeconomic importance of the disease in occidental countries there is a strong international effort focus in AD. The diagnosis of AD can be done after the exclusion of other forms of dementia but a definitive diagnosis can only be made after a post-mortem study of the brain tissue. This is one of the reasons why Magnetic Resonance Imaging (MRI) based early diagnosis is a current research hot topic in the neurosciences. The pharmaceutical companies have already recognized that imaging techniques especially MRI and Positron Emission Tomography (PET) provide "surrogate" information concerning the pattern and rate of neurodegeneration, which can be used to monitor the effects of treatments which slow the progression of neurodegeneration. Therefore, there is high interest in the development of automated detection procedures based on MRI and other medical imaging techniques.

Besides MRI, other medical imaging methods are being studied for AD diagnosis. There are studies applying Support Vector Machine (SVM) either with linear [65, 39, 64] or nonlinear [20, 43] kernels, to discriminate AD patients from controls based on Positron Emission Tomography (PET), Single-Photon Emission Tomography (SPECT) functional volumes [24, 46, 38, 53] or studies that combine structural and functional information such as [19], where sMRI and PET volumes are used.

Many of the classification studies on the detection of AD were done with both men and women. However, it has been demonstrated that brains of women are different from men's to the extent that it is possible to discriminate the gender via MRI analysis [42]. Moreover, it has been shown that VBM is sensitive to the gender differences. For these reasons, we have been very cautious in this study. We have selected a set of 98 MRI women's brain volumes. It must be noted that this is a large number of subjects compared with the other studies referred above.

2.2 Myotonic Dystrophy Type 1

Myotonic Dystrophy type 1 (MD1) is a slowly progressive myopathy characterized by varying multisystemic involvement, affecting skeletal and smooth muscles, the heart (arrhythmia, electrical conductivity defects), the endocrine system (hyperinsulinemia) and eyes (cataract) [34]. It is transmitted in an autosomal dominant manner and it is due to an unstable pathological expansion of (CTG)n repeats [6]. Epidemiologically, MD1 is the most frequent neuromuscular disorder with a reported prevalence between 69 to 90 cases per million [50]. However, the prevalence is significantly higher in Gipuzkoa (North of Spain), reaching 300 cases per million inhabitants [17].

Previous neuroimaging studies using MRI of MD1 patients have found corti-

cal atrophy, increased ventricular size with periventricular hypodensity, subcortical white matter involvement and calcification of the basal ganglia [12, 15, 35]. Many brain disorders have subtle morphological abnormalities of the brain not easily detected on routine examination of MR images [52]; VBM methods have become popular for detecting these abnormalities [3]. In MD1, volumetric studies have identified atrophy of the GM along different cortical areas (mainly in prefrontal area) but these previous studies are methodologically limited regarding to the sample size and the data correction level [2, 51]. Besides, these studies have analyzed the association between brain volumes and some clinical as well as genetic data, but none but none of them have measured the correlation with neuropsychological data.

3 Materials

In this section we will describe the main characteristics of the sMRI data used for the computational experiments. The AD experiments were performed on a subset of the publicly available OASIS database, while the DM1 experiments were performed on a database that has been developed in the Donostia Hospital along the past years of clinical practice with this disease. The data have been obtained from diverse MRI scanners and under different imaging protocols, therefore they can not be combined at the present state of our research to produce AD versus MD1 discriminant systems.

3.1 MD1 Subjects

The MD1 patients analysed in this work were selected from those attending in the outpatient consultancies at the Neurology Department of the Donostia Hospital (San Sebastian), a tertiary public hospital which covers a population of 650,000 inhabitants (almost all of Guipuzcoa province). All patients were explored by a neurologist and had previously participated in another study in which we assessed them neuropsychologically [59]. The patient-selection criteria were as follows: Inclusion criteria for MD1 patients: Between 18 and 65 years old and molecular confirmation of the clinical diagnosis. Exclusion criteria: A history of a major psychiatric or somatic disorder (in accordance with DSM-IV criteria), acquired brain damage or alcohol or drug abuse, the presence of corporal paramagnetic body devices (pacemaker, etc.) that impedes a MRI study and the presence of cerebral anomalies which could affect the volumetric analysis. An age and sex matched healthy control subject (CS) was included for each MD1 patient. This control group consisted of unaffected family members and healthy volunteers with none of these pathologies. All patients were informed of the objectives and details of the study and signed an informed consent. The study was approved by the hospital's ethics committee.

		MD1	CS
Socio-demographic characteristics			
Number of subjects		30	30
Age	Mean (SD)	44.0 (11.6)	44.2 (11.7)
	Min-Max	24-62	22-62
Sex n (%)	Male	14 (47%)	14 (47%)
	Female	16 (53%)	16 (53%)
Educational level n (%)	Primary	18 (60%)	5 (21%)
	Secondary	7 (23%)	9 (37%)
	Higher	5 (17%)	10 (41%)
Clinical and molecular characteristics			
Muscle weakness (MIRS[1])	Mean (SD)	2.9 (1.2)	–
	Min-Max	1-5	
Molecular defect (CTG)	Mean (SD)	635 (472)	–
	Min-Max	65-1833	
White matter lesions n (%)	Yes	16 (53%)	5 (18%)
	No	14 (47%)	22 (82%)

Table 1: Summary of subject demographics and MD1 status. [1]Muscular Impairment Rating Scale.

3.1.1 Imaging Protocol for MD1 data

MR scanning was performed on a 1.5 Tesla scanner (Achieva Nova, Philips). The current results are based on a high-resolution volumetric "turbo field echo" (TFE) series (sagital 3D T1 weighted acquisition, TR = 7.2, TE = 3.3, flip angle = 8, matrix = 256 x 232, slice thickness 1mm, voxel dimensions of 1mm x 1mm x 1mm, NSA = 1, nº slices 160, slice thickness= 1, gap= 0, total scan duration 5´34¨). In addition to 3DT1 weighted images, conventional axial dual T2 turbo spin echo images (TR = 1800, TE = 20, flip angle = 90º , FOV= 230, matrix = 256 x 154, slice thickness= 5, gap= 1, nº acquisition =2, nº slices= 22) and fluid attenuation inversion recovery images (FLAIR) in coronal plane (TR = 10000, TI = 2800, TE= 140 , FOV= 230, matrix = 256 x 159, slice thickness= 5, gap= 1, nº acquisition =2, nº slices= 25) were acquired to evaluate the presence of white matter lesions (WMLs). All the scans were acquired on the same MR scanner and no hardware or software upgrades of the equipment were carried out within the study period.

3.2 OASIS subjects

Ninety eight right-handed women (aged 65-96 yr) were selected from the Open Access Series of Imaging Studies (OASIS) database [48]. OASIS data set has a cross-sectional collection of 416 subjects covering the adult life span aged 18 to 96 including individuals with early-stage Alzheimer's Disease. We have ruled out a set of 200 subjects whose demographic, clinical or derived anatomic volumes information was incomplete. For the present study there are 49 subjects

	Very mild to mild AD	CS
No. of subjects	49	49
Age	78.08 (66-96)	77.77 (65-94)
Education	2.63 (1-5)	2.87 (1-5)
Socioeconomic status	2.94 (1-5)	2.88 (1-5)
CDR (0.5 / 1 / 2)	31 / 17 / 1	0
MMSE	24 (15-30)	28.96 (26-30)

Table 2: Summary of subject demographics and dementia status. Education codes correspond to the following levels of education: 1 less than high school grad., 2: high school grad., 3: some college, 4: college grad., 5: beyond college. Categories of socioeconomic status: from 1 (biggest status) to 5 (lowest status). MMSE score ranges from 0 (worst) to 30 (best).

who have been diagnosed with very mild to mild AD and 49 non-demented. A summary of subject demographics and dementia status is shown in table 3.2.

3.2.1 OASIS Imaging Protocol

The OASIS database has been built following a strict imaging protocol, to avoid variations due to imaging protocol which would pose big image normalization problems. Multiple (three or four) high-resolution structural T1-weighted magnetization-prepared rapid gradient echo (MP-RAGE) images were acquired [21] on a 1.5-T Vision scanner (Siemens, Erlangen, Germany) in a single imaging session. Image parameters: TR= 9.7 msec., TE= 4.0 msec., Flip angle= 10, TI= 20 msec., TD= 200 msec., 128 sagittal 1.25 mm slices without gaps and pixels resolution of 256×256 (1×1mm).

4 Methods

In this section we will describe the different computational processes applied to the data. First, we summarize the Voxel Based Morphometry (VBM) process, and we give details of its independent application to the AD and MD1 data. Second, we describe the feature extraction process. Finally, we give summary descriptions of the diverse approaches used to build the classifiers, both single and combinations of classifiers.

4.1 Voxel-based Morphometry (VBM)

Morphometry analysis has become a common tool for computational brain anatomy studies. It allows a comprehensive measurement of structural differences within a group or across groups, not just in specific structures, but throughout the entire brain. Voxel Based Morphometry (VBM) is a computational approach to neuroanatomy that measures differences in local concentrations of brain tissue, through a voxel-wise comparison of multiple brain images

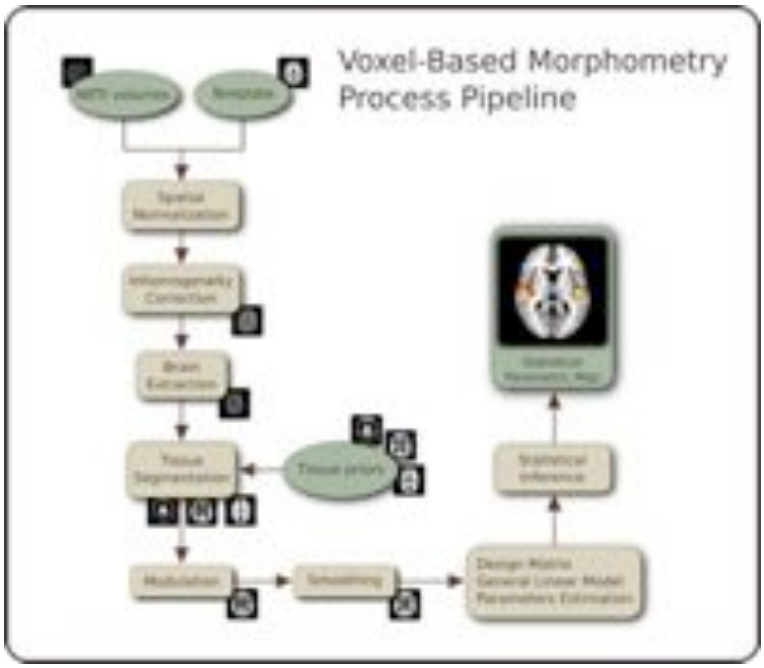

Figure 1: The processing pipeline of the Voxel Based Morphometry (VBM) on structural MRI volumes.

[3]. For instance, VBM has been applied to study volumetric atrophy of the grey matter (GM) in areas of neocortex of AD patients vs. control subjects [9, 57, 23]. The processing pipeline of VBM is illustrated in figure 1. The procedure involves the spatial normalization of subject images into a standard space, segmentation of tissue classes using *a priori* probability maps, smoothing to correct noise and small variations, and voxel-wise statistical tests. Smoothing is done by convolution with a Gaussian kernel whose the Full-Width at Half-Maximum (FWHM) is tuned to the data of ech case study. Statistical analysis is based on the General Linear Model (GLM) to describe the data in terms of experimental and confounding effects, and residual variability, applied to each voxel independently. Statistical inference is used to test hypotheses that are expressed as linear functions of the GLM estimated regression parameters. These linear scalar functions are called contrasts in SPM terminology. The value of this contrast at each voxel constitutes a Statistical Parametric Map (SPM), which is thresholded according to the Random Field theory.

4.1.1 Image processing and VBM for OASIS

We have used the average MRI volume for each subject, provided in the OASIS data set. These images are already registered and re-sampled into a 1-mm isotropic image in atlas space and the bias field has been already corrected [48].

The Statistical Parametric Mapping software (SPM8) [1] was used to compute the VBM which gives us the spatial mask to obtain the classification features. Images were reoriented into a right-handed coordinate system to work with SPM8. The tissue segmentation step does not need to perform bias correction. We performed the modulation normalization for GM, because we are interested in this tissue for this study. We performed a spatial smoothing before performing the voxel-wise statistics, setting the FWHM of the Gaussian kernel to 10mm isotropic. A GM mask was created from the average of the GM segmentation volumes of the subjects under study. Thresholding the average GM segmentation, we obtain a binary mask that includes all voxels with probability greater than 0.1 in the average GM segmentation volume. This interpretation is not completely true, since the data is modulated, but it is close enough for the mask to be reasonable. We designed the statistical analysis as a two-sample t-test in which the first group corresponds with AD subjects. In SPM software jargon: the contrast has been set to [-1 1], a right-tailed (groupN $>$ groupAD), correction FWE, p-value=0.05. The VBM detected clusters are used for the feature extraction for the classification procedures. Statistical significance was determined using an extent threshold of 0 adjacent voxels for two sample comparisons. The clusters of significant voxels detected by the VBM analysis are displayed in figure 2, they agree with the findings reported in the literature [9, 57, 23].

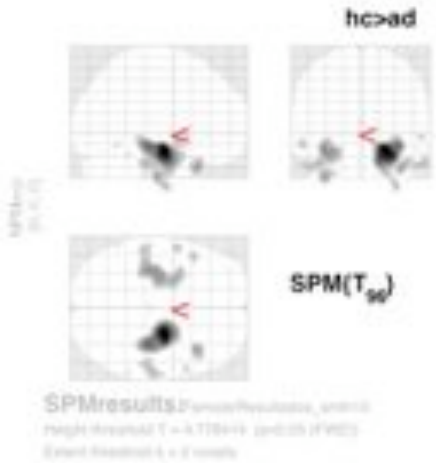

Figure 2: SPM results: clusters of significant voxels with increased gray matter density in the controls relative to the patient subjects, detected by the VBM process.

4.1.2 Image processing and VBM for MD1

The Statistical Parametric Mapping software (SPM8) [1] was used to compute the VBM which gives us the spatial mask to obtain the classification features.

Images were reoriented into a right-handed coordinate system to work with SPM8. The tissue segmentation step does not need to perform bias correction. We performed the modulation normalization for GM, because we are interested in this tissue for this study. We performed a spatial smoothing before performing the voxel-wise statistics, setting the FWHM of the isotropic Gaussian kernel to 8mm, 9mm, 10mm, 11mm and 12mm . For all comparisons we have applied a significance probability threshold of $p<0.05$ FWE corrected for multiple comparisons at a voxel-level. Statistical significance was determined using spatial extent thresholds of 0, 100 and 200 adjacent voxels for two sample comparisons.

4.2 Feature extraction

We have tested two different feature vector extraction processes, based on the voxel location clusters detected as a result of the VBM analysis. The process is illustrated in figure 3. The VBM detected clusters are used as masks to determine the voxel positions where the features are extracted. These masks are applied to the GM density volumes result of the segmentation step in the VBM analysis.

1. The first feature extraction process computes the mean and standard deviation of the GM voxel values of each voxel location cluster, we denote these features as MSD in the result tables given below.

2. The second feature extraction process computes a very high dimensional vector with all the GM segmentation values for the voxel locations included in each VBM detected cluster. The voxel values were ordered in this feature vector according to the coordinate lexicographical ordering. We denote these features as VV in the result tables below.

4.3 Neural Network and Statistical Classification Algorithms

We deal with two class classification problems, given a collection of training/testing input feature vectors $X = \{\mathbf{x}_i \in \mathbb{R}^n,\ i = 1, \ldots, l\}$ and the corresponding labels $\{y_i \in \{-1, 1\},\ i = 1, \ldots, l\}$, which sometimes can be better denoted in aggregated form as a binary vector $\mathbf{y} \in \{-1, 1\}^l$. The algorithms described below build some classifier systems based on this data. The simplest algorithm is the 1-NN which involves no adaptation and uses all the training data samples. The classification rule is of the form:

$$c(\mathbf{x}) = y_{i^*} \text{ where } i^* = \arg \min_{i=1,\ldots,l} \{\|\mathbf{x} - \mathbf{x}_i\|\},$$

that is, the assigned class is that of the closest training vector. To validate their generalization power we use ten fold cross-validation.

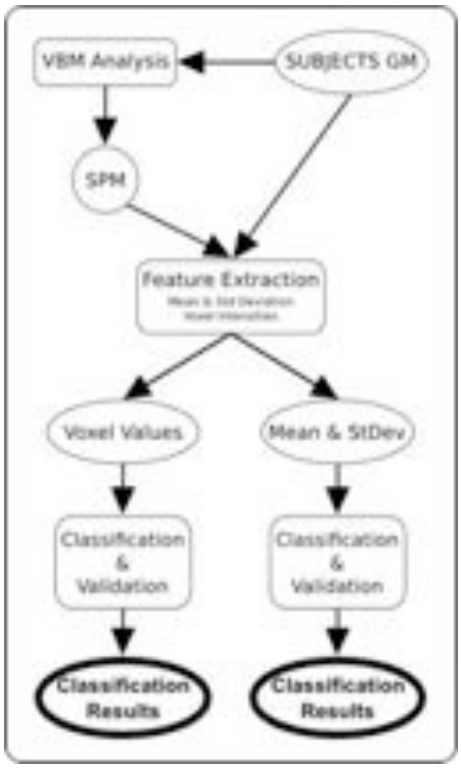

Figure 3: Flow diagram of the feature extraction process from the subjects' GM segmentation volumes.

4.3.1 Support Vector Machines

The Support Vector Machines (SVMs) have attracted attention from the pattern recognition community [24, 62] owing to a number of theoretical and computational merits derived from [63]. SVM separates a given set of binary labelled training data with a hyperplane that is maximally distant from the two classes (known as the maximal margin hyperplane). The objective is to build a discriminating function using training data that will correctly classify new examples $(\mathbf{x}, y)$. When no linear separation of the training data is possible, SVMs can work effectively in combination with kernel techniques using the kernel trick, so that the hyperplane defining the SVMs corresponds to a nonlinear decision boundary in the input space that is mapped to a linearised higher- dimensional space [63]. In this way the decision function can be expressed in terms of the support vectors only:

$$f(\mathbf{x}) = sign\left(\sum \alpha_i y_i K(\mathbf{s}_i, \mathbf{x}) + w_0\right)$$

where $K(.,.)$ is a kernel function, α_i is a weight constant derived from the SVM process and the $\mathbf{s}_i$ are the support vectors [63].

The Support Vector Machine (SVM)[63] algorithm used for this study is included in the libSVM (`http://www.csie.ntu.edu.tw/~cjlin/libsvm/`) software package. The implementation is described in detail in [13]. Given training vectors $\mathbf{x}_i \in \mathbb{R}^n, i = 1, \ldots, l$ of the subject features of the two classes, and a vector $\mathbf{y} \in \mathbb{R}^l$ such that $y_i \in \{-1, 1\}$ labels each subject with its class, in our case, for example, patients were labeled as -1 and control subject as 1. To construct a classifier, the SVM algorithm tries to maximize the classification margin. To this end it solves the following optimization problem:

$$\min_{w,b,\xi} \frac{1}{2}\mathbf{w}^T\mathbf{w} + C\sum_{i=1}^{l} \boldsymbol{\xi}_i$$

subject to $y_i(\mathbf{w}^T\phi(\mathbf{x}_i) + b) \geq (1 - \xi_i),\ \xi_i \geq 0, i = 1, 2, \ldots, n$. The dual optimization problem is

$$\min_{\alpha} \frac{1}{2}\boldsymbol{\alpha}^T\mathbf{Q}\boldsymbol{\alpha} - \mathbf{e}^T\boldsymbol{\alpha},$$

subject to $\mathbf{y}^T\boldsymbol{\alpha} = 0,\ 0 \leq \alpha_i \leq C,\ i = 1, \ldots, l$, where $\mathbf{e}$ is the vector of all ones, $C > 0$ is the upper bound on the error, $\mathbf{Q}$ is an $l \times l$ positive semi-definite matrix, $Q_{ij} \equiv y_i y_j K(\mathbf{x}_i, \mathbf{x}_j)$, and $K(\mathbf{x}_i, \mathbf{x}_j) \equiv \phi(\mathbf{x}_i)^T\phi(\mathbf{x}_j)$ is the kernel function that describes the behavior of the support vectors. Here, the training vectors $\mathbf{x}_i$ are mapped into a higher (maybe infinite) dimensional space by the function $\phi(\mathbf{x}_i)$. C is a regularization parameter used to balance the model complexity and the training error.

The kernel function chosen results in different kinds of SVM with different performance levels, and the choice of the appropriate kernel for a specific application is a difficult task. In this study two different kernels were tested: the

linear and the radial basis function (RBF) kernel. The linear kernel function is defined as $K(\mathbf{x}_i, \mathbf{x}_j) = 1+\mathbf{x}_i^T\mathbf{x}_j$, this kernel shows good performance for linearly separable data. The RBF kernel is defined as $K(\mathbf{x}_i, \mathbf{x}_j) = exp(-\frac{||\mathbf{x}_i-\mathbf{x}_j||^2}{2\sigma^2})$. This kernel is best suited to deal with data that have a class-conditional probability distribution function approaching the Gaussian distribution [8]. The RBF kernel is largely used in the literature because it corresponds to the mapping into an infinite dimension feature space, and it can be tuned by its variance parameter σ.

4.3.2 Multi Layer Perceptron trained with Backpropagation

Backward propagation of errors, or backpropagation (BP), [54, 36, 33] is a nonlinear generalization of the squared error gradient descent learning rule for updating the weights of artificial neurons in a single-layer perceptron, generalized to feed-forward networks, also called Multi-Layer Perceptron (MLP). Backpropagation requires that the activation function used by the artificial neurons (or "nodes") is differentiable with its derivative being a simple function of itself. The backpropagation of the error allows to compute the gradient of the error function relative to the hidden units. It is analytically derived using the chain rule of calculus. During on-line learning, the weights of the network are updated at each input data item presentation. We have used the resilient backpropagation, which uses only the derivative sign to perform the weight updating.

We restrict our presentation of BP to train the weights of the MLP for the current two class problem. Let the instantaneous error E_p be defined as:

$$E_p(\mathbf{w}) = \frac{1}{2}\left(y_p - z_K(\mathbf{x}_p)\right)^2, \tag{1}$$

where y_p is the p-th desired output y_p, and $z_K(x_p)$ is the network output when the p-th training exemplar x_p is inputted to the MLP composed of K layers, whose weights are aggregated in the vector $\mathbf{w}$. The output of the j-th node in layer k is given by:

$$z_{k,j}(\mathbf{x}_p) = f\left(\sum_{i=0}^{N_{k-1}} w_{k,j,i} z_{k-1,i}(\mathbf{x}_p)\right), \tag{2}$$

where $z_{k,j}$ is the output of node j in layer k, N_k is the number of nodes in layer k, $w_{k,j,i}$ is the weight which connects the i-th node in layer $k-1$ to the j-th node in layer k, and $f(\cdot)$ is the sigmoid nonlinear function, which has a simple derivative:

$$f'(\alpha) = \frac{df(\alpha)}{d\alpha} = f(\alpha)(1 - f(\alpha)). \tag{3}$$

The convention is that $z_{0,j}(\mathbf{x}_p) = \mathbf{x}_{p,j}$. Let the total error E_T be defined as follows:

$$E_T(\mathbf{w}) = \sum_{p=1}^{l} E_p(\mathbf{w}), \tag{4}$$

where l is the cardinality of X. Note that E_T is a function of both the training set and the weights in the network. The backpropagation learning rule is defined as follows:

$$\Delta w(t) = -\eta \frac{\partial E_p(\mathbf{w})}{\partial w} + \alpha \Delta w(t-1), \tag{5}$$

where $0 < \eta < 1$, which is the learning rate, the momentum factor α is also a small positive number, and w represents any single weight in the network. In the above equation, $\Delta w(t)$ is the change in the weight computed at time t. The momentum term is sometimes used ($\alpha \neq 0$) to improve the smooth convergence of the algorithm. The algorithm defined by equation (5) is often termed as *instantaneous backpropagation* because it computes the gradient based on a single training vector. Another variation is *batch backpropagation*, which computes the weight update using the gradient based on the total error E_T.

To implement this algorithm we must give an expression for the partial derivative of E_p with respect to each weight in the network. For an arbitrary weight in layer k this can be written using the Chain Rule:

$$\frac{\partial E_p(\mathbf{w})}{\partial w_{k,j,j}} = \frac{\partial E_p(\mathbf{w})}{\partial z_{k,j}(\mathbf{x}_p)} \frac{\partial z_{k,j}(\mathbf{x}_p)}{\partial w_{k,j,i}}. \tag{6}$$

Because the derivative of the activation function follows equation 3, we get:

$$\frac{\partial z_{k,j}(\mathbf{x}_p)}{\partial w_{k,j,i}} = z_{k,j}(\mathbf{x}_p)(1 - z_{k,j}(\mathbf{x}_p)) z_{k-1,j}(\mathbf{x}_p), \tag{7}$$

and

$$\frac{\partial E_p(\mathbf{w})}{\partial z_{k,j}(\mathbf{x}_p)} = \sum_{m=1}^{N_{k+1}} \frac{\partial E_p(\mathbf{w})}{\partial z_{k+1,m}(\mathbf{x}_p)} z_{k+1,m}(\mathbf{x}_p)(1 - z_{k+1,m}(\mathbf{x}_p)) w_{k+1,m,j},$$

which at the output layer corresponds to the output error :

$$\frac{\partial E_p(\mathbf{w})}{\partial z_K(\mathbf{x}_p)} = z_L(\mathbf{x}_p) - y_p. \tag{8}$$

4.3.3 Radial Basis Function Networks

Radial Basis Function networks (RBF) [14, 36] are a type of ANN that use radial basis functions as activation functions. RBFs consist of a two layer neural network, where each hidden unit implements a radial activated function. The output units compute a weighted sum of hidden unit outputs. Training consists of the unsupervised training of the hidden units followed by the supervised training of the output units' weights. RBFs have their origin in the solution of

a multivariate interpolation problem [7]. Arbitrary function $g(\mathbf{x}) : \mathbb{R}^n \to \mathbb{R}$ can be approximated by a map defined by a RBF network with a single hidden layer of K units:

$$\hat{g}_{\boldsymbol{\theta}}(\mathbf{x}) = \sum_{j=1}^{K} w_j \phi(\sigma_j, \|\mathbf{x} - \mathbf{c}_j\|), \tag{9}$$

where $\boldsymbol{\theta}$ is the vector of RBF parameters including $w_j, \sigma_j \in \mathbb{R}$, and $\mathbf{c}_j \in \mathbb{R}^n$; let us denote $\mathbf{w} = (w_1, w_2, \ldots, w_p)^T$, then the vector of RBF parameters can be expressed as $\boldsymbol{\theta}^T = \left(\mathbf{w}^T, \sigma_1, \mathbf{c}_1^T, \ldots, \sigma_K, \mathbf{c}_K^T\right)$. Each RBF is defined by its center $\mathbf{c}_j \in \mathbb{R}^n$ and width $\sigma_j \in \mathbb{R}$, and the contribution of each RBF to the network output is weighted by w_j. The RBF function $\phi(\cdot)$ is a nonlinear function that monotically decreases as $\mathbf{x}$ moves away from its center $\mathbf{c}_j$. The most common RBF used is the isotropic Gaussian:

$$\hat{g}_{\boldsymbol{\theta}}(\mathbf{x}) = \sum_{j=1}^{p} w_j \exp\left(-\frac{\|\mathbf{x} - \mathbf{c}_j\|^2}{2\sigma_j^2}\right).$$

The network can be thought as the composition of two functions $\hat{g}_{\boldsymbol{\theta}}(\mathbf{x}) = W \circ \Phi(\mathbf{x})$, the first one implemented by the RBF units $\Phi : \mathbb{R}^n \to \mathbb{R}^K$ performs a data space transformation which can be a dimensionality reduction or not, depending on whether $K > n$. The second function corresponds to a single layer linear Perceptron $W : \mathbb{R}^K \to \mathbb{R}$ giving the map of the RBF transformed data into the class labels. Training is accordingly decomposed into two phases. First a clustering algorithm is used to estimate the Gaussian RBF parameters (centres and variances). Afterwards, linear supervised training is used to estimate the weights from the hidden RBF to the output. In order to obtain a binary class label output, a hard limiter function is applied to the continuous output of the RBF network.

4.3.4 Probabilistic Neural Networks

A Probabilistic Neural Network (PNN) [61] uses a kernel-based approximation to form an estimate of the probability density function of categories in a classification problem. In fact, it is a generalization of the Parzen windows distribution estimation, and a filtered version of the 1-NN classifier. The distance of the input feature vector $\mathbf{x}$ to the stored patterns is filtered by a RBF function. Let us denote the data sample partition as $X = X_1 \cup X_{-1}$, where $X_1 = \left\{\mathbf{x}_1^1, \ldots, \mathbf{x}_{n_1}^1\right\}$ and $X_1 = \left\{\mathbf{x}_1^{-1}, \ldots, \mathbf{x}_{n_{-1}}^{-1}\right\}$. That is, superscripts denote the class of the feature vector and $n_1 + n_{-1} = n$. Each pattern $\mathbf{x}_j^i$ of training data sample is interpreted as the weight of the j-th neuron of the i-th class. Therefore the response of the neuron is computed as the probability of the input feature vector according to a Normal distibution centered at the stored pattern:

$$\Phi_{i,j}(\mathbf{x}) = \frac{1}{(2\pi)^{n/2}\sigma^n} \exp\left[-\frac{\left\|\mathbf{x} - \mathbf{x}_j^i\right\|}{2\sigma^2}\right], \tag{10}$$

Therefore the output of the neuron is inside $[0, 1]$. The tuning of a PNN network depends on selecting the optimal sigma value of the spread σ of the RBF functions, which can be different for each class. In this paper an exhaustive search for the optimal spread value in the range (0, 1) for each training set has been done. The output of the PNN is an estimation of the likelihood of the input pattern $\mathbf{x}$ being from class $i \in \{-1, 1\}$ by averaging the output of all neurons that belong to the same class:

$$p_i(x) = \frac{1}{n_i} \sum_{j=1}^{n_i} \Phi_{i,j}(\mathbf{x}). \tag{11}$$

The decision rule based on the output of all the output layer neurons is simply:

$$\hat{y}(\mathbf{x}) = \arg\max_i \{p_i(\mathbf{x})\}, \quad i \in \{-1, 1\}. \tag{12}$$

where $\hat{y}(\mathbf{x})$ denotes the estimated class of the pattern $\mathbf{x}$. If the a priori probabilities for each class are the same, and the losses associated with making an incorrect decision for each class are the same, the decision layer unit classifies the pattern $\mathbf{x}$ in accordance with the optimal Bayes' rule.

4.3.5 Learning Vector Quantization

Learning vector quantization (LVQ) [40, 60] Learning Vector Quantization (LVQ) as introduced by Kohonen [41] represents every class $c \in \{-1, 1\}$ by a set $W(c) = \{\mathbf{w}_i \in \mathbb{R}^n; i = 1, \ldots, N_c\}$ of weight vectors (prototypes) which tesselate the input feature space. Let us denote W the union of all prototypes, regardless of class. If we denote c_i the class the weight vector $\mathbf{w}_i \in W$ is associated with, the decision rule that classifies a feature vector $\mathbf{x}$ is as follows:

$$c(\mathbf{x}) = c_{i^*}$$

where

$$i^* = \arg\min_i \{\|\mathbf{x} - \mathbf{w}_i\|\}.$$

The training algorithm of LVQ aims at minimizing the classification error on the given training set, i.e., $E = \sum_j (y_j - c(\mathbf{x}_j))^2$, modifying the weight vectors on the presentation of input feature vectors. The heuristic weight updating rule is as follows:

$$\Delta\mathbf{w}_{i^*} = \begin{cases} \epsilon \cdot (\mathbf{x}_j - \mathbf{w}_{i^*}) & \text{if } c_{i^*} = y_j \\ -\epsilon \cdot (\mathbf{x}_j - \mathbf{w}_{i^*}) & \text{otherwise} \end{cases}, \tag{13}$$

that is, the input's closest weight is adapted either toward the input if their classes match, or away from it if not. This rule is highly unstable, therefore, the practical approach consists in performing an initial clustering of each class data samples to obtain an initical weight configuration using equation 13 to perform the fine tuning of the classification boundaries. This equation corresponds to

a LVQ1 approach. The LVQ2 approach involves determining the two input vector's closest weights. They are moved toward or away the input according to the matching of their classes.

4.3.6 Combination of independent SVMs trained per VBM cluster

We have considered also the construction of independent SVM classifiers for each VBM detected cluster, meaning that only the corresponding features are used for train/test, and the combination of their responses in two ways:

1. By a simple majority voting, using the cluster with greatest statistical significance to resolve ties. This can be viewed as a simplified combination of classifiers. We denote this system Indep-SVM in the results reported below.

2. We have defined a combination of classifiers weighted by the individual training errors, where the classifier weights are computed using the AdaBoost SVM algorithm [44], assuming an uniform weighting of the data samples. We present this approach in Algorithm 1. We denote AB-SVM this approach in the tables below.

4.3.7 Adaptive Boosting

Adaptive Boosting (AdaBoost)[58, 22] is a meta-algorithm for machine learning that can be used in conjunction with many other learning algorithms to improve their performance. AdaBoost is adaptive in the sense that subsequent classifiers built are tweaked in favor of those instances misclassified by previous classifiers. AdaBoost is sensitive to noisy data and outliers. Otherwise, it is less susceptible to the over-fitting problem than most learning algorithms.

AdaBoost calls a weak classifier repeatedly in a series of rounds $t = 1, ..., T$. For each call a distribution of weights W_t is updated and indicates the importance of examples in the data set for the classification. On each round, the weights of each incorrectly classified example are increased (or alternatively, the weights of each correctly classified example are decreased), so that the new classifier focuses more on those examples.

Following these ideas, we have also tested a combination of SVM classifiers following the the Diverse-AdaBoost-SVM [44], shown here as Algorithm 2. In this approach we built a sequence of SVM classifiers of increasing variance parameter. The results of the classifiers are weighted according to their statistical error to obtain the response to the test inputs in the 10-fold validation process. We denote DAB-SVM this approach in the tables below.

5 Computational Experiments Results

We evaluate the performance of the classifiers built with the diverse strategy using a 10-fold cross-validation methodology, illustrated in figure 4. We have

Algorithm 1 Combining the independent SVM trained per cluster

1. **Input:** as many sets of training samples with labels as clusters in the statistical parametric map $T_k = \{(x_1, y_1), \ldots, (x_N, y_N)\}, k = 1..C$, where N is the number of samples of each cluster.

2. **Initialize:** the weights of training samples: $w_i^k = 1/N$, for all $i = 1, ..., N$

3. **For each *k* cluster do**

   (a) Search the best γ for the RBF kernel for the training set T_k, we denote it as γ_k.

   (b) Train the SVM with T_k and γ_k, we denote the classifier as h_k.

   (c) Classify the same training T_k set with h_k.

   (d) Calculate the training error of h_k: $\epsilon_k = \sum_{i=1}^{N} w_i^k, \quad y_i \neq h_k(x_i)$.

   (e) Compute the weight of the cluster classifier h_k: $\alpha_k = \frac{1}{2} \ln(\frac{\epsilon_k}{1-\epsilon_k})$.

4. **Output:** for each test data x its classification is $f(x) = sign(\sum_{k=1}^{C} \alpha_k h_k(x))$.

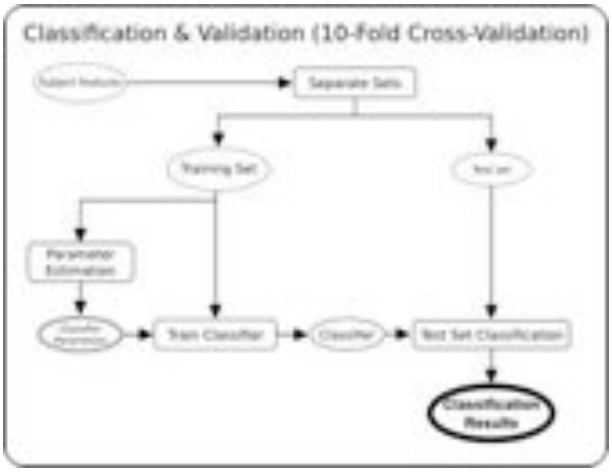

Figure 4: Flow chart of the 10-fold cross validation procedure followed in the experiments reported in this paper.

Algorithm 2 Diverse AdaBoostSVM

1. **Input:** a set of training samples with labels $\{(x_1, y_1), \ldots, (x_N, y_N)\}$; the initial σ, σ_{ini}; the minimal σ, σ_{min}; the step of σ, σ_{step}; the threshold on diversity DIV.
2. **Initialize:** the weights of training samples: $w_i^t = 1/N$, for all $i = 1, ..., N$
3. **Do while** ($\sigma > \sigma_{ini}$)
   (a) Calculate gamma: $\gamma = \left(2\sigma^2\right)^{-1}$.
   (b) Use σ to train a component classifier h_t on the weighted training set.
   (c) Calculate the training error of h_t: $\epsilon_t = \sum_{i=1}^{N} w_i^t, \quad y_i \neq h_t(x_i)$.
   (d) Calculate the diversity of h_t: $D_t = \sum_{i=1}^{N} d_t(x_i)$, where $d_t(x_i) = \begin{cases} 0 & if\ h_t(x_i) = y_i \\ 1 & if\ h_t(x_i) \neq y_i \end{cases}$
   (e) Calculate the diversity of weighted component classifiers and the current classifier: $D = \sum_{t=1}^{T} \sum_{i=1}^{N} d_t(x_i)$.
   (f) If $\epsilon_t > 0.5$ or $D < DIV$: decrease σ by σ_{step} and go to (a).
   (g) Set weight of the component classifier h_t: $\alpha_t = \frac{1}{2} \ln(\frac{\epsilon_t}{1-\epsilon_t})$.
   (h) Update the weights of training samples: $w_i^{t+1} = w_i^t exp(-\alpha y_i h_t(x_i))$.
   (i) Normalize the weights of training samples: $w_i^{t+1} = w_i^{t+1}(\sum_{i=1}^{N} w_i^{t+1})^{-1}$.
4. **Output:** $f(x) = sign(\sum_{k=1}^{C} \alpha_k h_k(x))$.

enconded the classes as follows: 0 for patients, 1 for controls. Positives correspond to class 0. To quantify the results we measured the Accuracy defined as the ratio of the number of test volumes correctly classified to the total of tested volumes. We also quantified the sensitivity and specificity of each test defined as $Sensitivity = \frac{TP}{TP+FN}$ and $Specificity = \frac{TN}{TN+FP}$, where true positives (TP) is the number of patient volumes correctly classified; true negatives (TN) is the number of control volumes correctly classified; false positives (FP) is the number of control volumes classified as diseased patients and false negatives (FN) is the number of diseased patient volumes classified as control subjects. As the image assessment is an additional finding meant to support other diagnostic information sources, there is a specific need for high sensitivity and specificity systems. Thus, these performance measure were preferred above others, like the F-measure or the Area under ROC, which are better suited to explore and discuss the parameter sensitivity of the classification building algorithm [47].

5.1 Results on AD detection on the OASIS data

We report the average accuracy, sensitiviy and specificity of the 10-fold cross-validation of the systems developed for AD detection computed over the OASIS data. For all the classifiers, we have determined the optimal values of the classifier parameters via independent grid searches performed at each cross-validation fold. For the SVM we searched for the optimal C and γ values. For the MLP-BP we look for the optimal number of hidden units. For the RBF and PNN, the spread of the radial basis functions was determined. For the LVQ the number of hidden units was determined. For the Diverse AdaBoost SVM (DAB-SVM) the parameters of the AdaBoost were set as follows: $\sigma_{min} = 0.1$, $\sigma_{ini} = 100$, $\sigma_{step} = 0.1$. The DIV value is set as as 0.6.

The results on the MSD features (24 values from each volume) are presented in table 3. The best accuracy results were obtained by the non linear SVM with RBF kernels, specially when embedded in the AdaBoost process (0.85). The LVQ approach give almost comparable results. Overall, it must be noted that the specificity is systematically higher than the sensitivity for all the classification strategies tested. Detailed examination of the results reveals that the decrease of sensitivity is due to the bad recognition results on the AD subjects at early stages of the disease. As the trend is common to all the classification algorithms tested, this lack of sensitivity must be attributed to the feature vector computed from the VBM detected clusters.

The average results of 10-fold cross-validation tests computed on the VV features, are presented in table 4. For this definition of the feature vector, the number of features is 3611. Again the specificity is systematically greater than the classifier's sensitivity at all cases, suggesting that the feature vector definition must be improved to cope with the early detection cases. We obtain a best accuracy result with the AdaBoost applied to the SVM with RBF kernel trained independently at each VBM detected cluster (rbf-AB-SVM). Despite this result, which is the best accuracy found, the remaining classifier results are significatively worse for the VV features than for the MSD features. This must

Classif.	Accuracy	Sensitivity	Specificity
linear SVM	0.78	0.72	0.88
rbf SVM	**0.81**	0.75	0.89
MLP-BP	0.78	0.69	0.88
RBF	0.66	0.65	0.68
PNN	0.78	0.62	0.94
LVQ1	**0.81**	0.72	0.90
LVQ2	**0.83**	0.74	0.92
Indep-linear-SVM	0.74	0.51	0.97
Indep-rbf-SVM	0.75	0.56	0.95
linear-AB-SVM	0.71	0.54	0.88
rbf-AB-SVM	0.79	0.78	0.80
rbf-DAB-SVM	**0.85**	0.78	0.92

Table 3: Results over the MSD features computed from the OASIS data for AD detection

be accounted to fact that the VV dimensionality is several orders of magnitude greater than the MSD and the proposed classifiers are unable to deal with that and the the consequent data scarcity. Note that the best result in table 4 corresponds to the independent training of SVM for each detected cluster. This "divide and conquer" strategy seems to produce good results in this case.

5.2 MD1 Results

In the computational experiments done on the MD1 data, we focus on the SVM classifier and explore the effect of the various VBM parameters on the resulting classification accuracy, sensitivity and specificity. In the tables below we show results for various FWHM and spatial cluster extent threshold (Size-Thr) value settings in the SPM processing to obtain the VBM clusters of pixels with significant differences. Note that the increase in the FWHM parameter naturally implies an increase in the number of features considered. The increase of the Size-Thr parameter implies that more clusters are rejected because of their small size, and the resulting feature vector has lower dimensionality. The results on the MSD features are presented in table 5, while the results on the VV features are presented in table 6. Note that there are few instances that reach the 80% accuracy. Notice also in both tables that the specificity is systematically greater than the sensitivity. As was said in the AD study above, this trend forces to attribute the lack of sensitivity to the feature extraction process. In order to deal with the milder dementia cases, the process must be improved. It must be also taken into account that until now there have not been findings in sMRI associated with the MD1, meaning that the works reported here are the among the first published results in this sense. Another interesting effect that can be appreciated in the tables 5 and 6 is that growing number of features, obtained with stronger smoothing does not imply growing classification

Classif.	Accuracy	Sensitivity	Specificity
linear SVM	0.73	0.72	0.75
rbf SVM	0.76	0.77	0.76
MLP-BP	0.78	0.72	0.84
RBF	0.72	0.65	0.80
PNN	0.74	0.68	0.81
LVQ1	0.79	0.76	0.82
LVQ2	0.77	0.76	0.78
Indep-linear-SVM	0.77	0.74	0.80
Indep-rbf-SVM	0.78	0.76	0.82
linear-AB-SVM	0.73	0.76	0.70
rbf-AB-SVM	**0.86**	0.80	0.92
rbf-DAB-SVM	0.78	0.71	0.85

Table 4: Results over the VV features computed fom the OASIS data for AD detection

accuracy. This goes contrary to the assessments by human experts that favor stronger smoothing in order to obtain better and bigger detections of the effect.

5.3 Discussion of results.

The classifiers applied to the data features make decisions based on the whole of the feature vector. However, the locations of the feature sources, the voxel cluster found by VBM, has some clinical interpretations. For AD the voxel cluster findings were mostly located in the temporal lobe, though some voxels in the frontal lobe have also been detected. These results confirm previous findings of temporal lobe atrophic changes in AD [4, 11, 10] [...], and suggest that these abnormalities may be confined to specific sites within that lobe, rather than showing a widespread distribution. The classification results are a second level assessment of these findings, because they show that it is possible some degree of AD prediction from them.

For MD1 the most discriminant voxels were in the caudate nucleus, fronto-parietal lobe lobe and thalamus. These results involving the fronto-parietal areas, agree with previous studies [2] and with the profile suggested by our previous neuropsychological results in a large DM1 sample [59]. In fact, we have found the volume corresponding to the caudate nuclei and the thalamus to be smaller in DM1 patients than in the CS. Basal ganglia have traditionally been associated with motor processes, although there is increasing evidence to support their role in cognitive functions [49]. Basal ganglia nuclei relate to one another and to the cortex through different cortico-striatal loops, which emphasizes the functional interrelationship between the neocortex, the striatum and the thalamus. Three of the five loops in which the striatum is involved pass through the caudate and the thalamus on the way to the cortex: the oculomotor, dorsolateral prefrontal and lateral orbitalfrontal loops [31]. The

FWHM(mm)	Size-Thr	#Features	Accuracy	Sensitivity	Specificity
8	0	76	0.78	0.73	0.83
	100	8	0.77	0.67	0.87
	200	4	0.77	0.67	0.87
9	0	76	**0.80**	0.70	0.90
	100	16	0.75	0.67	0.83
	200	4	0.76	0.67	0.87
10	0	70	0.78	0.63	0.93
	100	22	0.77	0.73	0.80
	200	8	0.78	0.70	0.87
11	0	64	0.72	0.63	0.80
	100	24	0.75	0.63	0.87
	200	12	0.75	0.63	0.87
12	0	68	0.72	0.63	0.80
	100	36	0.73	0.63	0.83
	200	18	0.75	0.70	0.80

Table 5: SVM classification results (10-fold crossvalidation) for MSD features, based on t-test VBM of the data, FWE=0.05

FWHM	Threshold	Features	Accuracy	Sensitivity	Specificity
8	0	2059	**0.82**	0.83	0.80
	100	1226	0.78	0.70	0.87
	200	958	**0.80**	0.80	0.77
9	0	2826	0.78	0.73	0.83
	100	2044	0.77	0.73	0.80
	200	1182	0.75	0.67	0.83
10	0	3710	0.77	0.73	0.80
	100	3103	**0.80**	0.77	83
	200	2131	0.73	0.70	0.77
11	0	5022	0.73	0.73	0.73
	100	4278	0.78	0.73	0.83
	200	3434	0.75	0.70	0.80
12	0	6542	0.76	0.73	0.80
	100	6391	0.75	0.70	0.80
	200	5148	0.73	0.70	0.76

Table 6: SVM classification results (10-fold crossvalidation) for VV features, based on t-test VBM of the data, FWE=0.05

last two target two prefrontal cortical areas that are thought to be involved in various aspects of cognitive behaviour. In fact, the dorsolateral cortex is the structure mostly closely associated with executive functions and allows the organization of information to facilitate a response. The orbitofrontal circuit allows the integration of limbic and emotional information with behavioural responses [5].

6 Conclusions

In this work we have studied several supervised classification systems applied to discriminate patients with neurocognitive disorders (AD and MD1) from control subjects based on structural MRI (T1-weighted) data. The feature extraction processes is based on the voxel clusters detected by a VBM analysis. For the discrimination between AD patients and controls we achieve the construction of classifiers with an accuracy of 0.86 in the best case shown in table 4 in the case of OASIS females and 0.82 in case of MD1 subjects. A result of 86% of accuracy is really encouraging considering the number of subjects in the database and all the biases and errors involved in the registration, segmentation and smoothing processes performed in the pre-processing steps of the volumes in the VBM. After close examination of the results in the AD study, we have found that the subjects wrongly classified maybe the most critical ones: old control subjects classified as AD (false positives) and subjects with a very early or mild dementia classified as normal (false negatives), exactly the ones which are the target in these studies that try to perform early detection of AD. Post-mortem confirmation data of AD diagnosed subjects could improve the results. Something similar may be happening in the MD1 study. Therefore we may conclude that additional information sources and improved classification strategies are needed to reach this additional accuracy increase that would cover the most difficult cases.

Further work may be directed in the following lines:

- The consideration of features extracted on the basis of information obtained from other morphological measurement techniques, such as Deformation-based Morphometry and Tensor-based Morphometry.

- Use additional image modalities (PET, fMRI, DTI) and additional clinical data. Additional image modalities imply the mutual registration of volumes and the fusion of the diverse information sources. Additional clinical data may be used as covariates in the GLM resolution within the VBM analysis.

- Using new classification strategies, such as the uncertain classifiers, which may assign various grades to the data and provide new ways to evaluate the classifier response[47]. In the case of of pathologies with cognitive impairment, it would be more natural to try to rank the image data according to the neuropsychological scales than the binary decision that we

have been trying to implement in this paper, improving results in several ways. Also Lattice Computing approaches [28, 30, 26, 29, 27, 32]

- Future work may be addressed to the problem of three way discrimination AD vs. MD1 vs. controls. It needs an elaborated VBM using F test for the detection of clusters of voxels which can discriminate between the three classes, as well as multi-class classifiers, which in some cases requires some elaboration.

Acknowledgements

We thank the Washington University ADRC for making the OASIS database available. Research partially supported by Saiotek research projects BRAINER, S-PR07UN02, SOFLIMRI.

References

[1] http://www.fil.ion.ucl.ac.uk/spm/.

[2] G Antonini, C Mainero, A Romano, F Giubilei, V Ceschin, F Gragnani, S Morino, M Fiorelli, F Soscia, A Di Pasquale, and F Caramia. Cerebral atrophy in myotonic dystrophy: a voxel based morphometric study. *Journal of Neurology, Neurosurgery & Psychiatry*, 75(11):1611–1613, November 2004.

[3] J. Ashburner and K.J. Friston. Voxel-Based Morphometry–The methods. *NeuroImage*, 11(6):805–821, June 2000.

[4] J. C. Baron, G. Chetelat, B. Desgranges, G. Perchey, B. Landeau, V. de la Sayette, and F. Eustache. In vivo mapping of gray matter loss with Voxel-Based morphometry in mild alzheimer's disease. *Neuroimage*, 14(2):298–309, 2001.

[5] R.M. Bonelli and J.L. Cummings. Frontal-subcortical circuitry and behavior. *Dialogues Clin. Neurosci.*, 9:141–151, 2007.

[6] J.D. Brook, M.E. McCurrach, H.G. Harley, A.J. Buckler, D. Church, H. Aburatani, K. Hunter, V.P. Stanton, J.P. Thirion, and T. Hudson. Molecular basis of myotonic dystrophy: expansion of a trinucleotide (CTG) repeat at the 3' end of a transcript encoding a protein kinase family member. *Cell*, 68(4):799–808, February 1992. PMID: 1310900.

[7] D.S. Broomhead and D. Lowe. Multivariable functional interpolation and adaptive networks. *Complex Systems*, 2:321–355, 1988.

[8] C. Burges. A tutorial on support vector machines for pattern recognition. *Data Mining and Knowledge Discovery*, 2(2):167, 121, 1998.

[9] G. F. Busatto, G. E. J. Garrido, O. P. Almeida, C. C. Castro, C. H. P. Camargo, C. G. Cid, C. A. Buchpiguel, S. Furuie, and C. M. Bottino. A voxel-based morphometry study of temporal lobe gray matter reductions in alzheimer's disease. *Neurobiology of Aging*, 24(2):221–231, 2003.

[10] Geraldo Busatto. Voxel-Based Morphometry in Alzheimers disease. *Expert review of neurotherapeutics*, 8(11):1691–1702, 2008.

[11] G.F. Busatto, G.E. Garrido, O.P. Almeida, C.C. Castro, C.H. Camargo, C.G. Cid, C.A. Buchpiguel, S. Furuie, and C.M. Bottino. A Voxel-Based Morphometry study of temporal lobe gray matter reductions in Alzheimer's disease. *Neurobiol Aging*, 24(2):221–231, Mar-Apr 2003.

[12] B. Censori, L. Provinciali, M. Danni, L. Chiaramoni, M. Maricotti, N. Foschi, M. Del Pesce, and U. Salvolini. Brain involvement in myotonic dystrophy: MRI features and their relationship to clinical and cognitive conditions. *Acta Neurologica Scandinavica*, 90(3):211–217, September 1994. PMID: 7847063.

[13] C.C. Chang and C.J. Lin. *LIBSVM: a library for support vector machines*, 2001. Software available at `http://www.csie.ntu.edu.tw/~cjlin/libsvm`.

[14] S. Chen, C.F.N. Cowan, and P.M. Grant. Orthogonal least squares learning algorithm for radial basis function networks. *Neural Networks, IEEE Transactions on*, 2(2):302–309, 1991.

[15] M.S. Damian, G. Schilling, G. Bachmann, C. Simon, S. Stöppler, and W. Dorndorf. White matter lesions and cognitive deficits: relevance of lesion pattern? *Acta Neurologica Scandinavica*, 90(6):430–436, December 1994. PMID: 7892763.

[16] C. Davatzikos, Y. Fan, X. Wu, D. Shen, and S.M. Resnick. Detection of prodromal alzheimer's disease via pattern classification of magnetic resonance imaging. *Neurobiol Aging*, 29(4):514–523, Apr 2008.

[17] A. Lopez de Munain, A. Blanco, J. I. Emparanza, J. J. Poza, J. F. Marti Masso, A. Cobo, L. Martorell, M. Baiget, and J. M. Martinez Lage. Prevalence of myotonic dystrophy in guipuzcoa (Basque country, spain). *Neurology*, 43(8):1573, August 1993.

[18] A. Lopez de Munain, J. I. Emparanza, A. Blanco, A. Cobo, J. J. Poza, B. Basauri, and et al. Clinical manifestations of myotonic dystrophy: epidemiologic survey. *Med.Clin.(Barc.)*, 101:161–164, August 1993.

[19] Y. Fan, , S.M. Resnick, S. Wu, and C. Davatzikos. Structural and functional biomarkers of prodromal Alzheimer's disease: a high-dimensional pattern classification study. *NeuroImage*, 41(2):277–285, 2008.

[20] Y. Fan, D. Shen, and C. Davatzikos. Classification of structural images via high-dimensional image warping, robust feature extraction, and SVM. *Med Image Comput Comput Assist Interv Int Conf Med Image Comput Comput Assist Interv*, 8(Pt 1):1–8, 2005.

[21] A.F. Fotenos, A.Z. Snyder, L.E. Girton, J.C. Morris, and R.L. Buckner. Normative estimates of cross-sectional and longitudinal brain volume decline in aging and AD. *Neurology*, 64(6):1032–1039, March 2005.

[22] Y. Freund and R. Schapire. A decision-theoretic generalization of on-line learning and an application to boosting. In *European Conference on Computational Learning Theory*, pages 37, 23, 1995.

[23] G. B. Frisoni, C. Testa, A. Zorzan, F. Sabattoli, A. Beltramello, H. Soininen, and M. P. Laakso. Detection of grey matter loss in mild alzheimer's disease with voxel based morphometry. *Journal of Neurology, Neurosurgery & Psychiatry*, 73(6):657–664, 2002.

[24] G. Fung and J. Stoeckel. SVM feature selection for classification of SPECT images of Alzheimer's disease using spatial information. *Knowl. Inf. Syst.*, 11(2):243–258, 2007.

[25] M.T. García-Sebastián, A. Savio, M. Graña, and J. Villanúa. On the use of morphometry based features for Alzheimer's disease detection on MRI. In Alberto Prieto Juan M. Corchado (Editors) Joan Cabestany, Francisco Sandoval, editor, *Bio-Inspired Systems: Computational and Ambient Intelligence. / IWANN 2009 (Part I)*, volume 5517 of *LNCS*, pages 957–964. Springer-Verlag, 2009.

[26] M. Graña. A brief review of Lattice Computing. In *Fuzzy Systems, 2008. FUZZ-IEEE 2008. (IEEE World Congress on Computational Intelligence). IEEE International Conference on*, pages 1777–1781, June 2008.

[27] M. Graña, A. Manhaes-Savio, M. Garcia-Sebastian, and E. Fernandez. A Lattice Computing approach for on-line fMRI analysis. *Image and Vision Computing*, 28(7):1155–1161, 2010. Online pattern recognition and machine learning techniques for computer-vision: Theory and applications.

[28] M. Graña, P. Sussner, and G.X. Ritter. Associative Morphological Memories for endmember determination in spectral unmixing. In *Fuzzy Systems, 2003. FUZZ '03. The 12th IEEE International Conference on*, volume 2, pages 1285–1290, May 2003.

[29] M. Graña, I. Villaverde, J.O. Maldonado, and C. Hernandez. Two Lattice Computing approaches for the unsupervised segmentation of hyperspectral images. *Neurocomputing*, 72(10-12):2111–2120, 2009.

[30] M. Graña, I. Villaverde, R. Moreno, and F.X. Albizuri. *Computational Intelligence Based on Lattice Theory*, chapter Convex Coordinates From

Lattice Independent Sets for Visual Pattern Recognition, pages 99–126. Springer-Verlag, 2007.

[31] J.A. Grahn, J.A. Parkinson, and A.M. Owen. The cognitive functions of the caudate nucleus. *Prog Neurobiol.*, 86:141–155, 2008.

[32] M. Graña, D. Chyzhyk, M. García-Sebastián, and C. Hernández. Lattice independent component analysis for functional magnetic resonance imaging. *Information Sciences*, in press, 2010.

[33] M.T. Hagan, H.B. Demuth, and M.H. Beale. *Neural Network Design*. PWS Pub. Co., Har/Dsk edition, December 1995.

[34] P. Harper. *Myotonic Dystrophy*. Oxford University Press, USA, 2 edition, October 2009.

[35] T. Hashimoto, M. Tayama, M. Miyazaki, K. Murakawa, H. Kawai, H. Nishitani, and Y. Kuroda. Neuroimaging study of myotonic dystrophy. II. MRI measurements of the brain. *Brain and Development*, 17(1):28–32, 1995.

[36] S. Haykin. *Neural Networks: A Comprehensive Foundation*. Prentice Hall, 2 edition, July 1998.

[37] C. Huang, B. Yan, H. Jiang, and D. Wang. Combining voxel-based morphometry with artifical neural network theory in the application research of diagnosing alzheimer's disease. In *BioMedical Engineering and Informatics, 2008. BMEI 2008. International Conference on*, volume 1, pages 250–254, May 2008.

[38] I.A. Illan, J.M. Gorriz, J. Ramirez, D. Salas-Gonzalez, M.M. Lopez, F. Segovia, R. Chaves, M. Gomez-Rio, and C.G. Puntonet. 18f-fdg pet imaging analysis for computer aided alzheimer's diagnosis. *Information Sciences*, 181(4):903 – 916, 2011.

[39] S. Kloppel. Automatic classification of MR scans in Alzheimer's disease. *Brain*, 131(3):681–689, 2008.

[40] T. Kohonen. *Self-organization and associative memory: 3rd edition*. Springer-Verlag New York, Inc., 1989.

[41] T. Kohonen. Learning vector quantization. In *The handbook of brain theory and neural networks*, pages 537–540. MIT Press, 1998.

[42] Z. Lao, D. Shen, Z. Xue, B. Karacali, S. M. Resnick, and C. Davatzikos. Morphological classification of brains via high-dimensional shape transformations and machine learning methods. *Neuroimage*, 21(1):46–57, 2004.

[43] Z. Lao, D. Shen, Z. Xue, B. Karacali, S.M. Resnick, and C. Davatzikos. Morphological classification of brains via high-dimensional shape transformations and machine learning methods. *NeuroImage*, 21(1):46–57, Jan 2004.

[44] X. Li, L. Wang, and E. Sung. A study of AdaBoost with SVM based weak learners. In *Neural Networks, 2005. IJCNN '05. Proceedings. 2005 IEEE International Joint Conference on*, volume 1, pages 196–201 vol. 1, 2005.

[45] Y. Liu, L. Teverovskiy, O. Carmichael, R. Kikinis, M. Shenton, C.S. Carter, V.A. Stenger, S. Davis, H. Aizenstein, J.T. Becker, O.L. Lopez, and C.C. Meltzer. Discriminative MR image feature analysis for automatic schizophrenia and Alzheimer's disease classification. *Medical Image Computing and Computer-Assisted Intervention (MICCAI)*, 3216:393–401, 2004.

[46] M. Lopez, J. Ramirez, J.M. Gorriz, D. Salas-Gonzalez, I. Alvarez, F. Segovia, and C.G. Puntonet. Automatic tool for alzheimer's disease diagnosis using pca and bayesian classification rules. *Electronics Letters*, 45(8):389–391, 9 2009.

[47] O. Luaces, F. Taboada, G.M. Albaiceta, L.A. Domínguez, P. Enriquez, and A. Bahamonde. Predicting the probability of survival in intensive care unit patients from a small number of variables and training examples. *Artificial Intelligence in Medicine*, 45(1):63–76, 2009.

[48] D.S. Marcus, T.H. Wang, J. Parker, J.G. Csernansky, J.C. Morris, and R.L. Buckner. Open access series of imaging studies (OASIS): cross-sectional MRI data in young, middle aged, nondemented, and demented older adults. *Journal of Cognitive Neuroscience*, 19(9):1498–1507, September 2007. PMID: 17714011.

[49] F.A. Middleton and P.L. Strick. Basal ganglia output and cognition: evidence from anatomical, behavioral, and clinical studies. *Brain Cogn.*, 42:183–200, 2000.

[50] M. L. Mostacciuolo, G. Barbujani, M. Armani, G. A. Danieli, C. Angelini, and D. C. Rao. Genetic epidemiology of myotonic dystrophy. *Genetic Epidemiology*, 4(4):289–298, 1987.

[51] M. Ota, N. Sato, Y. Ohya, Y. Aoki, K. Mizukami, T. Mori, and T. Asada. Relationship between diffusion tensor imaging and brain morphology in patients with myotonic dystrophy. *Neuroscience Letters*, 407(3):234–239, October 2006.

[52] G.S. Pell, R.S. Briellmann, C.H. P. Chan, H. Pardoe, D. F. Abbott, and G. D. Jackson. Selection of the control group for VBM analysis: influence of covariates, matching and sample size. *NeuroImage*, 41(4):1324–1335, July 2008. PMID: 18467131.

[53] J. Ramirez, J.M. Gorriz, D. Salas-Gonzalez, A. Romero, M. Lopez, I. Alvarez, and M. Gomez-Rio. Computer-aided diagnosis of alzheimer's type dementia combining support vector machines and discriminant set of features. *Information Sciences*, In Press, Corrected Proof:–, 2009.

[54] D. E. Rumelhart, G. E. Hinton, and R. J. Williams. *Learning internal representations by error propagation*, pages 318–362. MIT Press, 1986.

[55] A. Savio, M.T. García-Sebastián, M. Graña, and J. Villanúa. Results of an adaboost approach on alzheimer's disease detection on mri. In J.R. Alvarez F. dela Paz F.J. Tolede (Eds.) J. Mira, J. M. Ferrández, editor, *Bioinspired applications in Artificial and Natural Computation, Proc. IWINAC 2009, Part II,*, volume 5602 of *LNCS*. Springer-Verlag, 2009.

[56] A. Savio, M.T. García-Sebastián, C. Hernandez, M. Graña, and J. Villanúa. Classification results of artificial neural networks for alzheimer's disease detection. In Hujun Yin (eds) Emilio Corchado, editor, *Intelligent Data Engineering and Automated Learning- IDEAL 2009*, volume 5788 of *LNCS*, pages 641–648. Springer-Verlag, 2009.

[57] R. I. Scahill, J. M. Schott, J. M. Stevens, M. N. Rossor, and N. C. Fox. Mapping the evolution of regional atrophy in alzheimer's disease: Unbiased analysis of fluid-registered serial MRI. *Proceedings of the National Academy of Sciences*, 99(7):4703, 2002.

[58] R.E. Schapire and Y. Singer. Improved boosting algorithms using confidence-rated predictions. *Machine Learning*, 37(3):297–336, December 1999.

[59] A. Sistiaga, I. Urreta, M. Jodar, A. M. Cobo, J. Emparanza, D. Otaegui, J. J. Poza, J. J. Merino, H. Imaz, J. F. Marti-Masso, and A. Lopez de Munain. Cognitive/Personality pattern and triplet expansion size in adult myotonic dystrophy type 1 (DM1): CTG repeats, cognition and personality in DM1. *Psychological Medicine*, First View:1–9, 2009.

[60] P. Somervuo and T. Kohonen. Self-Organizing maps and learning vector quantization for feature sequences. *Neural Process. Lett.*, 10(2):151–159, 1999.

[61] D.F. Specht. Probabilistic neural networks. *Neural Netw.*, 3(1):109–118, 1990.

[62] D. Tao, X. Tang, X. Li, and X. Wu. Asymmetric bagging and random subspace for Support Vector Machines-based relevance feedback in image retrieval. *IEEE Trans. Pattern Anal. Mach. Intell.*, 28(7):1088–1099, 2006.

[63] V. Vapnik. *Statistical learning theory*. Wiley-Interscience, 1998.

[64] P. Vemuri, J.L. Gunter, M.L. Senjem, J.L. Whitwell, K. Kantarci, D.S. Knopman, B.F. Boeve, R.C. Petersen, and C.R. Jack. Alzheimer's disease diagnosis in individual subjects using structural MR images: validation studies. *NeuroImage*, 39(3):1186–1197, Feb 2008.

[65] J. Zhang, B. Yan, X. Huang, P. Yang, and C. Huang. The diagnosis of Alzheimer's disease based on Voxel-Based Morphometry and Support Vector Machine. In *Proceedings of the 2008 Fourth International Conference on Natural Computation (ICNC)*, pages 197–201, Washington, DC, USA, 2008. IEEE Computer Society.

A Comparison of VBM Results by SPM, ICA and LICA

Darya Chyzyk, Maite Termenon, and Alexandre Savio

Computational Intelligence Group
Dept. CCIA, UPV/EHU, Apdo. 649, 20080 San Sebastian, Spain
www.ehu.es/ccwintco

Abstract. Lattice Independent Component Analysis (LICA) approach consists of a detection of independent vectors in the morphological or lattice theoretic sense that are the basis for a linear decomposition of the data. We apply it in this paper to a Voxel Based Morphometry (VBM) study on Alzheimer's disease (AD) patients extracted from a well known public database. The approach is compared to SPM and Independent Component Analysis results.

1 Introduction

Morphometry analysis has become a common tool for computational brain anatomy studies. It allows a comprehensive measurement of structural differences within a group or across groups, not just in specific structures, but throughout the entire brain. Voxel-based Morphometry (VBM) is a computational approach to neuroanatomy that measures differences in local concentrations of brain tissue through a voxel-wise comparison of multiple brain images [3]. For instance, VBM has been applied to study volumetric atrophy of the grey matter (GM) in areas of neocortex of AD patients vs. control subjects [4,17,6]. The procedure involves the spatial normalization of subject images into a standard space, segmentation of tissue classes using *a priori* probability maps, smoothing to correct noise and small variations, and voxel-wise statistical tests. Statistical analysis is based on the General Linear Model (GLM) to describe the data in terms of experimental and confounding effects, and residual variability. Classical statistical inference is used to test hypotheses that are expressed in terms of GLM estimated regression parameters. This computation is specified as a contrast that produces a scalar estimate which the Statistical Parametric Map (SPM) thresholds according to the Random Field theory to obtain clusters of significant voxels.

SPM has been also widely applied to fMRI voxel activation analysis. Alternative works on fMRI analysis are based on the Independent Component Analysis (ICA) [18] assuming that the time series observations are linear mixtures of independent sources which can not be observed. This leads us to consider here ICA and other approaches for VBM on transversal data. ICA assumes that the source signals are non-Gaussian and that the linear mixing process is unknown. The approaches to solve the ICA problem obtain both the independent sources

E.S. Corchado Rodriguez et al. (Eds.): HAIS 2010, Part II, LNAI 6077, pp. 429–435, 2010.

and the linear unmixing matrix. These approaches are unsupervised because no *a priori* information about the sources or the mixing process is included, hence the alternative name of Blind Deconvolution. Sources in VBM correspond to the pattern of intensities of a voxel across the population of subjects. We have used the FastICA algorithm implementation available at [2] . We have also used the implementations of Maximum Likelihood ICA [14] (which is equivalent to Infomax ICA), Mean Field ICA [13], Molgedey and Schouster ICA based on dynamic decorrelation [15], which are available at [1].

We have proposed [11,9] a Lattice Computing [8] approach that we call Lattice Independent Component Analysis (LICA) that consists of two steps. Firts it selects Strong Lattice Independent (SLI) vectors from the input dataset using an incremental algorithm, the Incremental Endmember Induction Algorithm (IEIA) [10]. Second, because of the conjectured equivalence between SLI and Affine Independence [12], it performs the linear unmixing of the input dataset based on these endmembers[1]. Therefore, the approach is a mixture of linear and nonlinear methods.

We assume that the data is generated as a convex combination of a set of endmembers which are the vertices of a convex polytope covering some region of the input data. This assumption is similar to the linear mixture assumed by the ICA approach, however we do not impose any probabilistic assumption on the data. The endmembers discovered by the IEIA are equivalent to the GLM design matrix columns, and the unmixing process is identical to the conventional least squares estimator so LICA is a kind of unsupervised GLM whose regressor functions are mined from the input dataset. If we try to stablish correspondences to the ICA, the endmembers correspond to the unknown sources and the mixing matrix is the one given by the abundance coefficients computed by least squares estimation.

The outline of the paper is as follows: Section 2 overviews the LICA. Section 3 presents results of the proposed approach on a VBM case study on an Alzheimer's Disease population with paired controls. Section 4 provides some conclusions.

2 The Lattice Independent Component Analysis

The linear mixing model can be expressed as follows: $\mathbf{x} = \sum_{i=1}^{M} a_i \mathbf{e}_i + \mathbf{w} = \mathbf{E}\mathbf{a} + \mathbf{w}$, where $\mathbf{x}$ is the d-dimension pattern vector corresponding to the fMRI voxel time series vector, $\mathbf{E}$ is a $d \times M$ matrix whose columns are the d-dimensional vectors, when these vectors are the vertices of a convex region covering the data they are called endmembers $\mathbf{e}_i, i = 1, .., M$, $\mathbf{a}$ is the M-dimension vector of linear mixing coefficients, which correspond to fractional abundances in the convex case, and $\mathbf{w}$ is the d-dimension additive observation noise vector. The linear mixing model is subjected to two constraints on the abundance coefficients when the data points fall into a simplex whose vertices are the endmembers, all abundance coefficients must be non-negative $a_i \geq 0, i = 1, .., M$ and normalized to unity

[1] The original works were devoted to unsupervised hyperspectral image segmentation, therefore the use of the name *endmember* for the selected vectors.

summation $\sum_{i=1}^{M} a_i = 1$. Under this circumstance, we expect that the vectors in $\mathbf{E}$ are affinely independent and that the convex region defined by them includes *all* the data points. Once the endmembers have been determined, the unmixing process is the computation of the matrix inversion that gives the coordinates of the point relative to the convex region vertices. The simplest approach is the unconstrained least squared error (LSE) estimation given by: $\widehat{\mathbf{a}} = \left(\mathbf{E}^T\mathbf{E}\right)^{-1}\mathbf{E}^T\mathbf{x}$. Even when the vectors in $\mathbf{E}$ are affinely independent, the coefficients that result from this estimation do not necessarily fulfill the non-negativity and unity normalization. Ensuring both conditions is a complex problem.

We call *Lattice Independent Component Analysis* (LICA) the following approach:

1. Induce from the given data a set of Strongly Lattice Independent vectors. In this paper we apply the Incremental Endmember Induction Algorithm (IEIA) [10,9]. These vectors are taken as a set of affine independent vectors. The advantages of this approach are (1) that we are not imposing statistical assumptions, (2) that the algorithm is one-pass and very fast because it only uses comparisons and addition, (3) that it is unsupervised and incremental, and (4) that it detects naturally the number of endmembers.
2. Apply the unconstrained least squares estimation to obtain the mixing matrix. The detection results are based on the analysis of the coefficients of this matrix. Therefore, the approach is a combination of linear and lattice computing: a linear component analysis where the components have been discovered by non-linear, lattice theory based, algorithms.

3 A VBM Case Study

3.1 Experimental Data

Ninety eight right-handed women (aged 65-96 yr) were selected from the Open Access Series of Imaging Studies (OASIS) database (http://www.oasis-brains.org) [16]. OASIS data set has a cross-sectional collection of 416 subjects covering the adult life span aged 18 to 96 including individuals with early-stage Alzheimer's Disease. We have ruled out a set of 200 subjects whose demographic, clinical or derived anatomic volumes information was incomplete. For the present study there are 49 subjects who have been diagnosed with very mild to mild AD and 49 nondemented. A summary of subject demographics and dementia status is shown in table 1.

Multiple (three or four) high-resolution structural T1-weighted magnetization-prepared rapid gradient echo (MP-RAGE) images were acquired [5] on a 1.5-T Vision scanner (Siemens, Erlangen, Germany) in a single imaging session. Image parameters: TR= 9.7 msec., TE= 4.0 msec., Flip angle= 10, TI= 20 msec., TD= 200 msec., 128 sagittal 1.25 mm slices without gaps and pixels resolution of 256×256 (1×1mm).

Table 1. Summary of subject demographics and dementia status. Education codes correspond to the following levels of education: 1 less than high school grad., 2: high school grad., 3: some college, 4: college grad., 5: beyond college. Categories of socioeconomic status: from 1 (biggest status) to 5 (lowest status). MMSE score ranges from 0 (worst) to 30 (best).

	Very mild to mild AD	Normal
No. of subjects	49	49
Age	78.08 (66-96)	77.77 (65-94)
Education	2.63 (1-5)	2.87 (1-5)
Socioeconomic status	2.94 (1-5)	2.88 (1-5)
CDR (0.5 / 1 / 2)	31 / 17 / 1	0
MMSE	24 (15-30)	28.96 (26-30)

3.2 Algorithms Applied

We have applied both SPM and FSL approaches to this data. Figure 1 shows the activation results from a FSL study on this data. We have used the preprocessed volumes as inputs for the ICA and LICA algorithms. Detection of significative voxels in ICA and LICA approaches is given by setting the threshold on the mixing/abundance coefficients to the 95% percentil of the empirical distribution (histogram) of this coefficients. We present in figure 2 the activation results corresponding to the 3d endmember detected by the LICA algorithm, for comparison with the FSL results. It can be appreciated a great agreement. Because both ICA and LICA are unsupervised in the sense that the pattern searched is not prescribed, they suffer from the identificability problem: we do not know beforehand which of the discovered sources/endmembers correspond to the sought significative pattern, while SPM and FSL approaches are supervised in the sense that we provide the a priori identification of controls and patients, searching for voxels that correlate well with this indicative variable.

In order to provide a quantitative assessment of the agreement between the discoveries of the ICA and LICA and the statistical significances computed by SPM and FSL we computed the correlations between the abundance/mixture matrices of the ICA approach. Table 2 shows the correlation between the mixing coefficients and the abundance coefficients of the corresponding ICA ML algorithm sources (the one with best results) and the LICA endmembers, both before (left) and after (right) the application of the 95% percentil threshold to determine the signficative voxels. We decide that the best relation is between the third LICA endmember and the second ICA source, because their correlation does not drop after thresholding, contrary to LICA#4 with ICA#1 whose correlation drops dramatically after thresholding for significance detection.

To give some measure of the meaningfulness of the unsupervised approaches, we must find out if they are able to uncover something that has a good agreement with the findings of either SPM or FSL approaches. Therefore we compute the correlation between the mixing/abundance coefficients of ICA/LICA and the

Fig. 1. FSL significative voxel detection

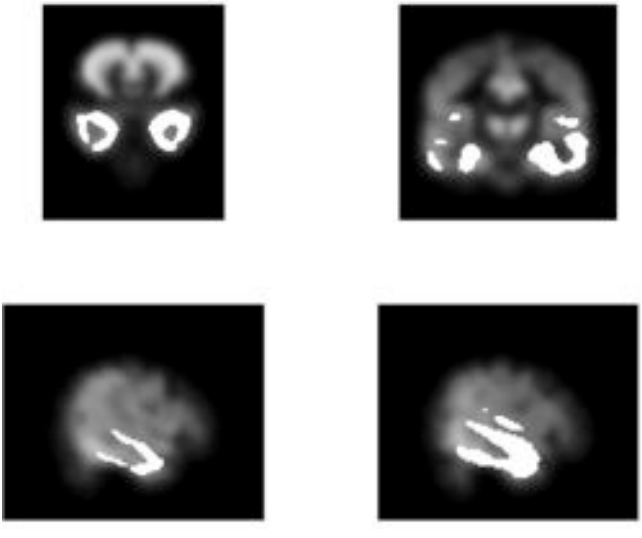

Fig. 2. LICA activation results for the endmember #3

Table 2. Correlation among ICA and LICA mixing coefficients, before (left) and after (right) thresholding for activation detection

	ICA ML					ICA ML			
LICA	#1	#2	#3	#4	LICA	#1	#2	#3	#4
#1	0.05	0.24	0.44	-0.01	#1	0.003	0.09	0.34	0.03
#2	0.19	0.12	-0.28	-0.60	#2	0.15	0.05	-0.02	-0.02
#3	0.38	0.67	0.30	0.24	#3	0.01	0.66	0.007	0.08
#4	0.69	0.04	0.26	-0.18	#4	0.26	-0.01	0.13	-0.00

Table 3. Agreement between SPM, FSL, ICA and LICA

	#1	#2	#3	#4
ICA vs SPM	-0.11	**0.32**	-0.02	0.02
LICA vs SPM	-0.03	-0.03	**0.23**	-0.06
ICA vs FSL	0.08	**0.56**	0.03	0.07
LICA vs FSL	0.07	0.02	**0.58**	0.20

statistics computed by SPM and FSL. Table 3 shows these correlations. Here the agreement between the third endmember of LICA and the secod source of ICA ML obtains a further support, because both are the ones that show maximal agreement with SPM and FSL, and in both ICA and LICA the agreement with FSL is greater than with SPM results.

4 Summary and Conclusions

We have proposed and applied a Lattice Independent Component Analysis (LICA) to the model-free (unsupervised) VBM analysis. The LICA is based on the application of a Lattice Computing based algorithm IEIA for the selection of the endmembers, and the linear unmixing of the data based on these endmembers. We compare our results with those obtained by the conventional SPM and FSL algorithms, as well as the ICA unsupervised approach. We find a strong agreement between LICA results and those of ICA, and we can identify endmembers and sources that correspond closely to the significative detection of results in agreement with SPM and FSL, providing a validation of the approach. The problem with VBM and similar morphometric approaches is that we need to be able to give some interpretation to the findings of the ICA and LICA algorithms, that is, besides the obvious identification of voxels that correlate well with the indicative variable, the problem is to find additional regularities and give them some sense. Some kind of hierachical analysis [7] could be advantageous in the future works.

References

1. http://isp.imm.dtu.dk/toolbox/ica/index.html
2. http://www.cis.hut.fi/projects/ica/fastica/
3. Ashburner, J., Friston, K.J.: Voxel-based morphometry: The methods. Neuroimage 11(6), 805–821 (2000)
4. Busatto, G.F., Garrido, G.E.J., Almeida, O.P., Castro, C.C., Camargo, C.H.P., Cid, C.G., Buchpiguel, C.A., Furuie, S., Bottino, C.M.: A voxel-based morphometry study of temporal lobe gray matter reductions in alzheimer's disease. Neurobiology of Aging 24(2), 221–231 (2003)
5. Fotenos, A.F., Snyder, A.Z., Girton, L.E., Morris, J.C., Buckner, R.L.: Normative estimates of cross-sectional and longitudinal brain volume decline in aging and AD. Neurology 64(6), 1032–1039 (2005)
6. Frisoni, G.B., Testa, C., Zorzan, A., Sabattoli, F., Beltramello, A., Soininen, H., Laakso, M.P.: Detection of grey matter loss in mild alzheimer's disease with voxel based morphometry. Journal of Neurology, Neurosurgery & Psychiatry 73(6), 657–664 (2002)
7. Graña, M., Torrealdea, F.J.: Hierarchically structured systems. European Journal of Operational Research 25, 20–26 (1986)
8. Graña, M.: A brief review of lattice computing. In: Proc. WCCI, pp. 1777–1781 (2008)
9. Graña, M., Chyzyk, D., García-Sebastián, M., Hernández, C.: Lattice independent component analysis for FMRI. Information Sciences (in press, 2010)
10. Graña, M., Villaverde, I., Maldonado, J.O., Hernandez, C.: Two lattice computing approaches for the unsupervised segmentation of hyperspectral images. Neurocomputing 72(10-12), 2111–2120 (2009)
11. Graña, M., Savio, A.M., Garcia-Sebastian, M., Fernandez, E.: A lattice computing approach for on-line FMRI analysis. Image and Vision Computing (in press, 2009)
12. Schmalz, M.S., Ritter, G.X., Urcid, G.: Autonomous single-pass endmember approximation using lattice auto-associative memories. Neurocomputing 72(10-12), 2101–2110 (2009)
13. Højen-Sørensen, P., Winther, O., Hansen, L.K.: Mean field approaches to independent component analysis. Neural Computation 14, 889–918 (2002)
14. Kolenda, T., Hansen, L.K., Larsen, J.: Blind detection of independent dynamic components. In: Proc. IEEE ICASSP 2001, vol. 5, pp. 3197–3200 (2001)
15. Schuster, H., Molgedey, L.: Separation of independent signals using time-delayed correlations. Physical Review Letters 72(23), 3634–3637 (1994)
16. Marcus, D.S., Wang, T.H., Parker, J., Csernansky, J.G., Morris, J.C., Buckner, R.L.: Open access series of imaging studies (OASIS): cross-sectional MRI data in young, middle aged, nondemented, and demented older adults. Journal of Cognitive Neuroscience 19(9), 1498–1507 (2007)
17. Scahill, R.I., Schott, J.M., Stevens, J.M., Rossor, M.N., Fox, N.C.: Mapping the evolution of regional atrophy in alzheimer's disease: Unbiased analysis of fluid-registered serial MRI. Proceedings of the National Academy of Sciences 99(7), 4703 (2002)
18. Calhoun, T.V.D., Adali, T.: Unmixing FMRI with independent component analysis. IEEE Engineering in Medicine and Biology Magazine 25(2), 79–90 (2006)

Hybrid Dendritic Computing with Kernel-LICA applied to Alzheimer's Disease detection in MRI

Darya Chyzhyk, Manuel Graña, Alexandre Savio, Josu Maiora

Computational Intelligence Group, Universidad del Pais Vasco, www.ehu.es/ccwintco

Abstract

Dendritic Computing has been proved to produce perfect approximation of any data distribution. This result guarantees perfect accuracy training. However, we have found great performance degradation when tested on conventional k-fold cross-validation schemes. In this paper we propose to use Lattice Independent Component Analysis (LICA) and the Kernel transformation of the data as an appropriate feature extraction that improves the generalization of Dendritic Computing classifiers. We obtain a big increase in classification performance applying with this schema over a database of features extracted from Magnetic Resonance Imaging (MRI) including Alzheimer's Disease (AD) patients and control subjects.

1. Introduction

Dendritic Computing (DC) [1, 9, 13, 14, 16] was introduced as a simple, fast, efficient biologically inspired method to build up classifiers for binary class problems, which could be extended to multiple classes. Specifically the single neuron lattice model with dendrite computation (SNLDC), has been proved to compute a perfect approximation to any data distribution [12, 16]. However it suffers from over-fitting problems. The results on cross-validation experiments result in very poor performance. We have confirmed that on a particular database that we have studied in previous works [2, 17, 18]. We found that SNLDC showed high sensitivity but very low specificity in a 10-fold cross-validation experiment. These baseline results are reproduced below in section 5. To improve the method, [1] proposed to compute the optimal rotation of each of the hyperboxes by some optimization method at each step of the training algorithm. This procedure is computationally very expensive and does not guarantee optimal generalization of classification performance. It depends on the local distribution of the data, as a local kernel transformation whose parameters must be fitted locally.

In this paper we propose to perform a transformation of the data which is appropriate for later DC based classification systems. This transformation is composed of a kernel transformation [19] followed by dimension reduction process realized by Lattice Independent Component Analysis (LICA). The com-

posite transformation is the Kernel-LICA approach. The kernel transformation is intended to produce a high dimensional feature representation of the data that eases the subsequent processes. The dimension reduction phase could be realized by other methods, such as Principal Component Analysis (PCA), which has also been tested in this paper. Notice taht both Dendritic Computing and LICA are Lattice Computing [5] algorithms.

The target application of our work is the detection of Alzheimer's Disease (AD) patients from brain magnetic resonance imaging (MRI) scans. We have worked over a database of MRI features[1] extracted from the OASIS database of MRI scans of AD patients and controls [18, 17, 2]. We selected a balanced set of AD patients and controls of the same sex, then we performed a Voxel Based Morphometry (VBM) analysis to determine the location of the voxel clusters most affected by the disease. These voxel clusters were collected in the gray matter segmentation of each MRI scan and used to compute feature vectors for classification. In this paper we use the mean and standard deviation of the voxel values of these clusters.

The structure of the paper is the following. Section 2 reviews the baseline dendritic approach used. Section 3 reviews the LICA approach. Section 4 describes our application of the kernel trick to LICA. Section 5 gives our experimental results on the AD database. Section 6 gives our conclusions.

2. Dendritic Computing

A single layer morphological neuron endowed with dendrite computation based on lattice algebra was introduced in [16]. Figure 1 illustrates the structure of a single output class single layer Dendritic Computing system, where D_j denotes the dendrite with associated inhibitory and excitatory weights $\left(w_{ij}^0, w_{ij}^1\right)$ from the synapses coming from the i-th input neuron. The response of the j-th dendrite is as follows:

$$\tau_j\left(\mathbf{x}^\xi\right) = p_j \bigwedge_{i \in I_j} \bigwedge_{l \in L_{ij}} (-1)^{1-l} \left(x_i^\xi + w_{ij}^l\right), \tag{1}$$

where $l \in L \subseteq \{0, 1\}$ identifies the existence and inhibitory/excitatory character of the weight, $L_{ij} = \emptyset$ means that there is no synapse from the i-th input neuron to the j-th dendrite; $p_j \in \{-1, 1\}$ encodes the inhibitory/excitatory response of the dendrite. It has been shown [16] that models based on dendritic computation have powerful approximation properties. In fact, they showed that this model is able to approximate any compact region in higher dimensional Euclidean space to within any desired degree of accuracy. They provide a constructive algorithm which is the basis for the present paper. The hard-limiter function of step 3 is the signum function. The algorithm starts building a hyperbox enclosing all pattern samples of class 1, that is, $C_1 = \{\xi : c_\xi = 1\}$. Then, the dendrites are

[1] http://www.ehu.es/ccwintco/index.php/GIC-experimental-databases

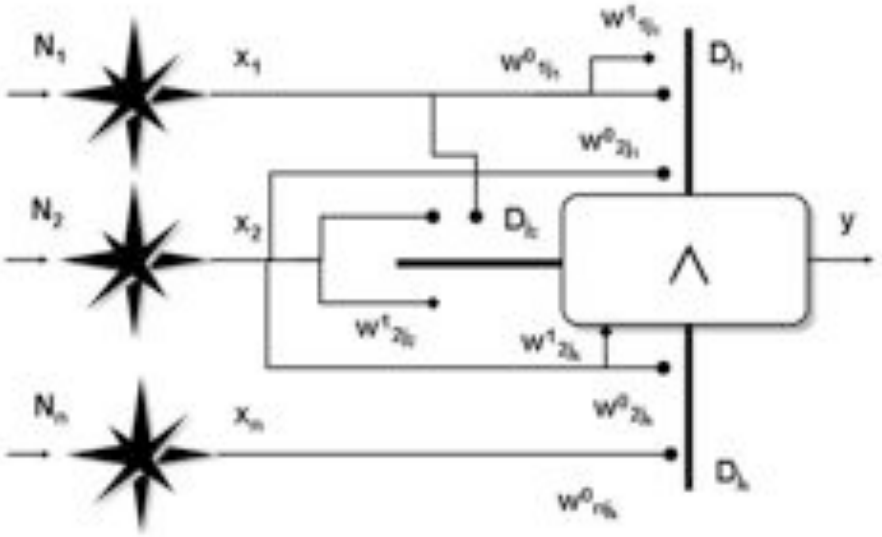

Figure 1: A single ouput single layer Dendritic Computing system.

added to the structure trying to remove misclasified patterns of class 0 that fall inside this hyperbox. In step 6 the algorithm selects at random one such misclassified patterns, computes the minimum Chebyshev distance to a class 1 pattern and uses the patterns that are at this distance from the misclassified pattern to build a hyperbox that is removed from the C_1 initial hyperbox. In this process, if one of the bounds is not defined, $L_{ij} \neq \{0, 1\}$, then the box spans to infinity in this dimension. One of the recent improvements [1] consists in considering rotations of the patterns obtained from some learning process. Then, the response of the dendrite is given by:

$$\tau_j\left(\mathbf{x}^{\xi}\right) = p_j \bigwedge_{i \in I_j} \bigwedge_{l \in L_{ij}} (-1)^{1-l} \left(R\left(\mathbf{x}^{\xi}\right)_i + w_{ij}^{l}\right),$$

where R denotes the rotation matrix. The process of estimating R can be very time consuming, it is a local process performed during steps 7 to 10 of the learning process of algorithm 1. Following this idea, we propose and test in this paper that the enhancement of the single layer neuron model with dendritic computation performance could be obtained from the transformation of the data using the kernel approach in combination with a lattice computing based feature extraction process, the LICA.

Algorithm 1 Dendritic Computing learning based on elimination

Training set $T = \left\{ \left(\mathbf{x}^{\xi}, c_{\xi} \right) \mathbf{x}^{\xi} \in \mathbb{R}^{n}, c_{\xi} \in \{0,1\}; \xi = 1, \ldots, m \right\}$,

1. Initialize $j = 1$, $I_j = \{1, \ldots n\}$, $P_j = \{1, \ldots, m\}$, $L_{ij} = \{0,1\}$,

$$w_{ij}^{1} = - \bigwedge_{c_{\xi}=1} x_i^{\xi};\ w_{ij}^{0} = - \bigvee_{c_{\xi}=1} x_i^{\xi},\ \forall i \in I$$

2. Compute response of the current dendrite D_j, with $p_j = (-1)^{\mathrm{sgn}(j-1)}$:

$$\tau_j \left(\mathbf{x}^{\xi} \right) = p_j \bigwedge_{i \in I_j} \bigwedge_{l \in L_{ij}} (-1)^{1-l} \left(x_i^{\xi} + w_{ij}^{l} \right),\ \forall \xi \in P_j.$$

3. Compute the total response of the neuron:

$$\tau \left(\mathbf{x}^{\xi} \right) = \bigwedge_{k=1}^{j} \tau_k \left(\mathbf{x}^{\xi} \right);\ \xi = 1, \ldots, m.$$

4. If $\forall \xi \left(f \left(\tau \left(\mathbf{x}^{\xi} \right) \right) = c_{\xi} \right)$ the algorithm stops here with perfect classification of the training set.
5. Create a new dendrite $j = j + 1$, $I_j = I' = X = E = H = \emptyset$, $D = C_1$
6. Select $\mathbf{x}^{\gamma}$ such that $c_{\gamma} = 0$ and $f \left(\tau \left(\mathbf{x}^{\xi} \right) \right) = 1$.
7. $\mu = \bigwedge_{\xi \neq \gamma} \left\{ \bigvee_{i=1}^{n} \left| x_i^{\gamma} - x_i^{\xi} \right| : \xi \in D \right\}$.
8. $I' = \left\{ i : \left| x_i^{\gamma} - x_i^{\xi} \right| = \mu, \xi \in D \right\}$; $X = \left\{ \left(i, x_i^{\xi} \right) : \left| x_i^{\gamma} - x_i^{\xi} \right| = \mu, \xi \in D \right\}$.
9. $\forall \left(i, x_i^{\xi} \right) \in X$
   (a) if $x_i^{\gamma} > x_i^{\xi}$ then $w_{ij}^{1} = -x_i^{\xi}$, $E_{ij} = \{1\}$
   (b) if $x_i^{\gamma} < x_i^{\xi}$ then $w_{ij}^{0} = -x_i^{\xi}$, $H_{ij} = \{0\}$
10. $I_j = I_j \bigcup I'$; $L_{ij} = E_{ij} \bigcup H_{ij}$
11. $D' = \left\{ \xi \in D : \forall i \in I_j, -w_{ij}^{1} < x_i^{\xi} < -w_{ij}^{0} \right\}$. If $D' = \emptyset$ then goto step 2, else $D = D'$ goto step 7.

3. LICA

Lattice Independent Component Analysis is based on the Lattice Independence discovered when dealing with noise robustness in Morphological Associative Memories [15]. Works on finding lattice independent sources (aka endmembers) for linear unmixing started on hyperspectral image processing [8, 11]. Since then, it has been also proposed for functional MRI analysis [7] among other.

Under the Linear Mixing Model (LMM) the design matrix is composed of endmembers which define a convex region covering the measured data. The linear coefficients are known as fractional abundance coefficients that give the contribution of each endmember to the observed data:

$$\mathbf{y} = \sum_{i=1}^{M} a_i \mathbf{s}_i + \mathbf{w} = \mathbf{S}\mathbf{a} + \mathbf{w}, \tag{2}$$

where $\mathbf{y}$ is the d-dimension measured vector, $\mathbf{S}$ is the $d \times M$ matrix whose columns are the d-dimension endmembers $\mathbf{s}_i, i = 1, .., M$, $\mathbf{a}$ is the M-dimension abundance vector, and $\mathbf{w}$ is the d-dimension additive observation noise vector. Under this generative model, two constraints on the abundance coefficients hold. First, to be physically meaningful, all abundance coefficients must be non-negative $a_i \geq 0, i = 1, .., M$, because the negative contribution is not possible in the physical sense. Second, to account for the entire composition, they must be fully additive $\sum_{i=1}^{M} a_i = 1$. As a side effect, there is a saturation condition $a_i \leq 1, i = 1, .., M$, because no isolate endmember can account for more than the observed material. From a geometrical point of view, these restrictions mean that we expect the endmembers in $\mathbf{S}$ to be an Affine Independent set of points, and that the convex region defined by them covers *all* the data points.

The *Lattice Independent Component Analysis* (LICA) approach assumes the LMM as expressed in equation 2. Moreover, the equivalence between Affine Independence and Strong Lattice Independence [10] is used to induce from the data the endmembers that compose the matrix $\mathbf{S}$. Briefly, LICA consists of two steps:

1. Use an Endmember Induction Algorithm (EIA) to induce from the data a set of Strongly Lattice Independent vectors. In our works we use the algorithm described in [3, 4, 8, 7]. These vectors are taken as a set of affine independent vectors that forms the matrix $\mathbf{S}$ of equation 2.
2. Apply the Full Constrained Least Squares estimation to obtain the abundance vector according to the conditions for LMM.

The advantages of this approach are (1) that we are not imposing statistical assumptions to find the sources, (2) that the algorithm is one-pass and very fast because it only uses lattice operators and addition, (3) that it is unsupervised and incremental, and (4) that it can be tuned to detect the number of endmembers by adjusting a noise-filtering related parameter. When $M \ll d$ the computation of the abundance coefficientes can be interpreted as a dimension

reduction transformation, or a feature extraction process. It is under this view that we will use LICA in the experimental works described in section 5.

3.1. Endmember Induction Algorithm

The EIA that we introduce in this section is a heuristic that is somehow simpler and faster than the formulations of the EIA algorithm proposed and used in [8, 6]. Let us denote $\left\{\mathbf{x}_i \in \mathbb{R}^d : i = 1, .., n\right\}$ a set of input patterns. Vectors $\overrightarrow{\boldsymbol{\mu}}$ and $\overrightarrow{\boldsymbol{\sigma}}$ are, respectively, the mean vector and the vector of standard deviations computed componentwise over the data sample, α the filtering factor related to data variability, and E the set of already discovered endmembers. For each input vector, first, the algorithm tests that the input vector is not too similar to the already discovered endmembers, we test for each component independently that the euclidean distance between input and endmembers is lower than the corresponding component $\alpha\overrightarrow{\boldsymbol{\sigma}_j}$. The gain parameter α controls the amount of flexibility in the discovering of new endmembers. It determines if a vector is interpreted as a random perturbation of an already selected endmember. It has a great impact on the number of endmembers found, where low values imply large number of endmembers. Lattice Independence is tested against the recall provided by the LAAM built from E. Strong Lattice Independence is verified testing the max- or min-dominance on the set of endmembers. The algorithm runs only once over the data. Discussion of its theoretical justification can be found in [8, 6] and will not be reproduced here. The detailed description of the steps in the heuristic algorithm is presented as algorithm 2.

4. Kernel approaches

The kernel transformation has been found very useful in statistics and pattern recognition applications [19]. A kernel is a function

$$\kappa\left(\mathbf{x}, \mathbf{z}\right) = \left\langle \phi\left(\mathbf{x}\right), \phi\left(\mathbf{z}\right) \right\rangle,$$

for all $\mathbf{x}, \mathbf{z} \in X$, where $X \subseteq \mathbb{R}^n$ is the input pattern space, and ϕ is a mapping into an (inner product) feature space F

$$\phi : X \to F.$$

Kernel functions make possible the use of feature spaces with an exponential or even infinite number of dimensions without explicitly computing the features. They are combined with other algorithms as a preprocessing step of the data. In the literature they have allowed to extend linear efficient solutions to non-linear problems. For instance, consider the linear regression problem of finding the linear function $g\left(\mathbf{x}\right) = \left\langle \mathbf{w}, \mathbf{x} \right\rangle$ that best interpolates a given training set $S = \left\{\left(\mathbf{x}_1, y_1\right), \ldots, \left(\mathbf{x}_m, y_m\right)\right\}$ with $y_i \in \mathbb{R}$, solved minimizing the function $f\left(\mathbf{x}, y\right) = \left|y - \left\langle \mathbf{w}, \mathbf{x} \right\rangle\right|$ by the well know least squares solution $\mathbf{w} = \left(\mathbf{X}\mathbf{X}'\right)^{-1}\mathbf{X}'\mathbf{y}$, where $\mathbf{X}$ is the matrix composed of all the sample input vectors, and $\mathbf{y}$ the vector composed of all the labels in the sample. The non-linear extension can be

Algorithm 2 A LAAM based Incremental Endmember Induction Algorithm

1. Shift the data sample to zero mean $\{\mathbf{x}_i^c = \mathbf{x}_i - \overrightarrow{\boldsymbol{\mu}}; i = 1, .., n\}$.
2. Initialize the set of endmembers with the first data sample $E = \left\{\mathbf{e}^1 = \mathbf{x}_1^c\right\}$. The initial set of endmember sample indices is $I = \{1\}$.
3. Construct the lattice autoassociative memory based on the set of endmembers: M_{EE}.
4. For each input data vector $\mathbf{x}_i^c$
   (a) If there is any $\mathbf{e} \in E$ such that $\forall j : \left\|\mathbf{x}_{ij}^c - \mathbf{e}_j\right\| < \alpha\overrightarrow{\boldsymbol{\sigma}_j}$ discard $\mathbf{x}_i^c$, otherwise proceed to test SLI
   (b) If $\mathbf{x}_i^c = M_{EE} \boxslash \mathbf{x}_i^c$ then discard $\mathbf{x}_i^c$ because it is lattice dependent on the already discovered endmembers.
   (c) Test max/min dominance on the enlarged set of endmembers $E' = E \cup \{\mathbf{x}_i^c\}$ to ensure SLI,
      i. $c_1 = c_2 = 0$
      ii. for $i = 1, \ldots, K+1$
      iii. $\mathbf{s}_1 = \mathbf{s}_2 = \mathbf{0}$
         A. for $j = 1, \ldots, K+1$ and $j \neq i$
            $\mathbf{d} = \mathbf{e}_i - \mathbf{e}_j$; $m_1 = \max(\mathbf{d})$; $m_2 = \min(\mathbf{d})$.
            $\mathbf{s}_1 = \mathbf{s}_1 + (\mathbf{d} == m_1)$, $\mathbf{s}_2 = \mathbf{s}_2 + (\mathbf{d} == m_2)$.
         B. $c_1 = c_1 + (\max(\mathbf{s}_1) == K)$ or $c_2 = c_2 + (\max(\mathbf{s}_2) == K)$.
      iv. If $c_1 = K+1$ or $c_2 = K+1$ then E' is a set of SLI vectors, go to 3 with the enlarged set of lattice sources and resume exploration with the next input.
5. The output set of endmembers is the set of original data vectors $\{\mathbf{f}(i) : i \in I\}$ corresponding to the vectors selected as members of E.

Figure 2: The experimental exploration.

obtained considering a transformation of the sample into the feature space $\hat{S} = \{(\phi(\mathbf{x}_1), y_1), \ldots, (\phi(\mathbf{x}_m), y_m)\}$. The function to be minimized is $f(\mathbf{x}, y) = |y - \langle \mathbf{w}, \phi(\mathbf{x}) \rangle|$. Using a dual approach that reformulates the predictive function as $g(\mathbf{x}) = \mathbf{y}'(\mathbf{G} - \lambda \mathbf{I})^{-1} \mathbf{k}$, where $\mathbf{G} = \mathbf{X}\mathbf{X}'$ with entries $\mathbf{G}_{ij} = \langle \phi(\mathbf{x}_i), \phi(\mathbf{x}_j) \rangle$, and $\mathbf{k}$ contains the values $k_i = \langle \phi(\mathbf{x}_i), \phi(\mathbf{x}) \rangle$. That is, all computations can be performed on the values of the kernel functions, solving the problem with the same procedure employed to solve the linear problem. The kernel matrix $\mathbf{G}$ is the central structure of all the kernel based approaches. For instance, Principal Component Analysis (PCA) of the kernel matrix can be interpreted (with some corrections [19]) as a PCA of the data in feature space. We have followed the approach as a heuristic, applying also the LICA on the kernel matrix. The obtained success would indicate the need to examine more closely this approach. Finally we define the Gaussian kernel that will be used in the experiments:

$$\kappa(\mathbf{x}, \mathbf{z}) = \exp\left(-\|\mathbf{x} - \mathbf{z}\|^2 / \left(2\sigma^2\right)\right).$$

5. Experimental results

Figure 2 describes the combinations of systems that we have tested over the AD versus controls database of feature vectors. Each the possible paths in

the graph from the OASIS data up to the classification results corresponds to a combination of systems tested. For each combination we have explored the corresponding parameters in a systematic way, using a 10-fold cross-validation approach, testing more than 50 partitions of the data to obtain each performance estimation. We tested the application of Principal Component Analysis (PCA) to the dimensional reduction of the data previous to DC, the application of LICA to the same end, the transformation of the data with a Gaussian kernel previous to DC or to the application of PCA or LICA. The lower path in figure 2 corresponds to the kernel-LICA approach. In the experiments we explored the effect of the diverse parameters. For PCA we computed transformations with up 10 eigenventors, accounting for 99% of the accumulated eigenvalues. For LICA we tested values in the ranges $\alpha \in [0.01, 0.09] \bigcup [0.1, 0.9] \bigcup [1, 10]$ with corresponding uniform sampling in these intervals. The Gaussian kernel parameter was computed as $\sigma = 10^k$ with $k = [-3, 1]$ sampled uniformly in this interval.

In figure 3 we plot the result of PCA-DC as a function of the number of eigenvectors. The average accuracy best result is obtained with one eigenvector and decreases dramatically after that. Figure 4 shows the plot of the LICA-DC results as a function of the α parameter that determines the number of endmembers. The best results are for the higher values, which imply less endmembers. Figure 5 shows the plot of the DC average accuracy when applied to the Gaussian Kernel transformation of the data with varying σ parameter. The kernel trick seems to work against the DC giving systematically poor results, regardless of the value of its σ parameter. The results of the combination of the Gaussian kernel and PCA are shown in figure 6 as surface depending on the number of eigenvectors selected and the value of the σ parameter. It can be appreciated the results are highly sensitive to the kernel parameter, low values giving better results. Overall the kernel PCA-DC transformation improves the results of the PCA-DC combination, although the best result is lower for the Kernel PCA-DC than for the PCA-DC. Finally, figure 7 shows the results of the combination of the Gaussian kernel preprocessing with the LICA feature extraction for DC. Values improve with low values of σ and moderate α. Both 3D surface responses in figures 6 and 7 have embedded the flat surface corresponding to the baseline DC result of 58% accuracy. Therefore the observed peaks correspond to parameter combinations where the combination of systems improves the baseline DC.

Figure 8 presents a summary plot of the results of all the approaches tested against the value of their respective parameters. The plot shows that some of the approaches do not improve in any case the baseline Dendritic Computing result. The best result is obtained when we apply LICA to a Gaussian kernel transformation of the data. Also we found that the bare application of LICA to the data gives better results than PCA, which only improves DC when reducing the data to one coefficient. The summary of the best results is presented in Table 1 where it can be appreciated that the baseline DC has a poor specificity and a high sensitivity. DC systematically produces low ratios of false negatives, however it produces a large ratio of false positives. Per construction, it is biased

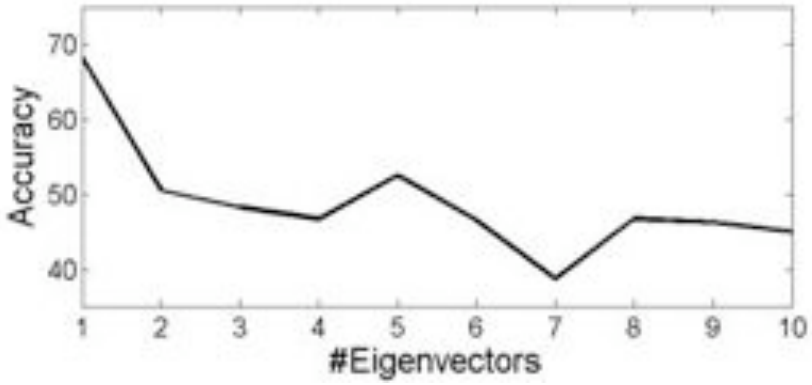

Figure 3: PCA-DC results as a function of the number of eigenvectors.

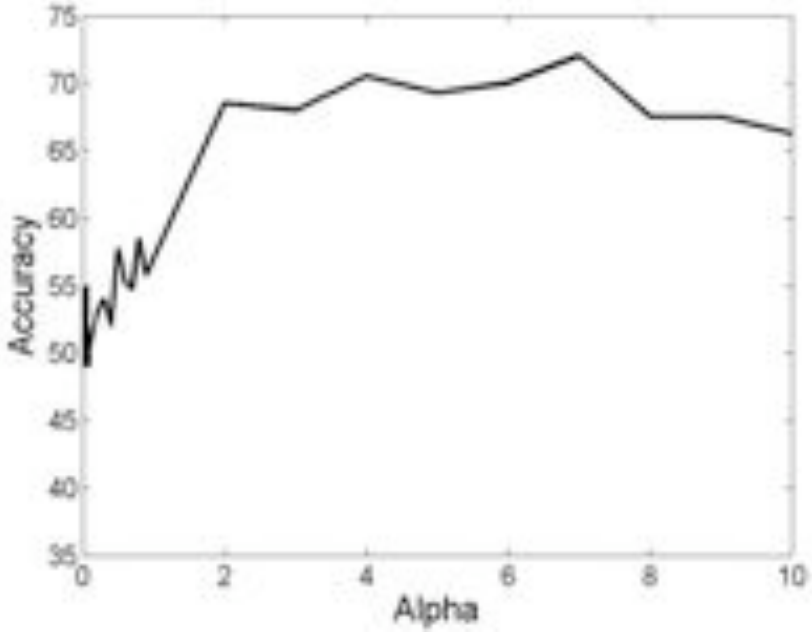

Figure 4: LICA-DC results as a function of the noise filter parameter α.

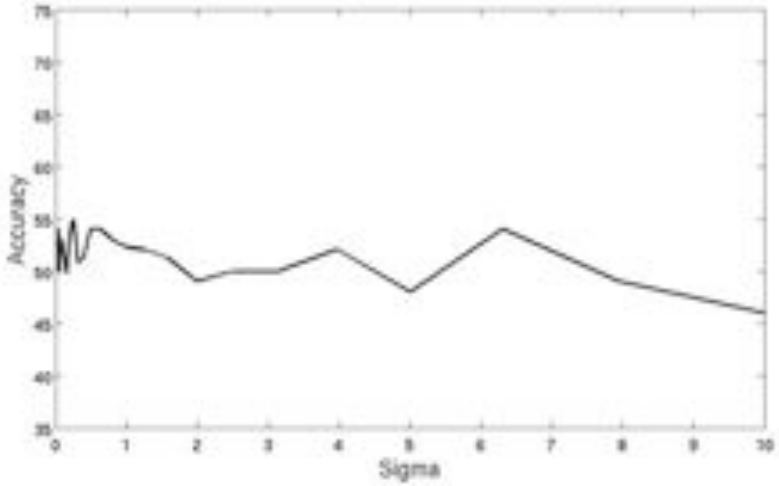

Figure 5: DC applied to Gaussian Kernel transformation of the data.

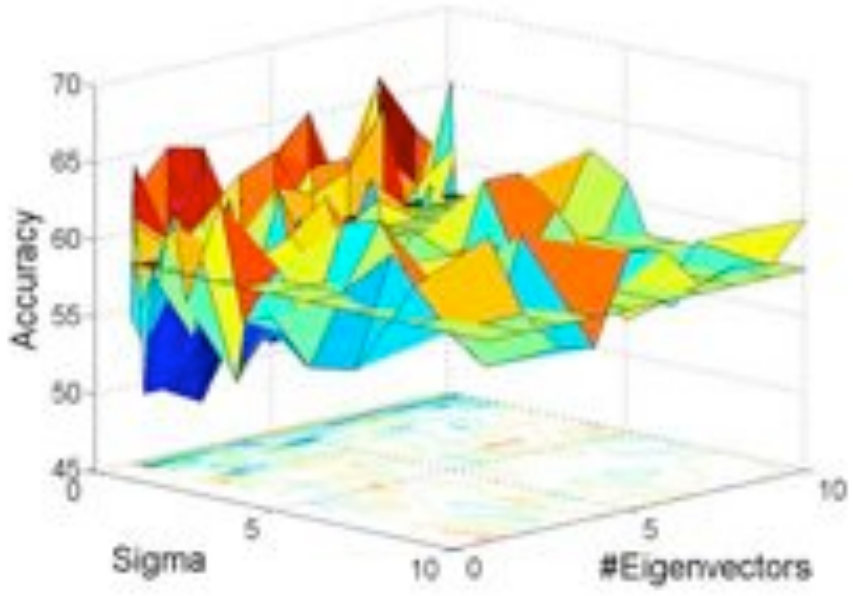

Figure 6: Kernel-PCA-DC results varying σ and the number of eigenvectors.

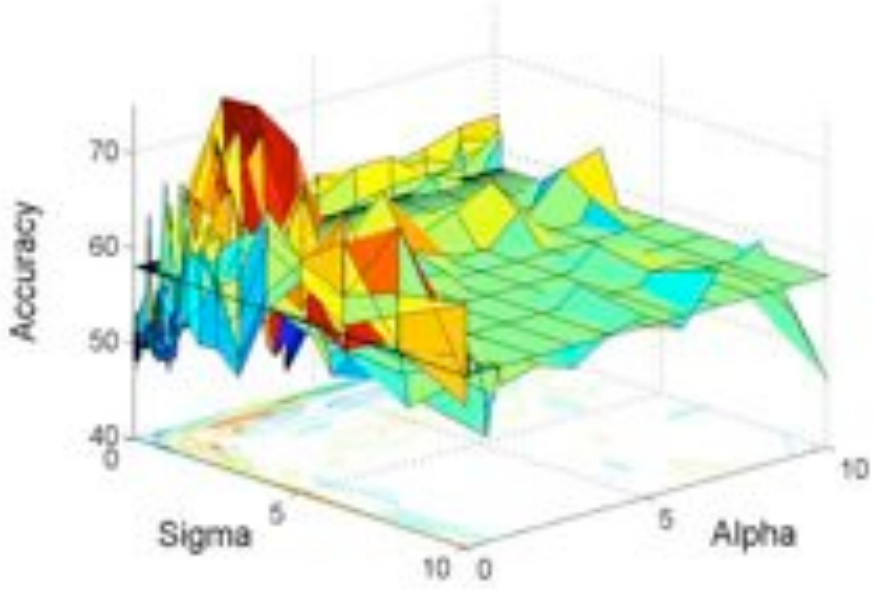

Figure 7: Kernel-LICA-DC results varying σ and α.

towards the positive class C_1. In fact, the main improvement introduced by the tested approaches is an increase in sensitivity. Comparing with previous results on this same database [2, 17], we find that the Support Vector Machine (SVM) approach obtains comparable values of sensitivity and specificity. The DC based approaches have a much higher sensitivity, but their worse specificity degrades their accuracy performance.

6. Conclusions

We found empirically, performing cross-validation on an Alzheimer's Disease database of features computed from MRI scans, that a single layer neuron

Method	NE	α	σ	Accuracy	Sensitivity	Specificity
DC	-	-	-	58	94	23
PCA - DC	1	-	-	68.25	85.5	51
LICA - DC	1	7	-	**72**	88	56
Kernel - DC	-	-	0.2512	55	98	12
Kernel - PCA - DC	8	-	0.0794	66.5	96	37
Kernel - LICA - DC	3	2	0.5012	**74.25**	96	52.5

Table 1: Summary of best results of validation experiments over AD feature database.

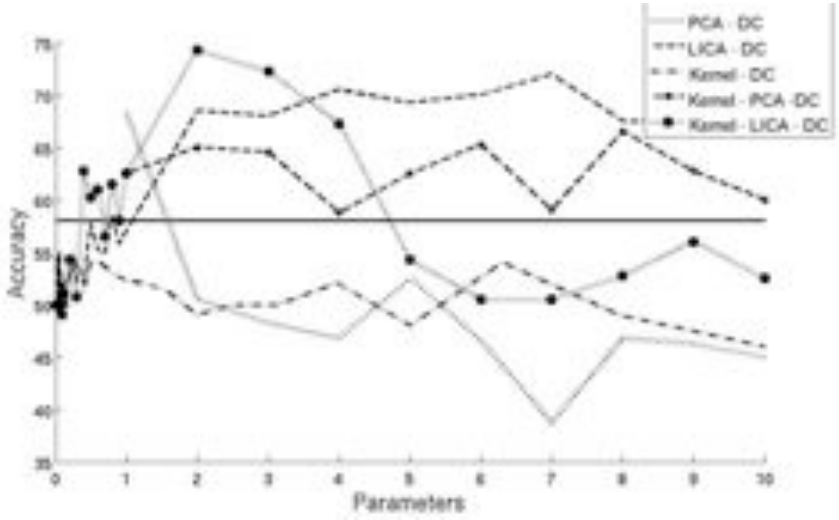

Figure 8: Comparison of the accuracy of all the approaches tested

model endowed with Dendritic Computing has poor generalization capabilities. The model shows high sensitivity but poor specificity. In this paper we have proposed the application of a composition of processes to enhance the model generalization properties. Specifically, we propose to perform a Lattice Independent Component Analysis on a kernel matrix generated applying a Gaussian kernel as the appropriate feature extraction for the Dendritic Computing model. Our approach improves over the application of PCA to the data and to the kernel matrix. Future work can be addressed to develop the theory of the combination of the kernel method with the LICA process.

[1] A. Barmpoutis and G.X. Ritter. Orthonormal basis lattice neural networks. In *Fuzzy Systems, 2006 IEEE International Conference on*, pages 331 –336, 2006.

[2] M. García-Sebastián, A. Savio, M. Graña, and J. Villanúa. On the use of morphometry based features for alzheimer's disease detection on mri. *Bio-Inspired Systems: Computational and Ambient Intelligence. / IWANN 2009 (Part I) Joan Cabestany, Francisco Sandoval, Alberto Prieto, Juan M. Corchado (Editors), LNCS 5517*, pages 957–964, 2009.

[3] M. Graña and J. Gallego. Associative Morphological Memories for endmember induction. In *Geoscience and Remote Sensing Symposium, 2003. IGARSS '03. Proceedings. 2003 IEEE International*, volume 6, pages 3757–3759, July 2003.

[4] M. Graña, P. Sussner, and G.X. Ritter. Associative Morphological Memories for endmember determination in spectral unmixing. In *Fuzzy Systems,*

2003. FUZZ '03. The 12th IEEE International Conference on, volume 2, pages 1285–1290, May 2003.

[5] M. Graña. A brief review of lattice computing. In *Proc. WCCI 2008*, pages 1777–1781, 2008.

[6] M. Graña, D. Chyzhyk, M. García-Sebastián, and C. Hernández. Lattice independent component analysis for functional magnetic resonance imaging. *Information Sciences*, in press, 2010.

[7] M. Graña, A. Manhaes-Savio, M. García-Sebastián, and E. Fernandez. A lattice computing approach for on-line fmri analysis. *Image and Vision Computing*, 28(7):1155–1161, 2010.

[8] M. Graña, I. Villaverde, J.O. Maldonado, and C. Hernandez. Two lattice computing approaches for the unsupervised segmentation of hyperspectral images. *Neurocomputing*, 72(10-12):2111–2120, 2009.

[9] Gerhard Ritter and Paul Gader. Fixed points of lattice transforms and lattice associative memories. volume 144 of *Advances in Imaging and Electron Physics*, pages 165 – 242. Elsevier, 2006.

[10] Gerhard X. Ritter and Gonzalo Urcid. A lattice matrix method for hyperspectral image unmixing. *Information Sciences*, In Press, Corrected Proof:–, 2010.

[11] Gerhard X. Ritter, Gonzalo Urcid, and Mark S. Schmalz. Autonomous single-pass endmember approximation using lattice auto-associative memories. *Neurocomputing*, 72(10-12):2101 – 2110, 2009. Lattice Computing and Natural Computing (JCIS 2007) / Neural Networks in Intelligent Systems Designn (ISDA 2007).

[12] G.X. Ritter and L. Iancu. Single layer feedforward neural network based on lattice algebra. In *Neural Networks, 2003. Proceedings of the International Joint Conference on*, volume 4, pages 2887 – 2892 vol.4, jul. 2003.

[13] G.X. Ritter and L. Iancu. A morphological auto-associative memory based on dendritic computing. In *Neural Networks, 2004. Proceedings. 2004 IEEE International Joint Conference on*, volume 2, pages 915 – 920 vol.2, jul. 2004.

[14] G.X. Ritter, L. Iancu, and G. Urcid. Morphological perceptrons with dendritic structure. In *Fuzzy Systems, 2003. FUZZ '03. The 12th IEEE International Conference on*, volume 2, pages 1296 – 1301 vol.2, may. 2003.

[15] G.X. Ritter, P. Sussner, and J.L. Diza-de Leon. Morphological associative memories. *Neural Networks, IEEE Transactions on*, 9(2):281 –293, mar. 1998.

[16] G.X. Ritter and G. Urcid. Lattice algebra approach to single-neuron computation. *Neural Networks, IEEE Transactions on*, 14(2):282 – 295, mar. 2003.

[17] A. Savio, M. García-Sebastián, M. Graña, and J. Villanúa. Results of an adaboost approach on alzheimer's disease detection on mri. *Bioinspired applications in Artificial and Natural Computation. J. Mira, J. M. Ferrández, J.R. Alvarez, F. dela Paz, F.J. Tolede (Eds.) LNCS 5602*, pages 114–123, 2009.

[18] A. Savio, M. García-Sebastián, C. Hernández, M. Graña, and J. Villanúa. Classification results of artificial neural networks for alzheimer's disease detection. *Intelligent Data Engineering and Automated Learning- IDEAL 2009, Emilio Corchado, Hujun Yin (eds) LNCS 5788*, pages 641–648, 2009.

[19] J. Shawe-Taylor and N. Cristianini. *Kernel Methods for Pattern Analysis*. Cambridge University Press, 2004.

On the Use of Morphometry Based Features for Alzheimer's Disease Detection on MRI

Maite García-Sebastián[1], Alexandre Savio[1], Manuel Graña[1], and Jorge Villanúa[2]

[1] Grupo de Inteligencia Computacional
www.ehu.es/ccwintco
[2] Osatek, Hospital Donostia Paseo Dr. Beguiristain 109, 20014 San Sebastián, Spain

Abstract. We have studied feature extraction processes for the detection of Alzheimer's disease on brain Magnetic Resonance Imaging (MRI) based on Voxel-based morphometry (VBM). The clusters of voxel locations detected by the VBM were applied to select the voxel intensity values upon which the classification features were computed. We have explored the use of the data from the original MRI volumes and the GM segmentation volumes. In this paper, we apply the Support Vector Machine (SVM) algorithm to perform classification of patients with mild Alzheimer's disease vs. control subjects. The study has been performed on MRI volumes of 98 females, after careful demographic selection from the Open Access Series of Imaging Studies (OASIS) database, which is a large number of subjects compared to current reported studies[1].

1 Introduction

Alzheimer's disease (AD) is a neurodegenerative disorder, which is one of the most common cause of dementia in old people. Currently, due to the socio-economic importance of the disease in occidental countries it is one of the most studied. The diagnosis of AD is done after the exclusion of other forms of dementia but definitive diagnosis can only be made after a post-mortem study of the brain tissue. This is one of the reasons why Magnetic Resonance Imaging (MRI) based early diagnosis is a current research goal in the neurosciences.

Morphometry analysis has become a common tool for computational brain anatomy studies. It allows a comprehensive measurement of structural differences within or across groups, not only in specific structures but throughout the entire brain. Voxel-based morphometry (VBM) is a computational approach to neuroanatomy that measures differences in local concentrations of brain tissue, through a voxel-wise comparison of multiple brain images [2]. For instance, VBM has been applied to study volumetric atrophy of the grey matter (GM) in areas of neocortex of AD patients vs. control subjects [4,9,16]. The procedure involves the spatial normalization of subject images into a standard space, segmentation

[1] Research partially supported by Saiotek research projects BRAINER and S-PR07UN02, and the MEC research project DPI2006-15346-C03-03.

J. Cabestany et al. (Eds.): IWANN 2009, Part I, LNCS 5517, pp. 957–964, 2009.

of tissue classes using *a priori* probability maps, smoothing to correct noise and small variations, and voxel-wise statistical tests. Statistical analysis is based on the General Linear Model (GLM) to describe the data in terms of experimental and confounding effects, and residual variability. Classical statistical inference is used to test hypotheses that are expressed in terms of GLM estimated regression parameters. The computation of a given contrast provides a Statistical Parametric Map, which is thresholded according to the Random Field Theory.

Machine learning methods have become very popular to classify functional or structural brain images to discriminate them into two classes: normal or a specific neurodegenerative disorder. The Support Vector Machine (SVM) either with linear [10,14] or non-linear [7,11] kernels, have been extensively applied for this task. There are studies applying SVM to discriminate AD patients from controls based on Positron Emission Tomography (PET) or Single-Photon Emission Tomography (SPECT) functional volumes [14,15,1]. There are different ways to extract features from MRI for SVM classification: based on morphometric methods [6,7], based on ROIs (region of interest) [12,11] or GM voxels in automated segmentation images [10]. Work has also been reported on the selection of a small set of the most informative features for classification, such as the SVM-Recursive Feature Elimination [7], the selection based on statistical tests [12,14], the wavelet decomposition of the RAVENS maps [11], among others.

Many of the classification studies on the detection of AD were done over populations mixing men and women. However, it has been demonstrated that brains of women are different from men's to the extent that it is possible to discriminate the gender via MRI analysis [11]. Moreover, it has been shown that VBM is sensitive to the gender differences. For these reasons, we have been very cautious in this study. We have selected a set of 98 MRI women's brain volumes. It must be noted that this is a large number of subjects compared with the other studies referred above.

The approach taken in this paper is to use the clusters detected as result of VBM as a mask on the MRI and Grey Matter (GM) segmentation images to select the potentially most discriminating voxels. Features for classification are either the voxel values or some summary statistics of each cluster. We assume for classification the standard SVM, testing linear and non-linear (RBF) kernels. Section Materials and Methods gives a description of the subjects selected for the study, the image processing, feature extraction details and the classifier system. Section Results gives our classification performance results and section Conclusions gives some conclusions and further work suggestions.

2 Materials and Methods

2.1 Subjects

Ninety eight right-handed women (aged 65-96 yr) were selected from the Open Access Series of Imaging Studies (OASIS) database (http://www.oasis-brains.org) [13]. OASIS data set has a cross-sectional collection of 416 subjects covering the adult life span aged 18 to 96 including individuals with early-stage Alzheimer's

Table 1. Summary of subject demographics and dementia status. Education codes correspond to the following levels of education: 1 less than high school grad., 2: high school grad., 3: some college, 4: college grad., 5: beyond college. Categories of socioeconomic status: from 1 (biggest status) to 5 (lowest status). MMSE score ranges from 0 (worst) to 30 (best).

	Very mild to mild AD	Normal
No. of subjects	49	49
Age	78.08 (66-96)	77.77 (65-94)
Education	2.63 (1-5)	2.87 (1-5)
Socioeconomic status	2.94 (1-5)	2.88 (1-5)
CDR (0.5 / 1 / 2)	31 / 17 / 1	0
MMSE	24 (15-30)	28.96 (26-30)

Disease. We have ruled out a set of 200 subjects whose demographic, clinical or derived anatomic volumes information was incomplete. For the present study there are 49 subjects who have been diagnosed with very mild to mild AD and 49 nondemented. A summary of subject demographics and dementia status is shown in table 1.

2.2 Imaging Protocol

Multiple (three or four) high-resolution structural T1-weighted magnetization-prepared rapid gradient echo (MP-RAGE) images were acquired [8] on a 1.5-T Vision scanner (Siemens, Erlangen, Germany) in a single imaging session. Image parameters: TR= 9.7 msec., TE= 4.0 msec., Flip angle= 10, TI= 20 msec., TD= 200 msec., 128 sagittal 1.25 mm slices without gaps and pixels resolution of 256×256 (1×1mm).

2.3 Image Processing and VBM

We have used the average MRI volume for each subject, provided in the OASIS data set. These images are already registered and resampled into a 1-mm isotropic image in atlas space and the bias field has been already corrected [13]. The Statistical Parametric Mapping (SPM5) (http://www.fil.ion.ucl.ac.uk/spm/) was used to compute the VBM which gives us the spatial mask to obtain the classification features. Images were reoriented into a right-handed coordinate system to work with SPM5. The tissue segmentation step does not need to perform bias correction. We performed the modulation normalization for grey matter, because we are interested in this tissue for this study. We performed a spatial smoothing before computing the voxel-wise statistics, setting the Full-Width at Half-Maximum (FWHM) of the Gaussian kernel to 10mm isotropic. A GM mask was created from the average of the GM segmentation volumes of the subjects under study. Thresholding the average GM segmentation, we obtain a binary mask that includes all voxels with probability greater than 0.1 in the average GM segmentation volume. This interpretation is not completely true, since the data are modulated, but it is

close enough for the mask to be reasonable. We design the statistical analysis as a Two-sample t-test in which the first group corresponds with AD subjects. We also have done some experiments with nWBV (normalized whole brain volume) as the covariate. The general linear model contrast has been set as [-1 1], a right-tailed (groupN > groupAD), correction FWE and p-value=0.05. The VBM detected clusters are used for the MRI feature extraction for the SVM classification.

2.4 Support Vector Machine Classification

The Support Vector Machine (SVM) [17] algorithm used for this study is included in the libSVM (`http://www.csie.ntu.edu.tw/~cjlin/libsvm/`) software package. The implementation is described in detail in [5]. Given training vectors $x_i \in R_n, i = 1, \ldots, l$ of the subject features of the two classes, and a vector $y \in R^l$ such that $y_i \in \{-1, 1\}$ labels each subject with its class, in our case, for example, patients were labeled as -1 and control subject as 1. To construct a classifier, the SVM algorithm solves the following optimization problem:

$$\min_{w,b,\xi} \frac{1}{2} w^T w + C \sum_{i=1}^{l} \xi_i$$

subject to $y_i(w^T \phi(x_i) + b) \geq (1 - \xi_i),\ \xi_i \geq 0, i = 1, 2, \ldots, n$. The dual optimization problem is

$$\min_{\alpha} \frac{1}{2} \alpha^T Q \alpha - e^T \alpha$$

subject to $y^T \alpha = 0,\ 0 \leq \alpha_i \leq C,\ i = 1, \ldots, l$. Where e is the vector of all ones, $C > 0$ is the upper bound on the error, Q is an l by l positive semidefinite matrix, $Q_{ij} \equiv y_i y_j K(x_i, x_j)$, and $K(x_i, x_j) \equiv \phi(x_i)^T \phi(x_j)$ is the kernel function that describes the behaviour of the support vectors. Here, the training vectors x_i are mapped into a higher (maybe infinite) dimensional space by the function $\phi(x_i)$. The decision function is $sgn(\sum_{i=1}^{l} y_i \alpha_i K(x_i, x) + b)$.

The chosen kernel function results in different kinds of SVM with different performance levels, and the choice of the appropriate kernel for a specific application is a difficult task. In this study two different kernels were tested: the linear and the radial basis function (RBF) kernel. The linear kernel function is defined as $K(x_i, x_j) = 1 + x_i^T x_j$, this kernel shows good performance for linearly separable data. The RBF kernel is defined as $K(x_i, x_j) = exp(-\frac{||x_i - x_j||^2}{2\sigma^2})$. This kernel is basically suited best to deal with data that have a class-conditional probability distribution function approaching the Gaussian distribution [3]. One of the advantages of the RBF kernel is that given a kernel, the number of support vectors and the support vectors are all automatically obtained as part of the training procedure, i.e., they don't need to be specified by the training mechanism.

2.5 Feature Extraction

We have tested three different feature extraction processes, based on the voxel location clusters obtained from the VBM analysis:

1. The first feature extraction process computes the ratio of GM voxels to the total number of voxels of each voxel location cluster
2. The second feature extraction process computes the mean and standard deviation of the GM voxel intensity values of each voxel location cluster
3. The third feature extraction process computes a very high dimensional vector with all the GM segmentation values for the voxel locations included in each VBM detected cluster. The GM segmentation voxel values were ordered in this feature vector according to the coordinate lexicographic order

2.6 Classifier Performance Indices

We evaluated the performance of the classifier using the 10-fold cross-validation test. To quantify the results we measured the accuracy, the ratio of the number of test volumes correctly classified to the total of tested volumes. We also quantified the specificity and sensitivity of each test defined as $Specificity = \frac{TP}{TP+FP}$ and $Sensitivity = \frac{TN}{TN+FN}$, where TP is the number of true positives: number of AD patient volumes correctly classified; TN is the number of true negatives: number of control volumes correctly classified; FP is the number of false positives: number of AD patient volumes classified as control; FN is the number of false negatives: number of control volumes classified as patient.

3 Results

In this section we present for each experiment the following data: the number of features, accuracy, specificity, which is related to AD patients and sensitivity, which is related to control subjects. We have performed the VBM twice, first without any covariate included in the GLM (Table 2) and second taking into account the normalized brain volume (nWBV) (Table 3). Each VBM process produces different sets of voxel location clusters, and, therefore, different sets of feature vectors. The covariate helps to focus the VBM, giving less and smaller clusters than the VBM without covariates. This implies that the feature vectors will be smaller. Each table entry contains the SVM results using the linear and RBF kernels upon the corresponding feature vector set. In both tables rows correspond to feature extraction processes as described in section 2.5.

The best accuracy result (Table 2) is 80.6% with the RBF kernel, but this result is not far away from the results of the linear SVM. The classification results of table 3, using the covariate nWBV in the design matrix of the GLM, confirm that the non-linear SVM is more accurate. However, as the size of the feature vectors is lower than in table 2, results in table 3 are systematically lower.

Overall the sensitivity results in tables 2 and 3 are much lower than the specificity. We hypothesize that the source of error is the confusion of mild demented AD patients with control subjects. Mild demented AD patients are subjects with CDR=0.5 (Clinical Dementia Ratio) and a high value for the MMSE (Minimental-State Examination), i.e. MMSE=30. Therefore we repeat the feature extraction and classification experiment taking out of the population

Table 2. Classification results with a linear kernel (lk) and a non-linear kernel (nlk). No covariates have been taken into account in the GLM used for the VBM. The values of $\gamma = \left(2\sigma^2\right)^{-1}$ for non linear kernel were 0.5, 0.031, 0.0078 for each feature extraction process, respectively.

Feature extracted	Features	Accuracy (lk/nlk)	Sensitivity (lk/nlk)	Specificity (lk/nlk)
GM proportion	12	69.39% / 68.36%	0.88 / 0.90	0.63 / 0.61
Mean & StDev	24	78.57% / 80.61%	0.88 / 0.89	0.72 / 0.75
Voxel intensities	3611	73.47% / 76.53%	0.75 / 0.76	0.72 / 0.77

Table 3. Classification results with a linear kernel (lk) and a non-linear kernel (nlk). The normalized brain volume (nWBV) covariate has been taken into account in the GLM for the VBM. The values of γ for nlk were 0.5, 2.7, 0.004 for GM proportion, Mean & StDev and voxel intensities respectively.

Feature extracted	Features	Accuracy (lk/nlk)	Sensitivity (lk/nlk)	Specificity (lk/nlk)
GM proportion	2	51% / 51%	1 / 1	0.50 / 0.50
Mean & StDev	4	69.38% / 72.45%	0.79 / 0.79	0.65 / 0.68
Voxel intensities	265	66.32% / 75.51%	0.67 / 0.80	0.65 / 0.72

Table 4. Classification results of 40 AD patients vs. 49 control subjects with the SVM and a RBF kernel, 9 possible outliers were taken out from the AD patients subset

Feature extracted	Features	γ	Accuracy	Sensitivity	Specificity
GM proportion	12	0.9	72.5%	0.84	0.66
Mean & StDev	24	0.6	87.5%	0.89	0.86
Voxel intensities	3611	1.5	86.25%	0.85	0.87

9 mild demented AD patients. The results for the RBF kernel SVM are given in table 4. The classification accuracy of the grows from 80.6% (in the best result of table 2) up to 87.5%. Also sensitivity and specificity improve if we compare table 2 and table 3 against table 4.

4 Conclusions

In this work we have studied feature extraction processes based on VBM analysis, to classify MRI volumes of AD patients and normal subjects. We have analyzed different designs for the SPM of the VBM and we have found that the basic GLM design without covariates can detect subtle changes between AD patients and controls that lead to the construction of SVM classifiers with a discriminative accuracy of 87.5%. In [6] they compare their results on a smaller population of controls and AD patients to the ones obtained with a standard VBM analysis using only one cluster and found a classification accuracy of 63.3% via cross-validation. Therefore, the results shown in this paper, along with the careful experimental methodology employed, can be of interest for the Neuroscience

community researching on the AD. Further work may address the extraction of features based on other morphometric methods, such as Deformation-based Morphometry.

References

1. Alvarez, I., Lopez, M., Gorriz, J.M., Ramirez, J., Salas-Gonzalez, D., Segovia, F., Puntonet, C.G.: Automatic classification system for the diagnosis of alzheimer disease using Component-Based SVM aggregations. In: 15th International Conference on Neural Information Processing of the Asia-Pacific Neural Network Assembly (ICONIP 2008) (2008)
2. Ashburner, J., Friston, K.J.: Voxel-based morphometry: The methods. Neuroimage 11(6), 805–821 (2000)
3. Burges, C.: A tutorial on support vector machines for pattern recognition. Data Mining and Knowledge Discovery 2(2), 167, 121 (1998)
4. Busatto, G.F., Garrido, G.E.J., Almeida, O.P., Castro, C.C., Camargo, C.H.P., Cid, C.G., Buchpiguel, C.A., Furuie, S., Bottino, C.M.: A voxel-based morphometry study of temporal lobe gray matter reductions in alzheimer's disease. Neurobiology of Aging 24(2), 221–231 (2003)
5. Chang, C.-C., Lin, C.-J.: LIBSVM: a library for support vector machines (2001), `http://www.csie.ntu.edu.tw/~cjlin/libsvm`
6. Davatzikos, C., Fan, Y., Wu, X., Shen, D., Resnick, S.M.: Detection of prodromal alzheimer's disease via pattern classification of magnetic resonance imaging. Neurobiology of Aging 29(4), 514–523 (2008)
7. Fan, Y., Shen, D., Davatzikos, C.: Classification of Structural Images via High-Dimensional Image Warping, Robust Feature Extraction, and SVM, pp. 1–8 (2005)
8. Fotenos, A.F., Snyder, A.Z., Girton, L.E., Morris, J.C., Buckner, R.L.: Normative estimates of cross-sectional and longitudinal brain volume decline in aging and AD. Neurology 64(6), 1032–1039 (2005)
9. Frisoni, G.B., Testa, C., Zorzan, A., Sabattoli, F., Beltramello, A., Soininen, H., Laakso, M.P.: Detection of grey matter loss in mild alzheimer's disease with voxel based morphometry. Journal of Neurology, Neurosurgery & Psychiatry 73(6), 657–664 (2002)
10. Kloppel, S., Stonnington, C.M., Chu, C., Draganski, B., Scahill, R.I., Rohrer, J.D., Fox, N.C., Jack Jr., C.R., Ashburner, J., Frackowiak, R.S.J.: Automatic classification of MR scans in alzheimer's disease. Brain 131(3), 681 (2008)
11. Lao, Z., Shen, D., Xue, Z., Karacali, B., Resnick, S.M., Davatzikos, C.: Morphological classification of brains via high-dimensional shape transformations and machine learning methods. Neuroimage 21(1), 46–57 (2004)
12. Liu, Y., Teverovskiy, L., Carmichael, O., Kikinis, R., Shenton, M., Carter, C.S., Stenger, V.A., Davis, S., Aizenstein, H., Becker, J.T.: Discriminative MR image feature analysis for automatic schizophrenia and alzheimer's disease classification. LNCS, pp. 393–401. Springer, Heidelberg (2004)
13. Marcus, D.S., Wang, T.H., Parker, J., Csernansky, J.G., Morris, J.C., Buckner, R.L.: Open access series of imaging studies (OASIS): cross-sectional MRI data in young, middle aged, nondemented, and demented older adults. Journal of Cognitive Neuroscience 19(9), 1498–1507 (2007) PMID: 17714011

14. Ramirez, J., Gorriz, J.M., Lopez, M., Salas-Gonzalez, D., Alvarez, I., Segovia, F., Puntonet, C.G.: Early detection of the alzheimer disease combining feature selection and kernel machines. In: 15th International Conference on Neural Information Processing of the Asia-Pacific Neural Network Assembly (ICONIP 2008) (2008)
15. Salas-Gonzalez, D., Gorriz, J.M., Ramirez, J., Lopez, M., Alvarez, I., Segovia, F., Puntonet, C.G.: Computer aided diagnosis of alzheimer disease using support vector machines and classification trees. In: 15th International Conference on Neural Information Processing of the Asia-Pacific Neural Network Assembly (ICONIP 2008) (2008)
16. Scahill, R.I., Schott, J.M., Stevens, J.M., Rossor, M.N., Fox, N.C.: Mapping the evolution of regional atrophy in alzheimer's disease: Unbiased analysis of fluid-registered serial MRI. Proceedings of the National Academy of Sciences 99(7), 4703 (2002)
17. Vapnik, V.N.: Statistical Learning Theory. Wiley Interscience, Hoboken (1998)

Neurocomputing 72 (2009) 3556–3569

Contents lists available at ScienceDirect

Neurocomputing

journal homepage: www.elsevier.com/locate/neucom

An adaptive field rule for non-parametric MRI intensity inhomogeneity estimation algorithm

Maite García-Sebastián *, Ana Isabel González, Manuel Graña

Basque Country University, Computational Intelligence Group, Paseo Manuel Lardizabal 1, Donostia-San Sebastian, Guipuzcoa, Spain

ARTICLE INFO

Available online 21 June 2009

Keywords:
MRI
Intensity inhomogeneity correction
Non-parametric methods

ABSTRACT

A widely accepted magnetic resonance imaging (MRI) model states that the observed voxel intensity is a piecewise constant signal intensity function corresponding to the tissue spatial distribution, corrupted with multiplicative and additive noise. The multiplicative noise is assumed to be a smooth bias field, it is called intensity inhomogeneity (IIH) field. Our approach to IIH correction is based on the definition of an energy function that incorporates some smoothness constraints into the conventional classification error function of the IIH corrected image. The IIH field estimation algorithm is a gradient descent of this energy function relative to the IIH field. We call it adaptive field rule (AFR). We comment on the likeness of our approach to the self-organizing map (SOM) learning rule, on the basis of the neighboring function that controls the influence of the neighborhood on each voxel's IIH estimation. We discuss the convergence properties of the algorithm. Experimental results show that AFR compares well with state of the art algorithms. Moreover, the mean signal intensity corresponding to each class of tissue can be estimated from the image data applying the gradient descent of the proposed energy function relative to the intensity class means. We test several variations of this gradient descent approach, which embody diverse assumptions about available *a priori* information.

1. Introduction

Magnetic resonance imaging (MRI) allows to visualize with great contrast the soft tissues in the body and has revolutionized the capacity to diagnose the pathologies that affect them [9]. The visualized signal results from the aggregated measurements of the tissue composition at the molecular level. MRI images are expected to be piecewise constant except for partial volume effects in the tissue boundaries and the inevitable additive noise. Thus, once the expected intensities of each tissue are known, we could construct a good approximation to the optimal Bayesian classifier of minimum classification error, assuming that the intensity probability distribution is a mixture of Gaussians whose means are the tissue expected intensities. Then, we could apply this classifier to perform the image segmentation task. However, several imaging conditions introduce an additional multiplicative noise factor, referred to as the intensity inhomogeneity (IIH) field in the literature. The sources of IIH are generally divided in two groups [42]: (a) related to properties of the MRI device such as static magnetic field inhomogeneity, RF signal energy spatial distribution and others; (b) related to the imaged object itself such as the specific magnetic permeability and dielectric properties of the imaged object.

In this paper we elaborate on our previous proposal of an IIH field estimation algorithm inspired in the self-organizing map (SOM) [14]. There, we proposed two adaptive rules stemming from two different formulations of energy function that represent two different ways of modeling the smoothness of the estimated inhomogeneity field. Here we focus on one of these energy functions and its subsequent adaptive rule. We call it adaptive field rule (AFR) for identification within the paper. We have included some reasoning about its convergence and how the IIH field estimates obtained after the adaptive process satisfy some smoothness requirements. We also add new experimental results and sensitivity studies that show the effectiveness of the proposed algorithm. We introduce several approaches for the estimation of the intensity class means, which in the bare AFR are assumed known. These approaches are tested empirically. We discuss their usefulness relative to the required *a priori* knowledge.

Section 2 reviews the state of the art. The algorithms are described in Section 3, and experimental results on real and simulated brain MRI volumes are presented in Section 4. Finally, conclusions are drawn in Section 5.

2. State of the art

There are two aspects of the state of the art that we think is relevant for this work. First is the state of the art of algorithms

* Corresponding author.
E-mail address: maitelasarte@yahoo.es (M. García-Sebastián).

0925-2312/$ - see front matter © 2009 Elsevier B.V. All rights reserved.
doi:10.1016/j.neucom.2008.12.034

that perform IIH correction and segmentation of MRI data. The second is the previous uses of SOM for MRI data analysis and segmentation, and how our work departs from other approaches.

2.1. IIH correction algorithms

Conventional clustering algorithms [10] can cope with the additive noise, but the multiplicative inhomogeneity field has catastrophic effects on them. A general algorithm for IIH correction is the lowpass filtering in the log-domain, which is equivalent to homomorphic filtering [19] in digital image processing for the correction of illumination inhomogeneity. However, it is of no use for MRI because there is a great overlapping of the Fourier spectra corresponding to the inhomogeneity field and the image. Most IIH correction algorithms in MRI are composed of a method for inhomogeneity field estimation and a classification algorithm applied to the restored image obtained removing the inhomogeneity field. In some algorithms, the classification and bias estimation steps are interleaved in the iterations. In others, like the gradient descent algorithm proposed in this paper, these steps are performed simultaneously.

A broad taxonomy of MRI IIH correction algorithms divides them between parametric and non-parametric algorithms. The first ones impose a parametric model of the inhomogeneity field [4,30,37,13] whose parameter values must be estimated to fit the model. The non-parametric algorithms [1,21,29,30,32,35,34,43,45] do not propose any model, so that they perform a non-parametric estimation of the inhomogeneity field value at each voxel position of the measured MRI volume. A similar taxonomy can be found in [23]. We have already made a short review in [13]. The adaptive field rule proposed in this paper is a non-parametric approach, the value of the inhomogeneity field is estimated independently at each voxel site. It could be easily programmed to run in parallel multiprocessor machines. The type of neighboring information used is similar to that of the self-organizing map, because the estimation of the inhomogeneity field at each voxel site is changed when its value at the neighboring sites is updated.

2.2. Relation of AFR to the state of the art

Non-parametric IIH correction methods are able to model local features, such as partial volumes or very local inhomogeneity effects. Parametric models are well suited to model smooth global IIH fields, but modeling of local effects would require extremely high order models and very sensitive fitting algorithms. The AFR is a non-parametric algorithm whose degree of locality is controlled by the neighboring function evolution parameters. It could be possible, therefore, to tune it to solve a diversity of problems. Results reported in this paper show that it can be easily tuned to perform comparable to state of the art algorithms on conventional benchmark datasets.

Relative to other non-parametric algorithms, AFR is fast and easily tuned. AFR computation is straightforward. Approaches based on Bayesian maximum a posteriori estimation [32] involve the computation of relaxation processes, which, even in the fastest ICM case, are time consuming. The early Bayesian approaches [43] needed to perform some linear filtering processes. Algorithms based on fuzzy clustering [1,34] need to compute membership functions and solve large sets of equations to obtain them. Algorithms based on the intensity probability distribution sharpening [35] need to perform a sequence of distribution deconvolutions. All of these processes are more computationally demanding than AFR. We have found that a small number of iterations, 20–30, are enough to obtain good results for most volumes treated.

On the modeling side, the Bayesian approaches need to build a probabilistic model, often a Markov random field, whose parameters need to be estimated somehow. AFR provides a dynamic process along the sensitive parameter values so that the response is less dependent on a critical parameter choice. The process works like an annealing process (it can also be interpreted as a graduated non-convex minimization or a continuation problem). This allows fitting it to solve global and local problems. To obtain this flexibility, the Bayesian methods need to work on the *a priori* model of the data. Fuzzy approaches have introduced averaging processes to obtain similar results, whose extent must be guessed.

The assumption of known intensity class means is common to several approaches [37,43]. In the fuzzy c-means and Bayesian approaches, intensity class means are computed all along, as the corrected image evolves. We show in this paper that several approaches can be combined with AFR to estimate the intensity class means with great efficiency. The simplest ones are the unsupervised on-line and k-means processes. The construction of an atlas from the available manual segmentations allows to manage spatial distribution information, like in the template based Bayesian approaches [30]. However, our experience described below shows that the use of templates or atlas must be taken with caution. Supervised training can also be combined with AFR aiming to obtain more accurate segmentations.

2.3. SOM for MRI processing

In early applications of the SOM to MRI data [3,38], it is used to estimate the clustering of intensity into several classes, either in multispectral or single modality images. In these works, the existence of IIH fields is not taken into account. The results that these papers report show an overestimation of the number of classes in the image. This is a natural effect when the IIH field is not considered. More recent works use the SOM as a preprocessing step previous to manual examination [16,31,40] or the supervised construction of classification systems. It is used to obtain the reference vectors for the construction of a supervised probabilistic neural network (PNN) [36], a multi-layer feedforward neural network with automated Bayesian regularization [24], support vector machine (SVM) [5]. Recent applications include the detection of activity patterns in fMRI [27] which are too low resolution to try to detect IIH effects.

The main departure of the AFR presented in this paper, to the previous SOM approaches to MRI processing, is that we focus on the estimation of the IIH field. This assumption is grounded in a widely accepted imaging model presented in the next section. When we propose adaptive algorithms for the estimation of the intensity class means, it is done in the precise context of the tissues we are looking for (i.e. cerebro-spinal fluid (CSF), gray matter (GM), and white matter (WM)).

3. Description of the AFR algorithm

We will denote $\mathbf{y} = (y_i; i \in I)$ the observed image and $\mathbf{x} = (x_i; i \in I, x_i \in \Omega)$ the underlying tissue classification image, where $i \in I \subset N^3$ is the voxel site in the discrete lattice of the image support for 3D images, and $\Omega = \{\omega_1, \ldots, \omega_c\}$ is the set of tissue classes in the image. The assumed image formation model is the following one:

$$y_i = \beta \cdot r_i + \eta_i, \tag{1}$$

where β_i is the multiplicative inhomogeneity field, r_i is the clean signal associated with the true voxel class x_i and η_i is the additive noise. In MRI we have the additional restriction that the signal

intensity values belong to a discrete (small) set, $\Gamma = \{\mu_{\omega_1}, \ldots \quad ., \quad \mu_{\omega_c}\}$, so that $r_i = \mu_{x_i}$. The IIH *robust segmentation problem* is the problem of estimating the image segmentation $\mathbf{x}$ and the inhomogeneity multiplicative field $\boldsymbol{\beta} = (\beta_i; i \in I)$ from $\mathbf{y}$. The IIH *correction problem* is that of estimating the inhomogeneity multiplicative field $\boldsymbol{\beta} = (\beta_i; i \in I)$ from $\mathbf{y}$ and computing the corrected image $\hat{x}_i = y_i/\beta_i$. Both problems are ill posed, and closely related. We have found that [35] is the only work that performs an IIH correction without resorting to image segmentation. In our work we perform the segmentation of the image to estimate the inhomogeneity field, so it is a kind of IIH robust segmentation.

In some algorithms the correction and estimation is performed on the image logarithm. If we discard the additive noise term, we have that the image formation model described in Eq. (1) becomes

$$Y_i = B_i + R_i, \tag{2}$$

where $Y_i = \ln y_i$, $B_i = \ln \beta_i$ and $R_i = \ln r_i$. The log-images are denoted as $\mathbf{Y} = (Y_i; i \in I)$, $\mathbf{B} = (B_i; i \in I)$ and $\mathbf{R} = (R_i; i \in I)$. The multiplicative field $\boldsymbol{\beta}$ becomes an additive term $\mathbf{B}$ and, because of that, it is usually named the *bias* field. We maintain the definition of the tissue classes and the corresponding intensity means, so that $R_i = M_{x_i}$, where $M_\omega = \ln \mu_\omega$. The distinction between the two image formation models is not as trivial as it may appear at first sight, because the log-model in Eq. (2) implies that the additive noise term η_i has been taken care of previously by means of some linear or non-linear filtering technique, i.e. anisotropic filtering [15,33], otherwise the model does not apply. However, we recall that in [21] a strong case was made against filtering of the image previously to IIH correction.

3.1. Adaptive field rule

Assuming the image formation model shown in Eq. (1), the image segmentation problem, subjected to the existence of IIH multiplicative noise, can be formulated as the minimization of the following energy function:

$$E(\mathbf{y}; \Gamma, \boldsymbol{\beta}) = \sum_i \left(\frac{y_i}{\beta_i} - \mu_{c(i)} \right)^2, \tag{3}$$

where $c(i) = \arg\min_k \{\| \mu_k - (y_i/\beta_i) \|\}$. That is, to solve the segmentation problem we need to find

$$\Gamma^*, \boldsymbol{\beta}^* = \arg \min_{\Gamma, \boldsymbol{\beta}} E(\mathbf{y}; \Gamma, \boldsymbol{\beta}).$$

When the intensity class means $\Gamma = \{\mu_{\omega_1}, \ldots \quad ., \quad \mu_{\omega_c}\}$ are known, the problem is reduced to that of IIH estimation:

$$\boldsymbol{\beta}^* = \arg \min_{\boldsymbol{\beta}} E(\mathbf{y}; \Gamma, \boldsymbol{\beta}).$$

That is, we try to minimize the quantization error over the IIH corrected image. This is an ill-posed problem because the number of parameters to estimate (the bias values at each voxel) is the same as the number of data samples (the values of the voxel intensities).

The logarithm is a monotonic transformation, therefore the segmentation problem can be stated as the following minimization problem:

$$\mathbf{B}^* = \arg \min_{\mathbf{B}} \sum_i (Y_i - B_i - M_{c(i)})^2 = \arg \min_{\mathbf{B}} E(\mathbf{Y}; \mathbf{B}, \mathbf{M}), \tag{4}$$

where $Y_i = \log y_i$, $B_i = \log \beta_i$ and $M_{c(i)} = \log \mu_{c(i)}$. This logarithmic transformation, which allows us to get rid of the multiplicative effect, is quite common in the MRI segmentation and IIH correction literature [1,32,35,43]. We consider a gradient descent rule for the minimization of this error function. We obtain the following adaptive estimation rule:

$$\Delta B_i = -2\alpha (Y_i - B_i - M_{c(i)}), \tag{5}$$

where $0 < \alpha < 1$ as usual. To take into account that IIH fields must be smooth, we propose an energy function formulation that involves the smoothing (averaging) of the errors in the neighborhood of the voxel:

$$E_\sigma(\mathbf{Y}; \mathbf{B}, \mathbf{M}) = \sum_i \sum_j h_\sigma(i-j)(Y_j - B_j - M_{c(j)})^2. \tag{6}$$

The energy function E_σ is an extended distortion function like the energy functions proposed for the derivation of topological preservation quantization and visualization approaches [22,11,39,28] inspired in the SOM [25] and the neural gas. The $h_\sigma(i-j)$ is a neighboring function defined in the space of the voxel index sites. Usually it is a Gaussian shaped windowing function.

The formulation of a gradient descent rule for the minimization of energy function E_σ gives the following adaptive field rule:

$$\Delta B_i = -2\alpha \sum_j h_\sigma(i-j)(Y_j - B_j - M_{c(j)}). \tag{7}$$

The AFR rule of Eq. (7) can be applied either as stochastic gradient descent or as batch rule. We have tested both in [14]; however, in this paper we apply AFR as a batch rule. The main reasons for this choice are, first, that the batch version has faster convergence both in computer time and in number of iterations, and, second, that the batch version has lower result variance. An exhaustive comparison between the batch and on-line versions does not contribute to the topic of this paper, so we will not dwell on it.

3.2. Similarities and differences with SOM

Although the AFR as defined in Eq. (7) was inspired by the SOM's weight adaptive rule, there are some strong differences. The first one is paradigmatic: the SOM is a quantization algorithm that achieves a clustering of high-dimensional data and a non-linear analog to the principal component analysis because of its topology-preserving property. Thus, the number of network nodes is at least several orders of magnitude smaller than the data sample. With AFR we try to perform a non-parametric estimation of the IIH field, which can be viewed as an image of the same size as the given MRI image which constitutes our data sample. The updating process is a one to one process. Each voxel of the MRI image is visited (in sequence or randomly) and its corresponding IIH field element is updated.

The role of the neighboring function in AFR as introduced in Eq. (7) works in the opposite direction to the one in the standard SOM. In the standard SOM the winning codevector determines the neighboring codevectors being updated. In Eq. (7) the updating of the bias estimated value at a voxel is influenced by the error at neighboring voxels.

Finally, let us consider the topographic preservation property of SOM [12,41]. According to it, neighboring data points in input space are mapped into network nodes with neighboring indices. The definition of AFR in Eq. (7) pursues that neighboring voxels have estimated inhomogeneity field neighboring values to ensure the smoothness of the bias field. Voxel site indices are defined in a 2D or a 3D space and bias values are scalar values, much unlike to the SOM, where dimension reduction is produced because the codevector indices are defined in a space of lower dimension than that of the input vectors.

3.3. Discussion of convergence properties

There are several causes for the fact that $Y_j \neq M_{c(j)}$. Among them, the most important is the partial volume phenomena, due to the fact that image voxels correspond to a volume of matter that contains a mixture of biological tissues. Variations of this mixture from voxel to voxel produce variations in the signal departing from the nominal value, although the tissue class (i.e. CSF, gray matter or white matter) may be the same. These and other uncorrelated signal variations can be accounted for by the additive term in the model of Eq. (1). There are other variations due to smooth spatial processes, such as the spatial inhomogeneity of the RF signal that excites the protons in the selected volume to produce the MRI signal [9]. The estimated IIH field $\hat{\mathbf{B}}$ must be smooth to be a model that accounts for such physical phenomena.[1] This smoothness constraint can be expressed in several ways (expressed in terms of the IIH field before/after the log transform):

1. The variation of the bias must be bounded. That can be expressed by either expression $\max_{j\in N(i)}\|\beta_i - \beta_j\| < \varepsilon$, or $\sum_{j\in N(i)}\|\beta_i - \beta_j\| < \varepsilon$.
2. Closer voxels in the image domain must have more similar bias values than those farther apart:

$$\forall i,j,k; |i-j| < |i-k| \Rightarrow \|\beta_i - \beta_j\| < \|\beta_i - \beta_k\|. \quad (8)$$

This condition means that there is some kind of topological preservation between voxel site indices and bias values.

The application of Eq. (7) leads to stationary states described by the following equation:

$$\hat{B}_i = \sum_j h_\sigma(i-j)(Y_j - M_{c(j)}), \quad (9)$$

that is, the estimation corresponds to the weighted average of the neighboring voxel residuals. This asymptotic result is independent of the shifts in $c(j)$ that may be due to the variation in values of the bias $\hat{B}_i$ during the estimation process. The simplistic appearance of Eq. (9) hides a recurrent relation between the bias estimations given by the class assignment $c(i) = \arg\min_k\{\|M_k - (Y_i - \hat{B}_i)\|\}$. If the neighboring function is an average mask $h_\sigma(k) = 1/\sigma^d$ for $|k| \leq \sigma$, where d is the dimension of the image support (2 or 3), the $\hat{B}_i$ would correspond to the average residual over a box or cube surrounding the voxel. Maintaining this definition of the neighboring function, the justification of the satisfaction of the smoothness constraints on the bias estimate after convergence of the updating rule comes from

$$|\hat{B}_i - \hat{B}_j| = \sum_{k\in N(i)\Delta N(j)} |Y_k - M_{c(k)}|, \quad (10)$$

where $A\Delta B$ stands for the symmetric difference between sets A and B, $N(i)$ is the set of voxel neighboring sites. Then, the magnitude of the difference will always be bounded, but we cannot set a bound because this difference will depend on the input image. The topological preservation condition (Eq. (8)) is also satisfied because

$$\forall i,j,k; |i-j| < |i-k| \;\Rightarrow\; N(i)\Delta N(j) \subset N(i)\Delta N(k).$$

When the neighboring function is a Gaussian or any other arbitrary normalized spatial function with restricted domain of radius N_σ,[2] Eq. (10) becomes

$$|B_i - B_j| = \sum_{k\in N_\sigma(i)\Delta N_\sigma(j)} |Y_k - M_{c(k)}||h_\sigma(i-k) - h_\sigma(j-k)|.$$

In this case, the decreasing nature of the neighboring function introduces an attenuation of the bias differences making the transition between bias values even more smooth.

The conventional application of the SOM and other neighborhood based competitive algorithms usually involves the progressive shrinking of the neighborhood radius, until it becomes null and the adaptive rule only applies to the actual winning or selected node. The conventional interpretation of this process is that the SOM and similar algorithms become the simple competitive learning or vector quantization to allow for refinement of the final codevectors. The big initial neighborhoods ensure global convergence or robustness against initial conditions [8,18,20]. In the AFR algorithm, the final neighborhood determines the closeness to the assignment of the bias values as the residual intensities, which the trivial minima of the error function in Eq. (3). The initial neighborhood size sets the background smoothness constraint. The shrinking neighborhoods allow refining the IHH field estimation adapting to local conditions. The shrinking schedule is of importance, because a long number of iterations with the null neighborhood will remove the smoothness obtained in the initial steps. This is the reason of the selection of the value for the shrinking speed parameter F defined in Eq. (15) of Section 4.

3.4. On the estimation of the class intensity means

Sometimes the assumption of the knowledge of the intensity class means M_k cannot be made. Then some means to estimate them from the data are needed. In this section we will discuss some approaches that can be combined with the AFR IIH estimation algorithm. These approaches are presented here in sequence of increasing requirements of *a priori* information about the data. We start with the basic unsupervised approach, ending with the supervised learning algorithm. One of the straightforward approaches is the realization of a k-means step after each step of inhomogeneity field estimation. This approach has already been tested in Section 4.1.

This estimation can also be performed as a gradient descent on the energy function of Eq. (6) relative to the intensity class means:

$$\frac{\partial E_\sigma}{\partial M_k} = -2\sum_i \sum_{c(j)=k} h_\sigma(i-j)(Y_j - B_j - M_k).$$

This gradient is well approximated by the following expression, which minimizes the average square error of the image quantization, given a fixed bias field:

$$\frac{\partial E_\sigma}{\partial M_k} \simeq -2\frac{1}{|\{j|c(j)=k\}|}\sum_{c(j)=k}(Y_j - B_j - M_k). \quad (11)$$

The process of estimating the intensity class means following the gradient in Eq. (11) is an unsupervised approach, without *a priori* information about the true class of the voxel's tissue. We will denote AFR-U this approach in the experimental results of Sections 4.2 and 4.3.

Sometimes we may have some information about the spatial distribution of the tissues, this usually takes the form of an atlas.[3]

[1] The assumption of negligible additive noise in log transformation of Eq. (2) forces some confusion additive and multiplicative effects. In fact, in some works, i.e. [37], it is unclear whether the additive correction/estimation was done on the original image or its log transform.

[2] For Gaussian neighborhoods we apply the rule of thumb $N_\sigma = 9\sigma$ to ensure appropriate sampling of the Gaussian function.

[3] In the literature, some authors define templates as average images and atlases as average images after warping into a known anatomical atlas, such as the

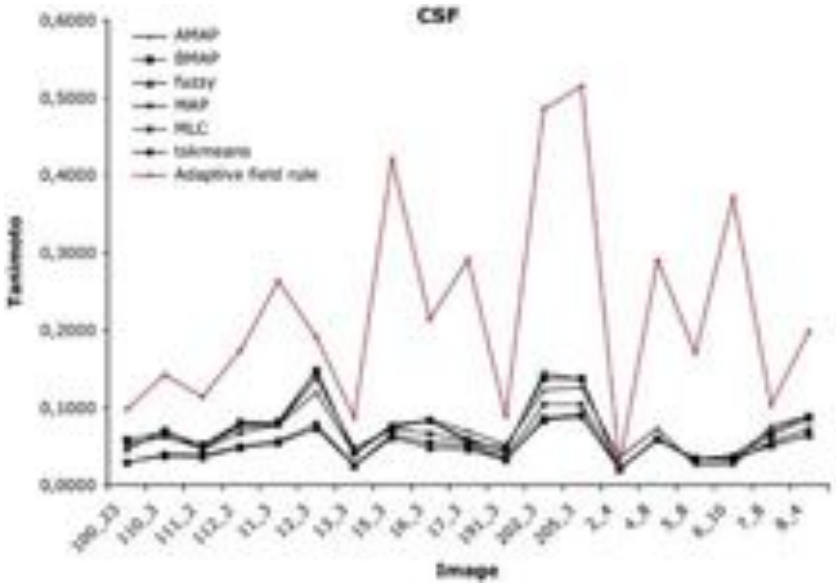

Fig. 1. Tanimoto coefficients of the CSF classification for all the images treated. AFR parameters $F = 1$, $\sigma_0 = 30$, $\sigma_0 = 15$, $\alpha = 0.5$, 20 iterations.

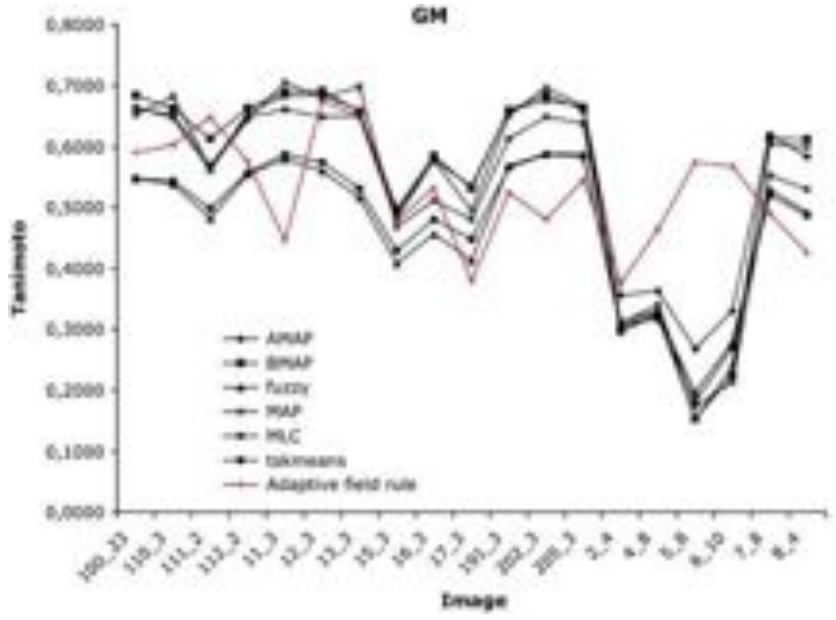

Fig. 2. Tanimoto coefficients of the GM classification for all the images treated. AFR parameters $F = 1$, $\sigma_0 = 30$, $\sigma_0 = 15$, $\alpha = 0.5$, 20 iterations.

A crisp atlas provides us a tissue class for each voxel. The gradient of Eq. (11) can be rewritten to profit from this information:

$$\frac{\partial E_\sigma}{\partial M_k} \simeq -2\frac{1}{|\{j|A(j)=k\}|}\sum_{\{j|A(j)=k\}}(Y_j - B_j - M_k), \tag{12}$$

where $A(j)$ denotes the class assigned to voxel site j in the crisp atlas. We denote AFR-A this approach in the experimental Section 4.3. The crisp atlas is computed following a majority voting schema over a set of images representative of some population of interest. A more precise representation is a probabilistic map, where we have the estimated frequency of each tissue for each voxel computed from the image database. The gradient expression for the intensity class means can then be written as follows:

$$\frac{\partial E_\sigma}{\partial M_k} \simeq -2\frac{1}{\sum_j AP(j,k)}\sum_j AP(j,k)(Y_j - B_j - M_k), \tag{13}$$

where $AP(j,k)$ denotes the estimated frequency of tissue class k in voxel site j. We denote AFR-PA this approach in the experimental Section 4.3. Both atlas based algorithms are partially supervised because they use some *a priori* information about the expected distribution of the tissue classes in the image, computed from the (manual) segmentation of the images. The fully supervised

(*footnote continued*)
Talairach atlas. Here we use the term to denote*a priori* information about the spatial distribution of tissue classes.

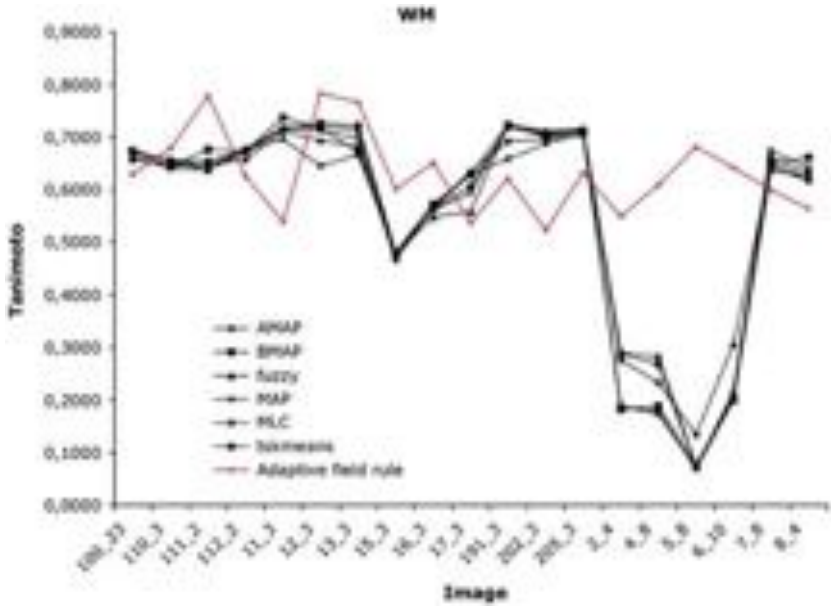

Fig. 3. Tanimoto coefficients of the WM classification for all the images treated. AFR parameters $F = 1$, $\sigma_0 = 30$, $\sigma_0 = 15$, $\alpha = 0.5$, 20 iterations.

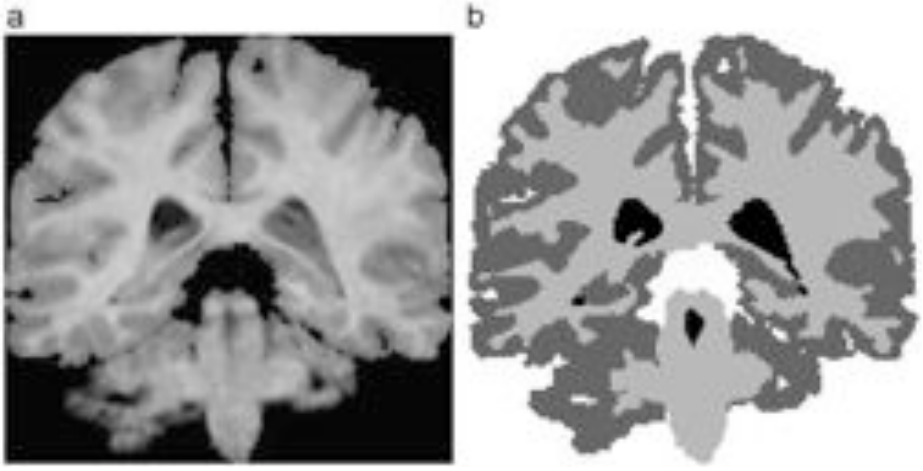

Fig. 4. (a) Original T1-weighted coronal slice from a volume in the IBSR collection and (b) its corresponding manual segmentation.

approach would use the manual segmentation of the image being processed as the ground truth, so the gradient expression can be written as follows:

$$\frac{\partial E_\sigma}{\partial M_k} \simeq -2\frac{1}{|\{j|GT(j)=k\}|}\sum_{\{j|GT(j)=k\}}(Y_j - B_j - M_k), \tag{14}$$

where $GT(j)$ denotes the ground truth class at voxel j given by the manual segmentation of the image being processed. We will denote AFR-S this approach in the experiments reported in Section 4.3.

4. Computational results

The scheduling of the neighboring function width follows the expression:

$$\sigma(t) = \sigma_0\left(\frac{\sigma_f}{\sigma_0}\right)^{t/F}, \tag{15}$$

where σ_0 is the initial width of the neighboring function, σ_f is its final value, t is the iteration number and F is the speed of convergence to the final value of the neighboring function width: after F iterations the width is set to its final value $\forall t > F : \sigma(t) = \sigma_f$. We have used this scheduling for the SOM parameters in previous works [18,20,17] following some works on the optimization of k-means algorithm [6]. Results are given in terms of the Tanimoto coefficient [10,13] which is the same statistic as the overlap metric reported in the Internet brain segmentation repository (IBSR) site, and it is defined as follows:

$$T = \frac{|A \cap B|}{|A \cup B|},$$

where A and B are the sets of voxels corresponding to different segmentations. The Tanimoto coefficient is a more precise measure of the algorithm accuracy than the ratio of success or the misclassification ratio (MCR) given by some authors, because it takes into account the error due to the false positives as well as the false negatives. In all the experimental works, we computed

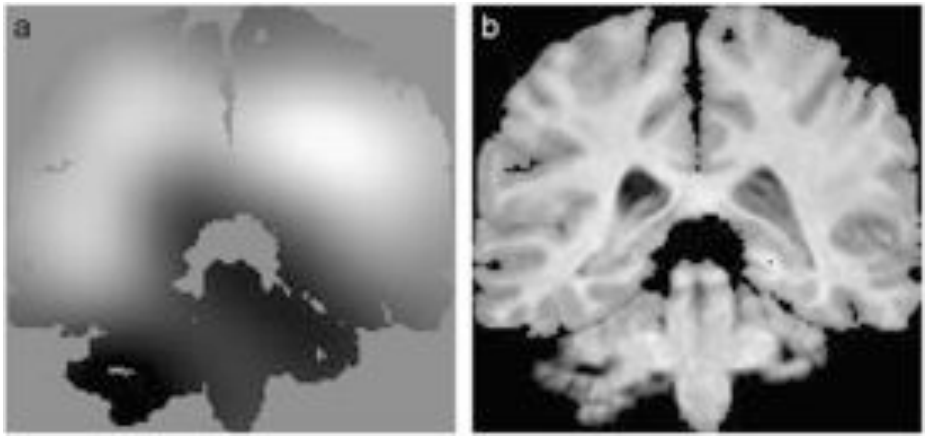

Fig. 5. Coronal slices of the (a) estimated IIH volume and (b) IIH corrected volume, corresponding to Fig. 4(a).

the classification of the cerebral spinal fluid, gray matter and white matter, and reported the Tanimoto coefficients for these classes. When visualizing the voxel classification results, the darkest gray corresponds to CSF tissues and the whitest voxels correspond to WM tissues. Intermediate gray values correspond to the GM tissues.

Sometimes we give the classification results performing the classification based on the means of the intensity classes without bias correction. We denote them basic supervised Gaussian (BGAUSS) classifier in the tables and figures. This approach corresponds to the basic supervised classification results, which we expect to be improved upon by the bias correction and adaptive intensity means estimation.

4.1. Experiments on real brain data

To start with, we apply the bare AFR to the collection of real brain Internet Brain Segmentation Repository (IBSR). The 20 normal MR brain datasets and their manual segmentations were provided by the Center for Morphometric Analysis at Massachusetts General Hospital and are available at http://www.cma.mgh.harvard.edu/ibsr/. This dataset has been extensively used for validation of segmentation approaches in the literature [2,13,30,32,34,44]. The images correspond to T1-weighted MRI brain scans of 20 normal subjects.[4] The images were obtained with two different imaging systems[5]: ten FLASH scans of four males and six females, ten 3D-CAPRY scans on six males and four females. The differences in the imaging systems drive some authors to consider them separately or to omit some of the scans when reporting results [2,32].

The mean intensities were computed according to the manual segmentation. The factor F was set to $F = 1$. This value of the convergence factor implies that there will be few iterations with the final neighborhood width and that its variation will be close to

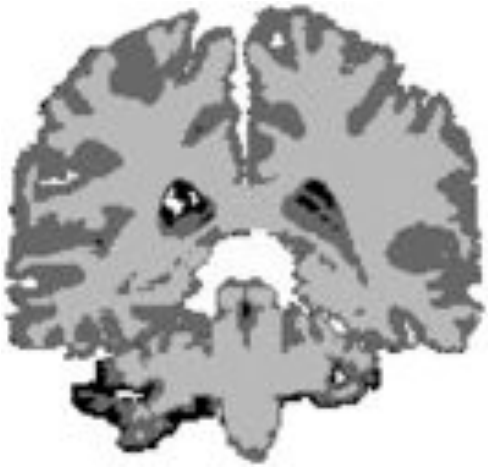

Fig. 6. Segmentation corresponding to the coronal slice shown in Fig. 4(a) computed on the IIH corrected slice shown in Fig. 5(b).

linear and far from an exponential decay. The initial value of the neighboring function parameter was always set to $\sigma_0 = 30$. The number of iterations was always 20. The slices of the volumes were processed independently, and the result given is the average over all the volume.

Figs. 1–3 show the plot of the Tanimoto coefficients for the CSF, GM and WM for each one of the brain datasets tested. The abscissa axis labels correspond to the identification of the image in the IBSR site. The results for the AFR were obtained with a $\sigma_f = 15$. The remaining algorithm results were extracted from the IBSR site. For the CSF, the results are very good and the above results reported in the IBSR site. However, the CSF is a very scarce class that many works omit in their reports. Examination of Figs. 2 and 3 shows that our approach gives results comparable to the state of the art algorithms. One remarkable feature of our approach is that it gives more steady results across datasets: it maintains an average performance for GM and WM detection for some datasets for which the remaining algorithms have a big drop of performance.

Fig. 4 shows a slice from one of the brain datasets and its manual segmentation as provided by the IBSR site. Fig. 5 shows the estimated IIH field for this slice and the corrected image, obtained dividing the original T1-weighted image by the estimated IIH field. Fig. 6 shows the automated segmentation of the corrected dataset. For a more precise evaluation of the sources

[4] We discarded one of the scans because the manually segmented volume did not seem to match with the T1 dataset applying the given offset.

[5] MRI image acquisition description: the coronal three-dimensional T1-weighted spoiled gradient echo MRI scans were performed on two different imaging systems. Ten FLASH scans on four males and six females were performed on a 1.5 T Siemens Magnetom MR System (Iselin, NJ) with the following parameters: TR = 40 ms, TE = 8 ms, flip angle = 50°, field of view = 30 cm, slice thickness = contiguous 3.1 mm, matrix = 256 × 256, and averages = 1. Ten 3D-CAPRY scans on six males and four females were performed on a 1.5 T General Electric Signa MR System (Milwaukee, WI), with the following parameters: TR = 50 ms, TE = 9 ms, flip angle = 50°, field of view = 24 cm, slice thickness = contiguous3.0 mm, matrix = 256 × 256, and averages = 1.

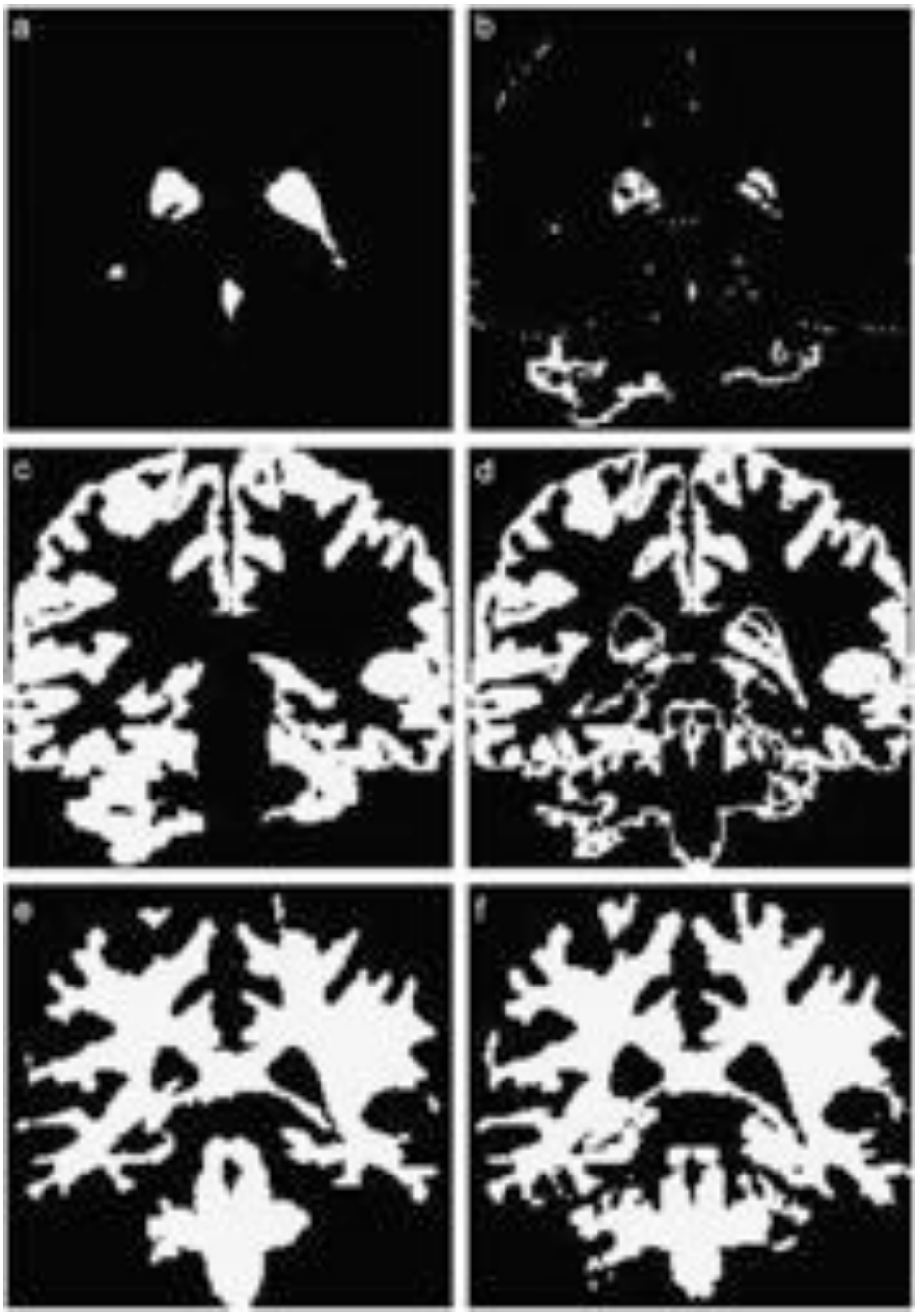

Fig. 7. Manual segmentation of the coronal slice shown in Fig. 4(a) into (a) CSF, (c) GM and (e) WM, and corresponding segmentation after AFR IIH correction into (b) CSF, (d) GM and (f) WM, extracted from the image in Fig. 6.

Table 1
Summary Tanimoto coefficient results for the AFR compared with data from the IBSR site.

Methods	CSF	GM	WM
Adaptive MAP [32]	0.0697	0.5588	0.5611
Biased MAP [32]	0.0714	0.5527	0.5559
Fuzzy c-means [1]	0.0484	0.4698	0.5608
Maximum A posteriori probability (MAP)	0.0714	0.5452	0.5473
Maximum-likelihood (MLC)	0.0631	0.5317	0.5444
Tree-structure k-means	0.0499	0.4742	0.5653
Adaptive field rule (AFR)	0.0918	0.5570	0.5867

Table 2
Sensitivity of Tanimoto coefficient results of AFR.

AFR settings	CSF	GM	WM
$\sigma_f = 0.01$, GTM	0.0918	0.5570	0.5867
$\sigma_f = 15$, GTM	0.1653	0.5427	0.6474
$\sigma_f = 0.01$, PM	0.1838	0.5286	0.6072
$\sigma_f = 15$, PM	0.1561	0.5436	0.6503
$\sigma_f = 0.01$, ME	0.2121	0.4981	0.6153
$\sigma_f = 15$, ME	0.2229	0.5273	0.6319

See text for explanation.

of error, we show in Fig. 7 the voxels corresponding to each class in the original and the AFR segmented dataset. It can be appreciated that a great source of error for the CSF and GM classes are the GM voxels at the contour of the brain. There the existence of voxels corresponding to air in the neighborhood introduces some boundary effects. It can also be appreciated that tissue boundaries of WM are confused with GM. Another source of error for the CSF and GM classes are the ventricles: Fig. 7(d) shows that many ventricle voxels are classified as GM, while it can be appreciated in Fig. 4(a) that their intensity is close to that of the GM voxels. This confusion suggests that *a priori* spatial information could be of great use for this process.

Table 3
Tanimoto coefficients for CSF, GM and WM tissue classes obtained on the BrainWeb simulated phantom corrupted with additive noise and IIH.

% IIH, % noise	BGAUSS	AFR	AFR-U
20, 0	(0.95, 0.88, 0.92)	(0.94, 0.89, 0.92)	(0.94, 0.90, 0.94)
20, 3	(0.94, 0.85, 0.90)	(0.93, 0.84, 0.92)	(0.93, 0.89, 0.93)
20, 5	(0.86, 0.80, 0.86)	(0.87, 0.82, 0.88)	(0.88, 0.86, 0.90)
20, 7	(0.81, 0.73, 0.81)	(0.82, 0.79, 0.85)	(0.83, 0.80, 0.86)
20, 9	(0.76, 0.66, 0.77)	(0.78, 0.70, 0.79)	(0.80, 0.76, 0.80)
40, 0	(0.91, 0.79, 0.85)	(0.89, 0.83, 0.90)	(0.89, 0.85, 0.92)
40, 3	(0.90, 0.78, 0.84)	(0.89, 0.81, 0.89)	(0.88, 0.83, 0.91)
40, 5	(0.84, 0.74, 0.82)	(0.88, 0.77, 0.86)	(0.86, 0.77, 0.87)
40, 7	(0.78, 0.65, 0.79)	(0.82, 0.67, 0.81)	(0.82, 0.67, 0.81)
40, 9	(0.73, 0.55, 0.75)	(0.75, 0.59, 0.75)	(0.76, 0.59, 0.75)

Table 1 gives the summary Tanimoto coefficient results comparing the AFR with the state of the art results reported in the IBSR site. We have computed the means withdrawing the dataset that we were unable to match with its manual segmentation. In this table the results of the AFR were obtained with $\sigma_f = 0.01$. The results are comparable to that of the state of the art algorithms, with some improvement on the WM. Table 2 shows the effect of changing some of the algorithm parameters. In this table, GTM denotes that the intensity class means were computed using the manual segmentation, PM denotes that the intensity class mean values were random perturbations around the nominal ones, and ME denotes that the intensity class mean values were estimated applying one k-means step after each iteration of the bias estimation process. The reference result is the one presented in Table 1, with $\sigma_f = 0.01$. Changing the final neighboring function standard deviation to $\sigma_f = 15$ gives some improvement on the CSF and the WM classes. This result is quite interesting, because it is against the conventional application of the neighboring shrinking scheduling. It seems that for this problem, a final neighborhood size (much) greater than the null neighborhood is more convenient to ensure smoothness and to avoid the trivial setting of the bias to the voxel residual relative to

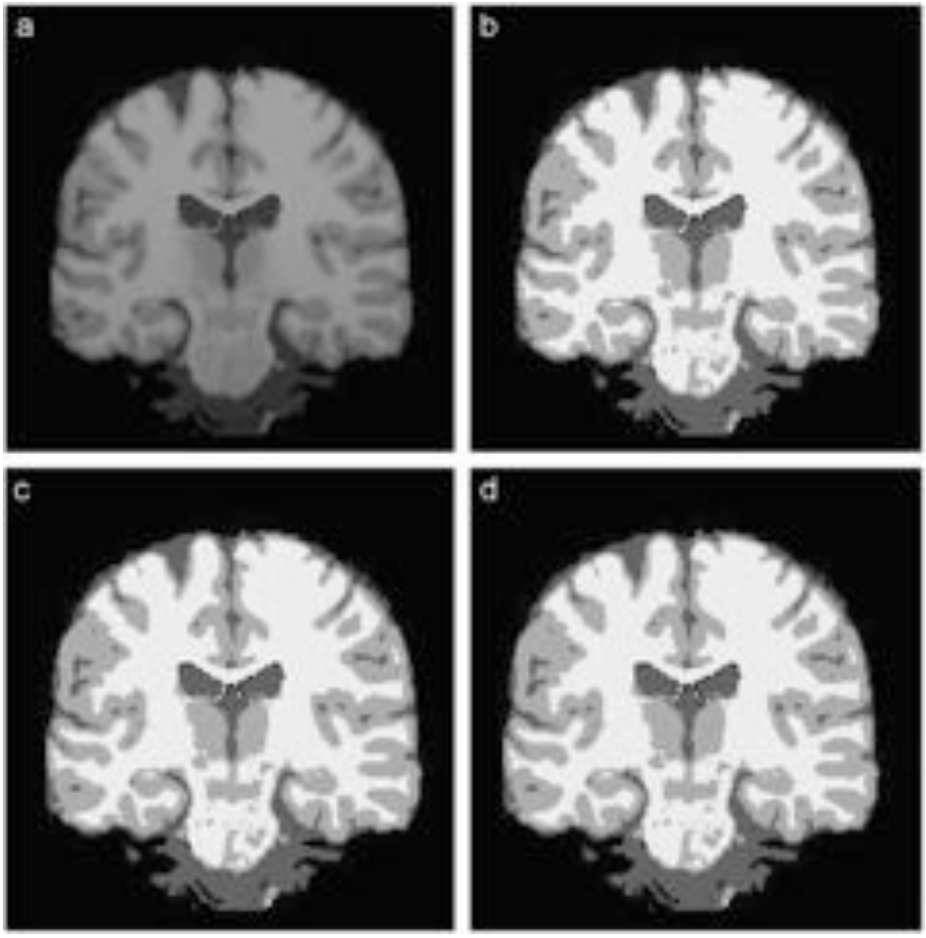

Fig. 8. Classification results for one coronal slice of the simulated brain phantom volume with 40% intensity inhomogeneity from the BrainWeb site. (a) Original skull stripped slice, (b) tissue distribution in the anatomic model providing the classification ground truth, (c) classification after IIH estimation and correction with AFR, and (d) classification after IIH and intensity class means estimation with AFR-U.

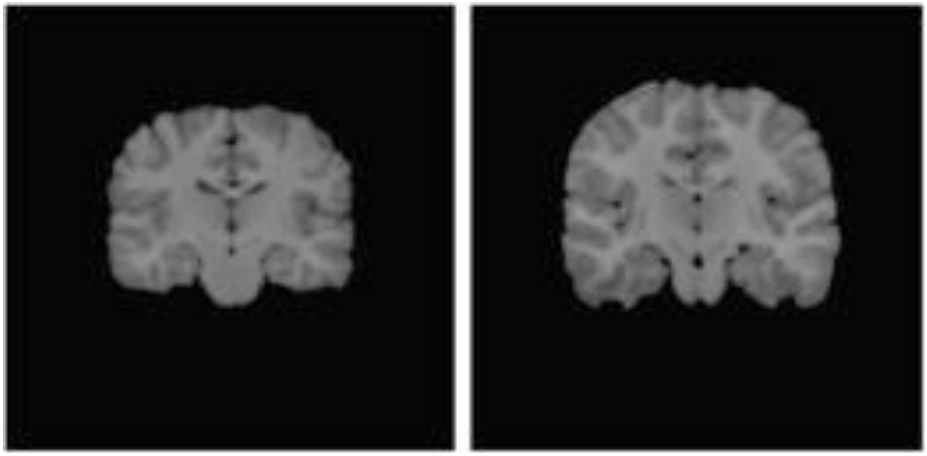

Fig. 9. Original coronal slices of brain volumes from IBSR V2.0 collection.

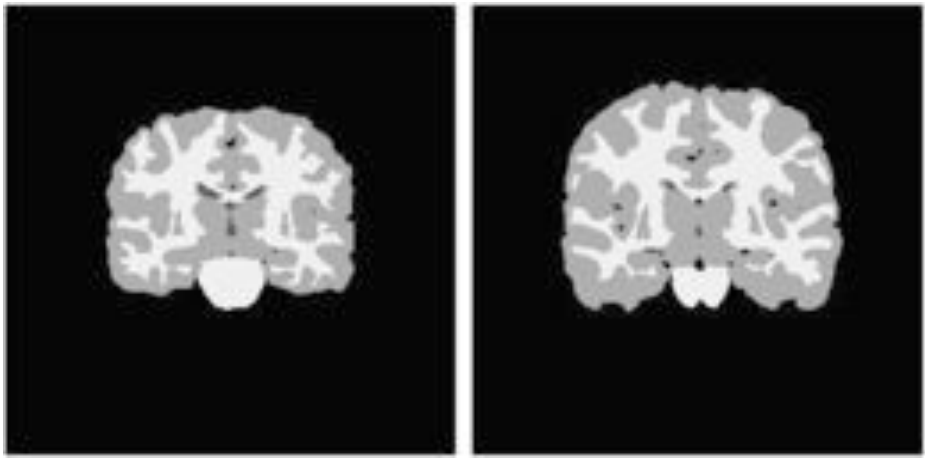

Fig. 10. Manual segmentation into CSF, GM and WM of the slice images in Fig. 9.

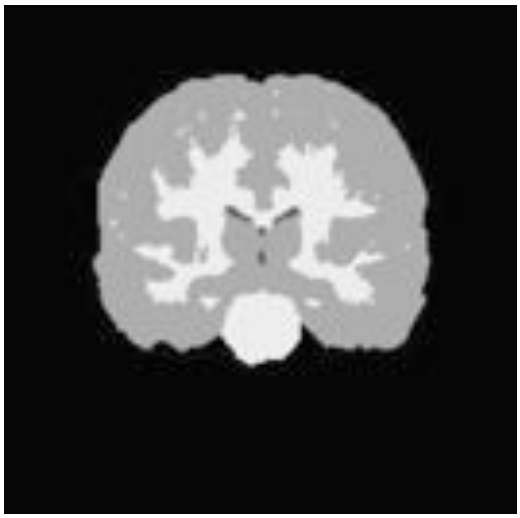

Fig. 11. Crisp atlas obtained from the manual segmentations of the IBSR v2.0 collection, by majority voting at each voxel. Coronal slice in the same position as those in Fig. 9.

the closest class intensity mean. When we perturb the class intensity means there is a general decrease of the results. Finally, performing the estimation of the class intensity means after each iteration of the bias estimation does produce improvements on the CSF and WM classes but a decrease in the GM class.

4.2. Experiments on a simulated brain phantom

We have applied the bare AFR and the unsupervised mean estimation algorithm AFR-U to the segmentation of two simulated brain MRI volumes [8] obtained from the BrainWeb web site http://www.bic.mni.mcgill.ca/brainweb/ at the McConnell Brain Imaging Center of the Montreal Neurological Institute, McGill University [7,26]. The volumes are generated from a normal anatomic model using a T1 sequence, corrupted with intensity inhomogeneities of magnitude 20% and 40% of the original clean image, and several levels of additive noise. For the bare AFR, the intensity means are computed as the intensity means according to the manual segmentation. When we perform the intensity class means unsupervised estimation, applying AFR-U as defined by Eq. (11) the initial values are computed with the k-means

algorithm. The factor F was set to $F = 1$. The initial value of the neighboring function parameter was set to $\sigma_0 = 30$ for the images with 40% IIH and to $\sigma_0 = 15$ for the images with 20% IIH. The number of iterations was 30.

Table 3 presents the results of the basic supervised Gaussian classifier, the AFR and the unsupervised AFR-U. Each table entry contains the triplet of Tanimoto coefficients for the CSF, GM and WM tissue classes. It can be appreciated that the proposed approach improves over the BGAUSS classifier, and that this improvement is more clear for the strongest IIH field, that is, improvements are greater for the 40% IIH volumes than for the 20% IIH volumes.

Besides, the unsupervised intensity mean estimation computed with AFR-U introduces further improvements. The CSF's Tanimoto coefficient follows a curious pattern, it is lower in the results obtained by the AFR and AFR-U algorithms than in the BGAUSS supervised approach for low additive noise levels. However, as the additive noise increases, the results are better for AFR and AFR-U than for BGAUSS.

Fig. 8 shows the classification results for a coronal slice of the 40% IIH brain volume. Fig. 8(a) shows the original slice image extracted from the volume. Fig. 8(b) shows the distribution of CSF, GM and WM in the anatomic model which is the gold standard for the image segmentation. This information has been used as a mask to perform the brain extraction to obtain the brain shown in Fig. 8(a). The result of classification after IIH correction with the bias estimated by the AFR algorithm is shown in Fig. 8(c). The result of slice classification into CSF, GM and WM after intensity class means estimation and IIH correction by the AFR-U algorithm is shown in Fig. 8(d). There are very small differences between both AFR and AFR-U results and between them and the gold standard.

4.3. Some results on intensity class means estimation

To explore the simultaneous estimation of the IIH field and the intensity class means we have used the IBSR V2.0 collection of brain volumes, the 1.5 mm data distribution, which is more recent than the collection used for the experiments in Section 4.1. The MR brain datasets and their manual segmentations were provided by the Center for Morphometric Analysis at Massachusetts General Hospital and are available at http://www.cma.mgh.harvard.edu/ibsr/. The data description mentions that an intensity inhomogeneity process has been realized on the data, therefore it can be expected that AFR will model local features like partial volumes.

In Fig. 9 we have coronal slices of two brain MRI volumes from the IBSR V2.0 collection. It must be noted that they have been normalized in position, but that their sizes are quite different, they have not been subjected to non-linear registration to a common atlas or atlas. Their respective ground truth for classification is given by the manual segmentation into CSF, GM and WM shown in Fig. 10. A coronal slice in the same position as the ones shown in Fig. 9 of the crisp atlas used by the algorithm AFR-A of Eq. (12), obtained from the image manual segmentations by majority voting on each voxel, is shown in Fig. 11. The differences in brain sizes produce an extended GM region in the crisp atlas, covering the GM regions of both small and bigger brains. The probabilistic atlases for CSF, GM and WM, estimated from the volume manual segmentations, used by AFR-PA of Eq. (13) are presented in Fig. 12. The variability of brain sizes produces a thick strip in the probabilistic GM atlas, and a star like shape in the probabilistic WM atlas. Finally, Fig. 13 shows the segmentation results obtained with AFR-U, AFR-A, AFR-PA and AFR-S from the k-means initialization.

Table 4 shows the average Tanimoto coefficients for the CSF, GM and WM over the collection of brain volumes. We call BGAUSS the results obtained with the basic Gaussian classifier using the manual segmentation of each volume as the ground truth to compute the tissue means. The GT denotes that the AFR variants are initialized with those means while KM denotes that the algorithms start from the means estimated by the k-means algorithm. The main conclusion that can be obtained from the table is that results are very poor in general. The standard application of AFR, assuming the manual segmentation intensity class means, barely improves the Gaussian supervised classifier.

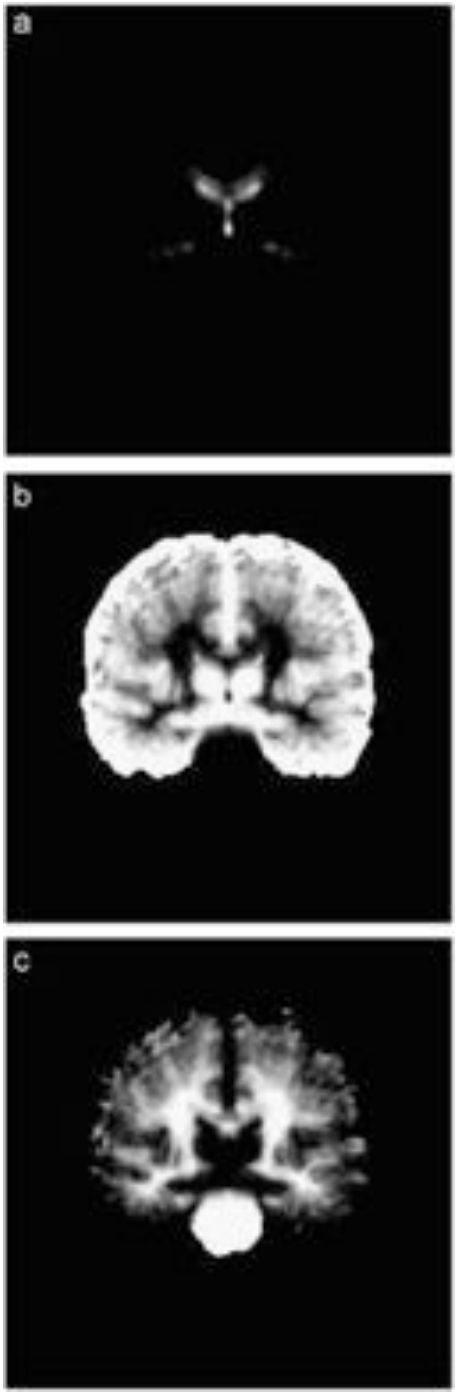

Fig. 12. Probabilistic atlases for (a) CSF, (b) GM and (c) WM computed from the manual segmentation of the volumes in the IBSR v2.0 collection. Coronal slices corresponding to those in Fig. 9.

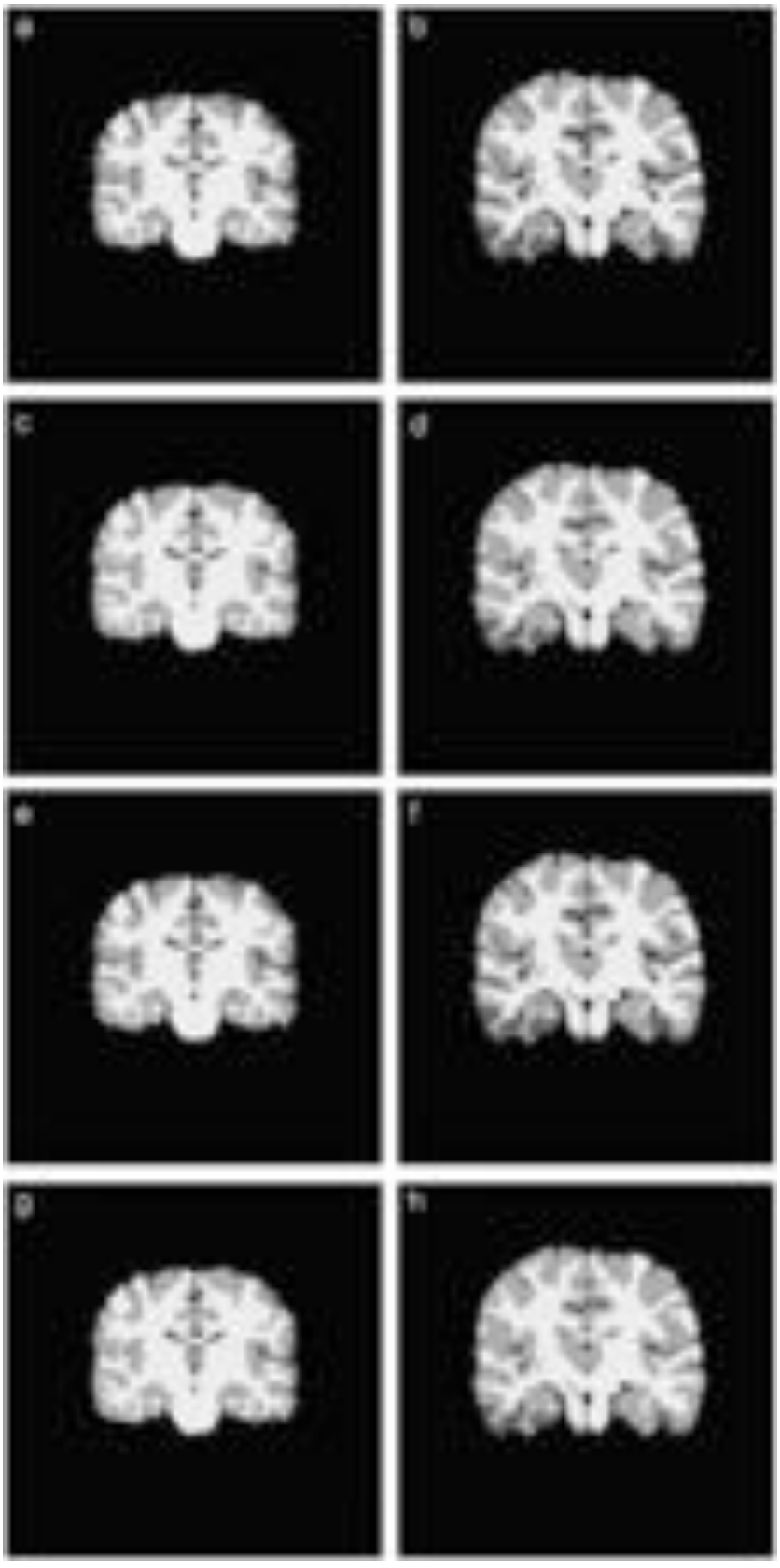

Fig. 13. Classification into CSF, GM and WM by the (a,b) AFR-U, (c,d) AFR-A, (e,f) AFR-PA and (g,h) AFR-S. Coronal slices corresponding to the ones shown in Fig. 9.

That can be due to the data being already intensity normalized. The AFR assuming the k-means initialization is very poor for the CSF and GM classes. The unsupervised estimation of the means performed by AFR-U does not improve the results any further. The crisp atlas used by the AFR-A seems to be of some help but the results do not improve much on the bare AFR with ground truth

Table 4
Average Tanimoto coefficients over the IBSR V2.0 collection of brain volumes of intensity class mean estimation approaches combined with AFR.

	CSF	GM	WM
BGAUSS	0.09	0.62	0.70
AFR GT	0.12	0.62	0.71
AFR KM	0.06	0.52	0.71
AFR-U GT	0.10	0.58	0.68
AFR-U KM	0.06	0.52	0.71
AFR-A KM	0.11	0.62	0.71
AFR-PA KM	0.07	0.52	0.72
AFR-S GT	0.16	0.63	0.67
AFR-S KM	0.12	0.64	0.71

initialization. It can be interpreted as the AFR-A being able to use collective *a priori* spatial distribution information to obtain results comparable to the knowledge of the manual segmentation for the computation of the intensity class means. The AFR-PA that uses the spatial information from the probabilistic atlas, on the other hand, does not give good results (and was tricky to tune to convergence). Finally, the supervised approach does not give the expected improvement.

The use of spatial distribution atlases holds many promises, but also hides many traps. The unsupervised segmentation of the images has severe limits, as many voxels from one tissue will have intensity values close to that of other classes. Having some spatial information about the distribution of tissues seems the sure way to solve the problem. But to compute this spatial distribution and to obtain the desired atlas we need to have either a way to spatially normalize the volumes without introducing much distortion, or to select very precisely the population of images from which the atlas will be computed. In the case at hand, the variation in brain size introduces some undesirable structures in the crisp and probabilistic atlases, because we have built them without taking into account that the size conditions the spatial distribution. Templates reported in the literature are built on the intensity domain, not upon the manual segmentations. Warping classification images is a technique unheard of. Performing linear scale transformation may pose problems, because we are dealing with discrete class information. Approaches reported in the literature that use some kind of template or atlas need to be taken with a precise definition of the population the atlas was derived from.

The examination of the manual segmentation gives an explanation for these results. Comparison of the segmentations shown in Fig. 10 with the BrainWeb model shown in Fig. 8(b) allows to appreciate that some inner brain regions that are classified as WM in the BrainWeb model are systematically classified as GM in the IBSR manual segmentations. The intensity values in these regions seem to correspond to WM voxels. We think that there is a systematic error in the manual segmentation that is reflected in the very low values of BGAUSS and the supervised AFR-S entries in Table 4.

5. Conclusions

We have proposed an adaptive field rule, which is the gradient descent of an energy function, for IIH field estimation in MRI. Our approach is based on a topological preservation formulation of the smoothness constraint on the IIH field. The proposed estimation rule is very similar to the SOM rule. The steady states of the adaptive rule satisfy some smoothness characterizations that allow assuming them as appropriate representations of the IIH fields in the image, minimizing the effect of partial volume and other sources of noise in the estimation of the IIH field. We have tested the approach on a benchmark set of real life brain images. The results show that AFR gives state of the art results, under the assumption of the knowledge of the intensity class means. We have proposed and discussed several ways to perform the estimation of the intensity class means along with the AFR IIH field estimation. On a simulated brain phantom we obtain better results with stronger intensity inhomogeneities. Combining AFR with the unsupervised learning of the intensity class means we consistently improve the AFR results on this brain phantom. When testing the use of spatial distribution atlases on the newest IBSR collection of brain datasets, computed from the manual segmentations, and the supervised learning the results are quite inconsistent, and disappointing. The positive result is that we find that the use of the crisp atlas by AFR-A can give results comparable to the Gaussian supervised classifier. On a closer inspection of both results and manual segmentation images, we find that the manual segmentation published in the ISBR site can be a source of error, both for the construction of supervised classifiers and for the evaluation of supervised and unsupervised approaches. Some of the regions that are consistently classified as gray matter in the IBSR manual segmentations correspond to white matter in comparable segmentations of the BrainWeb phantom. This may, at least partially, account for the poor results found by our attempts to apply AFR and the intensity means estimation algorithms to these data.

Acknowledgments

We thank the anonymous reviewers for their comments, which have been very useful to improve this paper. The MEC partially supports this work through Grant DPI2006-15346-C03-03. The Basque Government has awarded a *Grupo de Investigación Universitario* grant to the Computational Intelligence Group. Maite García holds a predoctoral grant from the UPV/EHU.

References

[1] M.N. Ahmed, S.M. Yamany, N. Mohamed, A.A. Farag, T. Moriarty, A modified fuzzy c-means algorithm for bias field estimation and segmentation of MRI data, IEEE Transactions on Medical Imaging 21 (2002) 193–199.
[2] M.S. Atkins, K. Siu, B. Law, J.J. Orchard, W.L. Rosenbaum, Difficulties of T1 brain MRI segmentation techniques, in: Medical Imaging 2002: Image Processing, Proceedings of SPIE, vol. 4684, SPIE Press, 2002, pp. 1837–1844.
[3] S.M. Bhandarkar, P. Nammalwar, Segmentation of multispectral MR images using a hierarchical self-organizing map, in: CBMS 2001, 2001, pp. 294–299.
[4] C. Brechbuhler, G. Gerig, G. Szekely, Compensation of spatial inhomogeneity in MRI based on a parametric bias estimate, in: The 4th International Conference on Visualization in Biomedical Computing, Hamburg, Germany, 1996.
[5] S. Chaplot, L.M. Patnaik, N.R. Jagannathan, Classification of magnetic resonance brain images using wavelets as input to support vector machine and neural network, Biomedical Signal Processing and Control 1 (1) (2006) 86–92.
[6] C. Chinrungrueng, C. Sequin, Optimal adaptive k-means algorithm with dynamic adjustment of learning rate, IEEE Transactions on Neural Networks 6 (1) (1995) 157–169.
[7] C.A. Cocosco, V. Kollokian, R.K.S. Kwan, BrainWeb: online interface to a 3D MRI simulated brain database, NeuroImage 5 (1997) S425.
[8] E. de Bodt, M. Cottrell, P. Letremy, M. Verleysen, On the use of self-organizing maps to accelerate vector quantization, Neurocomputing 56 (2004) 187–203.
[9] A.P. Dhawan, Medical Image Analysis, IEEE Press Series in Biomedical Engineering, Wiley, New York, July 2003.
[10] R.O. Duda, P.E. Hart, D.G. Stork, Pattern Classification, second ed., Wiley, New York, 2001.
[11] P.A. Estevez, C.J. Figueroa, Online data visualization using the neural gas network, Neural Networks 19 (6–7) (2006) 923–934.
[12] J.C. Fort, SOM's mathematics, Neural Networks 19 (6–7) (2006) 812–816.
[13] M. Garcia-Sebastian, E. Fernandez, M. Graña, F.J. Torrealdea, A parametric gradient descent MRI intensity inhomogeneity correction algorithm, Pattern Recognition Letters 28 (2007) 1657–1666.
[14] M. García-Sebastián, A.I. González, M. Graña, Derivation of SOM-like rules for intensity inhomogeneity correction in MRI, in: J. Cabestany, M. Graña, F.

Sandoval, A. Prieto (Eds.), Computational and Ambient Intelligence, Lecture Notes in Computer Science, vol. 4507, Springer, New York, 2007, pp. 669–676.
[15] G. Gerig, O. Kubler, R. Kikinis, F.A. Jolesz, Nonlinear anisotropic filtering of MRI data, IEEE Transactions on Medical Imaging 11 (1992) 221–232.
[16] J.O. Glass, W.E. Reddick, C.S. Li, F.H. Laningham, K.J. Helton, C.H. Pui, Computer-aided detection of therapy-induced leukoencephalopathy in pediatric acute lymphoblastic leukemia patients treated with intravenous high-dose methotrexate, Magnetic Resonance Imaging 24 (6) (2006) 785–791.
[17] A.I. Gonzalez, M. Graña, M. Cottrell, Basic competitive neural networks as adaptive mechanisms for non-stationary colour quantisation, Neural Computing & Applications 8 (4) (1999) 347–367.
[18] A.I. Gonzalez, M. Graña, Controversial empirical results on batch versus one pass online algorithms, in: WSOM 2005, 2005.
[19] R.C. Gonzalez, R.E. Woods, Digital Image Processing, Addison-Wesley, Reading, MA, 1987.
[20] M. Graña, A. D'Anjou, A.I. Gonzalez, F.X. Albizuri, M. Cottrell, Competitive stochastic neural networks for vector quantization of images, Neurocomputing 7 (2) (1995) 187–195.
[21] R. Guillemaud, M. Brady, Estimating the bias field of MR images, IEEE Transactions on Medical Imaging 16 (1997) 238–251.
[22] T. Heskes, Energy functions for self-organizing maps, in: E. Oja, S. Kaskied (Eds.), Kohonen Maps, Elsevier, Amsterdam, 1999, pp. 303–315.
[23] Z. Hou, A review on MR image intensity inhomogeneity correction, International Journal of Biomedical Imaging 2006 (2006) 1–11.
[24] K.M. Iftekharuddin, J. Zheng, M.A. Islam, R.J. Ogg, Fractal-based brain tumor detection in multimodal, MRI, Applied Mathematics and Computation 207 (2009) 23–41.
[25] T. Kohonen, Self-Organizing Maps, third ed., Springer, Berlin, 2000.
[26] R.K.S. Kwan, A.C. Evans, G.B. Pike, MRI simulation-based evaluation of image-processing and classification methods, IEEE Transactions on Medical Imaging 18 (1999) 1085–1097.
[27] O. Lange, A. Meyer-Baese, M. Hurdal, S. Foo, A comparison between neural and fuzzy cluster analysis techniques for functional MRI, Biomedical Signal Processing and Control 1 (3) (2006) 243–252.
[28] J.A. Lee, M. Verleysen, Self-organizing maps with recursive neighborhood adaptation, Neural Networks 15 (8–9) (2002) 993–1003.
[29] A.W.C. Liew, H. Yan, An adaptive spatial fuzzy clustering algorithm for 3-D MR image segmentation, IEEE Transactions on Medical Imaging 22 (2003) 1063–1075.
[30] J.L. Marroquin, B.C. Vemuri, S. Botello, E. Calderon, A. Fernandez-Bouzas, An accurate and efficient Bayesian method for automatic segmentation of brain MRI, IEEE Transactions on Medical Imaging 21 (2002) 934–945.
[31] T.W. Nattkemper, A. Wismuller, Tumor feature visualization with unsupervised learning, Medical Image Analysis 9 (4) (2005) 344–351.
[32] J.C. Rajapakse, F. Kruggel, Segmentation of MR images with intensity inhomogeneities, Image and Vision Computing 16 (1998) 165–180.
[33] J. Sijbers, A.J. den Dekker, A. Van der Linden, M. Verhoye, D. Van Dyck, Adaptive anisotropic noise filtering for magnitude MR data, Magnetic Resonance Imaging 17 (1999) 1533–1539.
[34] M.Y. Siyal, L. Yu, An intelligent modified fuzzy c-means based algorithm for bias estimation and segmentation of brain MRI, Pattern Recognition Letters 26 (2005) 2052–2062.
[35] J.G. Sled, A.P. Zijdenbos, A.C. Evans, A nonparametric method for automatic correction of intensity nonuniformity in MRI data, IEEE Transactions on Medical Imaging 17 (1998) 87–97.
[36] T. Song, M.M. Jamshidi, M.M. Jamshidi, R.R. Lee, R.R. Lee, M. Huang, A modified probabilistic neural network for partial volume segmentation in brain MR image, IEEE Transactions on Neural Networks 18 (5) (2007) 1424–1432.
[37] M. Styner, C. Brechbuhler, G. Szckely, G. Gerig, Parametric estimate of intensity inhomogeneities applied to MRI, IEEE Transactions on Medical Imaging 19 (2000) 153–165.
[38] Q. Tianbai, L. Minglu, Multispectral MR images segmentation using SOM network, in: CIT '04, 2004, pp. 155–158.
[39] M.E. Tipping, D. Lowe, Shadow targets: a novel algorithm for topographic projections by radial basis functions, Neurocomputing 19 (1–3) (1998) 211–222.
[40] C. Varini, A. Degenhard, T.W. Nattkemper, Visual exploratory analysis of DCE-MRI data in breast cancer by dimensional data reduction: a comparative study, Biomedical Signal Processing and Control 1 (1) (2006) 56–63.
[41] T. Villmann, R. Der, R. Der, M. Herrmann, M. Herrmann, T.M. Martinetz, Topology preservation in self-organizing feature maps: exact definition and measurement, IEEE Transactions on Neural Networks 8 (2) (1997) 256–266.
[42] U. Vovk, F. Pernus, B. Likar, A review of methods for correction of intensity inhomogeneity in MRI, IEEE Transactions on Medical Imaging 26 (2007) 405–421.
[43] W.M. Wells, W.E.L. Grimson, R. Kikinis, F.A. Jolesz, Adaptive segmentation of MRI data, IEEE Transactions on Medical Imaging 15 (1996) 429–442.
[44] A. Younis, M. Ibrahim, M. Kabuka, N. John, An artificial immune-activated neural network applied to brain 3D MRI segmentation, Journal of Digital Imaging, 2007.
[45] Y. Zhang, M. Brady, S. Smith, Segmentation of brain MR images through a hidden Markov random field model and the expectation-maximization algorithm, IEEE Transactions on Medical Imaging 20 (2001) 45–57.

Maite García-Sebastián received her Computer Engineer Graduation in 2005 at the UPV/EHU. She is doing her PhD on medical imaging. She has published Pattern Recognition Letters, Springer Verlag, LNCS, and IEEE Press conference proceedings. Her interest covers the early detection of Alzheimer disease and multiple sclerosis by using MRI data.

Ana Isabel González received her Computer Degree in 1993 at the UPV/EHU. Currently, she works as a collaborator professor of computer science at the UPV/EHU. She is doing her PhD on neural networks. She is part of Computational Intelligence Group. Has published in Neurocomputing, IEEE NN, LNCS, and IEEE Press conference proceedings. Her research interests cover self-organizing maps, GNC, clustering, neural networks, continuation methods.

Manuel Graña Romay, (PhD 1989) Professor of Computer Science at the Universidad del Pais Vasco (UPV/EHU) since 1998. His research interests cover simulation (continuous and discrete event), artificial neural networks and other Computational Intelligence techniques (Evolution Algorithms). He has edited several books in international editorials, as well as coauthored over fifty research papers in international journals. He is proposing Lattice Computing to be a new space for innovative research lines. He leads the "Grupo de Inteligencia Computacional" (www.ehu.es/ccwintco) which has been awarded by the Basque Government a category A grant as university research group.

Neurocomputing 72 (2009) 2146–2152

Contents lists available at ScienceDirect

Neurocomputing

journal homepage: www.elsevier.com/locate/neucom

Robustness of an adaptive MRI segmentation algorithm parametric intensity inhomogeneity modeling

Maite Garcia-Sebastian *, Carmen Hernandez, Alicia d'Anjou

Grupo Inteligencia Computacional, UPV/EHU, Spain

ARTICLE INFO

Available online 16 December 2008

PACS:
07.05.Mh
07.05.Pj
87.63.lm
83.85.Fg

Keywords:
MRI
Intensity inhomogeneity
Image segmentation
Parametric intensity inhomogeneity models
Adaptive image correction

ABSTRACT

We propose an unsupervised segmentation algorithm for magnetic resonance images (MRI) endowed with a parametric intensity inhomogeneity (IIH) correction schema and the on-line estimation of the image model intensity class means. The paper includes an extensive experimentation that shows that the algorithm is robust in the sense that it converges to good image segmentations despite the initial estimation of the image model intensity class means. The algorithm is, therefore, highly automatic requiring no interactive tuning to obtain good image segmentations, an appealing property in clinical environments. The IIH field and intensity class means estimation consists of the gradient descent of the restoration error of the intensity corrected image. Our algorithm does not work on the logarithmic transformation of the image, thus allowing for the explicit distinction between the smooth multiplicative field and the independent and identically distributed additive noise at each image voxel.

1. Introduction

Magnetic resonance images (MRI) allows to visualize with great contrast the soft tissues in the body and has revolutionized the capacity to diagnose the pathologies that affect them [1]. It is based on the phenomenon known as nuclear magnetic resonance (NMR). The image results from the aggregated measurements of the tissue composition at the molecular level. MRI are expected to be piecewise constant except for partial volume effects in the tissue boundaries and the additive noise. Thus, once the expected intensities of each tissue are known, we can built up a good approximation to the optimal Bayesian classifier of minimum classification error assuming that the intensity distribution is a mixture of Gaussians whose means are the tissue expected intensities, to perform the image segmentation task. However, several imaging conditions introduce an additional multiplicative noise factor, referred to as the intensity inhomogeneity (IIH) field in the literature. The sources of IIH are generally divided in two groups [2]: (a) related to properties of the MRI device such as static field inhomogeneity, radio frequency signal energy spatial distribution and others. (b) Related to the imaged object itself such as the specific magnetic permeability and dielectric properties of the imaged object.

A broad taxonomy of MRI IIH correction algorithms divides them between parametric and non-parametric algorithms. The first ones use a parametric model of the IIH field [3–5]. The non-parametric algorithms [6–9] perform a non-parametric estimation of the IIH bias, usually, a smoothing of the restored image classification residuals.

From the point of view of the estimation approach, the two approaches which have produced the greater number of works devoted to this issue are the Bayesian image processing algorithms and the fuzzy clustering. Bayesian algorithms [4,7,9–11] perform the maximum A posteriori (MAP) estimation of either the IIH field or the classification image, or both. The approach needs the formulation of an *a priori* model of the images and/or the inhomogeneity field probability density, and the conditional probability density of the observed image. The probability density of the observed image conditioned to the voxel classification and the inhomogeneity field is usually assumed to be Gaussian. The *a priori* model of the MRI images is sometimes specified by a Markov random field (MRF) that formalizes the smoothness constraints on the image classification [4,7]. In [9,10] modeling the bias as a Gaussian distributed random vector leads to the Expectation Maximization estimation algorithm of the inhomogeneity field. The Hidden MRF proposed in [11] is essentially identical to the MRF *a priori* probability density model of [7].

Fuzzy clustering algorithms [6,12,13] perform the estimation of the image classification minimizing an objective function given by the voxel quantization error weighted by the fuzzy membership coefficients. The algorithms estimate the membership coefficients, the intensity class means and the IIH bias through this minimization process.

We have been previously working on parametric approaches to IIH modeling, estimation and correction, following the approach

* Corresponding author.
E-mail address: maitelasarte@yahoo.es (M. Garcia-Sebastian).
URL: http://www.ehu.es/ccwintco (M. Garcia-Sebastian).

0925-2312/$ - see front matter © 2009 Elsevier B.V. All rights reserved.
doi:10.1016/j.neucom.2008.07.014

[3,5] of modeling the IIH field with 2D or 3D Legendre polynomials. In [14] we did propose a gradient descent algorithm of the restoration error of the image corrected with an estimation of a parametric IIH bias. The error function gradient is formulated relative to the IIH field model parameters. In this paper, is also formulated the error function gradient relative to the tissue intensity class means and we explore the robust response of the algorithm to random initial mean values. Uncertainty about the correct mean class intensities can be due to the variations on the imaging pulse sequence parameters or to the change from one machine to another. A robust segmentation algorithm able to obtain useful estimations of the class means is a needed step to obtain more automated segmentation procedures.

The image model and the algorithm is described in Section 2. Experimental results on simulated brain MRI volumes are presented in Section 3. In Section 4 we discuss the relationship of the algorithm with precedent algorithms. Finally, conclusions and further work are presented in Section 5.

2. Description of the algorithm

We will denote $\mathbf{y} = (y_i; i \in I)$ the observed image and $\mathbf{x} = (x_i; i \in I, x_i \in \Omega)$ the classification image, where $i \in I \subset \mathbb{N}^3$ is the voxel site in the discrete lattice of the image support for 3D images, and $\Omega = \{\omega_1, \ldots, \omega_c\}$ is the set of tissue classes in the image. The assumed image formation model is the following one:

$$y_i = \beta_i \cdot r_i + \eta_i, \tag{1}$$

where β_i is the multiplicative noise due to the IIH, r_i is the clean signal associated with the true voxel class x_i and η_i is the additive noise. In MRI we have the additional restriction that the reflectance values belong to a discrete (small) set, $\Gamma = \{\mu_{\omega_1}, \ldots, \mu_{\omega_c}\}$, so that $r_i = \mu_{x_i}$. Each μ_ω is the signal intensity mean value associated with a homogeneous tissue.[1]

Definition 1. The robust MRI segmentation and IIH correction problem is the problem of estimating the image segmentation $\mathbf{x}$, the values of the intensity class means Γ, and the IIH multiplicative field $\boldsymbol{\beta} = (\beta_i; i \in I)$ from $\mathbf{y}$.

2.1. The GradClassLeg algorithm

We call GradClassLeg [14] our own proposition of an IIH correction and voxel classification algorithm according to its definition as the Gradient descent of Classified images corrected by products of Legendre polynomials. We assume that IIH field model is a linear combination of 3D products of Legendre polynomials [3,5] given by

$$\beta_i(\mathbf{p}) = \sum_{j=0}^{m} \sum_{k=0}^{m-j} \sum_{l=0}^{m-k-j} p_{jkl} P_j(i_x) P_k(i_y) P_l(i_z), \tag{2}$$

where $i = (i_x, i_y, i_z)$ and $P_k(.)$ is a discretization of the Legendre polynomial of degree k that is consistent with the image size in each dimension, and $\mathbf{p} = \{p_{jkl}\}$ is the vector of the linear combination coefficients. The expression in Eq. (2) takes into account the symmetries in the composition of the bias, assuming that the volume discretization is identical in each spatial dimension. Then number of parameters that compose $\mathbf{p} = \{p_{jkl}\}$ is $n = (m+1)((m+2)/2)((m+3)/3)$. Given an IIH field estimation $\hat{\beta}$ we consider the image correction error relative to the intensity class means as the objective function

$$e(\mathbf{p}, \Gamma) = \sum_{i \in I} \left(\frac{y_i}{\widehat{\beta}_i(\mathbf{p})} - \mu_{x_i} \right)^2. \tag{3}$$

That is, we compute the restoration error as the difference between the predicted intensity associated with the tissue class and the observed intensity after bias correction.

GradClassLeg is a gradient descent algorithm of this error function on the vector of parameters $\mathbf{p}$ of the IIH field model

$$\mathbf{p}_{t+1} = \mathbf{p}_t + \boldsymbol{\alpha}_t^{\mathbf{p}} \nabla_{\mathbf{p}} e(\mathbf{p}, \Gamma), \tag{4}$$

and on the intensity class means

$$\Gamma_{t+1} = \Gamma_t + \boldsymbol{\alpha}_t^{\Gamma} \nabla_{\boldsymbol{\Gamma}} e(\mathbf{p}, \Gamma). \tag{5}$$

Eq. (4) gives the estimation $\hat{\mathbf{p}}$ of the IIH field model parameters starting from a random initial model, Eq. (5) gives the estimation $\hat{\Gamma}$ of the intensity class means, starting either from a random initial set of values or from a good guess. The IIH field parameter gradient vector in Eq. (4) is a vector $\nabla_{\mathbf{p}} e(\mathbf{p}, \Gamma) = \{(\partial/\partial p_{jkl}) e(\mathbf{p}, \Gamma)\}$, where each of its components is of the form

$$\frac{\partial}{\partial p_{jkl}} e(\mathbf{p}, \Gamma) = \sum_{i \in I} \left(\frac{y_i}{\widehat{\beta}_i(\mathbf{p})} - \widehat{\mu}_{\widehat{x}_i} \right) \frac{-y_i P_j(i_x) P_k(i_y) P_l(i_z)}{\widehat{\beta}_i^2(\mathbf{p})}, \tag{6}$$

where $\widehat{x}_i = \operatorname{argmin}_\omega \{y_i / \widehat{\beta}_i(\mathbf{p}) - \mu_\omega\}$ is the estimation of the classification of each voxel based on the current estimation of the class intensity means. The intensity class means gradient vector in Eq. (5) is a vector $\nabla_{\boldsymbol{\Gamma}} e(\mathbf{p}, \Gamma) = \{(\partial/\partial \mu_\omega) e(\mathbf{p}, \Gamma)\}$ where each of its components is of the form

$$\frac{\partial}{\partial \mu_\omega} e(\mathbf{p}, I) = \sum_{i \in I | \widehat{x}_i = \omega} -\frac{1}{2} \left(\frac{y_i}{\widehat{\beta}_i(\mathbf{p})} - \widehat{\mu}_\omega \right). \tag{7}$$

3. Computational experiment results

The experimental data is composed of simulated brain MRI volumes [15] obtained from the BrainWeb Internet site [16] at the McConnell Brain Imaging Center of the Montreal Neurological Institute, McGill University. The advantage of working with the simulated volume is that it is possible to compute the classification accuracy relative to the ground truth classes effectively defined in the generation model. There are available simulated brain MRI volumes corrupted with synthetic IIH fields with magnitude 20% and 40% of the original clean image. For short we will call them 20% and 40% IIH volumes. Using the voxel class information provided in the site we have masked out the pixels not belonging to the three classes of interest: white matter (WM), gray matter (GM), and cerebrospinal fluid (CSF). We have also downsampled the volume to allow for extensive experiments in a reasonable time frame. The GradClassLeg parameters are set to $\alpha^{\mathbf{p}} = 0.01$, $\alpha^{\Gamma} = 0.1$, and the maximum number of iterations allowed is 100. Initial IIH field parameter vector value $\hat{\mathbf{p}}$ is set to zero. The initial intensity class means $\hat{\Gamma}$ are generated with uniform probability in the interval $[0, 100]$ and ordered in ascendent order to preserve the meaning of the intensity classes for the purposes of visualization and computation of validation indices. The natural ascending order of intensities is CSF, GM and WM. If this order corresponds to ascending number of class, the visualization will not need further labeling neither for the human inspection nor for the computation of the Tanimoto coefficient.

To give a quantitative evaluation of GradClassLeg we have computed the Tanimoto (also known as Kappa or Dace) coefficient, as defined in [4,13], for the CSF, GM and WM tissue classes.

[1] Obviously the existence of such a thing as an homogeneous tissue is dependent on the imaging resolution, and always a source of critical debate.

Using our notation the Tanimoto coefficient can be expressed as

$$Tt(\omega) = \frac{|\{x_i = \omega \wedge \widehat{x}_i = \omega; i \in I\}|}{|\{x_i = \omega \vee \widehat{x}_i = \omega; i \in I\}|}, \quad (8)$$

where x_i is the voxel's ground truth and $\widehat{x}_i$ is the classification estimation performed by the algorithm. This definition is slightly different from the classical one found in the literature [17] which is the ratio of cardinalities of the symmetrical difference and the union of the sets. In Eq. (8) perfect overlapping gives a value of 1 while disjoint sets give a value of 0. Perfect overlapping means the perfect agreement between the manual and automatic segmentation.

The results shown in Figs. 1, 2, 4 and 5 are the evolution of the Tanimoto coefficient values as the algorithm proceeds. That is, the coefficients are computed at each iteration step. Figs. 1 and 2 present the averages of 50 experiments with different random initial means applying Eqs. (4) and (5) once at each iteration to the 20% and 40% IIH volumes, respectively. It can be appreciated that the algorithm recovers from very bad initial conditions up to acceptable results if we take into account that performing the image segmentation using as intensity class means estimation the average intensity of the voxels of each class as identified by the *a priori* model of the simulated volume, the Tanimoto coefficients obtained are below 0.92 for the simulated brain volume without any kind of noise.

To study the relation between the distribution of the initial intensity class means over the intensity range and the final segmentation, in Fig. 3 we present the plot of the Tanimoto coefficients obtained at the end of each of 250 executions of GradClassLeg with random initial values of the intensity class means against the minimum distance between any two of the initial means. It can be appreciated that low values of the minimum distance between initial class means produce very bad results very often, while minimum distances above 15 produce always good results.

In Figs. 4 and 5 we show the effect of varying the relative frequency of estimation of the intensity class means and the IIH field parameters. Eq. (5) was applied five times for each computation of the IIH rule 4. It can be appreciated that the results improve over Figs. 1 and 2. Inverting the relative frequency, that is, applying Eq. (4) several times for each computation of Eq. (5) usually lead to instability and divergent estimations of the intensity class means. Therefore, the intensity class means estimation is a computational process that runs on a time scale faster than the IIH field estimation.

For a further quantitative evaluation of the performance of the algorithm, we compute the misclassification rate (MCR) for the brain volumes having an 3% additive noise and 0%, 20% and 40% IIH volumes. We compare our algorithm with the results reported in [12] for a variety of algorithms. These quantitative results are presented in Table 1. in this table, FCM denotes the conventional FCM algorithm. FM-AFCM and TM-AFCM denote the full multigrid adaptive FCM algorithm and the truncated multigrid adaptive FCM algorithm, respectively [18]. EM1 and EM2 denote the unsupervised EM algorithm for finite Gaussian mixture models, where EM1 refers to the standard model and EM2 refers to the model where variances and mixture coefficients of the Gaussian

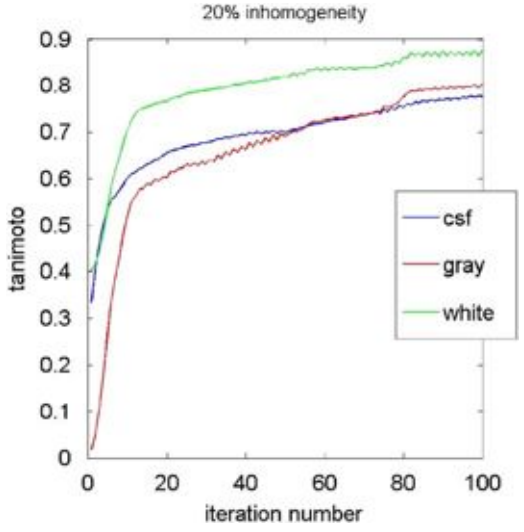

Fig. 1. Average, computed over 50 applications of the GradClassLeg algorithm starting with random initial intensity class means, of the evolution of the white matter (WM), gray matter (GM), and cerebrospinal fluid (CSF) Tanimoto coefficients. Simulated brain volume corrupted with a 20% IIH.

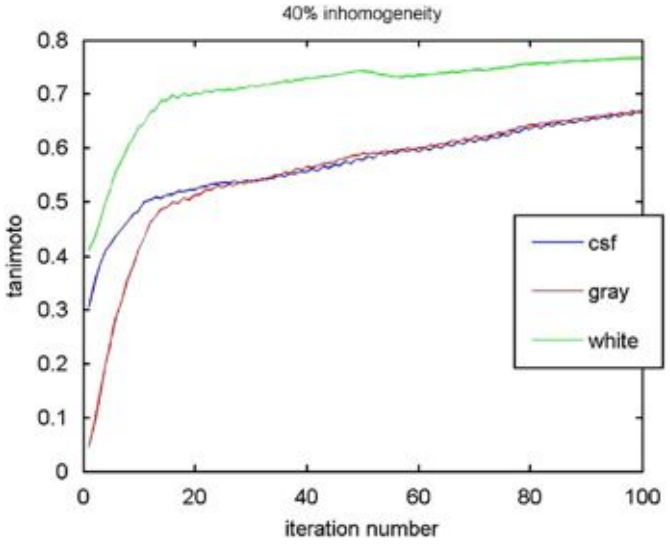

Fig. 2. Average, computed over 50 applications of the GradClassLeg algorithm starting with random initial intensity class means, of the evolution of the white matter (WM), gray matter (GM), and cerebrospinal fluid (CSF) Tanimoto coefficients. Simulated brain volume corrupted with a 40% IIH.

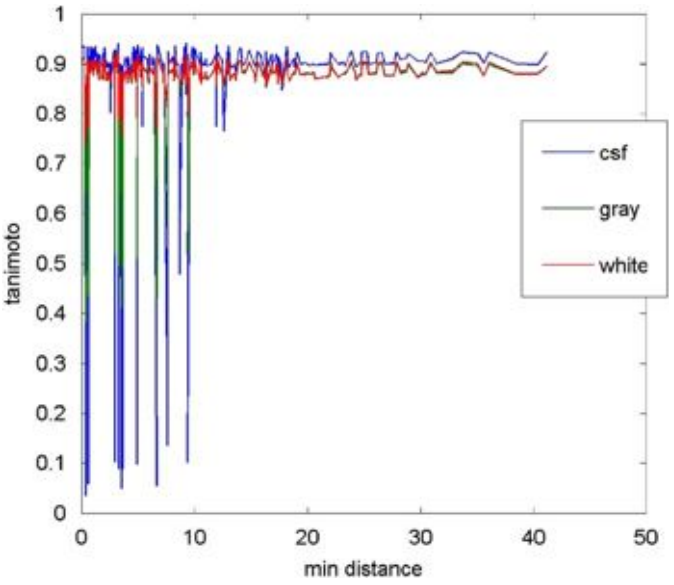

Fig. 3. Values of Tanimoto coefficients at iteration 100 versus minimum distance between initial class means for 250 instances of the execution of the GradClassLeg algorithm. Simulated brain volume corrupted with a 20% IIH.

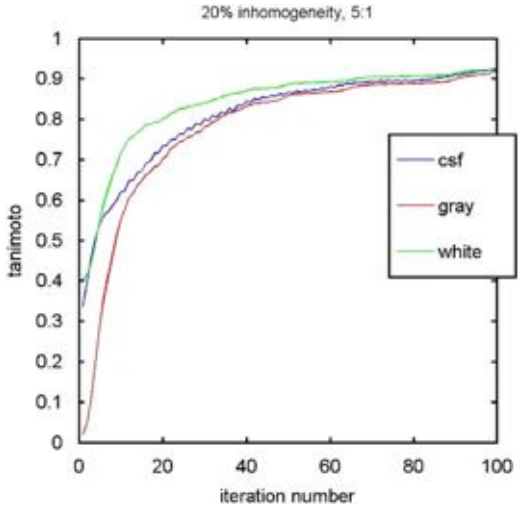

Fig. 4. Average, computed over 50 applications of the GradClassLeg algorithm starting with random initial intensity class means, of the evolution of the white matter (WM), gray matter (GM), and cerebrospinal fluid (CSF) Tanimoto coefficients. Simulated brain volume corrupted with a 20% IIH. Gradient computation relative frequency 5:1 (see text).

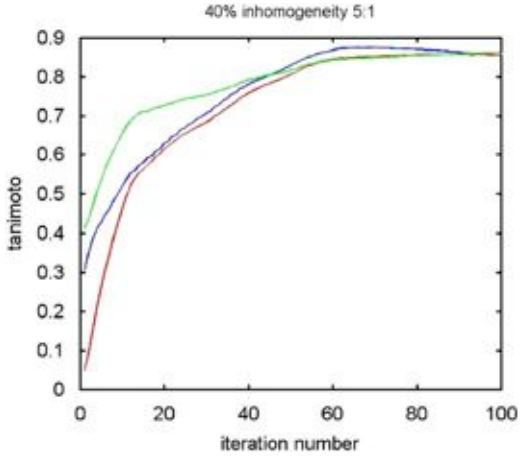

Fig. 5. Average, computed over 50 applications of the GradClassLeg algorithm starting with random initial intensity class means, of the evolution of the white matter (WM), gray matter (GM), and cerebrospinal fluid (CSF) Tanimoto coefficients. Simulated brain volume corrupted with a 40% IIH. Gradient computation relative frequency 5:1 (see text).

Table 1
Misclassification ratio (MCR) results comparing our proposed algorithm with results reported in [12], computed over simulated volumes with increasing IIH.

Method	0% IIH (%)	20% IIH (%)	40% IIH (%)
FCM	3.988	5.450	9.016
FM-AFCM	4.171	4.322	5.065
TM-AFCM	4.168	4.322	4.938
EM1	6.344	7.591	13.768
EM2	4.242	5.638	9.604
AMRF	3.876	4.795	6.874
MNI-FCM	4.979	4.970	5.625
AS-FCM	3.717	3.676	3.832
GradClassLeg	3.43	4.89	6.56

GradClassLeg results correspond to an execution of the algorithm with random initial intensity class means.

components are assumed equal [19]. AMRF denotes the adaptive MRF algorithm [20,21]. MNI-FCM denotes the method where the N3 inhomogeneity correction technique [8] from MNI is applied first, followed by FCM segmentation. AS-FCM denotes the adaptive spatial FCM algorithm [12]. From Table 1, we can see that MCR increases with growing IIH level for all the methods. Our algorithm has better performance than other pure unsupervised algorithms and it is competitive with state-of-the-art algorithms despite its bad initialization and its unsupervised nature. For 0% IIH level, the proposed algorithm has significantly better performance than supervised and unsupervised methods. When studying the results in Table 1 it must be taken into account that most works reported there work on a 2D slice basis while our algorithm is a fully 3D algorithm. Besides, the results seem to refer to a single execution of the algorithm with well chosen initial conditions, whereas the result that we report in Table 1 comes from a random initialization.

Finally, we provide some visual results. Fig. 6(a) shows an axial slice ($z = 90$) of the simulated brain volume corrupted with 3% additive noise and 20% IIH. The non brain voxels have been masked out. Fig. 6(b) shows the corresponding class labeling for this slice in the model used to generate the simulated brain volume. This class labeling is the gold standard for the validation of the segmentation algorithms. The classes are intensity coded as follows: white corresponds to WM, gray to GM and darkest gray to CSF. One application of GradClassLeg with random initial intensity class means produces the estimated bias field shown in Fig. 7(a), and the image segmentation given by the voxel classification obtained by our algorithm is shown in Fig. 7(b). The class intensity coding is the same as in Fig. 6(b). It can be appreciated that the algorithm provides state-of-the-art results despite its random initialization.

4. Discussion of algorithm relatives

The most outstanding precedents of the algorithm presented here is [3,5]. They proposed for the first time the Legendre polynomials as the basis for the definition of the IIH field model. There are some departures of our work from them, which were also discussed in [14]. The most important from the point of view of this paper is that [3,5] do not perform the estimation of the intensity class means, assuming them given. There are some other points of divergence that deserve more detailed discussion. We will end this section with a discussion of the shortcomings of our algorithm.

4.1. The valley function

The *valley* function is the basic building block of the energy function defined in [3,5]. It takes the shape of a filter imposed on the distance, inspired on the robust M-estimators [22,23]. The desired properties of this function are:

- Robustness against outliers. The aim is to avoid outliers biasing the parameter estimation. To this end, some non-linearity that saturates the function output outside the desired input value range. Outliers in the case of MRI are partial volume voxels, that is, voxels that contain signals from various tissues. It must be noted that [5] describes an explicit procedure to get rid of partial volume pixels (using spatial gradient information) so that they are not included in the energy function computation. That is, this role is not needed in the procedure described in [5].
- Normalization. The output value must be bounded in the $[0, 1]$ range. It is advisable in order to obtain energy values inside reasonable ranges.
- A minimum value corresponding to the desired image intensity value and a smooth attraction basin that allows to determine

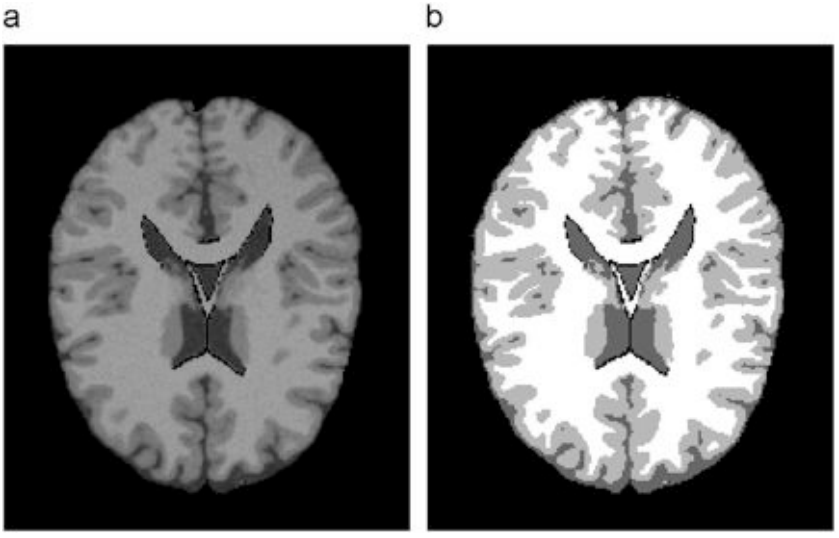

Fig. 6. (a) Original axial slice ($z = 90$) of the skull stripped 3% noise and 20% IIH volume and (b) voxel classification of the axial slice in the model used for the simulation. White, gray and dark gray correspond to WM, GM and CSF, respectively.

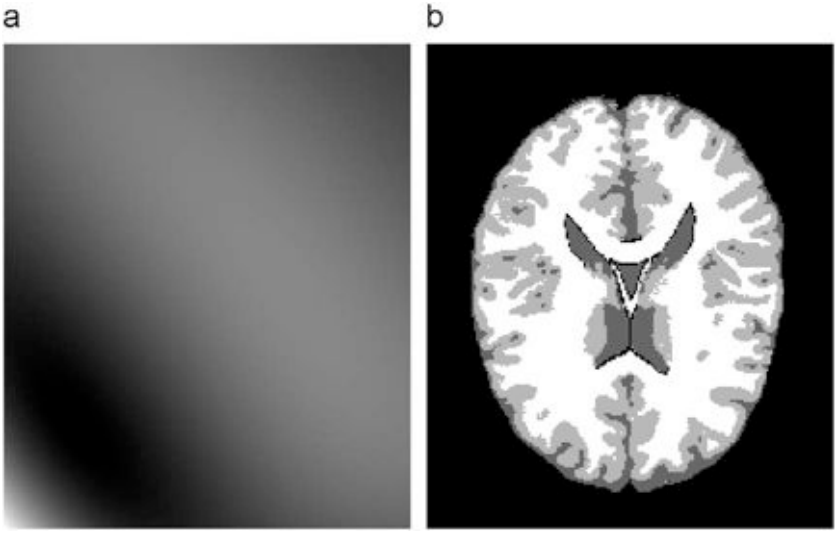

Fig. 7. For an execution of GradClassLeg with random initial intensity class means: (a) estimated bias axial slice ($z = 90$) and (b) estimated classification of the voxels for the slice of Fig. 6. White, gray and dark gray correspond to WM, GM and CSF, respectively.

the search advance direction to reach the desired minimum. The bare squared (Euclidean) distance provides a convenient alternative in this aspect [14], and some authors have discarded altogether the need of this kind of functions [24].

The *valley* function proposed in [5] is the following one:

$$valley(d) = \frac{-d^2}{d^2 + 3\sigma^2}, \tag{9}$$

where d is the distance to the image intensity desired value. This function is positive, the minimum corresponds to $d = 0$ and saturates to 1 as the distance grows. The width of the attraction basin depends on the σ parameter. The claim in [5] is that this function is an M-estimator similar to the one developed in [23]. However, the work in [23] refers to a simulated annealing schema that tries to avoid the need to specify an scale factor. The valley function of Eq. (9) does not correspond to any function proposed in [23] and σ is in fact an scale parameter which has a strong influence on the behavior of the algorithm conditioning the shape of the energy function.

The energy function proposed in [5] is a combination of *valley* function detectors of the following form:

$$e(y) = \prod_k valley(y - \mu_k), \tag{10}$$

where μ_i is a desired intensity value, corresponding to a tissue imaging signal, and y is the image intensity value at a pixel site. The idea is that the energy is close to zero when the pixel intensity is one of the desired intensity values. The aim of this definition seems to be to obtain a continuous and differentiable function, although the use of evolution strategies (ES) proposed in [5] does not need the energy function to be differentiable. In [25] the energy function gradient information was proposed to improve the ES strategy, using a kind of random gradient or memetic approach [26]. The problems that pose the use of this kind of energy building blocks were already discussed in [14]: the bad setting of the scale parameter, σ, may produce very narrow

attraction valleys for the desired minima of the *valley* function. The bad setting of the scale parameter may also introduce strong saturation effects that destroy the correspondence between the image distortion and the energy. Then minimization of the proposed energy does not imply minimization of the distortion of the corrected image relative to the undistorted original image. In other words, minimization of the energy does not imply image enhancement.

4.2. The image formation model and the energy function formulation

The underlying image formation model assumed in [5,25] and related works is the same assumed in Section 2

$$y_i = x_i \cdot \beta_i + \eta_i, \tag{11}$$

where y_i is the observed image, β_i is the smooth IIH, η_i is the Gaussian distributed additive noise and i is the pixel site. The inhomogeneity intensity field model is given by a linear combination of outer products of discretizations of Legendre polynomials $P_i(.)$. The inhomogeneity correction algorithms try to estimate the inhomogeneity field to minimize the error between the clean image x and the corrected image: $\min_{\hat{\beta}} \|y/\hat{\beta} - x\|$, where the corrected image is $y/\hat{\beta} = \hat{x}$. Contrary to our approach in this paper, the approach in [5] was to neglect the additive noise term in Eq. (11), and to consider the logarithm transform on the image: $\log(y_i) = \log(x_i) + \log(\beta_i)$, which can be written for short

$$Y = X + B. \tag{12}$$

The IIH model computed in [5] corresponds in fact to the log of the multiplicative inhomogeneity field

$$\hat{B} = \sum_i \sum_j \hat{a}_{ij} P_i P_j, \tag{13}$$

so that the minimization problem is in fact: $\min_{\hat{B}} \|Y - \hat{B} - X\|$. Where $Y - \hat{B} = \hat{X}$ is the corrected image. If we invert the logarithm transform to obtain the corrected image in its original range we obtain

$$\hat{x} = \exp(\hat{X}) = \frac{y}{\exp(\sum_i \sum_j \hat{a}_{ij} P_i P_j)}.$$

Therefore, when using Eq. (12) as the image formation model, and Eq. (13) as the inhomogeneity model we are in fact building a IIH field model which is an exponential of a linear combination of Legendre 2D or 3D products. It remains to be clarified if this exponential model is an appropriate model for the IIH in MRI data.

As stated in Section 2, the image formation model for MRI usually has the additional assumption that the original image intensities belong to a finite set of values $x \in \{\mu_1, \ldots, \mu_c\}$ corresponding to specific tissue classes. The energy function in [5] is the sum extended to all the image pixels of the energy in Eq. (10) for the corrected image

$$E = \sum_i \prod_{k=1}^{c} valley(Y_i - \hat{B}_i - \log u_k), \tag{14}$$

where the logarithmic model is used. If we denote the distortion of the inhomogeneity distorted image $\delta^2 = \sum_i (y_i - x_i)^2$, we may be interested in knowing the relationship between the energy function in Eq. (14) and the distortion. We would desire the decreasing of the energy function to be equivalent to decreasing the image distortion. A simple experiment reported in [14] shows that this monotonicity does not hold even in very simple circumstances. For a simple chessboard image we have generated a collection of inhomogeneity intensity corrupted images with randomly generated Legendre polynomials up to degree 2. The scatter plots of the image distortion versus energy shows great dispersion for some values of the scale parameter, which in practical optimization terms means that the energy function has little information regarding the image distortion, because images with the same energy have very diverse distortion values, and conversely images with the same distortion may have very diverse energy values. Minimizing the energy function may not have the effect of "cleaning" the image. The energy function that we have exploited for the derivation of our algorithm in this paper has none of these bad side effects.

4.3. Limitations of GradClassLeg

The GradClassLeg is a parametric IIH correction algorithm. Therefore, the estimations of IIH fields performed are very smooth and do not account for small local deviations from the model. These deviations usually correspond to partial volume voxels. If identification of partial volumes voxels is required for some reason, this cannot be attained with our approach. The maximum degree of the Legendre polynomials have implications on the degree of smoothing imposed to the IIH field. Low degree polynomials impose very smooth fields, while high degree polynomials may allow modeling local structures, approximating the identification of partial volume voxels. However, high degree polynomials imply that the energy function is more prone to have local minima which invalidate the gradient descent approach.

Although the robustness to initial values have been demonstrated in this paper, there is no procedure to assess the correct number of intensity classes, a pervasive problem in all the unsupervised approaches to data exploration and image segmentation. In this paper, we relied in the *a priori* knowledge that the images correspond to brain scans which have been skull stripped by a simple masking procedure.

5. Conclusions

We propose an unsupervised segmentation algorithm named GradClassLeg based on the gradient descent of an energy function that consists of the distortion of the IIH corrected image. The IIH field model is given by the linear combination of outer products of 1D Legendre polynomials. Our approach estimates both the IIH model parameters and the intensity class means. GradClassLeg demonstrates the power of parametric approaches to IIH correction in MRI images. In this paper, we have shown that it can be very robust against bad initial estimations of the intensity class means. The robustness of the algorithm makes it a good candidate to explore situations with less *a priori* information, when there are anomalies (i.e., tumorous tissues), in which unsupervised segmentation can be useful to detect unknown image structures. To further validate the algorithm we are planning to embed it in the code of the statistical parametric mapping software (SPM) (www.fil.ion.ucl.ac.uk/spm/) in order to have a better interaction with the medical experts when we apply the algorithm to real life images. SPM provides a suite of functions for registration and visualization that facilitates the pre-processing and evaluation of the algorithm results. Working with SPM provides also the opportunity to perform comparisons with other IIH intensity correction and segmentation algorithms.

Acknowledgments

The MEC partially supports this work through Grant DPI2006-15346-C03-03. The Basque Government has awarded a *Grupo de Investigación Universitario* funding to the Computational Intelligence Group. Maite García holds a predoctoral grant from the

UPV/EHU. Thanks to the anonymous reviewers for their comments, which helped to improve the paper.

References

[1] A.P. Dhawan, Medical Image Analysis, IEEE Press Series in Biomedical Engineering, Wiley, New York, July 2003.
[2] U. Vovk, F. Pernus, B. Likar, A review of methods for correction of intensity inhomogeneity in MRI, IEEE Trans. Med. Imaging 26 (2007) 405–421.
[3] C. Brechbuhler, G. Gerig, G. Szekely, Compensation of spatial inhomogeneity in MRI based on a parametric bias estimate, in: The Fourth International Conference on Visualization in Biomedical Computing, Hamburg, Germany, 1996.
[4] J.L. Marroquin, B.C. Vemuri, S. Botello, E. Calderon, A. Fernandez-Bouzas, An accurate and efficient Bayesian method for automatic segmentation of brain MRI, IEEE Trans. Med. Imaging 21 (2002) 934–945.
[5] M. Styner, C. Brechbuhler, G. Szckely, G. Gerig, Parametric estimate of intensity inhomogeneities applied to MRI, IEEE Trans. Med. Imaging 19 (2000) 153–165.
[6] M.N. Ahmed, S.M. Yamany, N. Mohamed, A.A. Farag, T. Moriarty, A modified fuzzy c-means algorithm for bias field estimation and segmentation of MRI data, IEEE Trans. Med. Imaging 21 (2002) 193–199.
[7] J.C. Rajapakse, F. Kruggel, Segmentation of MR images with intensity inhomogeneities, Image Vision Comput. 16 (1998) 165–180.
[8] J.G. Sled, A.P. Zijdenbos, A.C. Evans, A nonparametric method for automatic correction of intensity nonuniformity in MRI data, IEEE Trans. Med. Imaging 17 (1998) 87–97.
[9] W.M. Wells, W.E.L. Grimson, R. Kikinis, F.A. Jolesz, Adaptive segmentation of MRI data, IEEE Trans. Med. Imaging 15 (1996) 429–442.
[10] R. Guillemaud, M. Brady, Estimating the bias field of MR images, IEEE Trans. Med. Imaging 16 (1997) 238–251.
[11] Y. Zhang, M. Brady, S. Smith, Segmentation of brain MR images through a Hidden Markov random field model and the expectation-maximization algorithm, IEEE Trans. Med. Imaging 20 (2001) 45–57.
[12] A.W.C. Liew, H. Yan, An adaptive spatial fuzzy clustering algorithm for 3-d MR image segmentation, IEEE Trans. Med. Imaging 22 (2003) 1063–1075.
[13] M.Y. Siyal, L. Yu, An intelligent modified fuzzy c-means based algorithm for bias estimation and segmentation of brain MRI, Pattern Recognition Lett. 26 (2005) 2052–2062.
[14] M. Garcia-Sebastian, E. Fernandez, M. Grana, F.J. Torrealdea, A parametric gradient descent MRI intensity inhomogeneity correction algorithm, Pattern Recognition Lett. 28 (2007) 1657–1666.
[15] R.K.-S. Kwan, A.C. Evans, G.B. Pike, MRI simulation-based evaluation of image-processing and classification methods, IEEE Trans. Med. Imaging 18 (1999) 1085–1097.
[16] ⟨http://www.bic.mni.mcgill.ca/brainweb/⟩, 2004.
[17] R.O. Duda, P.E. Hart, D.G. Stork, Pattern Classification, second ed., Wiley, New York, 2001.
[18] D.L. Pham, J.L. Prince, An adaptive fuzzy c-means algorithm for image segmentation in the presence of intensity inhomogeneities, Pattern Recognition Lett. 20 (1999) 57–68.
[19] Z. Liang, R.J. Jaszczak, R.E. Coleman, Parameter estimation of finite mixtures using the EM algorithm and information criteria with application to medical image processing, IEEE Trans. Nucl. Sci. 39 (1992) 1126–1133.
[20] M.X.H. Yan, J.S. Karp, An adaptive Bayesian approach to three dimensional MR brain segmentation, in: Proceedings of Information Processing and Medical Imaging (IPMI'95), 1995, pp. 201–213.
[21] A.F. Goldszal, C. Davatzikos, D.L. Pham, M.X.H. Yan, R.N. Bryan, S.M. Resnick, An image processing system for qualitative and quantitative volumetric analysis of brain images, J. Comput. Assist. Tomogr. 22 (1998) 827–837.
[22] P. Huber, Robust Statistics, Wiley, New York, 1981.
[23] S.Z. Li, Robustizing robust m-estimation using deterministic annealing, Pattern Recognition 29 (1996) 159–166.
[24] V. Zagorodnov, M.F. Hansen, Performance evaluation of parametric bias field correction, in: ICIP'2005, vol. 3, 2005, pp. 732–735.
[25] E. Fernandez, M. Grana, J. Ruiz-Cabello, Gradient based evolution strategy for parametric illumination correction, Electron. Lett. 40 (9) (2004) 531–532.
[26] P. Moscato, A. Mendes, R. Berretta, Benchmarking a memetic algorithm for ordering microarray data, Biosystems 88 (1–2) (2007) 56–75.

Maite García-Sebastian received its Computer Engineer Graduation in 2005 at the UPV/EHU. She is doing her PhD on medical imaging. She has published in Pattern Recognition Letters, Springer Verlag LNCS and IEEE Press conference proceedings. Her interest covers early detection of Alzheimer disease and Multiple Sclerosis by using MRI data.

Carmen Hernandez (PhD 1997) Assistant Professor of Computer Science at the Universidad del Pais Vasco (UPV/EHU). She has published several papers in international journals and belongs to the "Grupo de Inteligencia Computacional" of the UPV/EHU. Her research interests range from hyperspectral image segmentation to voice recognition, with an specific emphasis on probabilistic models such as Markov random fields or Hidden Markov models.

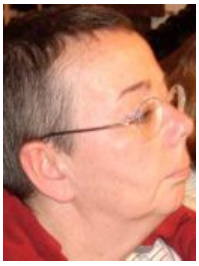

Alicia d'Anjou (PhD 1978) Professor of Computer Science at the Universidad del Pais Vasco (UPV/EHU). She has published more than thirty papers in international journals and belongs to the "Grupo de Inteligencia Computacional" of the UPV/EHU. Her research interests range from Artificial Neural Networks applied to pattern Recognition and Data Mining to Synchronization of Chaotic Systems.

Neuroimage Experimental Data Base Resources

Maria Teresa García Sebastian

Grupo de Inteligencia Computacional, UPV/EHU

Contents

1 Introduction

The goal of this report is to give an impression of the current status of the neuroscience databases of structural and functional techniques available through Internet, with an emphasis in Magnetic Resonance Imaging (MRI). Modern neuroimaging techniques such as structural (Computed Tomography (CT), Magnetic Resonance Imaging (MRI) and Diffusion Tensor Imaging (DTI)) or functional techniques (Positron emission tomography (PET), Single photon emission computed tomography (SPECT), Functional Magnetic Resonance Imaging (fMRI) and functional Diffusion Tensor Imaging (fDTI)) play an important role in the diagnosis of neurodegenerative diseases.

In recent years MRI has become one of the most popular techniques used in radiology to visualize the structure and function of the body, because it is a non-ionizing radiation medical imaging technique. It provides detailed images of the body in any plane and techniques based on the principles of MRI like fMRI, DTI or fDTI are being increasingly used in the preclinical study of certain neurodegenerative diseases.

The availability of public image databases for experimental purposes allows the validation of propositions of computational methods under a common experimental framework. They allow also to reproduce the results claimed by the research groups, both relative to diagnostic issues and to computational methods. In this regard, the simulated MRI images from the BrainWeb site [2], and the clinical images from the Internet Brain Segmentation Repository (IBSR) [7], which are provided with expert segmentations that can be used as the ground thruth for validation processes, have been widely used as benchmarks for a number of algorithms devoted to segmentation, filtering and correction of artifacts in MRI, such as the Intensity Inhomogeneity (IIH). A number of new resources have been added in recent years, the fruit of public funded ongoing research projects, to those early public database efforts. During last years new projects have been developed individually by research groups as the Laboratory of Neuro Image (LONI) [8] or through collaborations with other groups, which are working in the same research area related to image analysis and the study of neurodegenerative diseases, building consortiums such as [1, 6]. Resulting from these projects there are many public resources (images, clinical data, demographics and results of the studies) that are available for validation and refutation purposes of both clinical conclusions and computational algorithms, keeping pace with the fast evolution of the imaging devices and techniques. In fact, the filed is suffering such an explosive growth of public resources and an effervescence of results, techiniques and publications that the present account may well be outdated in a very short time. The works of the PhD candidate have profited from some of these databases, namely the IBSR, BrainWeb and OASIS repositories.

2 IBSR

The Internet Brain Segmentation Repository (IBSR) [7] is a repository of magnetic resonance (MR) brain images and segmentation results. The IBSR was initially created in April 1996 and is maintained by Andrew Worth at the CMA. Currently there are six MR brain data sets, which were provided by the Center for Morphometric Analysis at Massachusetts General Hospital and are available at [7]. Most of them have T1-weighted MR images of healthy subjects. Two data sets have images of two diferent patients with brain tumors.

There are three different directories in which data sets can be found organized into "img", "seg" and "otl" directories, which contain the raw, segmented and outlined images, respectively. However not all data sets have the "seg" and/or "otl" directories. Raw images are 256x256 of 16-bit, but some of them have also these images scaled to 8-bit. Segmented images are "trinary" images (pixels are labeled as a Grey Matter or White Matter tissue or as other), with the same dimensionality as the raw images. Outlined images are the result of semi-automated segmentation techniques performed by an expert and contain lists of points that define certain structures in each scan image. They are defined in a 512x512 grid, because they were created using oversampled images to double size. The difference with the segmentation directory is that the trinary files group all structures in to grey/white/other while the otl files list each neuroanatomical structure separately, so that the information provided by the segmentation trinary images is only a small subset of the information in outlined images. The data was intended to test MRI supervised and unsupervised segmentation algorithms.

2.1 Normal subject, 'Ideal' registered multi-echo brain scan

Data set 657 was created in 1996. It contains seven different image types of the same normal subject (conventional T1, PD and T2 Spin echo sequences; Fast T1, low signal/noise, SPGR (1 avg); Fast T1, better signal/noise, SPGR (2 avgs); Fast PD and T2 FSE sequence). Each of the volumes are registered scans of 18 slices (".img" format with no header information), 2.3 Mb (15.75 Mb total). Scans were acquired at the NMR Center of the Massachusetts General Hospital with a 1.5 tesla General Electric Signa. No segmentation information is provided.

2.2 Adult Male

Data set 788_6 was created in 1996. It contains T1-weighted MRI data with complete expert segmentations (trinary and outlines) from a 55 year old male subject. Each volume has been stored in 60 files that represent the slices through the brain, without header information. Scans were acquired with a 1.5 Tesla General Electric Signa. Contiguous 3.0 mm three-dimensional coronal T1-weighted spoiled gradient echo (SPGR) images of the entire brain was

atained with the following parameters: TR= 40 msec, TE= 5 msec, flip angle =40 degrees, field of view =24 cm, matrix =256x256, and averages =1.

Images were positionally normalized by imposing a standard three-dimensional brain coordinate system on each 3D MR scan [40, 23]. The repositioned scans are then resliced into normalized 3.0 mm coronal, 1.0 mm axial, and 1.0 mm sagittal scans which are used for subsequent analyses.

Gray-white matter segmentation (other=0; gray=128 and white=254) was performed with a semi-automated intensity contour mapping algorithm [29] and also using signal intensity histograms. Neuroanatomical regions of interest for gray/white segmentation include cortical grey matter, subcortical white matter, lateral, third and fourth ventricles, caudate, putamen, globus pallidus, hippocampus-amygdala complex, thalamus proper (including all thalamic nuclei except the lateral and medial geniculate bodies), ventral diencephalic complex (including hypo-, epi-, and subthalamus, substantia nigra, red nucleus medial and lateral geniculate bodies), brainstem, cerebellum cortex and cerebellar central mass, according to the anatomic definitions of [22], with one exception. The central gray nuclei was subdivided at the hypothalamic fissure into thalamus proper and ventral diencephalon.

2.3 5 year old child:

Data set 1320_2 was created in 1996. It contains T1-weighted MRI data with complete expert segmentations (trinary and otulines) from a 5 year old subject. Each volume has been stored in 128 files that represent the slices through the brain, without header information. The MRI scan was acquired with a 1.5 Tesla General Electric Signa. Contiguous 1.5 mm three-dimensional coronal T1-weighted spoiled gradient echo (SPGR) images of the entire brain was attained with the following parameters: TR = 40 msec, TE = 5 msec, flip angle = 40 degrees, field of view = 24cm, matrix = 256x256, and averages = 1.

Images were positionally normalized by imposing a standard three-dimensional brain coordinate system on each 3D MR scan [40, 23]. The repositioned scans are then resliced into normalized 1.5 mm coronal, 0.9375 mm axial, and 0.9375 mm sagittal scans which are used for subsequent analyses.

Gray-white matter segmentation (other=0; gray=128 and white=254) was performed following the procedure described in section 2.2.

2.4 20 Normal Subjects

Data set 20_Normal was created in 1997. It contains T1-weighted MR images, from 20 normal subjects, of 3.1mm slice thickness (16-bit data; 8-bit scaled 3D data and 8-bit scaled 3D data (brain regions only)) and expert segmentations (other=0; csf=128; gray=192; white=254). Volumes of 16-bit have been stored in 60 ".img" files that represent the slices through the brain. On the other hand 8-bit and segmented images have been stored in data files (.buchar) and header files (.hdr), where header files have four ascii numbers that give the size of the data set. The segmented and 8-bit images have less slices than the 16-bit image

data. The matching segmentation must be done using the offsets given at [7] for this data set.

Images are coronal three-dimensional T1-weighted spoiled gradient echo MRI scans, that were obtained on two different imaging systems. Ten FLASH scans performed on a 1.5 tesla Siemens Magnetom MR System (Iselin, NJ) with the following parameters: TR = 40 msec, TE = 8 msec, flip angle = 50 degrees, field of view = 30 cm, slice thickness = contiguous 3.1 mm, matrix = 256x256, and averages = 1. Ten 3D-CAPRY scans performed on a 1.5 tesla General Electric Signa MR System (Milwaukee, WI), with the following parameters: TR = 50 msec, TE = 9 msec, flip angle = 50 degrees, field of view = 24 cm, slice thickness = contiguous 3.0mm, matrix = 256x256, and averages = 1.

Images were positionally normalized by imposing a standard three-dimensional brain coordinate system on each 3D MR scan [40, 23]. The repositioned scans are then resliced into normalized 3.0 mm coronal, 1.0 mm axial, and 1.0 mm sagittal scans which are used for subsequent analyses.

Segmentation was performed on the positionally normalized scan by trained investigators using a semi-automated intensity contour mapping algorithm [29] and also using signal intensity histograms. Other neuroanatomical structures were segmented similarly [22].

Segmentation Performance Index

IBSR facilitates segmentation comparisons of six classification methods tested over this collection of images, provided by Jagath C. Rajapakse and SPM5 GM segmentation done by On Tsang. Results from Rajapakse are partially based on the method described in [36], where the comparison metric is the average overlap also called Tanimoto coefficient [21], eq. 1:

$$T = \frac{|A \cap B|}{|A \cup B|}, \tag{1}$$

where A and B are sets of voxels corresponding to different segmentations.

2.5 Tumor patients: various scans over time

Subject 126

This data set was created in 1999. It contains multiple scans of a 59 year old female with a tumor, taken at roughly 6 month intervals over three and a half years. The T1 + Gadolinium MRI scans were acquired with a 1.5 Tesla General Electric Signa and different parameters.

Subject 536

This data set was created in 1999. It contains multiple scans of a patient with a tumor (images and outlines), taken at roughly 6 month intervals over three and a half years. Each series has been stored in 60 .img files with no header information. The pixel resolutions on these are 0.9375 x 0.9375 mm in-plane

by 3.1 mm slice thickness. The outline files include 4 outlines: a contralateral reference region (the cerebral hemisphere of the right (unaffected) hemisphere), and three outlines of the enhancing tumor based upon intensity countours 1, 2 and 3 standard deviations above the mean of the contralateral reference region.

Images were registered using the CMA's standard positional normalization coordinate system.

2.6 IBSR V2.0

This data set was created in 2003 and 2004 and currently contains T1-weighted MR Image data from eighteen subjects, with expert segmentations of 43 individual structures (1.5mm slice thickness). Data are in CMA and analyze formats. For each subject there is T1-weighted volumetric images that have been 'positionally normalized' into the Talairach orientation (rotation only) and also have been processed by the CMA 'autoseg' biasfield correction routines.

Gray-white matter segmentation include segmentation of the 3rd Ventricle, 4th Ventricle, Brain Stem, and Left and Right: Accumbens area , Amygdala, Amygdala Anterior, Caudate, Cerebellum Cortex, Cerebellum Exterior, Cerebellum White Matter, Cerebral Cortex, Cerebral Exterior, Cerebral White Matter, Hippocampus, Inf Lat Vent, Lateral Ventricle, Pallidum, Putamen, Thalamus Proper, VentralDC, and vessel.

3 BrainWeb: Simulated Brain Database

This simulated brain database (SBD) [2] was provided by McConnell Brain Imaging Centre at the Montréal Neurological Institute [15], McGill University. It contains a set of realistic Magnetic Resonance Imaging (MRI) data volumes produced by an MRI simulator [18, 30, 38]. Currently contains simulated brain MRI data based on two types anatomical models [19] ("phantoms"): normal and multiple sclerosis (MS), which can serve as the ground truth for any analysis procedure. These anatomical models consist of a set of 3-dimensional "fuzzy" tissue membership volumes, one for each tissue class. The voxel values in these volumes reflects the proportion of tissue present in that voxel, in the range $[0, 1]$. The volumes are defined at a 1mm isotropic voxel grid in Talairach space, with dimensions 181x217x181 (XxYxZ) and origin coordinates -90,-126,-72 (x,y,z) in Talairach space.

In addition to the fuzzy tissue membership volumes, a discrete anatomical model is provided which consists of a class label (integer) at each voxel, representing the tissue which contributes the most to that voxel.

Volumes can be downloaded in MINC or raw format.

3.1 Normal Brain Volumes

Pre-computed simulated SBD

In the pre-computed SBD data are available for viewing in three orthogonal views (transversal, sagittal, and coronal) and for downloading with the parameter settings fixed to 3 modalities, 5 slice thicknesses, 6 levels of noise, and 3 levels of intensity non-uniformity. These simulations are based on an anatomical model of normal brain, which is available at a resolution of $1mm^3$ and also for thicker slices (in Z direction): 3mm, 5mm, 7mm and 9mm. Tissue classes available for this phantom are: Background, CSF, Grey Matter, White Matter, Fat, Muscle/Skin, Skin, Skull, Glial Matter and Connective.

Custom MRI simulations interface

Through the BrainWeb custom MRI simulations interface it is possible to choose arbitrary parameters and obtain different volumes based on the same normal anatomical model as in subsection 3.1.

20 sets of simulated data with specific parameters

Currently, it is only possible to download 20 different sets of T1-weighted simulated data, based on 20 anatomical models of 20 normal brains, with these specific parameters: SFLAH (spoiled FLASH) sequence with TR=22ms, TE=9.2ms, flip angle=30 deg and 1mm isotropic voxel size. Tissue classes available for these phantoms are: Background, CSF, Grey Matter, White Matter, Fat, Muscle/Skin, Skull, Blood vessels, Connective (region around fat), Dura Matter and Bone Marrow.

3.2 MS Lesion Brain Volumes

Pre-computed simulated SBD

In the pre-computed SBD data are available for viewing in three orthogonal views (transversal, sagittal, and coronal) and for downloading with the parameter settings fixed to 3 modalities, 5 slice thicknesses, 6 levels of noise, and 3 levels of intensity non-uniformity. These simulations are based on an anatomical model of a human brain with "moderate" MS lesions, which is available at a resolution of $1mm^3$. Tissue classes available for this phantom are: Background, CSF, Grey Matter, White Matter, Fat, Muscle/Skin, Skin, Skull, Glial Matter, Connective and MS lesion.

Custom MRI simulations interface

Through the BrainWeb custom MRI simulations interface it is possible to choose arbitrary parameters and obtain different volumes based on three different MS anatomical models with "moderate" (the same anatomical model as subsection 3.2), "mild" and "severe" MS lesions.

4 OASIS

The Open Access Series of Imaging Studies (OASIS) [32] provides brain imaging data that are freely available for distribution and data analysis [12]. It is made available by Dr. Randy Buckner at the Howard Hughes Medical Institute (HHMI) at Harvard University, the Neuroinformatics Research Group (NRG) at Washington University School of Medicine, and the Biomedical Informatics Research Network (BIRN). Currently available data set consists of a cross-sectional collection of 416 subjects covering the adult life span aged 18 to 96 including 100 individuals over the age of 60, who have been diagnosed with early-stage Alzheimer's Disease (AD).

For each subject 3-4 T1-weighted magnetization prepared rapid gradient-echo (MP-RAGE) MRI scans were acquired on a a 1.5-T Vision scanner (Siemens, Erlangen, Germany), corresponding to multiple repetitions of the same structural protocol within a single session; a motion-corrected coregistered average of all available data; a gain-field corrected atlas-registered image to an standard space [40, 17]; and a masked version of the atlas-registered image, a grey/white/CSF segmented image [41]. Aditionally, for 20 of the nondemented subjects, images from a subsequent scan session are also included as a means of assessing acquisition reliability. All images are in 16-bit big-endian Analyze 7.5 format.

This data set has been based on the following publications for demographic [37] (gender, handedness, age, education and socioeconomic status), clinical assessments [35, 37] (Mini-Mental State Examination (MMSE) and Clinical Dementia Rating (CDR)), and derived anatomic measures [17, 24] (total intracranial volume (eTIV), atlas scaling factor (ASF) and normalized whole brain volume (nWBV)).

The database has a complex structure, shown in figure 1. It contains, besides the raw MRI scans, the anatomic information, the registered images, the segmented and skull stripped images. Therefore, the database can be used to test several algorithms at different points in the processing pipeline. Figure 2 contains a table with the name codification and corresponding image types. Finally, figure 3 contains a summary of the database demographic information.

5 MORPHDTI_P0001

This data set contains high SNR DTI data and the co-registered DTI data for a healthy male volunteer scanned on three separate scanning sessions over 2 days [28, 31]. Fifteen DTI scans were performed in each scan session, producing 45 DTI datasets in total. Data was acquired on a 1.5T Philips MR unit at the F.M. Kirby Research Center for Functional Brain Imaging, Kennedy Krieger Institute, Johns Hopkins University.

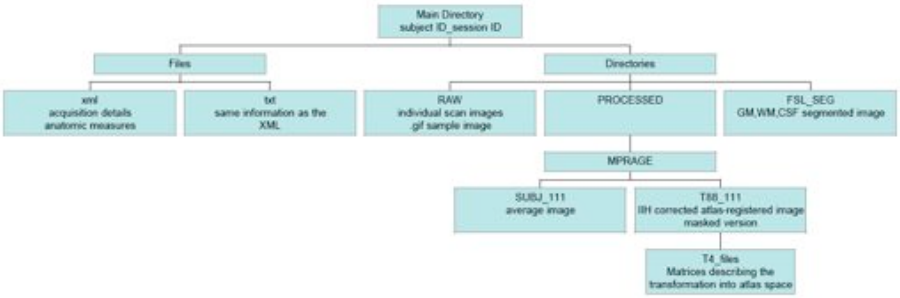

Fig. 1: File structure of OASIS Database

Name	Description	Dimensions	Vox. size	Orient
OAS1_xxxx_MRy_mpr-z_anon	Individual scan (z=repetition)	256x256x128	1x1x1.25	Sag
OAS1_xxxx_MRy_mpr_ni_anon _sbj_111	Image averaged across scans (i=# of scans)	256x256x160	1x1x1	Sag
OAS1_xxxx_MRy_mpr_ni_anon _111_t88_gfc	Gain-field corrected atlas registered average	176x208x176	1x1x1	Trans
OAS1_xxxx_MRy_mpr_ni_anon _111_t88_masked_gfc	Brain-masked version of atlas registered image	176x208x176	1x1x1	Trans
OAS1_xxxx_MRy_mpr_ni__anon 111_t88_masked_gfc_fseg	Brain tissue segmentation	176x208x176	1x1x1	Trans

Fig. 2: Types of Images included in the dataset

		Non-Demented				Demented				
Age Group	N	n	mean	male	female	n	mean	male	female	CDR 0.5/1/2
<20	19	19	18.53	10	9	0		0	0	0/0/0
20s	119	119	22.82	51	68	0		0	0	0/0/0
30s	16	16	33.38	11	5	0		0	0	0/0/0
40s	31	31	45.58	10	21	0		0	0	0/0/0
50s	33	33	54.36	11	22	0		0	0	0/0/0
60s	40	25	64.88	7	18	15	66.13	6	9	12/3/0
70	83	35	73.37	10	25	48	74.42	20	28	32/15/1
80s	62	30	84.07	8	22	32	82.88	13	19	22/9/1
>90	13	8	91.00	1	7	5	92.00	2	3	4/1/0
Total	416	316		119	197	100		41	59	70/28/2

Fig. 3: Demographic summary

6 MIRIAD

Multisite Imaging Research In the Analysis of Depression (MIRIAD) data set [9, 5] has dual-echo MRI scans (currently 100 subjects) acquired at Duke University, which have been anonymized and uploaded by the Neuropsychiatric Imaging Research Laboratory (NIRL) [10] to the Biomedical Informatics Research Network/Storage Resource Broker (BIRN/SRB) [1] where they are accessed at BWH (Surgical Planning Laboratory, SPL) [13] and UCLA (LONI) [8].

At the Laboratory of Neuro Imaging (LONI) a study-specific atlas is constructed from the MRI scans with both PD and T2 contrasts. Subjects' scans are linearly aligned to the study space to acquire spatial normalization factors, and a BWH tissue and structure probability field atlas is non-linearly aligned to each individual subject. Dual-echo scans are segmented utilizing the individual subject-aligned tissue probability atlases at the Surgical Planning Laboratory, SPL; regions of interest and cerebral tissues are classified by an expectation maximization algorithm.

LONI completes the scan processing with a measurement of lobar volumes via a non-linear registration of study-specific lobar atlas to native subject spaces, and regional and lobar tissue volumes are computed. The image processing results, both the images and volumetric measurements, are uploaded to the SRB. Initial statistical analyses were performed at Duke, as the associated metadata (e.g., age, sex, diagnosis, clinical scales) resided there at the beginning of the project.

7 ELUDE

The Efficient Longitudinal Upload of Depression in the Elderly (ELUDE) data set is an anonymized collection of a longitudinal study of late-life depression at Duke University. There are 281 depressed subjects and 154 controls included. An MR scan of each subject was obtained every 2 years for up to 8 years (total of 1093 scans). Clinical assessments occurred more frequently and consists of a battery of psychiatric tests including several depression-specific tests such as the HAM-D, CESD, and MADRS.

8 Alzheimer's CATX

This Data set [14] contains activation maps of 9 Alzheimer's disease patients & 9 elderly controls [39]. It was provided by Andrew Saykin, Dartmouth Medical School and the last updated was in May 10, 2004. The task is about semantic processing: category exemplar (CATX)-identify word pairs with correct category examplar relationships from among incorrect ones.

9 Realistic MRI data set

This Data set [14] contains realistic brain lesion distributions generated using a lesion-deficit simulator with spatial statistical model conforming to the Frontal Lobe Injury in Childhood Study [33, 27].

10 DTMRI Data

This is a DTI data set [3] acquired under Human Brain Project and National Research Resource Center grant. It contains raw and processed DTI data of 15 normal population, white matter atlases, DTI software. Currently the database has 2.5 mm isotropic resolution images and 2.2 mm isotropic resolution images. Only 2.5 mm data are available.

11 BIRN (Biomedical Informatics Research Network)

The Biomedical Informatics Research Network (BIRN) [1] was launched in 2001 with the goal of fostering large-scale collaborations in biomedical science by utilizing emerging cyberinfrastructure. An essential feature of the project is the collaboration of computer scientists and biomedical researchers from different research disciplines to design and implement a distributed architecture of shared resources usable by all biomedical researchers in order to advance the diagnosis and treatment of disease.

FBIRN_Traveling_Subject2003

This dataset includes five healthy subjects imaged twice at each of ten FBIRN MRI scanners on successive days. Functional and structural imaging, behavioral, and demographic data are available from 100 scanning sessions on these subjects.

BrainScape_BS002

This dataset includes seventeen healthy subjects with four resting state fixation scans plus one T1 scan and one T2 scan. The data were collected as part of a study on the behavioral effects of spontaneous BOLD fluctuations [26].

BrainScape_BS003

This dataset includes ten healthy subjects scanned 3 times with 3 conditions: eyes open, eyes closed, and fixating in addition to two anatomical scans (T1 and T2) [25].

fBIRN PhaseII

The Phase II multi-site clinical imaging study consists of approximately 250 subjects, both chronic schizophrenics and age- and gender- matched controls. The MRI data include structural and fMRI images from two separate scanning visits for each subject, including the Sternberg Item Recognition Paradigm and the Auditory Oddball paradigm, a breath hold task, and a sensorimotor task. The clinical assessments include behavioral measures, handedness and demographic measures, SES, smoking measurements, North American Adult Reading Test (NARRT), and clinical severity assessments for the clinical subjects. Currently data from three sites are released to the general research community; the remainder are awaiting IRB approvals for public data sharing.

12 ADNI (Alzheimer's Disease Neuroimaging Initiative)

The ADNI was launched in 2003 by the National Institute on Aging (NIA), the National Institute of Biomedical Imaging and Bioengineering (NIBIB), the Food and Drug Administration (FDA), private pharmaceutical companies and non-profit organizations, as a $60 million, 5-year public-private partnership.

The primary goal of ADNI has been to test whether serial magnetic resonance imaging (MRI), positron emission tomography (PET), other biological markers, and clinical and neuropsychological assessment can be combined to measure the progression of mild cognitive impairment (MCI) and early Alzheimer's disease (AD). Currently there are available more than 32,000 MR and PET scans.

The initial goal of ADNI was to recruit 800 adults, ages 55 to 90, to participate in the research, approximately 200 cognitively normal older individuals to be followed for 3 years, 400 people with MCI to be followed for 3 years, and 200 people with early AD to be followed for 2 years.

13 Functional Brain Imaging of Young, Nondemented, and Demented Older Adults

This fMRI data set is available on Internet [4] since the year 2000. A paradigm involving repeated presentation of sensory-motor response trails was administered to 41 participants (14 young adults (18-24), 14 nondemented older adults (66-89) and 13 demented older adults (68-83)) [16].

All subjects were right-handed, english speakers, with normal (corrected) visual acuity. A history of neurological or visual illness served as exclusion criteria for all potential subjects. Furthermore, older adults were excluded if they had neurologic, psychiatric or mental illness which could cause dementia. Dementia status was determined using recruitment and assessment procedures developed by the Alzheimer's Disease Research Center at Washington University. Clinicopathology studies in cognitively healthy aging and Alzheimer's disease; Relation of histologic markers to dementia severity, age, sex, and APOE genotype; CDR.

Stimulus display was controlled by a Power Macintosh computer (Apple, Cupernico, CA) using PsyScope software (Cohen, MacWhinney, Flatt, & Provost, 1993). Keypress responses were recorded using a fiber-optic light-sensitive keypress connected to a PsyScope button box (Carnegie Mellon University, Pittsburgh, PA). All buttons except one were physically covered to minimize response complexity.

Stimuli were rear projected (Am- Pro Model LCD-150, Ampro, Melbourne, FL) onto a screen placed at the back of the magnet bore. Participants viewed the screen through a mirror fastened to the top of the head coil. Participants requiring corrective lenses (mostly older adults) were supplied magnetcompatible glasses.

The basic task paradigm consisted of presentation of a 1.5-sec duration visual stimulus. Participants pressed a key with their right index fingers upon stimulus onset. The visual stimulus was an 8-Hz counterphase flickering (black to white) checkerboard subtending approximately 12^{o} of visual angle (6^{o} in each visual field). Stimulus parameters were identical to those used by [34]. The stimulus onset was triggered at the beginning of the image acquisition via the PsyScope button box. Spatial frequency of the checkerboard decreased with visual angle to be approximately constant in relation to acuity across the visual field. Runs were structured such that for every eight-image acquisition (21.44 sec), one of two kinds of trial condition were presented (15 trials per run for a total of 60 trials per subject).

Task trials either involved stimuli presented in isolation (one-trial condition) or in pairs with an inter-trial interval of 5.36 sec (two-trial condition). One-trial and two-trial conditions were pseudorandomly intermixed such that eight trials of one type and seven of the other appeared in each run. The logic of this design [20] is that the onetrial conditions can be examined to determine the evoked hemodynamic response to an isolated, transient event. The two-trial conditions further allowed the summation properties of the hemodynamic response to be examined: To the degree that the added responses in the two-trial conditions were similar to the responses in the one-trial conditions, the hemodynamic dynamic response exhibits linear summation. Four image acquisitions involving only fixation were acquired prior to the first trial and following the last trial in each run.

14 Neuroscience Database Gateway (NDG)

The Neuroscience Database Gateway (NDG) [11] began in 2004 as a pilot project developed by the Society's Brain Information Group (BIG). The NDG is now overseen by the Society's Neuroinformatics Committee and is hosted at Yale University (by Gordon Shepherd and Luis Marenco). The SfN Neuroscience Database Gateway provides links to five main types of database: Databases of experimental data; knowledge bases; software tools for neuroscience; bioinformatics resources; providers of research materials; all neuroscience databases.

15 LONI Image Data Archive (IDA)

The LONI Image Data Archive (IDA) [8] is a user-friendly environment for archiving, searching, sharing, tracking and disseminating neuroimaging and related clinical data. The IDA is utilized for dozens of neuroimaging research projects across North America and Europe and accommodates MRI, PET, MRA, DTI and other imaging modalities. A flexible data de-identification engine and encrypted file transmission help ensure compliance with patient-privacy regulations.

16 mBIRN Data Repository (mBDR)

The mBIRN Data Repository (mBDR) [9] is a public resource presented by the Morphometry testbed of the Biomedical Informatics Research Network (BIRN). It includes a range of raw and post-processed MRI images, related derived measures, and related subject measures. The data are organized by project OASIS, morphDTI_p0001, MIRIAD, ELUDE

17 fMRI Data Center (fMRIDC)

The fMRIDC is a public repository [4] of peer-reviewed fMRI publications projects and their underlying data. Currently there are 122 data sets available.

18 DEnLab Data Repository

The repository [14] contains both medical data such as the ones referred in secions 8 and 9, as well as some information about methods and computational techniques for medical image processing.

19 ICBM Human Atlases

The LONI Atlas site [8] consists of a collection of data, online viewers, images and animations that describe the various atlases (e.g. Alzheimer's Disease Template) developed at LONI. A complete description and discussion of these atlas requires a dedicated chapter.

References

[1] Biomedical informatics research network: http://www.nbirn.net/.

[2] Brainweb available at http://www.bic.mni.mcgill.ca/brainweb/.

[3] Dtmri data available at http://lbam.med.jhmi.edu/.

[4] The fmri data center (fmridc) at http://www.fmridc.org.

[5] Human imaging database available at http://nirlarc.duhs.duke.edu.

[6] International Consortium for Brain Mapping (ICBM): http://www.loni.ucla.edu/ICBM/.

[7] Internet Brain Segmentation Repository (IBSR) available at http://www.cma.mgh.harvard.edu/ibsr/.

[8] Laboratory of neuro imaging (loni), ucla at http://www.loni.ucla.edu/.

[9] mbirn data repository (mbdr) available at http://mbdr.nbirn.net/.

[10] Neuropsychiatric Imaging Research Laboratory, Departments of Psychiatry & Radiology at Duke University Medical Center: http://nirlweb.mc.duke.edu/.

[11] Neuroscience database gateway (ndg) at http://ndg.sfn.org/.

[12] Open access series of imaging studies (OASIS) available at http://www.oasis-brains.org/.

[13] Surgical Planning Laboratory at Brigham & Women's Hospital: http://www.spl.harvard.edu/.

[14] The Data Engineering Laboratory (DEnLab), Department of Computer and Information Sciences and the Center for Information Science and Technology at Temple University: http://denlab.temple.edu.

[15] The McConnell Brain Imaging Centre (BIC) at the Montreal Neurological Institute: http://www2.bic.mni.mcgill.ca/.

[16] R L Buckner, A Z Snyder, A L Sanders, M E Raichle, and J C Morris. Functional brain imaging of young, nondemented, and demented older adults. *J Cogn Neurosci*, 12 Suppl 2:24–34, 2000.

[17] Randy L Buckner, Denise Head, Jamie Parker, Anthony F Fotenos, Daniel Marcus, John C Morris, and Abraham Z Snyder. A unified approach for morphometric and functional data analysis in young, old, and demented adults using automated atlas-based head size normalization: reliability and validation against manual measurement of total intracranial volume. *Neuroimage*, 23(2):724–738, 2004 Oct.

[18] Chris A. Cocosco, Vasken Kollokian, Remi K. s. Kwan, and Alan C. Evans. Brainweb: Online interface to a 3d mri simulated brain database. *NeuroImage*, 5:425, 1997.

[19] D L Collins, A P Zijdenbos, V Kollokian, J G Sled, N J Kabani, C J Holmes, and A C Evans. Design and construction of a realistic digital brain phantom. *IEEE Trans Med Imaging*, 17(3):463–468, 1998 Jun.

[20] A. M. Dale and R. L. Buckner. Selective averaging of rapidly presented individual trials using fMRI. *Human brain mapping*, 5(5), 1997.

[21] R. O. Duda and P. E. Hart. *Pattern classification and scene analysis*. A Wiley-Interscience Publication, New York: Wiley, 1973, 1973.

[22] P. A. Filipek, C. Richelme, D. N. Kennedy, and V. S. Caviness. The young adult human brain: an mri-based morphometric analysis. *Cereb Cortex*, 4(4):344–360, 1994.

[23] P.A. Filipek, D.N. Kennedy, and V.S. Caviness. Volumetric analysis of central nervous system neoplasm based on mri. *Pediatric Neurology*, 7:347–351, 1991.

[24] A F Fotenos, A Z Snyder, L E Girton, J C Morris, and R L Buckner. Normative estimates of cross-sectional and longitudinal brain volume decline in aging and ad. *Neurology*, 64(6):1032–1039, 2005 Mar 22.

[25] Michael D Fox, Abraham Z Snyder, Justin L Vincent, Maurizio Corbetta, David C Van Essen, and Marcus E Raichle. The human brain is intrinsically organized into dynamic, anticorrelated functional networks. *Proc Natl Acad Sci U S A*, 102(27):9673–9678, 2005 Jul 5.

[26] Michael D. Fox, Abraham Z. Snyder, Justin L. Vincent, and Marcus E. Raichle. Intrinsic fluctuations within cortical systems account for intertrial variability in human behavior. *Neuron*, 56(1):171–184, October 2007.

[27] J. P. Gerring, K. D. Brady, A. Chen, C. B. Quinn, K. J. Bandeen-Roche, M. B. Denckla, and R. N. Bryan. Neuroimaging variables related to the development of secondary attention deficit hyperactivity disorder in children who have moderate and severe closed head injury. *Journal of the American Academy of Child and Adolescent Psychiatry*, 37:647–654, 1998.

[28] Craig K. Jones Seth A. Smith Jerry L. Prince Peter C.M. van Zijl Jonathan A.D Farrell, Bennett A. Landman and Susumu Mori. Effects of snr on the accuracy and reproducibility of dti-derived fractional anisotropy, mean diffusivity, and principal eigenvector measurements at 1.5t. *Journal of Magnetic Resonance Imaging*, 2007.

[29] D N Kennedy, P A Filipek, and V R Caviness. Anatomic segmentation and volumetric calculations in nuclear magnetic resonance imaging. *IEEE Trans Med Imaging*, 8(1):1–7, 1989.

[30] R K Kwan, A C Evans, and G B Pike. Mri simulation-based evaluation of image-processing and classification methods. *IEEE Trans Med Imaging*, 18(11):1085–1097, 1999 Nov.

[31] Bennett A Landman, Jonathan A D Farrell, Craig K Jones, Seth A Smith, Jerry L Prince, and Susumu Mori. Effects of diffusion weighting schemes on the reproducibility of dti-derived fractional anisotropy, mean diffusivity,

and principal eigenvector measurements at 1.5t. *Neuroimage*, 36(4):1123–1138, 2007 Jul 15.

[32] Daniel S Marcus, Tracy H Wang, Jamie Parker, John G Csernansky, John C Morris, and Randy L Buckner. Open access series of imaging studies (oasis): cross-sectional mri data in young, middle aged, nondemented, and demented older adults. *J Cogn Neurosci*, 19(9):1498–1507, 2007 Sep.

[33] V. Megalooikonomou, C. Davatzikos, and E. H. Herskovits. A simulator for evaluating methods for the detection of lesion-deficit associations. *Human Brain Mapping*, 10(2):61–73, 2000.

[34] F M Miezin, L Maccotta, J M Ollinger, S E Petersen, and R L Buckner. Characterizing the hemodynamic response: effects of presentation rate, sampling procedure, and the possibility of ordering brain activity based on relative timing. *NeuroImage*, 11(6 Pt 1):735–59, June 2000. PMID: 10860799.

[35] J C Morris. The clinical dementia rating (cdr): current version and scoring rules. *Neurology*, 43(11):2412–2414, 1993 Nov.

[36] J.C. Rajapakse and F. Kruggel. Segmentation of mr-images with intensity inhomogeneities. 16(3):165–180, March 1998.

[37] E H Rubin, M Storandt, J P Miller, D A Kinscherf, E A Grant, J C Morris, and L Berg. A prospective study of cognitive function and onset of dementia in cognitively healthy elders. *Archives of Neurology*, 55(3):395–401, March 1998. PMID: 9520014.

[38] Remi K. s. Kwan, Alan C. Evans, and G. Bruce Pike. An extensible mri simulator for post-processing evaluation. pages 135–140. Springer-Verlag, 1996.

[39] A.J. Saykin, L.A. Flashman, S.A. Frutiger, S.C. Johnson, A.C. Mamourian, C.H. Moritz, J.R. O'Jile, H.J. Riordan, R.B. Santulli, C.A. Smith, and J.B. Weaver. Neuroanatomic substrates of semantic memory impairment in alzheimer's disease: Patterns of functional mri activation. *Journal of the International Neuropsychological Society*, 5:377–392, 1999.

[40] Jean Talairach and Pierre Tournoux. *Co-planar Stereotaxic Atlas of the Human Brain*. 1988.

[41] Y Zhang, M Brady, and S Smith. Segmentation of brain mr images through a hidden markov random field model and the expectation-maximization algorithm. *IEEE Trans Med Imaging*, 20(1):45–57, 2001 Jan.

Machine Learning approach for Myotonic Dystrophy diagnostic support from MRI

Andone Sistiaga[a,c], Maite García-Sebastián[d], Alexandre Savio[d], Esther Fernández[b], Darya Chyzhyk[d], Fermín Moreno[c], Manuel Graña[d], Elsa Fernández[d], Jorge Villanúa[b], Adolfo López de Munain[a,c]

[a] *Departamento de Neurociencias, UPV/EHU*
[b] *Osatek Guipuzkoa*
[c] *Unidad Experimental del Hospital de Donostia*
[d] *Computational Intelligence Group UPV/EHU*

Abstract

In this paper we report the application of a Machine Learning approach to the diagnostic support of the Myotonic Dystrophy (MD) from structural Magnetic Resonance Imaging (sMRI). The approach consists of a feature extraction process based on the results of Voxel Based Morphometry (VBM) analysis of sMRI obtained from a set of patient and control subjects, followed by a classification step performed by Support Vector Machine (SVM) classifiers trained on the features extracted from the data set.
Key words: Myotonic Dystrophy, Support Vector Machines, Voxel Based Morphometry, MRI

1. Introduction

Nowadays, there is much research effort devoted to the development of ways to provide automatized diagnostic support tools that may help the clinicians to perform their work with additional assesment data and faster, to meet the ever increasing demands of primary attention of a rising population

of patients with neurological disorders. The present paper will be focused on the application of Machine Learning algorithms for the automatic detection of a very specific pathology, Myotonic Dystrophy of type 1 (MD1), from the analysis of MRI T1 weighted images. We describe a feature extraction method based on Voxel Based Morphology (VBM). These features will be the input for Support Vector Machine (SVM) classifiers. The volumetric study and conclusions will be reported elsewhere.

There are some antecedents on the use of Artificial Neural Networks (ANNs) and Voxel-Based Morphometry (VBM) for the detection of neurological disorders on sMRI data: AD detection has been reported in [22], where a single three-layer, feed-forward ANN trained with a backpropagation algorithm was used as a classifier over a small set of unpublished proprietary sMRI data. They perform data dimensionality reduction applying a PCA to improve the efficiency of the classifier. Also in [14] ANNs (multilayer perceptrons, polinomial nets and Kohonen LVQ classifiers) are used, but in this case they have analyzed three Diffussion weighted MR (DWI) images for the evaluation of cerebrospinal fluid (CSF) volume and its correlation with the advance of AD.

We have found in the literature several proposals on how to extract features from sMRI for classification using SVM: based on morphometric methods [12, 16, 46, 22], based on ROIs/VOIs (regions-of-interest/volumes-of-interest) [27, 26, 17] or grey matter (GM) voxels in automated segmentation images [24]. There are also studies aiming to explore the improvement obtained in the SVM classifier by adding covariates such as demographic or genotype information [43]. Work has also been reported on the selection of

a small set of the most informative features for classification, such as the SVM-Recursive Feature Elimination [16], the selection based on statistical tests [27, 37] or the wavelet decomposition of the RAVENS maps [26], among others. Our approach in this study is to use the VBM detected clusters of significant voxels as a mask over the original sMRI volume and GM segmentation images to select the potentially most discriminating voxels. Feature vectors for classification are either the voxel values or the second order statistics computed over the voxels of each cluster.

Section 2 presents the description of the Myotonic Dystrophy disease. Section 3 gives a summarized vision of the process followed in our approach. Section 4 describes the characteristics of the patients conforming the database for the study and methods. Section 5 gives a short review of SVMs. Section 6 describes the feature extraction process. Section 7 gives the results of our computational experiments. Section 7 gives our final comments and conclusions.

2. Myotonic Dystrophy

Myotonic Dystrophy (MD) is a neuromuscular disease characterised by the presence of varying degrees of muscle weakness and myotonia, as well as a plethora of extramuscular symptoms including the formation of cataracts. From a genetic point of view there are two types of MD: type 1, which involves mainly distal muscular atrophy and weakness (MD1); and type 2 (MD2), where there is no atrophy and a more proximal involvement. Here, we will only consider DM1 as this is the most common and best understood form.

With an incidence of 1 in 8000 cases and a prevalence of between 69 and 90 cases per million, DM1 is the most common neuromuscular disease in humans [15, 34]. However, its prevalence may be much higher in some locations, such as the Canadian population of Saguenay-Lac St Jean [5] and in the province of Guipúzcoa in the Spanish Basque Country [13]. Indeed, despite the availability of molecular diagnosis-based genetic counselling since 1993, the prevalence in Guipúzcoa has increased, particularly at the expense of oligosymptomatic carriers of this disease.

DM1 is transmitted by autosomal dominant inheritance, which means that the risk of transmission to offspring is 50%, with no gender-based differences in the risk of transmission. Furthermore, there is an anticipation phenomenon whereby the disease onset may be earlier in subsequent generations.

The molecular basis of DM1 is related to the expansion of a repetitive sequence of the CTG (Cytosine - Thymine - Guanine) triplet that may vary in length (5-35 repetitions) and that is stably transmitted across generations in normal individuals. However, in DM1 patients, the number of triplets increases to between 50 and up to 3000, and it displays unstable intergenerational transmission. This CTG triplet is located at the non-translated 3' end of the gene that codes for a protein kinase (DMPK) on the long-arm of chromosome 19 [6, 20]. The mechanism by which the pathological expansion produces the clinical symptoms involves translation of the CTG triplets into CUG-type residues, which induce the nuclear build-up of RNAs for various genes that affect the splicing process of numerous proteins, thereby explaining the multisystemic character of DM1's symptoms [41].

From a clinical point of view, DM1 is characterised by the presence of muscle weakness and myotonia and numerous extramuscular disorders, including heart conduction problems and endocrine, ophthalmological and central nervous system (CNS) disorders. The unusual molecular substrate of this disease results in considerable clinical variability, which explains the different DM1 classifications proposed in the literature[20].

- Minimum or partial DM1: Characterised mainly by the presence of cataracts, with no or very few neuromuscular symptoms, and an onset after 50 years of age. Patients usually carry an expansion of between 35 and 100 repeats that are unstably transmitted across generations.

- Classic or adult DM1: Myotonia and progressive weakness generally present during adult life. Between 100 and 900 repeats.

- Childhood DM1: Shares many of its symptoms with the congenital form, although these are not apparent at birth.

- Congenital DM1: Symptoms are present from birth or even in uterus. These include respiratory failure, hypotonia and retarded development. This form usually involves more than 1000 repeats. Cases with larger expansions are unstable in both the somatic and germ cells, which means that more repeats result in greater instability [30].

The clinical data available suggest that patients difficulties are focused on executive functions [23, 40], visuospatial/constructive abilities [28, 40], memory [39] and even on facial emotion recognition [44]. Although there is still no general consensus regarding the existence of DM1-related emotional and

personality disorders[7, 45], depression and anxiety [18], apathy [38] and avoidance[32] are features and symptoms most frequently associated with DM1. In addition, more than 50% of patients with classic DM1 are referred to therapy because of excessive daytime sleepiness [38, 36, 25].

Regarding neuroimaging studies, cortical atrophy, increased ventricular size with periventricular hypodensity and the involvement of the subcortical white matter, and calcification of the basal ganglia have been detected in a large proportion of DM1 patients by sMRI ([9, 11, 21]. Volumetric analyses based on these studies and using VBM, identified atrophy of the GM located mainly in the frontal and bilateral parietal lobes, the bilateral medial temporal gyrus and on the left side of the superior and occipital temporal [2]. There are also some studies that use diffusion tensor imaging (DTI) analyses in order to detect abnormalities associated with regional cortical atrophy [35]. They observe significantly lower fractional anisotropy and higher mean diffusivity values in the genu, rostral body, anterior midbody, posterior midbody and splenium in MyD patients than in control subjects.

Cortical atrophy has been reported in DM1 [9, 21, 4]. While performing the computational and statistical analyses reported in this paper, we observed that DM1 patients had a lower GM volume than the controls [2, 19], and that the patients had smaller white matter (WM) and larger CSF volumes than the controls. Observations about the distribution of total intracraneal volume (TIV) across patients and controls will be published elsewhere.

3. Summarized description of the process

Morphometry analysis has become a common tool for computational brain anatomy studies. It allows a comprehensive measurement of structural differences within or across groups, not only in specific structures but throughout the entire brain. Voxel-Based Morphometry (VBM) is a computational approach to neuroanatomy that measures differences in local concentrations of brain tissue, through a voxel-wise comparison of multiple brain images [3]. The procedure involves the spatial normalization of subject images into a standard space, segmentation of tissue classes using *a priori* probability maps, smoothing to correct noise and small variations, and voxel-wise statistical tests. Statistical analysis is based on the General Linear Model (GLM) to describe the data in terms of experimental and confounding effects, and residual variability. Classical statistical inference is used to test hypotheses that are expressed in terms of GLM estimated regression parameters. The computation of a given contrast provides a Statistical Parametric Map (SPM), which is thresholded according to the Random Field Theory. The result of the SPM analysis for VBM is the identification of clusters of voxels that show significant effects.

A flow chart of the whole detection process is shown in figures 1 and 2. The VBM process is illustrated in figure 1. The sMRI volumes are spatially normalized, then the GM is segmented, the resulting segmentation image is modulated to account for effects of the spatial normalization and smoothed, then the GLM is solved with a design matrix that may include some covariates besides the indicative variables, and, finally, statistical inference is applied to obtain the SPM and the clusters of significant voxels. The VBM is

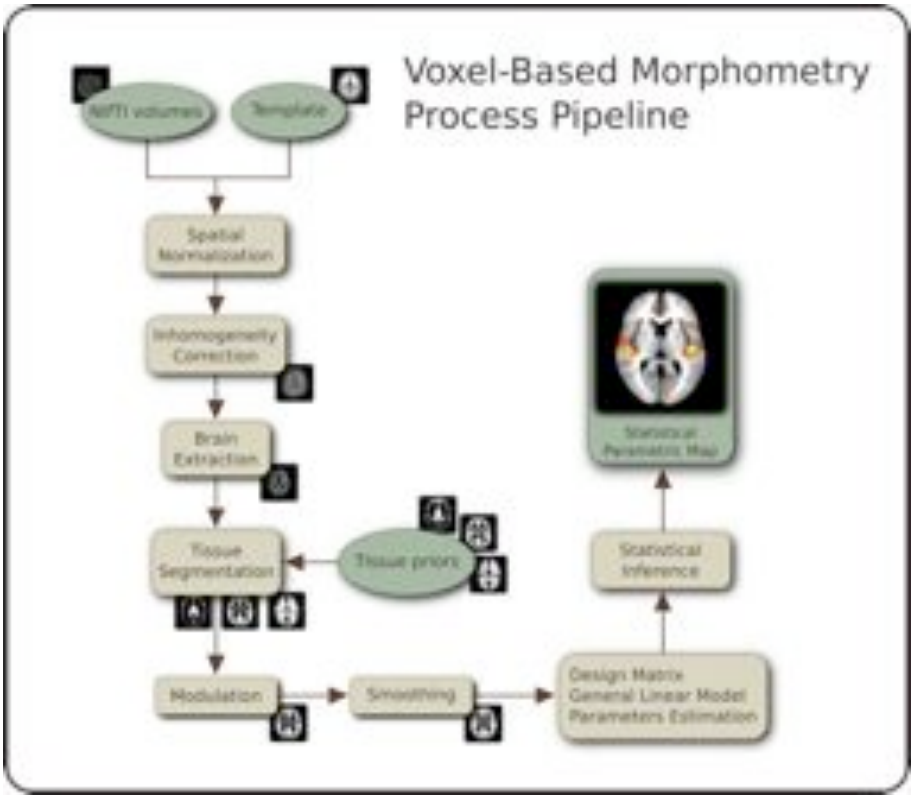

Figure 1: VBM flowchart

applied to the set of sMRI volumes used for the experiment. Figure 2 shows the global classification and validation process, wih the VBM represented by the box embedded in the figure. The loci of clusters of significant voxels are used to extract classification feature vectors which are used to train and validate the classification systems built with Machine Learning techniques, more precisely, with Support Vector Machines (SVM).

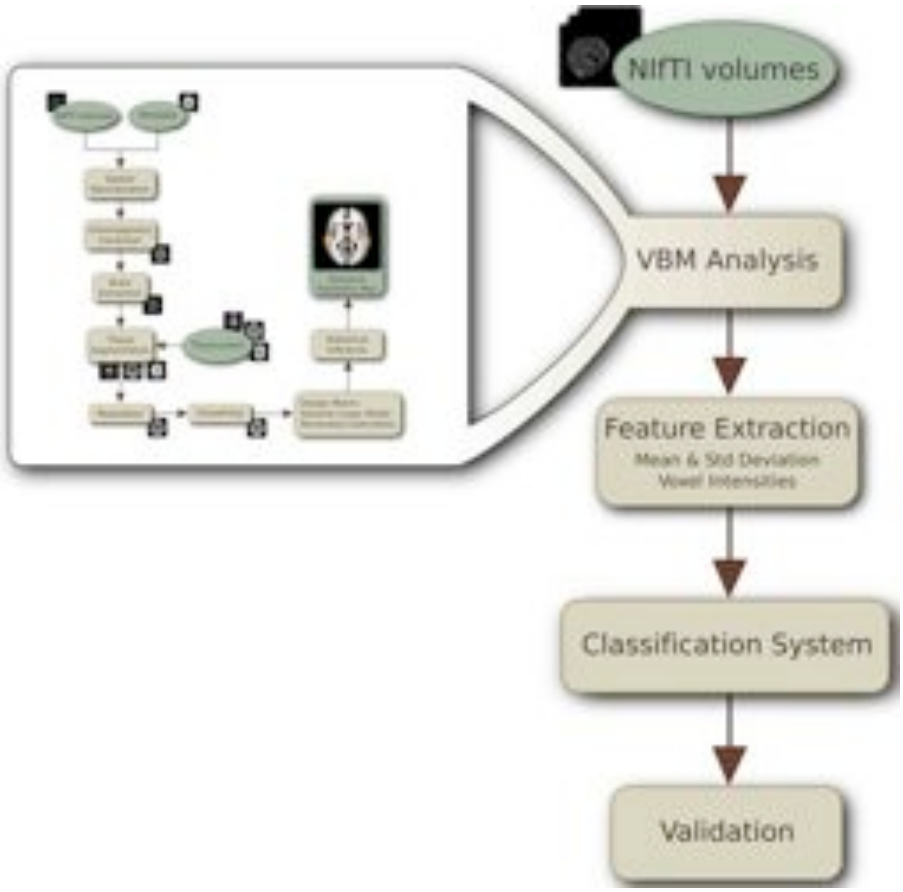

Figure 2: Whole process flowchart

4. Patients

The DM1 patients whose sMRI data is used in this work were selected from those attending the outpatient consultancies at the Neurology Department of the Donostia Hospital (San Sebastián). The patient-selection criteria were as follows:

- Inclusion criteria for DM1 patients: Between 18 and 65 years old and molecular confirmation of the clinical diagnosis.

- Exclusion criteria: A history of a major psychiatric or somatic disorder (in accordance with DSM-IV criteria), acquired brain damage or alcohol or drug abuse, and the presence of cerebral anomalies which could affect the volumetric analysis (fig. 3)

MR scanning was performed on a 1.5 Tesla scanner (Achieva Nova, Philips). The current results are based on a high-resolution volumetric "turbo field echo" (TFE) series (axial T1 weighted acquisition, TR = 25, TE = 4.6, flip angle = 8, matrix = 240 x 240, voxel dimensions of 1mm x 1mm x 1mm slice thickness).

A healthy control matched in terms of age and sex was included for each of the DM1 patients included. This control group consisted of unaffected family members and healthy volunteers with none of these pathologies. All patients were informed of the objectives and details of the study and signed an informed consent. The study was approved by the hospital's ethics committee. The socio-demographic characteristics and main symptoms of the subjects included in this study are listed in Table 1.

Variables		DM1 N=30	CONTROL DM1 N=30
Socio-demographic characteristics			
Age	Mean (SD)	44.0 (11.6)	44.2 (11.7)
	Min-Max	24-62	22-62
Sex n (%)	Male	14 (47%)	14 (47%)
	Female	16 (53%)	16 (53%)
Educational level n (%)	Primary	18 (60%)	5 (21%)
	Secondary	7 (23%)	9 (37%)
	Higher	5 (17%)	10 (41%)
Clinical and molecular characteristics			
Muscle weakness (MIRS1)	Mean (SD)		
	Min-Max	0-5	
Molecular defect (CTG)	Mean (SD)	635 (472)	
	Min-Max	65-1833	
White matter lesions3	Yes	16 (53%)	5 (18%)
	No	14 (47%)	22 (82%)

Table 1: Socio-demographic, clinical, molecular and radiological characteristics by group. 1 Muscular Impairment Rating Scale [31]. 3 White matter lesions were quantified using the Mirsen scale [33]. * p is the estimate of X2.

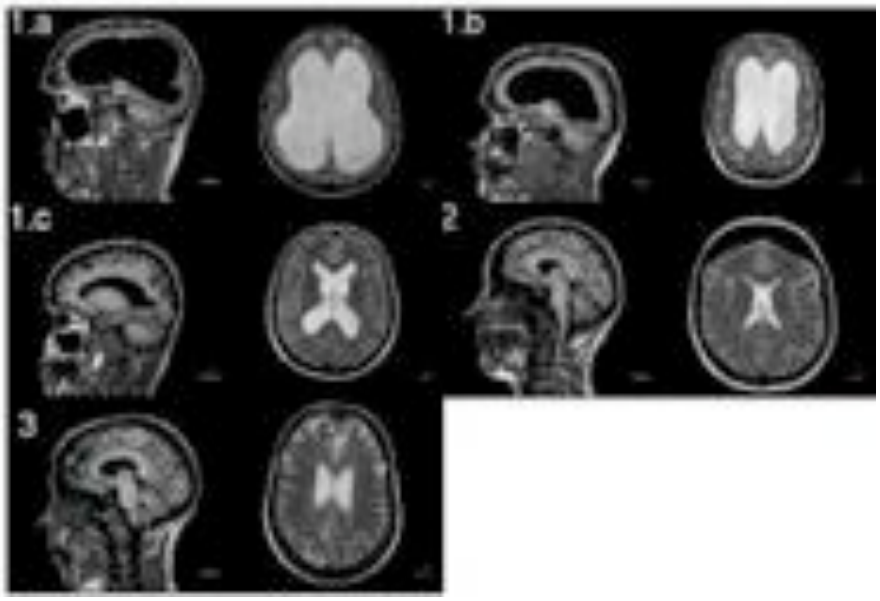

Figure 3: DM1 patients excluded from the study: sagittal T1 and transversal T2 images. 1.a. and 1.b. Grade 5 ventricular dilation (44-year-old male with 333 CTG and 41-year-old female with 667 CTG respectively), 1.c. grade 3 ventricular dilation (28-year-old female with 500 CTG), 2. Frontal hyperostosis (36-year-old female with 400 CTG) and 3. Frontal calcification (38-year-old female with 833 CTG).

5. Support Vector Machines

The Support Vector Machine (SVM) [42] algorithm used for this study is included in the libSVM (http://www.csie.ntu.edu.tw/ cjlin/libsvm/) software package. The implementation is described in detail in [10]. Given training vectors $\mathbf{x}_i \in \mathbb{R}^n,\ i = 1, \ldots, l$ of the subject features of the two classes, and a vector $\mathbf{y} \in \mathbb{R}^l$ such that $y_i \in \{-1, 1\}$ labels each subject with its class, in our case, for example, patients were labeled as -1 and control subject as 1. To construct a classifier, the SVM algorithm solves the following optimization problem:

$$\min_{\mathbf{w},b,\boldsymbol{\xi}} \frac{1}{2}\mathbf{w}^T\mathbf{w} + C\sum_{i=1}^{l}\xi_i,$$

subject to

$$y_i(\mathbf{w}^T\phi(\mathbf{x}_i) + b) \geq (1 - \xi_i),\ \xi_i \geq 0,\ i = 1, 2, \ldots, n.$$

The dual optimization problem is:

$$\min_{\alpha} \frac{1}{2}\alpha^T Q\alpha - e^T\alpha,$$

subject to

$$\mathbf{y}^T\alpha = 0,\ 0 \leq \alpha_i \leq C,\ i = 1, \ldots, l.$$

Where e is the vector of all ones, $C > 0$ is the upper bound on the error, Q is an l by l positive semidefinite matrix:

$$Q_{ij} \equiv y_i y_j K(\mathbf{x}_i, \mathbf{x}_j),$$

and

$$K(\mathbf{x}_i, \mathbf{x}_j) \equiv \phi(\mathbf{x}_i)^T \phi(\mathbf{x}_j),$$

is the kernel function that describes the behavior of the support vectors. Here, the training vectors x_i are mapped into a higher (maybe infinite) dimensional space by the function $\phi(\mathbf{x}_i)$. The decision function is:

$$sgn(\sum_{i=1}^{l} y_i \alpha_i K(\mathbf{x}_i, \mathbf{x}) + b).$$

The regularization parameter C is used to balance the model complexity and the training error. It was always set to 1.

The chosen kernel function results in different kinds of SVM with different performance levels, and the choice of the appropriate kernel for a specific application is a difficult task. In this study we have worked with the radial basis function (RBF) kernel defined as:

$$K(\mathbf{x}_i, \mathbf{x}_j) = exp\left(-\frac{||\mathbf{x}_i - \mathbf{x}_j||^2}{2\sigma^2}\right).$$

This kernel is basically suited best to deal with data that have a class-conditional probability distribution function approaching the Gaussian distribution [8]. One of the advantages of the RBF kernel is that given a kernel, the number of support vectors and the support vectors are all automatically obtained as part of the training procedure, i.e., they do not need to be specified by the training mechanism.

6. Feature extraction

We have tested two different feature extraction processes, based on the voxel location clusters obtained from the VBM analysis:

1. The first feature extraction process computes the mean and standard deviation of the GM voxel intensity values of each voxel location cluster.
2. The second feature extraction process computes a very high dimensional vector with all the GM segmentation values for the voxel locations included in each VBM detected cluster. The GM segmentation voxel values were ordered in this feature vector according to the coordinate lexicographic order.

We denote these features as MSD and VV, respectively in the result tables below.

We have illustrated the VBM pipeline in figure 1. To perform the VBM analysis we have used the average MRI volume for each subject. These images are already registered and re-sampled into a 1-mm isotropic image in atlas space and the bias field has been already corrected [29]. The Statistical Parametric Mapping (SPM8) [1] was used to compute the VBM which gives us the spatial mask to obtain the classification features. A bias correction step has been performed with the tissued segmentation step and also a modulation normalization for GM, because we are interested in this tissue for this study. We performed a spatial smoothing before executing the voxel-wise statistics, exploring the Full-Width at Half-Maximum (FWHM) of the Gaussian kernel in a range from 8mm up to 12mm isotropic. A GM mask was created from the average of the GM segmentation volumes of the subjects

under study. Thresholding the average GM segmentation, we obtain a binary mask that includes all voxels with probability greater than 0.1 in the average GM segmentation volume. This interpretation is not completely true, since the data is modulated, but it is close enough for the mask to be reasonable. We designed the statistical analysis both as a Two-sample t-test and as two-sided F-test, in which the first group corresponds with DM subjects. In SPM software terms: the contrast has been set to [-1 1], a right-tailed (groupN $>$ groupAD), correction FWE, p-value=0.05. The VBM detected clusters are used for the feature extraction for the classification procedures.

7. Results

As measures of classifier performance we use the classification accuracy, sensitivity and specificity. Al the results reported below are obtained through a ten fold crossvalidation process, repeated ten times.

In general, the Voxel-Based Morphometry (VBM) identified differences in GM volume both in the cortex and in subcortical areas. Figure 4 shows the clusters detected with a FWHM size of 8mm, and a 0 threshold on cluster size, localized over the GM template obtained from the collection of images in the database. These clusters provide the features which give one of the best results in the classification validation process.

SPM showed differences between patients and controls throughout practically the entire cortex, particularly in the frontal lobe and bilateral parietal. A smaller volume of the occipital lobe and bilateral cerebellum in the patients was also seen. The subcortical basal ganglia, specifically the left caudate and bilateral thalamus, had a smaller volume in DM1 patients than in controls.

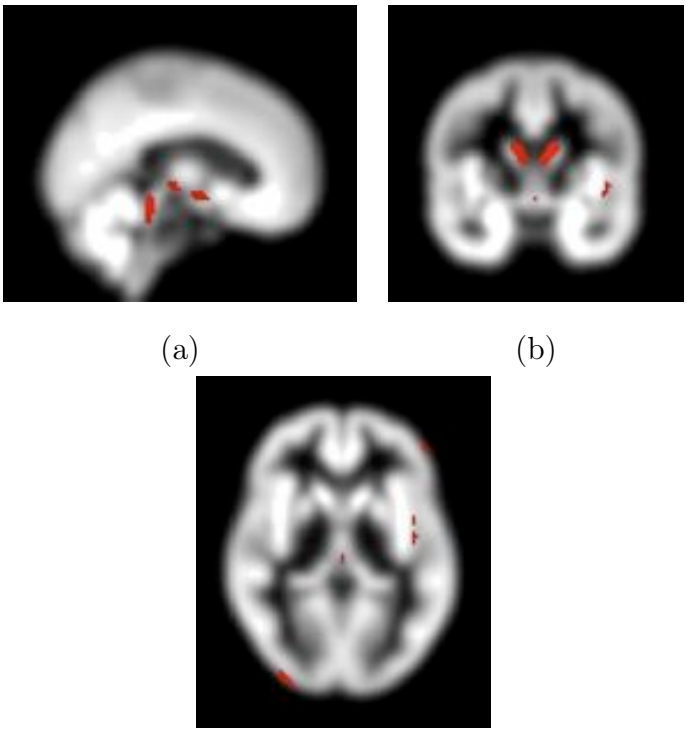

(a) (b)

(c)

Figure 4: SPM results shown as the most significative VBM clusters superimposed on the GM averaged image (obtained from subjects under study, 8 mm isotropic Gaussian FWHM kernel).

FWHM	Th	#fea	acc	sen	spec
8	0	76	78.3%	73.3%	83.3%
	100	8	76.7%	66.7%	86.7%
	200	4	76.7%	66.7%	86.7%
9	0	76	80.0%	70.0%	90.0%
	100	16	75.0%	66.7%	83.3%
	200	4	76.7%	66.7%	86.7%
10	0	70	78.3%	63.3%	93.3%
	100	22	76.7%	73.3%	80.0%
	200	8	78.3%	70.0%	86.7%
11	0	64	71.7%	63.3%	80.0%
	100	24	75.0%	63.3%	86.7%
	200	12	75.0%	63.3%	86.7%
12	0	68	71.6%	63.,3%	80%
	100	36	73.3%	63.3%	83.3%
	200	18	75%	70%	80%

Table 2: SVM classification results (10-fold crossvalidation) for MSD features, based on t-test VBM of the data, FWE=0.05

FWHM	th	#fea	acc	sen	spec
8	0	2059	81.7%	83.3%	80.0%
	100	1226	78.3%	70.0%	86.7%
	200	958	80.0%	80.0%	76.7%
9	0	2826	78.3%	73.3%	83.0%
	100	2044	76.7%	73.3%	80.0%
	200	1182	75.0%	66.7%	83.3%
10	0	3710	76.7%	73.3%	80.0%
	100	3103	80.0%	76.7%	83.3%
	200	2131	73.3%	70.0%	76.7%
11	0	5022	73.3%	73.3%	73.3%
	100	4278	78.3%	73.3%	83.3%
	200	3434	75.0%	70.0%	80.0%
12	0	6542	76.6%	73.3%	80%
	100	6391	75%	70%	80%
	200	5148	73.3%	70%	76.6%

Table 3: SVM classification results (10-fold crossvalidation) for VV features, based on t-test VBM of the data, FWE=0.05

FWHM	Th	#fea	acc	sen	spec
8	0	52	76.7%	70.0%	83.3%
	100	4	78.3%	70.0%	86.7%
	200	4	80.0%	73.3%	86.7%
9	0	48	78.3%	70.0%	86.7%
	100	8	75.0%	63.3%	86.7%
	200	4	73.3%	60.0%	86.7%
10	0	52	75.0%	63.3%	86.7%
	100	10	73.3%	63.3%	83.3%
	200	4	75.0%	63.3%	86.7%
11	0	58	76.7%	70.0%	83.3%
	100	12	80.0%	66.7%	93.3%
	200	2	78.3%	70.0%	86.7%
12	0	56	73.3%	63.3%	83.3%
	100	18	76.7%	66.7%	86.7%
	200	6	76.7%	63.3%	90.0%

Table 4: SVM classification results (10-fold crossvalidation) for MSD features, based on F-test VBM of the data, FWE=0.05

FWHM	th	#fea	acc	sen	spec
8	0	1293	78.3%	76.7%	80.0%
	100	769	76.7%	73.3%	80.0%
	200	769	76.7%	70.0%	83.3%
9	0	1665	80.0%	80.0%	80.0%
	100	1155	78.3%	70.0%	86.7%
	200	930	81.7%	80.0%	83.3%
10	0	2128	76.7%	73.3%	80.0%
	100	1481	75.0%	70.0%	80.0%
	200	1090	76.7%	70.0%	83.3%
11	0	2733	71.7%	66.7%	76.7%
	100	2050	75.0%	70.0%	80.0%
	200	1269	75.0%	70.0%	80.0%
12	0	3465	75.0%	70.0%	80.0%
	100	2887	75.0%	70.0%	80.0%
	200	2082	73.3%	66.7%	80.0%

Table 5: SVM classification results (10-fold crossvalidation) for VV features, based on F-test VBM of the data, FWE=0.05

We have performed a set of computational experiments consisting in performing a FWE=0.05 VBM on the subjects to obtain the features varying the smoothing parameter FWHM, and the threshold (th) on the size of the detected cluster. Then we performed a 10-fold crossvalidation with SVM classifiers, searching exhaustively for the optimal value of the RBF kernel parameter γ. The results of these experiments are displayed in tables 2, 3, 4 and 5. The results using the MSD features are given in tables 2 and 4, while the results obtained from VV features are given in tables 3 and 5. The results corresponding to the t-test VBM are in tables 2 and 3, while the results corresponding to the F-test VBM are in tables 4 and 5. The best results obtained are similar for the t-test and F-test, they are obtained from the VV features extracted according to VBM with relatively low smoothing. We have found relatively different VBM settings giving similar results (around 80% accuracy), whose careful study deserve further attention. In general sensitivity is lower than specificity. This may be due to the cases that are in the early stades of the disease, but that are included in the study because of the molecular test that identifies them as DM1 patients. The cases have not yet greatly developed the atrophy patterns and are confused with the controls.

Conclusions

We report in this paper the application of SVM with a RBF kernel to the problem of classifying MD1 patients from controls, on the basis of classification features obtained from the masks defined by the significative clusters detected by VBM analysis. We have performed an exhaustive computational

exploration varying the FWMH and the cluster size threshold parameters. The classification results obtained were not very optimistic, and we are still pursuing reasearch applying more powerful classifiers and defining new feature vectors. However we have found some interesting results regarding the qualitative evaluation of the VBM results performed by expert neurologists. To determine that there is an effect, neurologist need to observe big effects, obtained under big smoothing parameters, i.e FWMH=12, however, our best automated classification resuls are provided by relatively "sharp" images, obtained with lower smoothing kernel sizes. Stronger smoothing introduces more confusion and decreases the classifier performance. We have not detected influence of the kind of statistical inference test used (t-test or F-test). Also, although the the VV features have slightly better results, we can not conclude that they are much better features than the second order statistics (MSD) from the voxels in the detected clusters.

References

[1] Statistical Parametric Mapping available at http://www.fil.ion.ucl.ac.uk/spm/.

[2] G. Antonini, C. Mainero, A. Romano, F. Giubilei, V. Ceschin, F. Gragnani, S. Morino, M. Fiorelli, F. Soscia, P. Di, and F. Caramia. Cerebral atrophy in myotonic dystrophy: a voxel based morphometric study. *Journal of Neurology, Neurosurgery, and Psychiatry*, 75(11):1611–1613, November 2004. PMCID: PMC1738796.

[3] J. Ashburner and K. Friston. Voxel-Based Morphometry–The methods. *Neuroimage*, 11(6):805–821, 2000.

[4] G. Bachmann, M. S. Damian, M. Koch, G. Schilling, B. Fach, and S. Stöppler. The clinical and genetic correlates of MRI findings in myotonic dystrophy. *Neuroradiology*, 38(7):629–635, October 1996.

[5] G. Bouchard, R. Roy, M. Declos, J. Mathieu, and K. Kouladjian. Origin and diffusion of the myotonic dystrophy gene in the saguenay region (Quebec). *The Canadian journal of neurological sciences. Le journal canadien des sciences neurologiques*, 16(1):119–122, 1989.

[6] J D Brook, M E McCurrach, H G Harley, A J Buckler, D Church, H Aburatani, K Hunter, V P Stanton, J P Thirion, and T Hudson. Molecular basis of myotonic dystrophy: expansion of a trinucleotide (CTG) repeat at the 3' end of a transcript encoding a protein kinase family member. *Cell*, 68(4):799–808, February 1992.

[7] C. Bungener, R. Jouvent, and C. Delaporte. Psychopathological and emotional deficits in myotonic dystrophy. *Journal of Neurology, Neurosurgery, and Psychiatry*, 65(3):353–356, 1998.

[8] C. Burges. A tutorial on Support Vector Machines for pattern recognition. *Data Mining and Knowledge Discovery*, 2(2):121–167, 1998.

[9] B Censori, L Provinciali, M Danni, L Chiaramoni, M Maricotti, N Foschi, M Del Pesce, and U Salvolini. Brain involvement in myotonic dystrophy: MRI features and their relationship to clinical and cognitive

conditions. *Acta Neurologica Scandinavica*, 90(3):211–217, September 1994. PMID: 7847063.

[10] C.-C. Chang and C.-J. Lin. LIBSVM: a library for Support Vector Machines available at http://www.csie.ntu.edu.tw/ cjlin/libsvm/. 2001.

[11] M. S. Damian, G. Schilling, G. Bachmann, C. Simon, S. Stöppler, and W. Dorndorf. White matter lesions and cognitive deficits: relevance of lesion pattern? *Acta Neurologica Scandinavica*, 90(6):430–436, 1994.

[12] C. Davatzikos, Y. Fan, X. Wu, D. Shen, and S.M. Resnick. Detection of prodromal alzheimer's disease via pattern classification of magnetic resonance imaging. *Neurobiol Aging*, 29(4):514–523, Apr 2008.

[13] A. Lopez de Munain, A. Blanco, J. I. Emparanza, J. J. Poza, J. F. Marti Masso, A. Cobo, L. Martorell, M. Baiget, and J. M. Martinez Lage. Prevalence of myotonic dystrophy in guipuzcoa (Basque country, spain). *Neurology*, 43(8):1573, August 1993.

[14] W.P. dos Santos, R.E. de Souza, A.F.D. e Silva, and P.B. Santos Filho. Evaluation of Alzheimer's disease by analysis of MR images using Multilayer Perceptrons, Polynomial Nets and Kohonen LVQ classifiers. *Computer Vision/Computer Graphics Collaboration Techniques*, pages 12–22, 2007.

[15] A E Emery. Population frequencies of inherited neuromuscular diseases–a world survey. *Neuromuscular Disorders: NMD*, 1(1):19–29, 1991.

[16] Y. Fan, D. Shen, and C. Davatzikos. Classification of structural images via high-dimensional image warping, robust feature extraction, and

SVM. *Med Image Comput Comput Assist Interv Int Conf Med Image Comput Comput Assist Interv*, 8(Pt 1):1–8, 2005.

[17] G. Fung and J. Stoeckel. SVM feature selection for classification of SPECT images of Alzheimer's disease using spatial information. *Knowl. Inf. Syst.*, 11(2):243–258, 2007.

[18] G. G. Antonini, F. Soscia, F. Giubilei, A. De Carolis, F. Gragnani, S. Morino, A. Ruberto, and R. Tatarelli. Health-related quality of life in myotonic dystrophy type 1 and its relationship with cognitive and emotional functioning. *Journal of Rehabilitation Medicine*, 38(3):181–185, 2006.

[19] Antonio Giorgio, Maria T. Dotti, Marco Battaglini, Silvia Marino, Marzia Mortilla, Maria L. Stromillo, Placido Bramanti, Alfredo Orrico, Antonio Federico, and Nicola De Stefano. Cortical damage in brains of patients with adult-form of myotonic dystrophy type 1 and no or minimal MRI abnormalities. *Journal of Neurology*, 253(11):1471–1477, November 2006.

[20] H. G. Harley, Rundle S. A., J. C. Myring, and J. Brook. Size of the unstable ctg repeat sequence in relation to phenotype and parental transmission in myotonic dystrophy. *Am.J.Hum.Genet.*, 52:1164–1174, 1993.

[21] T. Hashimoto, M. Tayama, M. Miyazaki, K. Murakawa, H. Kawai, H. Nishitani, and Y. Kuroda. Neuroimaging study of myotonic dystrophy. II. MRI measurements of the brain. *Brain and Development*, 17(1):28–32, 1995.

[22] C. Huang, B. Yan, H. Jiang, and D. Wang. Combining Voxel-Based Morphometry with Artifical Neural Network theory in the application research of diagnosing Alzheimer's disease. In *BMEI '08: Proceedings of the 2008 International Conference on BioMedical Engineering and Informatics*, pages 250–254, Washington, DC, USA, 2008. IEEE Computer Society.

[23] A. Hunter, C. Tsilfidis, G. Mettler, P. Jacob, M. Mahadevan, L. Surh, and R. Korneluk. The correlation of age of onset with CTG trinucleotide repeat amplification in myotonic dystrophy. *Journal of Medical Genetics*, 29(11):774–779, 1992.

[24] S. Kloppel. Automatic classification of MR scans in Alzheimer's disease. *Brain*, 131(3):681–689, 2008.

[25] L. Laberge, P. Bégin, J. Montplaisir, and J. Mathieu. Sleep complaints in patients with myotonic dystrophy. *Journal of Sleep Research*, 13(1):95–100, 2004.

[26] Z. Lao, D. Shen, Z. Xue, B. Karacali, S.M. Resnick, and C. Davatzikos. Morphological classification of brains via high-dimensional shape transformations and machine learning methods. *NeuroImage*, 21(1):46–57, Jan 2004.

[27] Y. Liu, L. Teverovskiy, O. Carmichael, R. Kikinis, M. Shenton, C.S. Carter, V.A. Stenger, S. Davis, H. Aizenstein, J.T. Becker, O.L. Lopez, and C.C. Meltzer. Discriminative MR image feature analysis for automatic schizophrenia and Alzheimer's disease classification. *Medi-*

cal Image Computing and Computer-Assisted Intervention (MICCAI), 3216:393–401, 2004.

[28] P. Malloy, S. K. Mishra, and S. H. Adler. Neuropsychological deficits in myotonic muscular dystrophy. *Journal of Neurology, Neurosurgery, and Psychiatry*, 53(11):1011–1013, 1990.

[29] D.S. Marcus, T.H. Wang, J. Parker, J.G. Csernansky, J.C. Morris, and R.L. Buckner. Open Access Series of Imaging Studies (OASIS): cross-sectional MRI data in young, middle aged, nondemented, and demented older adults. *J. Cognitive Neuroscience*, 19(9):1498–1507, 2007.

[30] L. Martorell, G Monckton D., and Gamez J. Progression of somatic CTG repeat length heterogeneity in the blood cells of myotonic dystrophy patients – martorell et al. 7 (2): 307 – human molecular genetics. *Hum.Mol.Genet.*, 7:307–312, 1998.

[31] J. Mathieu, H. Boivin, D. Meunier, M. Gaudreault, and P. Begin. Assessment of a disease-specific muscular impairment rating scale in myotonic dystrophy. *Neurology*, 56(3):336–340, 2001.

[32] G. Meola, V. Sansone, D. Perani, S. Scarone, S. Cappa, C. Dragoni, E. Cattaneo, M. Cotelli, C. Gobbo, F. Fazio, et al. Executive dysfunction and avoidant personality trait in myotonic dystrophy type 1 (DM-1) and in proximal myotonic myopathy (PROMM/DM-2). *Neuromuscular Disorders*, 13(10):813–821, 2003.

[33] Thomas R. Mirsen, Donald H. Lee, Cindy J. Wong, J. Fernando Diaz, Allan J. Fox, Vladimir C. Hachinski, and Harold Merskey. Clinical

correlates of White-Matter changes on magnetic resonance imaging scans of the brain. *Arch Neurol*, 48(10):1015–1021, October 1991.

[34] M. L. Mostacciuolo, G. Barbujani, M. Armani, G. A. Danieli, C. Angelini, and D. C. Rao. Genetic epidemiology of myotonic dystrophy. *Genetic Epidemiology*, 4(4):289–298, 1987.

[35] Miho Ota, Noriko Sato, Yasushi Ohya, Yoshitsugu Aoki, Katsuyoshi Mizukami, Takeyuki Mori, and Takashi Asada. Relationship between diffusion tensor imaging and brain morphology in patients with myotonic dystrophy. *Neuroscience Letters*, 407(3):234–239, October 2006.

[36] M. F. Phillips, H. M. Steer, J. R. Soldan, C. M. Wiles, and P. S. Harper. Daytime somnolence in myotonic dystrophy. *Journal of neurology*, 246(4):275–282, 1999.

[37] J. Ramírez, M. Górriz, M. López, D. Salas-González, I. Álvarez, F. Segovia, and C.G. Puntonet. Early detection of the Alzheimer disease combining feature selection and kernel machines. *International Conference on Neural Information Processing of the Asia-Pacific Neural Network Assembly (ICONIP)*, 2:410–417, 2008.

[38] J. S. Rubinsztein, D. C. Rubinsztein, S. Goodburn, and A. J. Holland. Apathy and hypersomnia are common features of myotonic dystrophy. *Journal of neurology, neurosurgery, and psychiatry*, 64(4):510–515, 1998.

[39] J. S. Rubinsztein, D. C. Rubinsztein, P. J. McKenna, S. Goodburn, and A. J. Holland. Mild myotonic dystrophy is associated with memory

impairment in the context of normal general intelligence. *Journal of medical genetics*, 34(3):229–233, 1997.

[40] A. Sistiaga, I. Urreta, M. Jodar, A. M. Cobo, J. Emparanza, D. Otaegui, J. J. Poza, J. J. Merino, H. Imaz, J. F.Martí-Massó, et al. Cognitive/personality pattern and triplet expansion size in adult myotonic dystrophy type 1 (dm1): Ctg repeats, cognition and personality in dm1. *Psychological medicine*, page 1, 2009.

[41] L. T. Timchenko, J. W. Miller, N. A. Timchenko, D. R. DeVore, K. V. Datar, L. Lin, R. Roberts, C. T. Caskey, and M. S. Swanson. Identification of a (CUG) n triplet repeat RNA-binding protein and its expression in myotonic dystrophy. *Nucleic acids research*, 24(22):4407–4414, 1996.

[42] V. Vapnik. *Statistical learning theory*. Wiley-Interscience, 1998.

[43] P. Vemuri, J.L. Gunter, M.L. Senjem, J.L. Whitwell, K. Kantarci, D.S. Knopman, B.F. Boeve, R.C. Petersen, and C.R. Jack. Alzheimer's disease diagnosis in individual subjects using structural MR images: validation studies. *NeuroImage*, 39(3):1186–1197, Feb 2008.

[44] S. Winblad, P. Hellstrom, C. Lindberg, and S. Hansen. Facial emotion recognition in myotonic dystrophy type 1 correlates with CTG repeat expansion. *Journal of neurology, neurosurgery, and psychiatry*, 77(2):219–223, 2006.

[45] S. Winblad, C. Lindberg, and S. Hansen. Temperament and character in patients with classical myotonic dystrophy type 1 (DM-1). *Neuromuscular Disorders*, 15(4):287–292, 2005.

[46] J. Zhang, B. Yan, X. Huang, P. Yang, and C. Huang. The diagnosis of Alzheimer's disease based on Voxel-Based Morphometry and Support Vector Machine. In *Proceedings of the 2008 Fourth International Conference on Natural Computation (ICNC)*, pages 197–201, Washington, DC, USA, 2008. IEEE Computer Society.

Lattice Independent Component Analysis for fMRI

Manuel Graña, Darya Chyzhyk, Maite García-Sebastián, Carmen Hernández

Computational Intelligence Group
Dept. CCIA, UPV/EHU, Apdo. 649, 20080 San Sebastian, Spain
www.ehu.es/ccwintco

Abstract

We introduce a Lattice Independent Component Analysis (LICA) approach to fMRI analysis based on an Incremental Lattice Source Induction Algorithm (ILSIA). The ILSIA is grounded in recent theoretical results on Lattice Associative Memories (LAM). It aims to select a set of Strong Lattice Independent (SLI) vectors from the input dataset. Those SLI vectors can be assumed to be an Affine Independent set of vectors which define a convex polytope on the input data space. We call them *lattice sources*. They are used to compute the linear unmixing of each voxel's time series independently. The resulting mixing coefficients roughly correspond to the Independent Component Analysis (ICA) mixing matrix, while the set of lattice sources corresponds to the statistically independent sources found by ICA. The proposed approach is unsupervised or model free because the design matrix containing the regressors is not fixed *a priori* but induced from the data. Our approach does not impose any probabilistic model on the searched sources, although we assume a linear mixture model. We show on simulated fMRI data that our approach can discover the meaningful sources with efficiency comparable to that of ICA. Besides, on a well-known case study our approach can discover activation patterns in good agreement with the state of the art Statistical Parametric Mapping (SPM) software, and some state of the art ICA variants.

Key words: Lattice Independence, Lattice Associative Memories, fMRI, Independent Component Analysis

1. Introduction

Human brain mapping is a rapidly expanding discipline, and in recent years interest has grown in novel methods for imaging human brain functionality. Noninvasive techniques can measure cerebral physiologic responses during neural activation. One of the relevant techniques is functional Magnetic Resonance Imaging (fMRI) [18], which uses the blood oxygenation level dependent (BOLD) contrast to detect physiological alterations, such as neuronal activation resulting in changes of blood flow and blood oxygenation. The signal changes are related to changes in the concentration of deoxyhemoglobin, which acts as an intravascular contrast agent for fMRI. Most of the fMRI examinations are performed using T2 weighted spin echo pulse sequences or T2* weighted gradient echo pulse sequences. The various fMRI-methods have a good

spatial and temporal resolution, limited only by the precision with which the autoregulatory mechanisms of the brain adjust blood flow in space to the metabolic demands of neuronal activity. Since these methods are completely noninvasive, using no contrast agent or ionizing radiation, repeated single-subject studies are becoming feasible [17].

An fMRI experiment consists of a functional template or protocol (e.g., alternating activation and rest for a certain time) that induces a functional response in the brain. The aim of the experiment is to detect the response to this time varying stimulus, through the examination of the signal resulting from the BOLD effect, in a defined volume element (voxel). The functional information of a voxel has to be extracted from its time series. One fMRI volume is recorded at each sampling time instant during the experiment. The time sampling frequency is determined by the resolution of the fMRI imaging pulse sequence. The complete four-dimensional dataset (three dimensions in space, one dimension in time) consists of subsequently recorded three-dimensional (3-D) volumes. The acquisition of these functional volumes runs over periods lasting up to several minutes.

The most extended analysis approach for fMRI signals is the Statistical Parametric Maps (SPM) [6, 5], which has evolved into a free software package. This method consists in the separate voxel estimation of the regression parameters of General Linear Model (GLM), whose design matrix has been built corresponding to the experimental design. A contrast is then defined on the estimated regression parameters, which can take the form of a t-test or an F-test. The theory of Random Fields is then applied to correct the test thresholds, taking into account the spatial correlation of the independent test results.

There have been also approaches to the fMRI analysis based on the Independent Component Analysis (ICA) [3] assuming that the time series observations are linear mixtures of independent sources which can not be observed. ICA assumes that the source signals are non-Gaussian and that the linear mixing process is unknown. The approaches to solve the ICA problem obtain both the independent sources and the linear unmixing matrix. These approaches are unsupervised because no *a priori* information about the sources or the mixing process is included, hence the alternative name of Blind Deconvolution.

In this paper we propose an approach that we call Lattice Independent Component Analysis (LICA) that consists of two steps. Firts it selects Strong Lattice Independent (SLI) vectors from the input dataset using an incremental algorithm, the Incremental Lattice Source Induction Algorithm (ILSIA). Second, because of the conjectured equivalence between SLI and Affine Independence, it performs the linear unmixing of the input dataset based on these lattice sources. Therefore, the approach is a mixture of linear and nonlinear methods.

The original works were devoted to unsupervised hyperspectral image segmentation, therefore the use of the term *endmembers* for the selected vectors in previous works, however we find more appropriate the term *lattice source*. We maintain the basic assumption that the data is generated as a convex combination of a set of lattice sources which are the vertices of a convex polytope covering some region of the input data. This assumption is similar to the linear mixture assumed by the ICA approach, however we do not impose any probabilistic assumption on the data. The lattice sources discovered by the ILSIA are equivalent to the GLM design matrix columns, and the

unmixing process is identical to the conventional least squares estimator. Therefore, LICA is a kind of unsupervised GLM whose regressor functions are mined from the input dataset. If we try to establish correspondences to the ICA, the lattice sources correspond to the unknown statistically independent sources and the mixing matrix is the one given by the abundance coefficients computed by least squares estimation.

The ILSIA is an improved formulation of the Endmember Induction Heuristic Algorithm proposed in [7]. Our approach to lattice source selection from the data is based on the conjecture equivalence between the Strong Lattice Independence and the Affine Independence [24]. The SLI needs two conditions: Lattice Independence and max/min dominance. Lattice Independence is detected based on results on fixed points for Lattice Autoassociative Memories (LAM) [22, 24, 29], and max/min dominance is tested using algorithms inspired in the ones described in [30]. An important improvement relative to previous attempts is the use of Chebyshev best approximation results [29] in order to reduce the number of selected vectors. The ILSIA is a greedy incremental algorithm that passes only once over the sample. It starts with a randomly picked input vector and tests each vector in the input dataset to add it to the set of lattice sources.

There are other methods [8, 24] based on LAM to obtain a set of SLI vectors. However these methods produce initially a large set of lattice sources that must be reduced somehow, either resorting to a priori knowledge or to selections based on Mutual Information or other similarity measures. In the ILSIA the candidate SLI vectors are discarded on the basis of the existence of a fixed point that gives a good approximation of it in the Chebyshev distance sense, which is a natural distance in this Lattice Computing setting.

The LICA approach falls in the field of Lattice Computing algorithms, which have been introduced in [7] as the class of algorithms that either apply lattice operators inf and sup or use lattice theory to produce generalizations or fusions of previous approaches. In [7] an extensive and updated list of references that can be labeled Lattice Computing can be found. This paper is an extension of the one presented at the LBM 2008 workshop inside the CLA 2008 conference [9].

The outline of the paper is as follows: Section 2 gives a brief recall of ICA. Section 3 introduces the linear mixing model. Section 4 presents a sketch of the theoretical relation between Lattice Independence and Linear (Affine) Independence through the LAM theory. Section 6 gives results on synthetic fMRI like data. Section 5 gives the definition of our Incremental Lattice Source Induction Algorithm (ILSIA). Section 7 presents results of the proposed approach on a case study. Section 8 provides some conclusions.

2. Independent Component Analysis (ICA)

The *Independent Component Analysis* (ICA) [13] assumes that the data is a linear combination of non Gaussian, mutually independent latent variables with an unknown mixing matrix. The ICA reveals the hidden independent sources and the mixing matrix. That is, given a set of observations represented by a d-dimensional vector $\mathbf{x}$, ICA assumes a generative model

$$\mathbf{x} = \mathbf{A}\mathbf{s}, \tag{1}$$

where $\mathbf{s}$ is the M dimensional vector of independent sources and $\mathbf{A}$ is the $d \times M$ unknown basis matrix. The ICA searches for the linear transformation of the data $\mathbf{W}$, such that the projected variables

$$\mathbf{W}\mathbf{x} = \mathbf{s}, \tag{2}$$

are as independent as possible. It has been shown that the model is completely identifiable if the sources are statistically independent and at least $M - 1$ of them are non Gaussian. If the sources are gaussian the ICA transformation could be estimated up to an orthogonal transformation. Estimation of mixing and unmixing matrices can be done maximizing diverse objective functions, among them the non gaussianity of the sources and the likelihood of the sample.

We have used the FastICA [14] algorithm implementation available at [26]. We have also used the implementations of Maximum Likelihood ICA [11] (ML-ICA) which is equivalent to Infomax ICA, Mean Field ICA [12] (MF-ICA), and Molgedey and Schouster ICA (MS-ICA) based on dynamic decorrelation [16], which are available at [27].

Application of ICA to fMRI has been reviewed by [3]. Reports on the research application of ICA to fMRI signals include the identification of signal types (task related and physiology related) and the analysis of multisubject fMRI data. The most common approach is the spatial ICA that looks for spatial disjoint regions corresponding to the identified signal types. It has been claimed that ICA has identified several physiological noise sources as well as other noise sources (motion, thermodynamics) identifying task related signals. Diverse ICA algorithms have been tested in the literature with inconclusive results. Among them, FastICA, the one that we will apply in the case study, did identify the task related signals consistently. Among the clinical applications, ICA has been used to study the brain activation due to pain in healthy individuals versus those with chronic pain [1], the discrimination of Alzheimer's patients from healthy controls [10], the classification of schizophrenia [4] and studies about the patterns of brain activation under alcohol intoxication [4].

3. The linear mixing model and the Lattice Independent Component Analysis

The linear mixing model can be expressed as follows:

$$\mathbf{x} = \sum_{i=1}^{M} a_i \mathbf{e}_i + \mathbf{w} = \mathbf{E}\mathbf{a} + \mathbf{w}, \tag{3}$$

where $\mathbf{x}$ is the d-dimensional pattern vector corresponding to the fMRI voxel time series vector, $\mathbf{E}$ is a $d \times M$ matrix whose columns are the d-dimensional vectors $\mathbf{e}_i, i = 1, .., M$, which are called endmembers when they are the vertices of a convex region covering the data, $\mathbf{a}$ is the M-dimensional vector of linear mixing coefficients, which correspond to fractional abundances in the convex case, and $\mathbf{w}$ is the d-dimensional additive observation noise vector. The linear mixing model is subjected to two constraints on the abundance coefficients when the data points fall into a simplex whose vertices are the endmembers, all abundance coefficients must be non-negative $a_i \geq 0, i = 1, .., M$ and normalized to unity summation $\sum_{i=1}^{M} a_i = 1$. Under this

circumstance, we expect that the vectors in $\mathbf{E}$ are affinely independent and that the convex region defined by them includes *all* the data points. We recall that a set of vectors $X = \{\mathbf{x}_1, \ldots, \mathbf{x}_k\}$ is said to be linearly independent if the unique solution to the equation $\sum_{i=1}^{k} a_i \mathbf{x}_i = \mathbf{0}$ is given by $a_i = 0$ for all $i \in \{1, \ldots, k\}$. A set X is an affinely independent set if the solution to the simultaneous equations $\sum_{i=1}^{k} a_i \mathbf{x}_i = \mathbf{0}$ and $\sum_{i=1}^{k} a_i = \mathbf{0}$ is given by $a_i = 0$ for all $i \in \{1, \ldots, k\}$. Therefore, linear independence is a necessary condition for affine independence but not viceversa. The model in equation (3) is shared by other linear analysis approaches, such as the General Linear Model (GLM) [5] and the Independent Component Analysis (ICA) [13] which do not view $\mathbf{E}$ as a set of endmembers but as regressors or independent sources.

Once the enmembers have been determined the unmixing process is the computation of the matrix inversion that gives the coordinates of each data point relative to the convex region vertices. The simplest approach is the unconstrained least squared error (LSE) estimation given by:

$$\widehat{\mathbf{a}} = \left(\mathbf{E}^T \mathbf{E}\right)^{-1} \mathbf{E}^T \mathbf{x}. \tag{4}$$

Even when the vectors in $\mathbf{E}$ are affine independent, the coefficients that result from equation (4) do not necessarily fulfill the non-negativity and unity normalization. Ensuring both conditions is a difficult computational problem. Some authors (i.e. [24]) use Non Negative Least Squares algorithms [15] to ensure at least non-negative coefficients. However in our works we use these mixture coefficients in a more qualitative way and we do not feel the need to enforce these conditions. Moreover, although the heuristic algorithm described in section 5 always produces the vertices of convex regions, these simplices always lie inside the data cloud, so that enforcing the non-negative and normalization conditions on the linear mixing coefficients would be impossible for some sample data points. Negative values are considered as zero values, for interpretation and visualization purposes, and the additivity to one condition is not important as long as we are looking for the maximum abundances to assign meaning to the resulting spatial distribution of the coefficients. These coefficients are interpreted as the regressor coefficients corresponding to the decomposition of the fMRI voxel time series into a basis of vectors. That is, high positive values are interpreted as high positive correlation with the time pattern of the corresponding lattice source. Therefore, to avoid confusion with the orthodox meaning of endmember, we will call *lattice source* to the set of affine independent vectors found by our algorithm.

We call *Lattice Independent Component Analysis* (LICA) the approach grounded in the results and algorithm that will be described in the following sections. LICA consists of two steps:

1. Induce from the given data a set of Strongly Lattice Independent vectors. In this paper we apply the Incremental Lattice Source Induction Algorithm (ILSIA) described in section 5. These vectors are taken as a set of affine independent vectors. The advantages of this approach are (1) that we are not imposing statistical assumptions, (2) that the algorithm is one-pass and very fast because it only uses comparisons and addition, (3) that it is unsupervised and incremental, and (4) that it detects naturally the number of lattice sources.
2. Apply the unconstrained least squares estimation to obtain the mixing matrix. The detection results are based on the analysis of the coefficients of this matrix.

Therefore, the approach is a combination of Linear and Lattice Computing: a linear component analysis where the components have been discovered by non-linear algorithms based on Lattice Theory.

4. Theoretical background on Lattice Independence and Lattice Autoassociative Memories

The work on Lattice Associative Memories (LAM) stems from the consideration of the bounded lattice ordered group (blog) $(\mathbb{R}_{\pm\infty}, \vee, \wedge, +, +')$ as the alternative to the computational framework given by the mathematical field $(\mathbb{R}, +, \cdot)$ for the definition of Neural Network algorithms. There $\mathbb{R}$ denotes the set of real numbers, $\mathbb{R}_{\pm\infty}$ the extended real numbers, $\wedge$ and $\vee$ denote, respectively, the binary $\max$ and $\min$ operations, and $+$, $+'$ denote addition and its dual operation. In our current context addition is self-dual. If $x \in \mathbb{R}_{\pm\infty}$, then its additive conjugate is $x^* = -x$. For a matrix $A \in \mathbb{R}_{\pm\infty}^{n\times m}$ its conjugate matrix is given by $A^* \in \mathbb{R}_{\pm\infty}^{n\times m}$, where each entry $a_{ij}^* = [A^*]_{ij}$ is given by $a_{ij}^* = (a_{ji})^*$.

The LAM were first introduced in [21, 20] as Morphological Associative Memories, a name still used in recent publications [29], but we follow the new convention introduced in [22, 24] because it sets the works in the more general framework of Lattice Computing. Given a set of input/output pairs of pattern $(X, Y) = \left\{\left(\mathbf{x}^\xi, \mathbf{y}^\xi\right); \xi = 1, .., k\right\}$, a linear heteroassociative neural network based on the pattern's cross correlation is built up as $W = \sum_\xi \mathbf{y}^\xi \cdot \left(\mathbf{x}^\xi\right)'$. Mimicking this constructive procedure [21, 20] propose the following constructions of Lattice Heteroassociative Memories (LHAM):

$$W_{XY} = \bigwedge_{\xi=1}^{k} \left[\mathbf{y}^\xi \times \left(-\mathbf{x}^\xi\right)'\right] \text{ and } M_{XY} = \bigvee_{\xi=1}^{k} \left[\mathbf{y}^\xi \times \left(-\mathbf{x}^\xi\right)'\right], \tag{5}$$

where $\times$ is any of the $\boxtimes$ or $\boxtimes$ operators. Here $\boxtimes$ and $\boxtimes$ denote the $\max$ and $\min$ matrix product [21, 20]. respectively defined as follows:

$$C = A \boxtimes B = [c_{ij}] \Leftrightarrow c_{ij} = \bigvee_{k=1,\ldots,n} \{a_{ik} + b_{kj}\}, \tag{6}$$

$$C = A \boxtimes B = [c_{ij}] \Leftrightarrow c_{ij} = \bigwedge_{k=1,\ldots,n} \{a_{ik} + b_{kj}\}. \tag{7}$$

If $X = Y$ then the LHAM memories are Lattice Autoassociative Memories (LAAM). Conditions of perfect recall by the LHAM and LAAM of the stored patterns proved in [21, 20] encouraged the research on them, because in the continuous case, the LAAM is able to store and recall any set of patterns: $W_{XX} \boxtimes X = X = M_{XX} \boxtimes X$, for any X. However, this result holds when we deal with noise-free patterns. Research on robust recall [19, 23, 20] based on the so-called kernel patterns lead to the notion of morphological independence, in the erosive and dilative sense, and finally to the definition of Lattice Independence (LI) and Strong Lattice Independence (SLI). We gather theoretical results from [22, 24, 29, 30] that set the theoretical background for the approach to lattice source induction described in section 5.

Definition Given a set of vectors $X = \left\{\mathbf{x}^1, ..., \mathbf{x}^k\right\} \subset \mathbb{R}^n$ a *linear minimax combination* of vectors from this set is any vector $\mathbf{x} \in \mathbb{R}^n_{\pm\infty}$ which is a *linear minimax sum* of these vectors:

$$x = \mathcal{L}\left(\mathbf{x}^1, ..., \mathbf{x}^k\right) = \bigvee_{j \in J} \bigwedge_{\xi=1}^{k} \left(a_{\xi j} + \mathbf{x}^\xi\right),$$

where J is a finite set of indices and $a_{\xi j} \in \mathbb{R}_{\pm\infty}$ $\forall j \in J$ and $\forall \xi = 1, ..., k$.

Definition The *linear minimax span* of vectors $\left\{\mathbf{x}^1, ..., \mathbf{x}^k\right\} = X \subset \mathbb{R}^n$ is the set of all linear minimax sums of subsets of X, denoted $LMS\left(\mathbf{x}^1, ..., \mathbf{x}^k\right)$.

Definition Given a set of vectors $X = \left\{\mathbf{x}^1, ..., \mathbf{x}^k\right\} \subset \mathbb{R}^n$, a vector $\mathbf{x} \in \mathbb{R}^n_{\pm\infty}$ is *lattice dependent* if and only if $x \in LMS\left(\mathbf{x}^1, ..., \mathbf{x}^k\right)$. The vector $\mathbf{x}$ is *lattice independent* if and only if it is not lattice dependent on X. The set X is said to be *lattice independent* if and only if $\forall \lambda \in \{1, ..., k\}$, $\mathbf{x}^\lambda$ is lattice independent of $X \setminus \left\{\mathbf{x}^\lambda\right\} = \left\{\mathbf{x}^\xi \in X : \xi \neq \lambda\right\}$.

The definition of lattice independence supersedes and improves the early definitions [23] of erosive and dilative morphological independence. This definition of lattice dependence is closely tied to the study of the fixed points of the LAAM's taken as operators.

Theorem 4.1. *[22, 29] Given a set of vectors $X = \left\{\mathbf{x}^1, ..., \mathbf{x}^k\right\} \subset \mathbb{R}^n$, a vector $\mathbf{y} \in \mathbb{R}^n_{\pm\infty}$ is a fixed point of W_{XX}, that is $W_{XX} \boxtimes \mathbf{y} = \mathbf{y}$, if and only if $\mathbf{y}$ is lattice dependent on X.*

Definition A set of vectors $X = \left\{\mathbf{x}^1, ..., \mathbf{x}^k\right\} \subset \mathbb{R}^n$ is said to be *max dominant* if and only if for every $\lambda \in \{1, ..., k\}$ there exists and index $j_\lambda \in \{1, ..., n\}$ such that

$$x^\lambda_{j_\lambda} - x^\lambda_i = \bigvee_{\xi=1}^{k} \left(x^\xi_{j_\lambda} - x^\xi_i\right) \forall i \in \{1, ..., n\}.$$

Similarly, X is said to be *min dominant* if and only if for every $\lambda \in \{1, ..., k\}$ there exists and index $j_\lambda \in \{1, ..., n\}$ such that

$$x^\lambda_{j_\lambda} - x^\lambda_i = \bigwedge_{\xi=1}^{k} \left(x^\xi_{j_\lambda} - x^\xi_i\right) \forall i \in \{1, ..., n\}.$$

The expressions that compound this definition appeared in the early theorems about perfect recall of Morphological Associative Memories [21, 20]. Their value as an identifiable property of the data has been discovered in the context of the formalization of the relationship between strong lattice independence, defined below, and the affine independence in the classical linear analysis.

Definition A set of lattice independent vectors $\left\{\mathbf{x}^1, ..., \mathbf{x}^k\right\} \subset \mathbb{R}^n$ is said to be *strongly lattice independent* (SLI) if and only if X is max dominant or min dominant or both.

As said before, min and max dominance are the conditions for perfect recall. Per construction, the column vectors of Lattice Autoassociative Memories are diagonally min or max dominant, depending of their erosive or dilative nature, therefore they will be strong lattice independent, *if* they are lattice independent.

Conjecture 4.2. *[24] If* $X = \left\{\mathbf{x}^1, ..., \mathbf{x}^k\right\} \subset \mathbb{R}^n$ *is strongly lattice independent then* X *is affinely independent.*

This conjecture (stated as theorem in [22]) is the key result whose proof would relate the linear convex analysis and the non-linear lattice analysis. If true, it means that the construction of the LAAM provides the starting point for obtaining sets of affine independent vectors that could be used as lattice sources for the unmixing algorithms described in section 3. We have found it to be true in our computational experiences, but a formal proof is still lacking.

Theorem 4.3. *[24] Let* $X = \left\{\mathbf{x}^1, ..., \mathbf{x}^k\right\} \subset \mathbb{R}^n$ *and let* W *(* M*) be the set of vectors consisting of the columns of the matrix* W_{XX} *(*M_{XX}*). Let* $F(X)$ *denote the set of fixed points of the LAAM constructed from set* X*. There exist* $V \subset W$ *and* $N \subset M$ *such that* V *and* N *are strongly lattice independent and* $F(X) = F(V) = F(N)$ *or, equivalently,* $W_{XX} = W_{VV}$ *and* $M_{XX} = M_{NN}$*.*

The key idea of this theorem is that it is possible to built a set of SLI vectors from the column vectors of a LAAM. Taking into account that the column vectors of a LAAM are diagonally max or min dominant (depending on the kind of LAAM), it suffices to find a subset which is lattice independent. It is also grounded in the fact that a subset of a set of max or min dominant vectors is also min or max dominant. The proof of the theorem is constructive giving way to algorithms to find these sets of SLI. It removes iteratively the detected lattice dependent column vectors. Detection lies in the fact that $W_{XX} = W_{WW} = W_{VV}$ and $M_{XX} = M_{MM} = M_{NN}$ when the vectors removed from W or M to obtain V or N are lattice dependent on the remaining ones. Algorithms discussed in [8, 24] apply this result. The experience shows that most of the column vectors of the LAAM are lattice independent, so that the sets of SLI vectors are large and need some kind of selection algorithm to find the salient ones. One way to perform this selection is discarding those that can be interpreted as close approximations of others already selected, in the incremental framework of the algorithm described in section 5.

To deal with approximation in this Lattice Computing setting it seems natural [29] to use the Chebyshev distance given by the greatest componentwise absolute difference between two vectors, it is denoted $\varsigma(\mathbf{x}, \mathbf{y})$ and can be computed as follows: $\varsigma(\mathbf{x}, \mathbf{y}) = (\mathbf{x}^* \boxtimes \mathbf{y}) \vee (\mathbf{y}^* \boxtimes \mathbf{x})$. The Chebyshev-best approximation of $\mathbf{c}$ by $f(\mathbf{x})$ subject to $\mathbf{x} \in S$, is the minimization of $\varsigma(f(\mathbf{x}), \mathbf{c})$ subject to $\mathbf{x} \in S$.

Theorem 4.4. *[29] Given* $B \in \mathbb{R}^{m \times n}$ *and* $\mathbf{c} \in \mathbb{R}^m$*, a Chebyshev-best solution to the approximation of* $\mathbf{c}$ *by* $B \boxtimes \mathbf{x}$ *subject to the constraint* $B \boxtimes \mathbf{x} < \mathbf{c}$ *is given by* $\mathbf{x}^{\#} = B^* \boxtimes \mathbf{c}$ *and* $\mathbf{x}^{\#}$ *is the greatest such solution.*

In our incremental algorithm we will need to solve the unconstrained minimization problem

$$\min \varsigma \left(B \boxtimes \mathbf{x}, \mathbf{c} \right),$$

in order to decide if the input vector is already well approximated by a fixed point of the LAAM constructed from the selected enmembers.

Theorem 4.5. *[29]Given $B \in \mathbb{R}^{m \times n}$ and $\mathbf{c} \in \mathbb{R}^m$, a Chebyshev-best solution to the approximation of $\mathbf{c}$ by $B \boxtimes \mathbf{x}$ is given by $\mu + \mathbf{x}^{\#}$ where μ is such that $2\mu = \varsigma \left(B \boxtimes \mathbf{x}^{\#}, \mathbf{c} \right) = \left(B \boxtimes \mathbf{x}^{\#} \right)^{*} \boxtimes \mathbf{c}$.*

This theorem has resulted in enhanced robust recall for LAAM under general noise conditions, compared with other Associative Memories proposed in the literature. It has also been applied to produce a lattice based nearest neighbor classification scheme with good results on standard benchmark classification problems.

5. Incremental Lattice Source Induction Algorithm (ILSIA)

The algorithm described in this section is a further step in the formulation of a search of SLI sets of vectors from the Endmember Induction Heuristic Algorithm introduced in [8]. It is grounded in the formal results on continuous LAAM reviewed in the previous section. The dataset is denoted by $Y = \{\mathbf{y}_j; j = 1, \ldots, N\} \in \mathbb{R}^{n \times N}$ and the set of lattice sources induced from the data at any step of the algorithm is denoted by $X = \{\mathbf{x}_j; j = 1, \ldots, K\} \in \mathbb{R}^{n \times K}$. The number of lattice sources K will vary from the initial value $K = 1$ up to the number of lattice sources found by the algorithm, we will skip indexing the set of lattice sources with the iteration time counter. The algorithm makes only one pass over the sample as in [8]. The auxiliary variables $\mathbf{s}_1, \mathbf{s}_2, \mathbf{d} \in \mathbb{R}^n$ serve to count the times that a row has the maximum and minimum, and the component wise differences of the lattice source and input vectors. Borrowing Matlab notation, the expression $(\mathbf{d} == m_1)$ denotes a vector of 0 and 1, where 1 means that corresponding components are equal.

The algorithm aims to produce sets of SLI vectors extracted from the input dataset. Assuming the truth of conjecture 4.2 the resulting sets are affine independent, that is, they define convex polytopes that cover some (most of) the data points in the dataset. To ensure that the resulting set of vectors are SLI, we first ensure that they are lattice independent in step 3(a) of Algorithm 1 by the application of theorem 4.1: each new input vector is applied to the LAAM constructed with the already selected lattice sources. If the recall response evoked by the vector is perfect, then it is lattice dependent on the lattice sources, and can be discarded. If not, then the new input vector is a candidate lattice source. We test in step 3(c) the min and max dominance of the set of lattice sources enlarged with the new input vector. We need to test the whole enlarged lattice source set because min and max dominance are not preserved when adding a vector to a set of min/max dominant vectors. Note that this is contrary to the fact that subsets of min or max dominant sets of vectors are also min or max dominant [24]. Note also that to test lattice independence we need only to build W_{XX} because the set of fixed points is the same for both kinds of LAAM, i.e. $F\left(W_{XX}\right) = F\left(M_{XX}\right)$. However, we need

Algorithm 1 Incremental Lattice Source Induction Algorithm (ILSIA)

1. Initialize the set of lattice sources $X = \{\mathbf{x}_1\}$ with a randomly picked vector in the input dataset Y.
2. Construct the LAAM based on the strong lattice independent (SLI) vectors: W_{XX}.
3. For each data vector $\mathbf{y}_j$;j=1,. . .,N
   (a) if $\mathbf{y}_j = W_{XX} \boxtimes \mathbf{y}_j$ then $\mathbf{y}_j$ is lattice dependent on the set of lattice sources X, skip further processing.
   (b) if $\varsigma\left(W_{XX} \boxtimes \left(\mu + \mathbf{x}^{\#}\right), \mathbf{y}_j\right) < \theta$, where $\mathbf{x}^{\#} = W^{*}_{XX} \boxtimes \mathbf{y}_j$ and $\mu = \frac{1}{2}\left(\left(W_{XX} \boxtimes \mathbf{x}^{\#}\right) \boxtimes \mathbf{y}_j\right)$, then skip further processing.
   (c) test max/min dominance to ensure SLI, consider the enlarged set of lattice sources $X' = X \cup \{\mathbf{y}_j\}$
      i. $\mu_1 = \mu_2 = 0$
      ii. for $i = 1, \ldots, K+1$
      iii. $\mathbf{s}_1 = \mathbf{s}_2 = \mathbf{0}$
         A. for $j = 1, \ldots, K+1$ and $j \neq i$
            $\mathbf{d} = \boldsymbol{x}_i - \mathbf{x}_j$; $m_1 = \max(\mathbf{d})$; $m_2 = \min(\mathbf{d})$.
            $\mathbf{s}_1 = \mathbf{s}_1 + (\mathbf{d} == m_1)$, $\mathbf{s}_2 = \mathbf{s}_2 + (\mathbf{d} == m_2)$.
         B. $\mu_1 = \mu_1 + (\max(\mathbf{s}_1) == K)$ or $\mu_2 = \mu_2 + (\max(\mathbf{s}_2) == K)$.
      iv. If $\mu_1 = K+1$ or $\mu_1 = K+1$ then $X' = X \cup \{\mathbf{y}_j\}$ is SLI, go to 2 with the enlarged set of lattice sources and resume exploration from $j+1$.
4. The final set of lattice sources is X.

to test both min and max dominance because SLI needs one of them or both to hold. This part of the algorithm is an adaptation of the procedure proposed in [30].

If SLI was the only criteria to be tested to include input vectors in the set of lattice sources, then we will end up detecting a large number of lattice sources so that there will be little significance of the abundance coefficients because many of them will be closely placed in the input vector space. This is in fact the main inconvenient of the algorithms proposed in [8, 24] that use the columns of a LAAM constructed from the data as the SLI vector set, after removing lattice dependent vectors. To reduce the set of lattice sources selected we apply the results on Chebyshev-best approximation in theorem 4.5 discarding input vectors that can be well approximated by a fixed point of the LAAM constructed from the current set of lattice sources. In step 3(b) this approximation of a candidate is tested before testing max/min dominance: if the Chebyshev distance from the best approximation to the input vector is below a given threshold, the input vector is considered a noisy version of a vector which is lattice dependent on the current set of lattice sources.

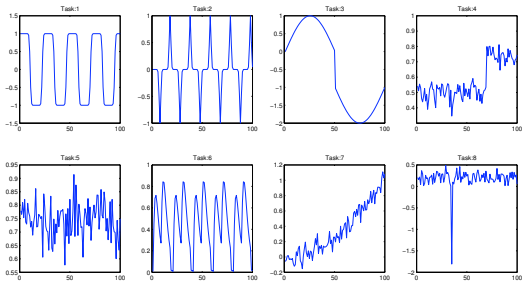

Figure 1: Simulated sources (time courses) in the experimental data.

6. Results on simulated fMRI images

We have used the simulated fMRI data [2, 31] [1]. In fMRI the spatial distribution of data sources can be classified into locations of interest and artifacts. The locations of interest include task-related, transiently task-related, and function-related locations. Their spatial distribution are typically super-gaussian in nature because of the high localization of brain functionality. A task-related location and its corresponding source (component) closely match the experimental paradigm. A transiently task-related source, on the other hand, is similar to a task-related source but with an activation that may be pronounced during the beginning of each task cycle and may fade out or change as time progresses. Functional locations are those activated areas which are related to a particular functional area of the brain and the source for these may not exhibit a particular pattern. The class of uninteresting sources or artifacts include motion related sources due to head movement, respiration, and cardiac pulsation. Figure 1 shows the sources used in the simulated fMRI data. Source #1 corresponds to the task related time course, source #6 corresponds to a transient task-related time course. Figure 2 shows the spatial distribution of the locations of the sources, corresponding to the mixing matrices in the linear models of both ICA and LICA. Spatial locations #1 and #6 are the ones with most interest from the task point of view. To form the fMRI mixture, first the image data is reshaped into vectors by concatenating columns of the image matrix. The source matrix is multiplied by the time course matrix to obtain a mixture that simulates 100 scans of a single slice of fMRI data.

We have applied the LICA and MS-ICA algorithms to this simulated data. We obtain five lattice sources with the LICA approach using standard settings of the algorithm, and we set the MS-ICA number of sources to that number. Figure 3 presents the lattice sources found by ILSIA, with the best correlated simulated time course overlaid in red. Figure 4 shows the sources found by the MS-ICA together with the best correlated simulated time course. Note that ILSIA finds both a task related and a function-related source. We show in figure 5 the abundance images that correspond to the spatial

[1] Simulated data can be generated with the tools provided in http://mlsp.umbc.edu/simulated_fmri_data.html

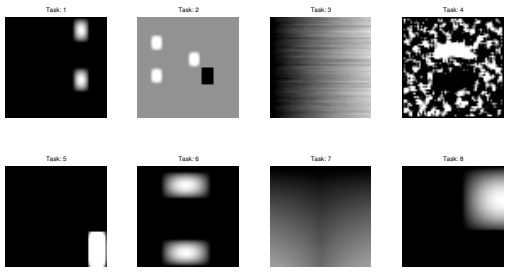

Figure 2: Simulated spatial distribution of location of the sources

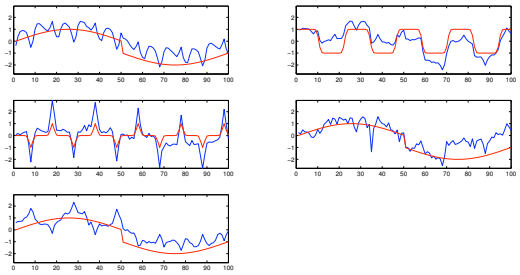

Figure 3: Sources found by the ILSIA on the simulated data

distributions of the lattice sources. Notice that the spatial location of the task-related source is well detected in the second image, while the transient task-related source location is also well detected despite that it does not appear as one of the best correlated sources in figure 14. Because the LICA and ICA algorithms are unsupervised, they can discover sources which indirectly help discover the spatial locations of interest, although the sources themselves are not precise matches of the underlying true sources. Figure 6 shows the spatial distribution of the MS-ICA sources. The detection is noisier than in the results obtained by LICA, and the task-related spatial locations are not so clearly detected. Table 1 contains the quantitative measure of the goodness of spatial discovery, given by the Mutual Information similarity measure between the simulated spatial distributions of the simulated sources and the mixing coefficients that give the estimation of the spatial distribution of the discovered sources. We have highlighted the maximum values per column, and we have highlighted the closest one when it is near the maximum of the column. The MS-ICA has more ambiguous columns than the LICA, which is in agreement with the visual assessment of figures 5 and 6.

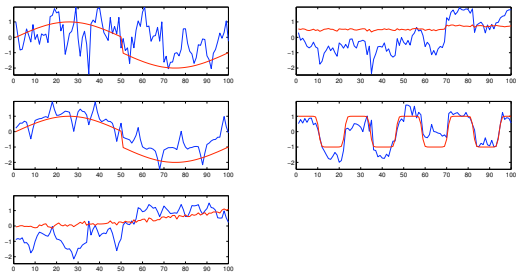

Figure 4: Sources found by MS-ICA on the simulated data

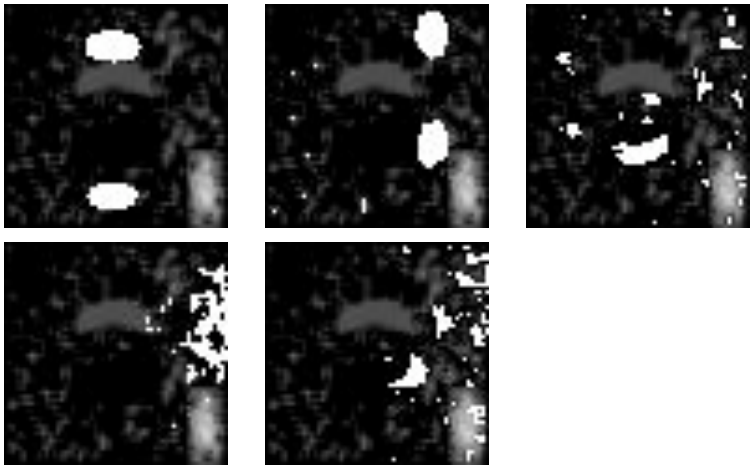

Figure 5: Spatial distributions found by LICA on the simulated data.

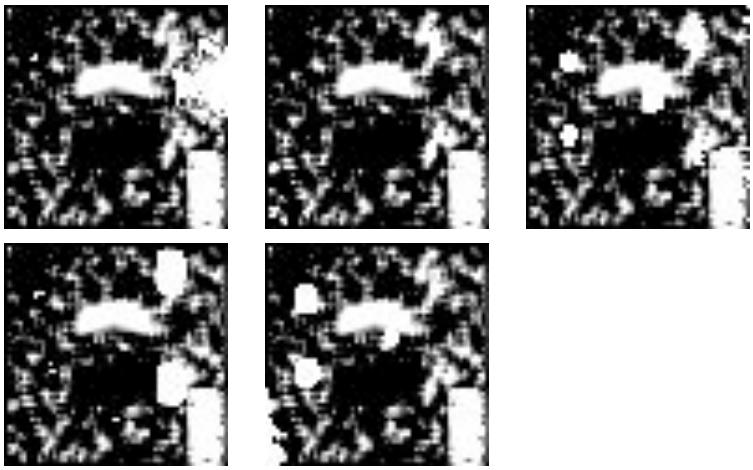

Figure 6: Spatial distribution of the sources given by the mixing matrices of MS-ICA on the simulated data.

	MS-ICA					LICA				
Source	#1	#2	#3	#4	#5	#1	#2	#3	#4	#5
#1	-0,16	0,15	0,03	**1,18**	-0,36	-0,52	**2,51**	-0,37	-0,23	0,02
#2	-0,45	-0,78	-0,13	-0,38	-0,29	-0,48	-0,33	**2,26**	-0,13	-0,38
#3	**1,29**	**1,09**	**2,32**	**0,79**	**1,18**	0,31	1,66	0,25	**2,42**	**2,24**
#4	-0,28	0,68	-0,56	-0,63	-0,38	-0,57	-0,72	-0,53	-0,52	-0,50
#5	-1,42	-1,05	-0,80	-0,69	-0,70	-0,71	-0,76	-0,70	-0,57	-0,72
#6	**1,33**	-0,79	-0,30	-0,39	-0,60	**2,26**	-0,44	0,36	-0,50	-0,54
#7	0,62	**1,51**	0,17	-0,24	**0,80**	0,30	-0,20	-0,57	-0,01	0,55
#8	-0,92	-0,81	-0,72	-0,63	-0,62	-0,59	-0,71	-0,68	-0,47	-0,67

Table 1: Mutual Information similitude between the spatial locations discovered by LICA and MA-ICA and the ground truth spatial locations.

7. Results on a standard case study

The experimental data for this benchmarking corresponds to auditory stimulation test data of a single person[2]. These whole brain BOLD/EPI images were acquired on a modified 2T Siemens MAGNETOM Vision system. Each acquisition consisted of 64 contiguous slices. Each slice being a 2D image of one head volume cut. There are 64x64x64 voxels of size 3mm x 3mm x 3mm. The data acquisition took 6.05s., with the scan-to-scan repeat time (RT) set arbitrarily to 7s., 96 acquisitions were made (RT=7s.) in blocks of 6, i.e., 16 blocks of 42s. duration. The condition for successive blocks alternated between rest and auditory stimulation, starting with rest. Auditory stimulation was bi-syllabic words presented binaurally at a rate of 60 per minute. Due to T1 effects it is advisable to discard the first few scans (there were no "dummy" lead-in scans). We have discarded the first 10 scans. An standard results obtained with the SPM software is presented in figure 7 as localized in the Talairach space, in sagital, coronal and axial cuts.

There are a number of sources of noise in the fMRI signal [28] that must be dealt with in appropriate preprocessing steps [25]. We have dealt with these noise sources following the standard procedures in SPM software, so that all the algorithms applied have the same input data quality. First, we realigned the volumes to account for head motion artifacts. Second, we coregistered the functional volumes with the structural MRI T1-weighted volume. Third, we performed spatial normalization guided by the structural volume segmentation. Finally, we performed a smoothing step with an isotropic Gaussian kernel.

As already discussed in [9], we perform a Lattice Normalization, subtracting the mean value of each voxel time series independently so that the plots are collapsed around the origin. This mean subtraction corresponds to an scale normalization in the Lattice Computing sense. It removes scale effects that hinder the detection of meaningful lattice independent vectors. Note that, although we are shifting the voxel vector

[2]The dataset is freely available from ftp://ftp.fil.ion.ucI.ac.uk/spm/data, the file name is snrfM00223.zip. The functional data starts at acquisition 4, image snrfMOO223-004.

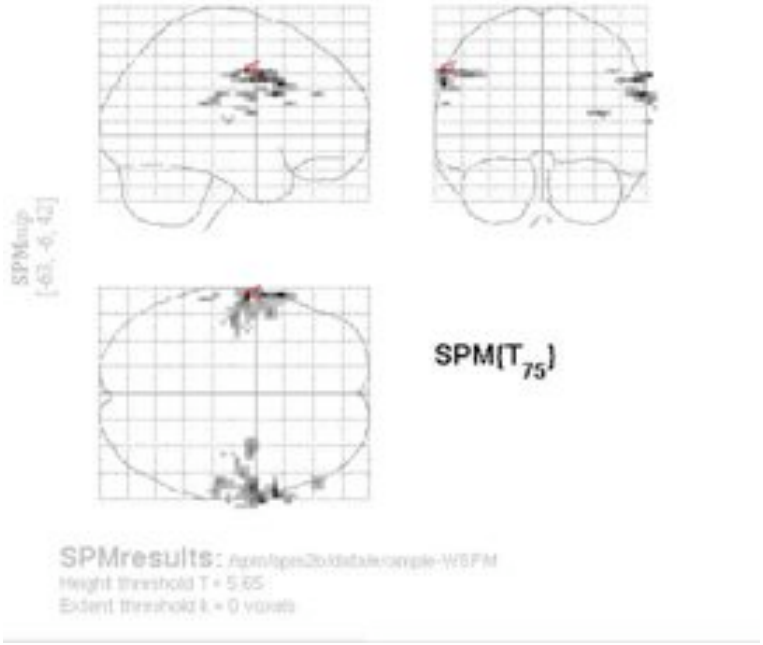

Figure 7: Activation maps obtained with an execution of SPM software with nominal parameters over the case study data.

#	PCA	ML-ICA	MF-ICA	MS-ICA	FastICA	LICA
1	0.04	-0.14	-0.13	-0.04	-0.06	**0.20**
2	0.02	0.09	-0.14	**0.22**	-0.16	0.09
3	-0.08	-0.01	0.12	-0.07	0.08	-0.07
4	-0.22	-0.03	-0.13	0.07	-0.12	0.17
5	0.03	**0.37**	-0.13	-0.20	-0.18	0.14
6	0.10	0.12	-0.12	-0.13	0.11	0.09
7	0.33	0.12	-0.04	-0.07	-0.10	-0.15
8	**0.34**	-0.09	0.05	0.19	0.03	-0.07
9	-0.15	0.18	0.11	0.06	**0.25**	0.06
10	-0.09	-0.14	-0.18	0.16	0.05	0.02
11	0.24	-0.15	**0.15**	-0.25	-0.07	0.09

Table 2: Correlation between lattice sources found by LICA, the sources found by the ICA algorithms, the PCA's eigenvectors and the task control variable.

to the origin, we are not aiming to perform a normalization in the statistical sense.

We have proceeded as follows: first we have applied the ILSIA algorithm, described in section 5, obtaining a number of lattice sources. Then we have applied the comparative algorithms (PCA, ML-ICA, MF-ICA, MS-ICA and FastICA) setting the number of lattice sources to the number obtained by LICA. Table 2 shows the correlation of the induced lattice sources and independent sources with the time plot of the experiment control variable, which is zero during the resting state and one while the auditory stimulation is taking place. This correlation is a measure of how well each lattice source/source is related to the task. The source with the maximum correlation for each algorithm is an indication of the a corresponding spatial distribution of mixing coefficients that may have the best similitude with the SPM activation results of figure 7. To verify this hypothesis, we further computed the Mutual Information similitude measure among the mixing coefficients of each source and the SPM t-statistics map before thresholding. Table 3 contains these Mutual Information values, which in general confirm the results of table 2. Therefore, we discover both the underlying task (which is set for the GLM in SPM) and the activation pattern. A qualitative assessment of the algorithms follows by visual comparison of the results of SPM (shown in figure 7) with the voxel clusters detected on the mixing coefficient volumes with highest Mutual Information for each algorithm. Cluster detection in the abundance images corresponds to voxels with abundance value above the 99% percentile of the distribution of this lattice source/source abundance coefficients over the whole volume. Cluster detection is shown as white voxels in the corresponding images. The goal is to reproduce the activity detection in the auditory cortex that the SPM is able to find. To asses this detection we reproduce selected axial, coronal and sagital cuts that correspond approximately to the brain cuts shown in the reference SPM result image shown in figure 7. In figures 8 to 13, the top row shows the axial and coronal cuts and the bottom row will show the sagital cuts lying approximately in the auditory cortex at both sides of the brain. Notice that in some cases there are activations detected over the air region, which an undesirable result.

#	PCA	ML-ICA	MF-ICA	MS-ICA	FastICA	LICA
1	-0.30	-0.21	-0.17	-0.37	-0.97	**3,02**
2	0.02	-045	-0.46	**1.48**	-1.60	-0.30
3	-0.30	-0.71	-0.46	-1.17	0.34	-0.30
4	-0.22	-0.85	-0.43	0.53	1.11	-0.30
5	-0.03	**2.60**	-0.46	-0.39	-0.76	-0.30
6	-0.30	-0.56	-0.46	-0.98	0.18	-0.30
7	0.33	-0.78	-0.46	-0.13	-0.59	-0.30
8	**3.020**	-0.09	-0.38	1.35	0.30	-0.30
9	-0.35	-0.52	0.02	-1.29	**1.99**	-0.30
10	-0.39	0.75	0.35	-0.21	-0.30	-0.30
11	0.24	-0.06	**2.91**	1.17	0.31	-0.30

Table 3: Mutual Information similarity between the mixing volumes computed by LICA, the ICA algorithms, the PCA and the t-statistic computed by the SPM software (before thresholding).

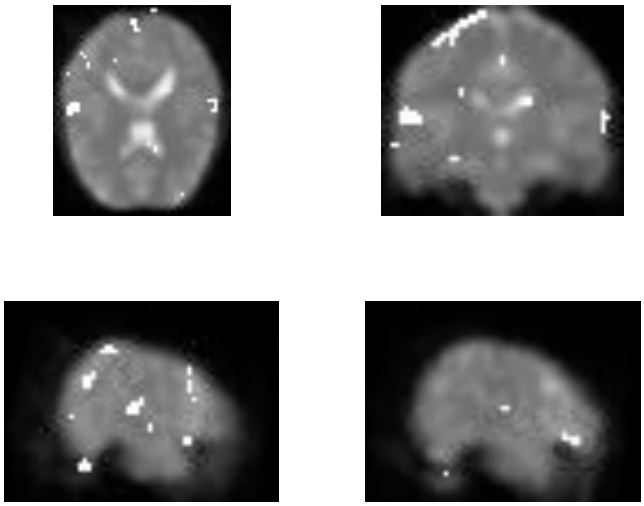

Figure 8: Best matching activation detection over the abundances of the LICA approach.

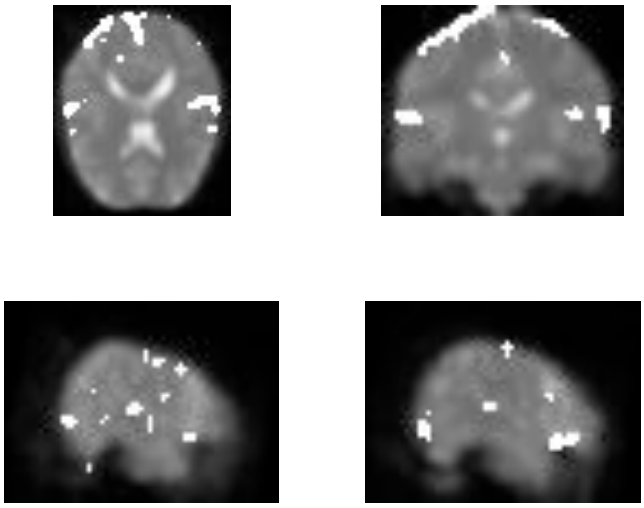

Figure 9: Best matching activation detection over the abundances of the PCA approach.

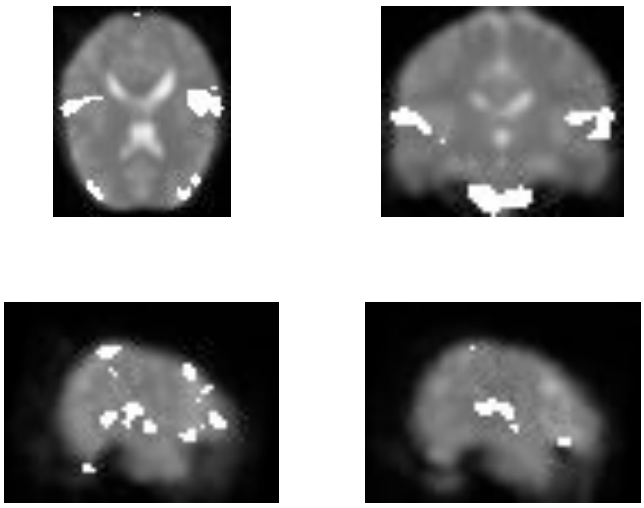

Figure 10: Best matching activation detection over the abundances of the ML-ICA approach.

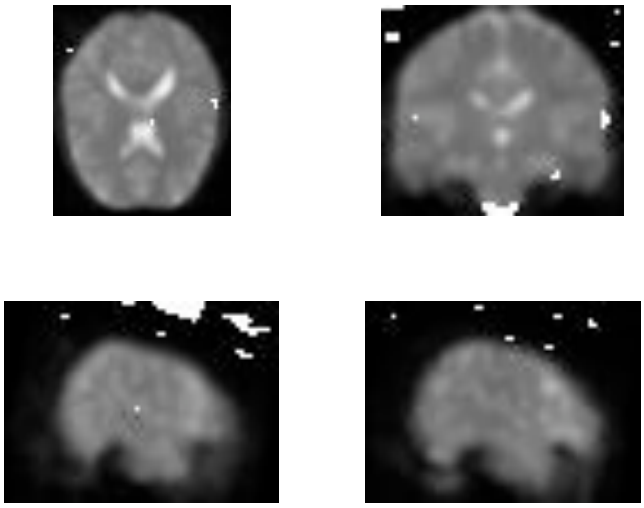

Figure 11: Best matching activation detection over the abundances of the MS-ICA approach.

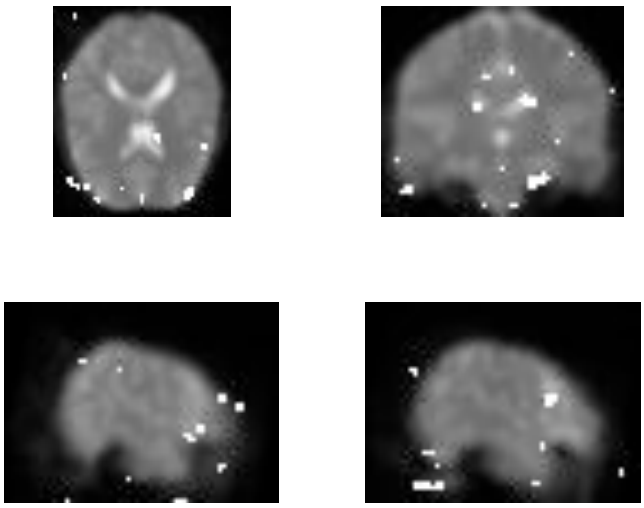

Figure 12: Best matching activation detection over the abundances of the FastICA approach.

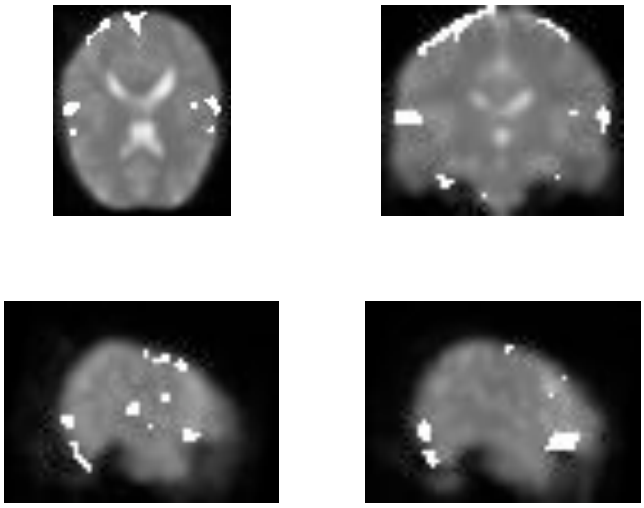

Figure 13: Best matching activation detection over the abundances of the MF-ICA approach.

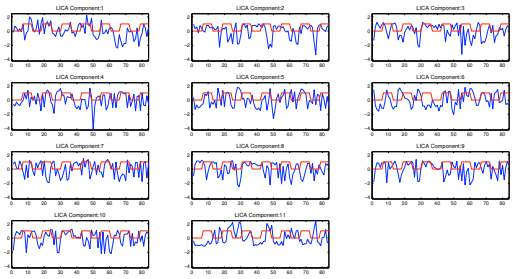

Figure 14: Lattice sources found by ILSIA, after normalization, for the LICA approach. Task indicator variable overlaid in red.

To show the degree of discovery of the control variable that models the control task by each algorithm, we reproduce in figures 14 to 19 the sources found by each algorithm, the lattice sources of LICA, the statistically independent sources of ICA, and the eigenvectors of the PCA. For this visualization, each source has been normalized computing its z-score, in order to highlight its structure and made it visually comparable with the control variable. The control variable plot is overlaid in read on each source plot.

We note that our approach gives qualitative and quantitative results comparable to the well established ICA approaches. That seems to support the idea that Lattice Independence involves properties somehow least similar to that of Statistical Independence.

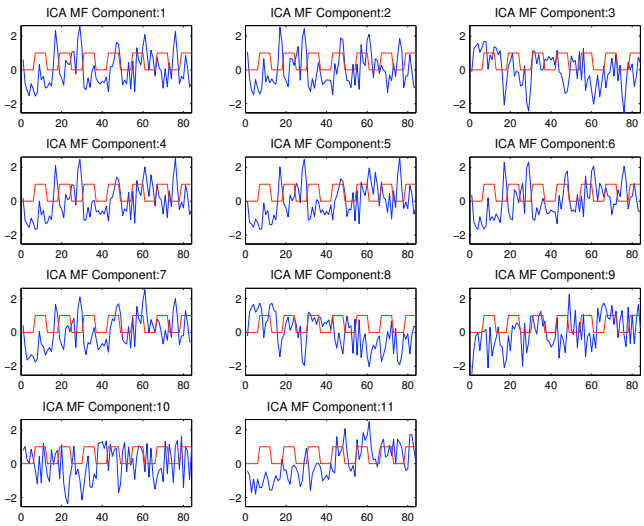

Figure 15: Sources found by MF-ICA, after normalization. Task indicator variable overlaid in red.

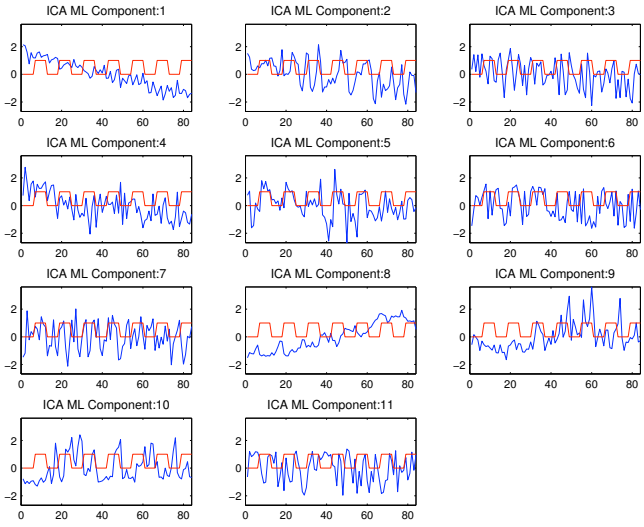

Figure 16: Sources found by ML-ICA, after normalization. Task indicator variable overlaid in red.

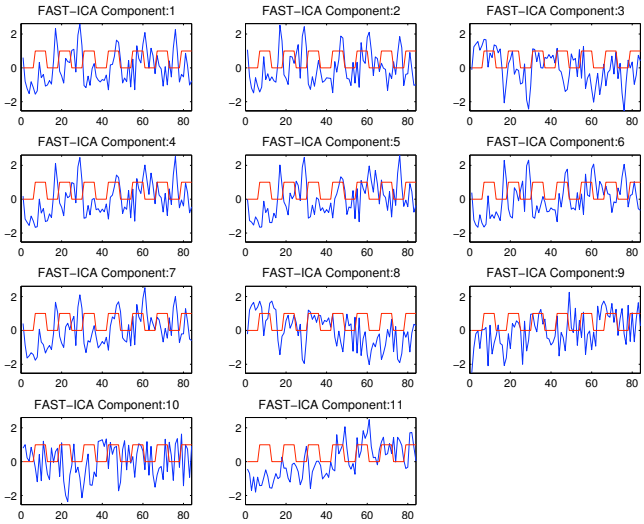

Figure 17: Sources found by FastICA, after normalization. Task indicator variable overlaid in red.

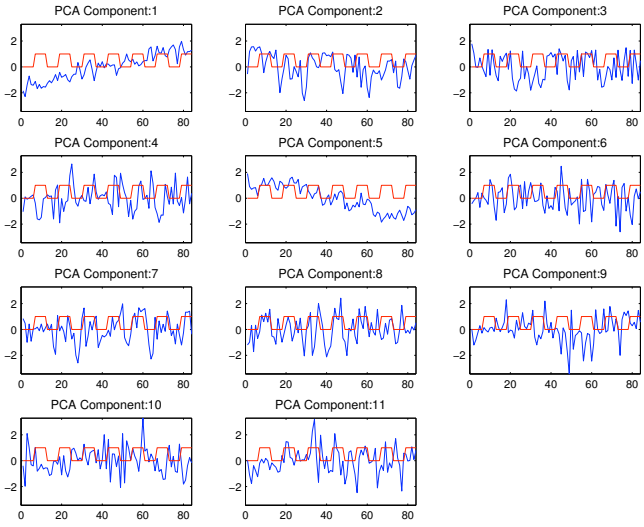

Figure 18: Eigenvectors found by PCA, after normalization. Task indicator variable overlaid in red.

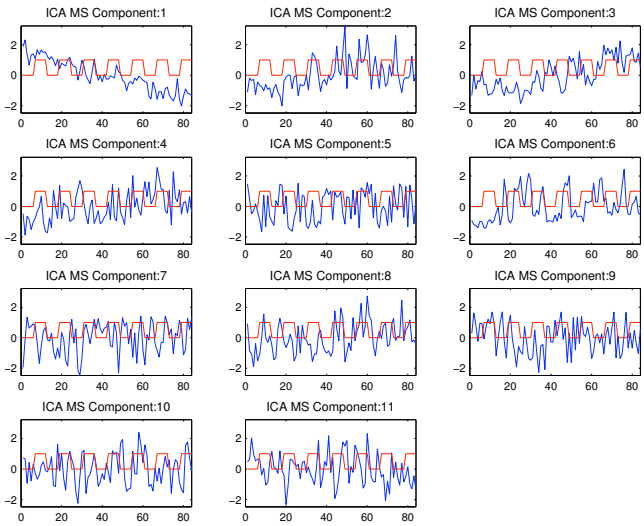

Figure 19: Sources found by MS-ICA, after normalization. Task indicator variable overlaid in red.

8. Summary and Conclusions

We have proposed and applied a Lattice Independent Component Analysis (LICA) to the model-free (unsupervised) analysis of fMRI. The LICA is based on the application of the Lattice Computing based algorithm ILSIA for the selection of the lattice sources, and the linear unmixing of the data based on these lattice sources. We have discussed the similarities of our approach with the application of ICA to fMRI activation detection [3, 25]. In our approach the temporal sources correspond to lattice sources detected by the ILSIA algorithm and the spatial mixing coefficients correspond to the abundance volumes obtained by unmixing the voxel time series on the basis of the found lattice sources. We have benefited from recent results on the Chebyshev best approximation and on the equivalence between SLI and affine independence. After a normalization consisting in the subtraction of the vector mean value, we look for SLI vectors that can not be well approximated by a fixed point of the LAAM constructed with the selected lattice sources. The LICA approach then uses this set of vectors to compute the mixing coefficients that characterize the data and the lattice source. We perform the activation detection thresholding these coefficients on the basis of its histogram. Work on simulated fMRI data shows that LICA performance is comparable to or improves over the ICA approach in the sense of discovering task-related sources and their spatial locations. Working with a well-known case study, have found that LICA gives results consistent with the SPM standard approach. Compared to ICA algorithms, LICA reproduces also the SPM results. An important feature of our approach is that it is an unsupervised algorithm, where we do not need to postulate *a priori* information or models. Also, LICA does not impose a probabilistic model on the sources. The lattice independence condition may be a more relaxed restriction to find meaningful sources in data where ICA approaches can fail due to their statistical properties.

Besides some other open theoretical questions, we want to state conveniently, and solve, the problem of finding the *right* number of lattice sources, and the *right* lattice sources. Those are non trivial problems in many other context (i.e. clustering), stated and solved as some kind of minimization problem. In our context, the problem is further complicated by the intrinsic non-linearity of ILSIA and the interleaving of the linear and non-linear procedures in LICA. It is not evident at this moment how to formulate a *well behaved* objective function for such purposes. Besides these fundamental problems, we will extend the validation evidence that may give the confidence to apply the method to new fMRI data sets as an exploratory tool by itself. We wishfully think that it could be applied to event oriented experiments, and to the task of discovering networks of activation in the brain.

Acknowledgements

We are grateful to the comments of the anonymous reviewers, which have helped us to improve the paper. The fruitful discussions with Dr. A. López de Munain and Dr. Sistiaga, from the Neurology Department, Donostia Hospital, which is embedded in the *Centro de Investigación Biomédica en Red sobre Enfermedades Neurodegenerativas* (CIBERNED) are also appreciated.

References

[1] A.L. Buffington, C.A. Hanlon, and M.J. McKeown. Acute and persistent pain modulation of attention-related anterior cingulate fmri activations. *Pain*, 113:172–184, 2005.

[2] V. Calhoun, G. Pearlson, and T. Adali. Independent component analysis applied to fMRI data: A generative model for validating results. *The Journal of VLSI Signal Processing*, 37(2):281–291, June 2004.

[3] V.D. Calhoun and T. Adali. Unmixing fMRI with independent component analysis. *Engineering in Medicine and Biology Magazine, IEEE*, 25(2):79–90, 2006.

[4] V.D. Calhoun, J.J. Pekar, and G.D. Pearlson. Alcohol intoxication effects on simulated driving: Exploring alcohol-dose effects on brain activation using functional mri. *Neuropsychopharmacology*, 29(11):2097–2107, 2004.

[5] K.J. Friston, J.T. Ashburner, S.J. Kiebel, T.E. Nichols, and Penny W.D. (eds.). *Statistical Parametric Mapping, the analysis of functional brain images*. Academic Press, 2007.

[6] K.J. Friston, A.P. Holmes, K.J. Worsley, J.P. Poline, C.D. Frith, and R.S.J. Frackowiak. Statistical parametric maps in functional imaging: A general linear approach. *Hum. Brain Map.*, 2(4):189–210, 1995.

[7] M. Graña. A brief review of lattice computing. In *Proc. WCCI 2008*, pages 1777–1781, 2008.

[8] M. Graña, I. Villaverde, J.O. Maldonado, and C. Hernandez. Two lattice computing approaches for the unsupervised segmentation of hyperspectral images. *Neurocomputing*, 72(10-12):2111–2120, 2009.

[9] Manuel Graña, M. García-Sebastian, I. Villaverde, and E. Fernández. An approach from lattice computing to fMRI analysis. In *LBM 2008 (CLA 2008), Proceedings of the Lattice-Based Modeling Workshop*, pages 33–44, 2008.

[10] M.D. Greicius, G. Srivastava, A.L. Reiss, and V. Menon. Default-mode network activity distinguishes alzheimer's disease from healthy aging: Evidence from func- tional mri. *Proc. Nat. Acad. Sci. U.S.A.*, 101(13):4637–4642, 2004.

[11] L. K. Hansen, J. Larsen, and T. Kolenda. Blind detection of independent dynamic components. *In proc. IEEE ICASSP'2001*, 5:3197–3200, 2001.

[12] P. Højen-Sørensen, O. Winther, and L.K. Hansen. Mean field approaches to independent component analysis. *Neural Computation*, 14:889–918, 2002.

[13] A. Hyvärinen, J. Karhunen, and E. Oja. *Independent Component Analysis*. John Wiley & Sons, New York, 2001.

[14] A. Hyvärinen and E. Oja. A fast fixed-point algorithm for independent component analysis. *Neural Comp.*, 9:1483–1492, 1997.

[15] C.L. Lawson and H.J. Hanson. *Solving least squares problems*. Prentice-Hall, (1974) Englewoods Cliffs NJ, 1974.

[16] L. Molgedey and H. Schuster. Separation of independent signals using time-delayed correlations. *Physical Review Letters*, 72(23):3634–3637, 1994.

[17] H.-P. Muller, E. Kraft, A. Ludolph, and S.N. Erne. New methods in fMRI analysis. *Engineering in Medicine and Biology Magazine, IEEE*, 21(5):134–142, 2002.

[18] J.J. Pekar. A brief introduction to functional MRI. *Engineering in Medicine and Biology Magazine, IEEE*, 25(2):24–26, 2006.

[19] B. Raducanu, M. Graña, and X. Albizuri. Morphological scale spaces and associative morphological memories: results on robustness and practical applications. *J. Math. Imaging and Vision*, 19(2):113–122, 2003.

[20] G. X. Ritter, J. L. Diaz-de Leon, and P. Sussner. Morphological bidirectional associative memories. *Neural Networks*, 12:851–867, 1999.

[21] G. X. Ritter, P. Sussner, and J. L. Diaz-de Leon. Morphological associative memories. *IEEE Trans. on Neural Networks*, 9(2):281–292, 1998.

[22] G.X. Ritter and P. Gader. Fixed points of lattice transforms and lattice associative memories. In P. Hawkes, editor, *Advances in Imaging and Electron Physics*, volume 144, pages 165–242. Elsevier, San Diego, CA., 2006.

[23] G.X. Ritter, G. Urcid, and L. Iancu. Reconstruction of patterns from noisy inputs using morphological associative memories. *J. Math. Imaging and Vision*, 19(2):95–112, 2003.

[24] G.X. Ritter, G. Urcid, and M.S. Schmalz. Autonomous single-pass endmember approximation using lattice auto-associative memories. *Neurocomputing*, 72(10-12):2101–2110, 2009.

[25] G.E. Sarty. *Computing Brain Activation Maps from fMRI Time-Series Images*. Cambridge University Press, 2007.

[26] FastICA site. http://www.cis.hut.fi/projects/ica/fastica/.

[27] ICA site. http://isp.imm.dtu.dk/toolbox/ica/index.html.

[28] S.C. Strother. Evaluating fMRI preprocessing pipelines. *Engineering in Medicine and Biology Magazine, IEEE*, 25(2):27–41, 2006.

[29] P. Sussner and M.E. Valle. Gray-scale morphological associative memories. *IEEE trans. Neural Networks*, 17(3):559–570, 2006.

[30] G. Urcid and J.C. Valdiviezo. Generation of lattice independent vector sets for pattern recognition applications. In *Mathematics of Data/Image Pattern Recognition, Compression, Coding, and Encryption X with Applications*, volume 6700, pages 1–12. Proc of SPIE, 2007.

[31] W Xiong, Y-O Li, H. Li, T. Adali, and V. D Calhoun. On ICA of complex-valued fMRI: advantages and order selection. In *Acoustics, Speech and Signal Processing, 2008. ICASSP 2008. IEEE International Conference on*, pages 529 –532, April 2008.

Results of an Adaboost Approach on Alzheimer's Disease Detection on MRI

Alexandre Savio[1], Maite García-Sebastián[1], Manuel Graña[1,⋆], and Jorge Villanúa[2]

[1] Grupo de Inteligencia Computacional
www.ehu.es/ccwintco
[2] Osatek, Hospital Donostia Paseo Dr. Beguiristain 109, 20014 San Sebastián, Spain

Abstract. In this paper we explore the use of the Voxel-based Morphometry (VBM) detection clusters to guide the feature extraction processes for the detection of Alzheimer's disease on brain Magnetic Resonance Imaging (MRI). The voxel location detection clusters given by the VBM were applied to select the voxel values upon which the classification features were computed. We have evaluated feature vectors computed over the data from the original MRI volumes and from the GM segmentation volumes, using the VBM clusters as voxel selection masks. We use the Support Vector Machine (SVM) algorithm to perform classification of patients with mild Alzheimer's disease vs. control subjects. We have also considered combinations of isolated cluster based classifiers and an Adaboost strategy applied to the SVM built on the feature vectors. The study has been performed on MRI volumes of 98 females, after careful demographic selection from the Open Access Series of Imaging Studies (OASIS) database, which is a large number of subjects compared to current reported studies. Results are moderately encouraging, as we can obtain up to 85% accuracy with the Adaboost strategy in a 10-fold cross-validation.

1 Introduction

Alzheimer's disease (AD) is a neurodegenerative disorder, which is one of the most common cause of dementia in old people. Currently, due to the socioeconomic importance of the disease in occidental countries it is one of the most studied. The diagnosis of AD can be done after the exclusion of other forms of dementia but a definitive diagnosis can only be made after a post-mortem study of the brain tissue. This is one of the reasons why Magnetic Resonance Imaging (MRI) based early diagnosis is a current research hot topic in the neurosciences.

Morphometry analysis has become a common tool for computational brain anatomy studies. It allows a comprehensive measurement of structural differences within a group or across groups, not just in specific structures, but throughout the entire brain. Voxel-based morphometry (VBM) is a computational approach

⋆ Research partially supported by Saiotek research projects BRAINER and S-PR07UN02, and the MEC research project DPI2006-15346-C03-03.

J. Mira et al. (Eds.): IWINAC 2009, Part II, LNCS 5602, pp. 114–123, 2009.

to neuroanatomy that measures differences in local concentrations of brain tissue, through a voxel-wise comparison of multiple brain images [1]. For instance, VBM has been applied to study volumetric atrophy of the grey matter (GM) in areas of neocortex of AD patients vs. control subjects [3,16,9]. The procedure involves the spatial normalization of subject images into a standard space, segmentation of tissue classes using *a priori* probability maps, smoothing to correct noise and small variations, and voxel-wise statistical tests. Statistical analysis is based on the General Linear Model (GLM) to describe the data in terms of experimental and confounding effects, and residual variability. Classical statistical inference is used to test hypotheses that are expressed in terms of GLM estimated regression parameters. This computation of given contrast provides a Statistical Parametric Map (SPM), which is thresholded according to the Random Field theory.

Machine learning methods have become very popular to classify functional or structural brain images to discriminate them into normal or a specific neurodegenerative disorder. The Support Vector Machine (SVM) either with linear [10,15] or non-linear [6,11] kernels are the state of the art to build up classification and regression systems. Besides MRI, other medical imaging methods are being studied for AD diagnosis. There are different ways to extract features from MRI for SVM classification: based on morphometric methods [5,6], based on regions of interest (ROI) [13,11] or GM voxels in automated segmentation images [10]. Work has also been reported on the selection of a small set of the most informative features for classification, such as the SVM-Recursive Feature Elimination [6], the selection based on statistical tests [13,15], the wavelet decomposition of the RAVENS maps [11], among others.

Many of the classification studies on the detection of AD were done with both men and women. However, it has been demonstrated that brains of women are different from men's to the extent that it is possible to discriminate the gender via MRI analysis [11]. Moreover, it has been shown that VBM is sensitive to the gender differences. For these reasons, we have been very cautious in this study. We have selected a set of 98 MRI women's brain volumes. It must be noted that this is a large number of subjects compared with the other studies referred above.

Our approach is to use the VBM detected clusters as a mask on the MRI and Grey Matter (GM) segmentation images to select the potentially most discriminating voxels. Feature vectors for classification are either the voxel values or some summary statistics of each cluster. We both consider the feature vector computed from all the VBM clusters and the combination of the individual classifiers built from the clusters independently. We build our classification systems using the standard SVM, testing linear and non-linear (RBF) kernels. Best results are obtained with an Adaptive Boosting (AdaBoost) strategy tailored to the SVM [12]. Section 2 gives a description of the subjects selected for the study, the image processing, feature extraction details and the classifier system. Section 3 gives our classification performance results and section 4 gives the conclusions of this work and further research suggestions.

2 Materials and Methods

2.1 Subjects

Ninety eight right-handed women (aged 65-96 yr) were selected from the Open Access Series of Imaging Studies (OASIS) database (http://www.oasis-brains.org) [14]. OASIS data set has a cross-sectional collection of 416 subjects covering the adult life span aged 18 to 96 including individuals with early-stage Alzheimer's Disease. We have ruled out a set of 200 subjects whose demographic, clinical or derived anatomic volumes information was incomplete. For the present study there are 49 subjects who have been diagnosed with very mild to mild AD and 49 non-demented. A summary of subject demographics and dementia status is shown in table 1.

Table 1. Summary of subject demographics and dementia status. Education codes correspond to the following levels of education: 1 less than high school grad., 2: high school grad., 3: some college, 4: college grad., 5: beyond college. Categories of socioeconomic status: from 1 (biggest status) to 5 (lowest status). MMSE score ranges from 0 (worst) to 30 (best).

	Very mild to mild AD	Normal
No. of subjects	49	49
Age	78.08 (66-96)	77.77 (65-94)
Education	2.63 (1-5)	2.87 (1-5)
Socioeconomic status	2.94 (1-5)	2.88 (1-5)
CDR (0.5 / 1 / 2)	31 / 17 / 1	0
MMSE	24 (15-30)	28.96 (26-30)

2.2 Imaging Protocol

Multiple (three or four) high-resolution structural T1-weighted magnetization-prepared rapid gradient echo (MP-RAGE) images were acquired [7] on a 1.5-T Vision scanner (Siemens, Erlangen, Germany) in a single imaging session. Image parameters: TR= 9.7 msec., TE= 4.0 msec., Flip angle= 10, TI= 20 msec., TD= 200 msec., 128 sagittal 1.25 mm slices without gaps and pixels resolution of 256×256 (1×1mm).

2.3 Image Processing and VBM

We have used the average MRI volume for each subject, provided in the OASIS data set. These images are already registered and resampled into a 1-mm isotropic image in atlas space and the bias field has been already corrected [14]. The Statistical Parametric Mapping (SPM5) (http://www.fil.ion.ucl.ac.uk/spm/) was used to compute the VBM which gives us the spatial mask to obtain the classification features. Images were reoriented into a right-handed coordinate system to work

with SPM5. The tissue segmentation step does not need to perform bias correction. We performed the modulation normalization for grey matter, because we are interested in this tissue for this study. We performed a spatial smoothing before performing the voxel-wise statistics, setting the Full-Width at Half-Maximum (FWHM) of the Gaussian kernel to 10mm isotropic. A GM mask was created from the average of the GM segmentation volumes of the subjects under study. Thresholding the average GM segmentation, we obtain a binary mask that includes all voxels with probability greater than 0.1 in the average GM segmentation volume. This interpretation is not completely true, since the data are modulated, but it is close enough for the mask to be reasonable. We design the statistical analysis as a Two-sample t-test in which the first group corresponds with AD subjects. The general linear model contrast has been set as [-1 1], a right-tailed (groupN ¿ groupAD), correction FWE, p-value=0.05. The VBM detected clusters are used for the MRI feature extraction for the SVM classification.

2.4 Support Vector Machine Classification

The Support Vector Machine (SVM)[18] algorithm used for this study is included in the libSVM (`http://www.csie.ntu.edu.tw/~cjlin/libsvm/`) software package. The implementation is described in detail in [4]. Given training vectors $x_i \in R_n, i = 1, \ldots, l$ of the subject features of the two classes, and a vector $y \in R^l$ such that $y_i \in \{-1, 1\}$ labels each subject with its class, in our case, for example, patients were labeled as -1 and control subject as 1. To construct a classifier, the SVM algorithm solves the following optimization problem:

$$\min_{w,b,\xi} \frac{1}{2} w^T w + C \sum_{i=1}^{l} \xi_i$$

subject to $y_i(w^T \phi(x_i) + b) \geq (1 - \xi_i),\ \xi_i \geq 0, i = 1, 2, \ldots, n$. The dual optimization problem is

$$\min_{\alpha} \frac{1}{2} \alpha^T Q \alpha - e^T \alpha$$

subject to $y^T \alpha = 0,\ 0 \leq \alpha_i \leq C,\ i = 1, \ldots, l$. Where e is the vector of all ones, $C > 0$ is the upper bound on the error, Q is an l by l positive semi-definite matrix, $Q_{ij} \equiv y_i y_j K(x_i, x_j)$, and $K(x_i, x_j) \equiv \phi(x_i)^T \phi(x_j)$ is the kernel function that describes the behavior of the support vectors. Here, the training vectors x_i are mapped into a higher (maybe infinite) dimensional space by the function $\phi(x_i)$. The decision function is $sgn(\sum_{i=1}^{l} y_i \alpha_i K(x_i, x) + b)$. C is a regularization parameter used to balance the model complexity and the training error.

The kernel function chosen results in different kinds of SVM with different performance levels, and the choice of the appropriate kernel for a specific application is a difficult task. In this study two different kernels were tested: the linear and the radial basis function (RBF) kernel. The linear kernel function is defined as $K(x_i, x_j) = 1 + x_i^T x_j$, this kernel shows good performance for linearly separable data. The RBF kernel is defined as $K(x_i, x_j) = exp(-\frac{||x_i - x_j||^2}{2\sigma^2})$. This

kernel is basically suited best to deal with data that have a class-conditional probability distribution function approaching the Gaussian distribution [2]. One of the advantages of the RBF kernel is that given the kernel, the number of support vectors and the support vectors are all automatically obtained as part of the training procedure, i.e., they do not need to be specified by the training mechanism.

2.5 Feature Extraction

We have tested three different feature vector extraction processes, based on the voxel location clusters detection obtained from the VBM analysis.

1. The first feature extraction process computes the ratio of GM voxels to the total number of voxels of each voxel location cluster.
2. The second feature extraction process computes the mean and standard deviation of the GM voxel intensity values of each voxel location cluster.
3. The third feature feature extraction process computes a very high dimensional vector with all the GM segmentation values for the voxel locations included in each VBM detected cluster. The GM segmentation voxel values were ordered in this feature vector according to the coordinate lexicographic order.

First, we have considered all the VBM detected clusters together, so that each feature vector characterizes the whole MRI volume.

2.6 Combination of SVM

We have considered also the construction of independent SVM classifiers for each VBM detected cluster and the combination of their responses by a simple majority voting, and to use the cluster with greatest statistical significance to resolve ties. This can be viewed as a simplified combination of classifiers. Furthermore, we have defined a combination of classifiers weighted by the individual training errors, where the classifier weights are computed as in the AdaBoost-SVM algorithm in [12] (Algorithm 1), assuming an uniform weighting of the data samples.

2.7 Adaptive Boosting

Adaptive Boosting (AdaBoost)[17,8] is a meta-algorithm for machine learning that can be used in conjunction with many other learning algorithms to improve their performance. AdaBoost is adaptive in the sense that subsequent classifiers built are tweaked in favor of those instances misclassified by previous classifiers. AdaBoost is sensitive to noisy data and outliers. Otherwise, it is less susceptible to the over-fitting problem than most learning algorithms.

AdaBoost calls a weak classifier repeatedly in a series of rounds $t = 1, ..., T$. For each call a distribution of weights W_t is updated and indicates the importance of examples in the data set for the classification. On each round, the weights

Algorithm 1. Combining the independent SVM trained per cluster

1. **Input:** as many sets of training samples with labels as clusters in the statistical parametric map $T_k = \{(x_1, y_1), \ldots, (x_N, y_N)\}, k = 1..C$, where N is the number of samples of each cluster.
2. **Initialize:** the weights of training samples: $w_i^k = 1/N$, for all $i = 1, ..., N$
3. **For each *k* cluster do**
   (a) Search the best γ for the RBF kernel for the training set T_k, we denote it as γ_k.
   (b) Train the SVM with T_k and γ_k, we denote the classifier as h_k.
   (c) Classify the same training T_k set with h_k.
   (d) Calculate the training error of h_k: $\epsilon_k = \sum_{i=1}^{N} w_i^k, \quad y_i \neq h_k(x_i)$.
   (e) Compute the weight of the cluster classifier h_k: $\alpha_k = \frac{1}{2} \ln(\frac{\epsilon_k}{1-\epsilon_k})$.
4. **Output:** for each test data x its classification is $f(x) = sign(\sum_{k=1}^{C} \alpha_k h_k(x))$.

of each incorrectly classified example are increased (or alternatively, the weights of each correctly classified example are decreased), so that the new classifier focuses more on those examples.

Following these ideas, we have also tested a combination of SVM classifiers along the ideas from the Diverse AdaBoost SVM [12], presented as Algorithm 2. In this approach we built a sequence of SVM classifiers of increasing variance parameter. The results of the classifiers are weighted according to their statistical error to obtain the response to the test inputs in the 10-fold validation process.

2.8 Classifier Performance Indices

We evaluated the performance of the classifiers built with the diverse strategy using 10 times the 10-fold cross-validation methodology. To quantify the results we measured the accuracy, the ratio of the number of test volumes correctly classified to the total of tested volumes. We also quantified the specificity and sensitivity of each test defined as $Specificity = \frac{TP}{TP+FP}$ and $Sensitivity = \frac{TN}{TN+FN}$, where TP is the number of true positives: number of AD patient volumes correctly classified; TN is the number of true negatives: number of control volumes correctly classified; FP is the number of false positives: number of AD patient volumes classified as control volume; FN is the number of false negatives: number of control volumes classified as patient. The regularization parameter C of all the SVM classifiers trained for this study was set to 1.

Algorithm 2. Diverse AdaBoostSVM

1. **Input:** a set of training samples with labels $\{(x_1, y_1), \ldots, (x_N, y_N)\}$; the initial σ, σ_{ini}; the minimal σ, σ_{min}; the step of σ, σ_{step}; the threshold on diversity DIV.
2. **Initialize:** the weights of training samples: $w_i^t = 1/N$, for all $i = 1, ..., N$
3. **Do while** $(\sigma > \sigma_{ini})$
   (a) Calculate gamma: $\gamma = \left(2\sigma^2\right)^{-1}$.
   (b) Use σ to train a component classifier h_t on the weighted training set.
   (c) Calculate the training error of h_t: $\epsilon_t = \sum_{i=1}^{N} w_i^t, \quad y_i \neq h_t(x_i)$.
   (d) Calculate the diversity of h_t: $D_t = \sum_{i=1}^{N} d_t(x_i)$, where $d_t(x_i) = \begin{cases} 0 & if\ h_t(x_i) = y_i \\ 1 & if\ h_t(x_i) \neq y_i \end{cases}$
   (e) Calculate the diversity of weighted component classifiers and the current classifier: $D = \sum_{t=1}^{T} \sum_{i=1}^{N} d_t(x_i)$.
   (f) If $\epsilon_t > 0.5$ or $D < DIV$: decrease σ by σ_{step} and go to (a).
   (g) Set weight of the component classifier h_t: $\alpha_t = \frac{1}{2} \ln(\frac{\epsilon_t}{1-\epsilon_t})$.
   (h) Update the weights of training samples: $w_i^{t+1} = w_i^t exp(-\alpha y_i h_t(x_i))$.
   (i) Normalize the weights of training samples: $w_i^{t+1} = w_i^{t+1}(\sum_{i=1}^{N} w_i^{t+1})^{-1}$.
4. **Output:** $f(x) = sign(\sum_{k=1}^{C} \alpha_k h_k(x))$.

3 Results

In this section we present for each experiment the following data: the number of features, accuracy, specificity, which is related to AD patients and sensitivity, which is related to control subjects. We will give results on the global feature vectors, the simple voting of independent classifiers based on statistical significance of VBM, the weighted combination of individual cluster SVM based on training errors, and an adaptive boosting strategy for combining classifiers.

3.1 Global Feature Vectors

The VBM performed for this study was described in section 2. We present in table 2 the results of the three feature computation processes applied to the whole set of VBM clusters to obtain a single feature vector for the whole volume. Each table entry contains the SVM results using the linear (lk) and RBF (nlk) kernels upon the corresponding feature vector set. The table rows correspond to the feature extraction processes described in section 2.5. Table 2 best accuracy result is 80.6% with the RBF kernel, but this result is not too far from the results of the linear kernel SVM. This best accuracy result is obtained with a rather straightforward feature extraction method: the mean and standard deviation of the MRI voxel intensities. This means that MRI intensities may have discriminant value.

Table 2. Classification results with a linear kernel (lk) and a non-linear RBF kernel (nlk). The values of $\gamma = \left(2\sigma^2\right)^{-1}$ for non linear kernel were 0.5, 0.031, 0.0078 for each feature extraction process, respectively.

Feature extracted	#Features	Accuracy (lk/nlk)	Sensitivity (lk/nlk)	Specificity (lk/nlk)
GM proportion	12	69.39 / 68.36	0.63 / 0.61	0.88 / 0.90
Mean & StDev	24	78.57 / 80.61	0.72 / 0.75	0.88 / 0.89
Voxel intensities	3611	73.47 / 76.53	0.72 / 0.77	0.75 / 0.76

Overall the sensitivity results in table 2 is much lower than the specificity. We believe that the source of error is the confusion of mild demented AD patients with control subjects. Upon inspection, this hypothesis seems to be correct for this data.

3.2 Combination of Individual Cluster SVM

Table 3 presents the results of the combination of SVM classifiers built up over each cluster independently, searching for the best kernel parameter σ in each classifier independently. The voxel clusters are selected according to the VBM performed as described above. The results do not improve over the ones obtained with the whole image feature vector. We note that, contrary to the global feature vector, the results improve when considering the whole collection of MRI voxel intensities.

Table 4 presents the results of the combination of individual weighted SVM classifiers. Each SVM classifier was trained with one VBM cluster feature set and the weights were computed according to its training error. We obtain a

Table 3. Majority voting classification results with linear kernel (lk) and non-linear kernel (nlk) SVM built independently for each VBM cluster

Feature extracted	#Features	Accuracy (lk/nlk)	Sensitivity (lk/nlk)	Specificity (lk/nlk)
Mean & StDev	24	74% / 75%	0.51 / 0.56	0.97 / 0.95
Voxel intensities	3611	77% / 78%	0.74 / 0.76	0.80 / 0.82

Table 4. Weighted individual SVM per cluster classification results. The value of the RBF kernels for the nonlinear (nlk) classifiers were searched for the best fit to the training set.

Feature extracted	Features	Accuracy (lk/nlk)	Sensitivity (lk/nlk)	Specificity (lk/nlk)
Mean & StDev	24	71% / 79%	0.54 / 0.78	0.88 / 0.80
Voxel intensities	3611	73% / 86%	0.76 / 0.80	0.70 / 0.92

Table 5. Diverse AdaBoostSVM classification results

Feature extracted	Features	Accuracy	Sensitivity	Specificity
Mean & StDev	24	85%	0.78	0.92
Voxel intensities	3611	78%	0.71	0.85

significant improvement of the accuracy when considering the voxel intensities as features for the non-linear RBF SVM.

Table 5 shows the results of the Diverse . The σ_{min} is set as 0.1, the σ_{ini} is set as 100 and σ_{step} is set as 0.1. The DIV value is set as as 0.6.

4 Conclusions

In this work we have studied feature extraction processes based on VBM analysis, to classify MRI volumes of AD patients and normal subjects. We have analyzed different designs for the SPM of the VBM and we have found that the basic GLM design without covariates can detect subtle changes between AD patients and controls that lead to the construction of SVM classifiers with a discriminative accuracy of 86% in the best case. The weighted cluster SVM and the Diverse AdaBoostSVM methods improved remarkably the results, mainly the sensitivity of the classification models. In [5] they compare their results on a smaller population of controls and AD patients to the ones obtained with a standard VBM analysis, using a cluster and found a classification accuracy of 63.3% via cross-validation. Therefore, the results shown in this paper, along with the careful experimental methodology employed, can be of interest for the Neuroscience community researching on the AD diagnosis based on MRI. Further work may address the extraction of features based on other morphological measurement techniques, such as the Deformation-based Morphometry.

Acknowledgments

We thank the Washington University ADRC for making MRI data available.

References

1. Ashburner, J., Friston, K.J.: Voxel-based morphometry: The methods. Neuroimage 11(6), 805–821 (2000)
2. Burges, C.: A tutorial on support vector machines for pattern recognition. Data Mining and Knowledge Discovery 2(2), 167 (1998)
3. Busatto, G.F., Garrido, G.E.J., Almeida, O.P., Castro, C.C., Camargo, C.H.P., Cid, C.G., Buchpiguel, C.A., Furuie, S., Bottino, C.M.: A voxel-based morphometry study of temporal lobe gray matter reductions in alzheimer's disease. Neurobiology of Aging 24(2), 221–231 (2003)
4. Chang, C.-C., Lin, C.-J.: LIBSVM: a library for support vector machines. Software (2001), `http://www.csie.ntu.edu.tw/~cjlin/libsvm`
5. Davatzikos, C., Fan, Y., Wu, X., Shen, D., Resnick, S.M.: Detection of prodromal alzheimer's disease via pattern classification of magnetic resonance imaging. Neurobiology of Aging 29(4), 514–523 (2008)
6. Fan, Y., Shen, D., Davatzikos, C.: Classification of Structural Images via High-Dimensional Image Warping, Robust Feature Extraction, and SVM, pp. 1–8 (2005)

7. Fotenos, A.F., Snyder, A.Z., Girton, L.E., Morris, J.C., Buckner, R.L.: Normative estimates of cross-sectional and longitudinal brain volume decline in aging and AD. Neurology 64(6), 1032–1039 (2005)
8. Freund, Y., Schapire, R.: A decision-theoretic generalization of on-line learning and an application to boosting. In: European Conference on Computational Learning Theory, pages 37, 23 (1995)
9. Frisoni, G.B., Testa, C., Zorzan, A., Sabattoli, F., Beltramello, A., Soininen, H., Laakso, M.P.: Detection of grey matter loss in mild alzheimer's disease with voxel based morphometry. Journal of Neurology, Neurosurgery & Psychiatry 73(6), 657–664 (2002)
10. Kloppel, S., Stonnington, C.M., Chu, C., Draganski, B., Scahill, R.I., Rohrer, J.D., Fox, N.C., Jack Jr., C.R., Ashburner, J., Frackowiak, R.S.J.: Automatic classification of MR scans in alzheimer's disease. Brain 131(3), 681 (2008)
11. Lao, Z., Shen, D., Xue, Z., Karacali, B., Resnick, S.M., Davatzikos, C.: Morphological classification of brains via high-dimensional shape transformations and machine learning methods. Neuroimage 21(1), 46–57 (2004)
12. Li, X., Wang, L., Sung, E.: A study of AdaBoost with SVM based weak learners. In: Proceedings of IEEE International Joint Conference on Neural Networks, IJCNN 2005, vol. 1, pp. 196–201 (2005)
13. Liu, Y., Teverovskiy, L., Carmichael, O., Kikinis, R., Shenton, M., Carter, C.S., Stenger, V.A., Davis, S., Aizenstein, H., Becker, J.T.: Discriminative MR image feature analysis for automatic schizophrenia and alzheimer's disease classification. In: Barillot, C., Haynor, D.R., Hellier, P. (eds.) MICCAI 2004. LNCS, vol. 3216, pp. 393–401. Springer, Heidelberg (2004)
14. Marcus, D.S., Wang, T.H., Parker, J., Csernansky, J.G., Morris, J.C., Buckner, R.L.: Open access series of imaging studies (OASIS): cross-sectional MRI data in young, middle aged, nondemented, and demented older adults. Journal of Cognitive Neuroscience 19(9), 1498–1507 (2007) PMID: 17714011
15. Ramirez, J., Gorriz, J.M., Lopez, M., Salas-Gonzalez, D., Alvarez, I., Segovia, F., Puntonet, C.G.: Early detection of the alzheimer disease combining feature selection and kernel machines. In: 15th International Conference on Neural Information Processing of the Asia-Pacific Neural Network Assembly (ICONIP 2008) (2008)
16. Scahill, R.I., Schott, J.M., Stevens, J.M., Rossor, M.N., Fox, N.C.: Mapping the evolution of regional atrophy in alzheimer's disease: Unbiased analysis of fluid-registered serial MRI. Proceedings of the National Academy of Sciences 99(7), 4703 (2002)
17. Schapire, R.E., Singer, Y.: Improved boosting algorithms using confidence-rated predictions. Machine Learning 37(3), 297–336 (1999)
18. Vapnik, V.N.: Statistical Learning Theory. Wiley-Interscience, Hoboken (1998)

Classification Results of Artificial Neural Networks for Alzheimer's Disease Detection

Alexandre Savio[1], Maite García-Sebastián[1], Carmen Hernández[1], Manuel Graña[1,⋆], and Jorge Villanúa[2]

[1]Grupo de Inteligencia Computacional
www.ehu.es/ccwintco
[2]Osatek, Hospital Donostia Paseo Dr. Beguiristain 109, 20014 San Sebastián, Spain

Abstract. Detection of Alzheimer's disease on brain Magnetic Resonance Imaging (MRI) is a highly sought goal in the Neurosciences. We used four different models of Artificial Neural Networks (ANN): Backpropagation (BP), Radial Basis Networks (RBF), Learning Vector Quantization Networks (LVQ) and Probabilistic Neural Networks (PNN) to perform classification of patients of mild Alzheimer's disease vs. control subjects. Features are extracted from the brain volume data using Voxel-based Morphometry (VBM) detection clusters. The voxel location detection clusters given by the VBM were applied to select the voxel values upon which the classification features were computed. We have evaluated feature vectors computed from the GM segmentation volumes using the VBM clusters as voxel selection masks. The study has been performed on MRI volumes of 98 females, after careful demographic selection from the Open Access Series of Imaging Studies (OASIS) database, which is a large number of subjects compared to current reported studies.

1 Introduction

Alzheimer's disease (AD) is a neurodegenerative disorder, which is one of the most common cause of dementia in old people. Currently, due to the socioeconomic importance of the disease in occidental countries it is one of the most studied. The diagnosis of AD can be done after the exclusion of other forms of dementia but a definitive diagnosis can only be made after a post-mortem study of the brain tissue. This is one of the reasons why early diagnosis based on Magnetic Resonance Imaging (MRI) is a current research hot topic in the neurosciences.

Morphometry analysis has become a common tool for computational brain anatomy studies. It allows a comprehensive measurement of structural differences within a group or across groups, not just in specific structures, but throughout the entire brain. Voxel-based Morphometry (VBM) is a computational approach to neuroanatomy that measures differences in local concentrations of brain tissue through a voxel-wise comparison of multiple brain images [2]. For instance, VBM

⋆ Research partially supported by Saiotek research projects BRAINER and S-PR07UN02, and the MEC research project DPI2006-15346-C03-03.

E. Corchado and H. Yin (Eds.): IDEAL 2009, LNCS 5788, pp. 641–648, 2009.

has been applied to study volumetric atrophy of the grey matter (GM) in areas of neocortex of AD patients vs. control subjects [3,18,7]. The procedure involves the spatial normalization of subject images into a standard space, segmentation of tissue classes using *a priori* probability maps, smoothing to reduce noise and small variations, and voxel-wise statistical tests. Statistical analysis is based on the General Linear Model (GLM) to describe the data in terms of experimental and confounding effects, and residual variability. Classical statistical inference is used to test hypotheses that are expressed in terms of GLM estimated regression parameters. This computation of given contrast provides a Statistical Parametric Map (SPM), which is thresholded according to the Random Field theory.

Machine learning methods have become very popular to classify functional or structural brain images to discriminate them into normal or a specific neurodegenerative disorder. The Artificial Neural Networks (ANN) used for this study were the Feedforward Networks (sometimes called Multilayer Perceptron) trained with the Backpropagation of errors algorithm (BP), Radial Basis Networks (RBF), Learning Vector Quantization (LVQ) and Probabilistic Neural Networks (PNN) [10]. Support Vector Machine (SVM) both with linear [12] and non-linear [14] kernels have been tested in a previous work for the same task [8]. There are different ways to extract features from MRI for classification: based on morphometric methods [5], based on regions of interest (ROI) [15,14] or GM voxels in automated segmentation images [12]. Our approach is to use the VBM detected clusters as a mask on the Grey Matter (GM) segmentation images to select the potentially most discriminating voxels. Feature vectors for classification are either the voxel values or some summary statistics of each cluster. We considered the feature vector computed from all the VBM clusters together.

A work using ANNs and VBM for AD detection have been reported in [11], where a single three-layer, feed-forward ANN trained with a backpropagation algorithm was used as a classifier over a small set of unpublished proprietary MRI data. They perform data dimensionality reduction applying a Principal Component Analysis (PCA) to improve the efficiency of the classifier. Although their results can not be reproduced, this work confirms that the approach that we follow is a promising area of research.

Section Materials and Methods gives a description of the subjects selected for the study, the image processing, feature extraction details and the classifier system. Section Results gives our classification performance results and section Conclusions gives the conclusions of this work and further research suggestions.

2 Materials and Methods

Subjects. Ninety eight right-handed women (aged 65-96 yr) were selected from the Open Access Series of Imaging Studies (OASIS) database [16]. OASIS data set has a cross-sectional collection of 416 subjects covering the adult life span aged 18 to 96 including individuals with early-stage Alzheimer's Disease. We have ruled out a set of 200 subjects whose demographic, clinical or derived anatomic volumes information was incomplete. For the present study there are 49 subjects

Table 1. Summary of subject demographics and dementia status. Education codes correspond to the following levels of education: 1 less than high school grad., 2: high school grad., 3: some college, 4: college grad., 5: beyond college. Categories of socioeconomic status: from 1 (biggest status) to 5 (lowest status). MMSE score ranges from 0 (worst) to 30 (best).

	Very mild to mild AD	Normal
No. of subjects	49	49
Age	78.08 (66-96)	77.77 (65-94)
Education	2.63 (1-5)	2.87 (1-5)
Socioeconomic status	2.94 (1-5)	2.88 (1-5)
CDR (0.5 / 1 / 2)	31 / 17 / 1	0
MMSE	24 (15-30)	28.96 (26-30)

who have been diagnosed with very mild to mild AD and 49 non-demented. A summary of subject demographics and dementia status is shown in table 1.

Imaging protocol. Multiple (three or four) high-resolution structural T1-weighted magnetization-prepared rapid gradient echo (MP-RAGE) images were acquired [6] on a 1.5-T Vision scanner (Siemens, Erlangen, Germany) in a single imaging session. Image parameters: TR= 9.7 msec., TE= 4.0 msec., Flip angle= 10, TI= 20 msec., TD= 200 msec., 128 sagittal 1.25 mm slices without gaps and pixels resolution of 256×256 (1×1mm).

Image processing and VBM. We have used the average MRI volume for each subject, provided in the OASIS data set. These images are already registered and re-sampled into a 1-mm isotropic image in atlas space and the bias field has been already corrected [16]. The Statistical Parametric Mapping software (SPM5) [1] was used to compute the VBM which gives us the spatial mask to obtain the classification features. Images were reoriented into a right-handed coordinate system to work with SPM5. The tissue segmentation step does not need to perform bias correction. We performed the modulation normalization for GM, because we are interested in this tissue for this study. We performed a spatial smoothing before performing the voxel-wise statistics, setting the Full-Width at Half-Maximum (FWHM) of the Gaussian kernel to 10mm isotropic. A GM mask was created from the average of the GM segmentation volumes of the subjects under study. Thresholding the average GM segmentation, we obtain a binary mask that includes all voxels with probability greater than 0.1 in the average GM segmentation volume. This interpretation is not completely true, since the data is modulated, but it is close enough for the mask to be reasonable. We designed the statistical analysis as a Two-sample t-test in which the first group corresponds with AD subjects. In SPM software terms: the contrast has been set to [-1 1], a right-tailed (groupN > groupAD), correction FWE, p-value=0.05. The VBM detected clusters are used for the feature extraction for the classification procedures.

Backpropagation. Backward propagation of errors or Backpropagation (BP) [17,10,9] is a supervised learning method, and it is a non-linear generalization of the squared error gradient descent learning rule for updating the weights of the artificial neurons in a single-layer perceptron, generalized to feed-forward networks . Backpropagation requires that the activation function used by the artificial neurons (or "nodes") is differentiable with its derivative being a simple function of itself. The backpropagation of the error allows to compute the gradient of the error function relative to the hidden units. It is analytically derived using the chain rule of calculus. During on-line learning the weights of the network are updated at each input data item presentation. We have used the resilient backpropagation, which uses only the derivative sign to perform the weight updating.

Radial Basis Function Networks. Radial basis function networks (RBF) [4] are ANN that use radial basis functions as activation functions. RBF's consist of a two layer neural network, where each hidden unit implements a radial activated function. The output units compute a weighted sum of hidden unit outputs. Training consists of the unsupervised training of the hidden units followed by the supervised training of the output units' weights.

Probabilistic Neural Networks. A Probabilistic Neural Network (PNN) [20] is a special type of neural network that uses a kernel-based approximation to form an estimate of the probability density function of categories in a classification problem. The distance is computed from the point being evaluated to each of the other points, and a *radial basis function* (RBF) is applied to the distance to compute the weight (influence) for each point.

Different types of radial basis functions could be used, but the most common is the Gaussian function. The sigma value of the function determines the *spread* of the RBF function; that is, how quickly the function declines as the distance increased from the point. With larger sigma values the function has more spread, so that distant points have a greater influence. PNN are a kind of Nearest Neighbor classifier that uses all the data samples as reference values and the only functional transformation is the computation of the posterior probability of the classes as a combination (sum/average) of the evidence given by each data sample through its RBF window.

The tuning of a PNN network depends on selecting the optimal sigma value of the spread of the RBF functions. In this paper an exhaustive search for the optimal spread value in the range (0, 1) for each training set has been done. The results shown in Table 4 correspond to the best spread value found.

Learning Vector Quantization. Learning vector quantization (LVQ) [13,19] provides a method for training competitive layers in a supervised manner. The system is composed of an unsupervisedly trained competitive layer which performs a partitioning of the input space. The supervisedly trained output layer provides the labeling of the input data according to its belonging to an input region (crisp clustering) or to its degree of membership (soft clustering). In the

original proposition of the LVQ, the competitive units were cluster centers with the Euclidean distance as the similitude measure. Training of the competitive units can be performed by Kohonen's Self Organizing Map. Supervised training was simply the assignment of a label to a competitive unit according to a majority voting on the data samples falling in the partition corresponding to the unit. LVQ provides fine tuning of the competitive units using class information. The basic versions proposed by Kohonen are known as the LVQ1 and LVQ2. Both start with the unsupervised learning of the competitive units, and its initial majority voting labeling. In the LVQ1 a supervised training is performed as follows: for each data sample we compare its label with the one of its corresponding competitive unit, if the labels match (the data item is correctly classified) then the competitive unit is moved towards the input data sample, otherwise it is moved in the opposite direction. This rule may cause an unstable and oscillatory behavior if the discriminant boundary among classes is very complex. The LVQ2 rule is proposed to improve the learning, sometimes it is recommended to apply it *after* the LVQ1. In LVQ2, for each input data sample we find the two closest competitive units. If one correctly classifies the input and the other belongs to a wrong class, and the input data lies in a window around the mid-plane between them, then the correct class unit is moved towards the input and the incorrect unit is moved away from the input. We have used the simplest implementations.

Feature extraction. We have tested two different feature vector extraction processes, based on the voxel location clusters detection obtained from the VBM analysis. The features were extracted from the output volumes of the segmentation step in the VBM analysis, they are a GM density volume for each subject.

1. The first feature extraction process computes the mean and standard deviation of the GM voxel values of each voxel location cluster, we denote these features as MSD in the result tables given below.
2. The second feature extraction process computes a very high dimensional vector with all the GM segmentation values for the voxel locations included in each VBM detected cluster. The voxel values were ordered in this feature vector according to the coordinate lexicographical ordering. We denote these features as VV in the result tables below.

3 Results

We evaluated the performance of the classifiers built with the diverse training and architecture strategies using 10 times the 10-fold cross-validation methodology. In this section we present for each experiment the following data: the number of features extracted from each subject, classification accuracy, sensitivity, which is related to AD patients and specificity, which is related to control subjects. The results shown are the mean values of the classification results from the 10-fold crossvalidation process, also the standard deviation (stdev) is shown. We will give results of each different classifiers: Backpropagation (Table 2), RBF (Table 3), PNN (Table 4), LVQ1 (Table 5) and LVQ2 (6).

Table 2. Classification results with a BP network with resilient backpropagation. Mean (Standard deviation) of 10 cross-validations.

Feature extracted	#Features	#Hidden units	%Accuracy	Sensitivity	Specificity
MSD	24	10	78.0 (0.12)	0.69 (0.14)	0.88 (0.13)
VV	3611	10	78.0 (0.11)	0.72 (0.17)	0.84 (0.18)

Table 3. Classification results with a RBF network. Mean (Standard deviation) of 10 cross-validations.

Feature extracted	#Features	Spread	%Accuracy	Sensitivity	Specificity
MSD	24	0.02	66.00 (0.13)	0.65 (0.24)	0.68 (0.14)
VV	3611	0.852	72.5 (0.10)	0.65 (0.21)	0.80 (0.17)

Table 4. Classification results with a PNN network. Mean (Standard deviation) of 10 cross-validations.

Feature extracted	#Features	Spread	%Accuracy	Sensitivity	Specificity
MSD	24	0.02;	77.8 (0.09)	0.62 (0.14)	0.94 (0.1)
VV	3611	0.852	74.2 (0.14)	0.68 (0.20)	0.81 (0.17)

Table 5. Classification results with a LVQ1 network . Network training parameters:MSD: 200 epochs, goal: 0.01 and learning rate: 0.01 ; VV : 150 epochs, goal: 0.10 and learning rate: 0.010.Mean (Standard deviation) of 10 cross-validations.

Feature extracted	#Features	#Hidden units	%Accuracy	Sensitivity	Specificity
MSD	24	10	81.0 (0.18)	0.72 (0.27)	0.90 (0.14)
VV	3611	10	79.3 (0.13)	0.76 (0.23)	0.82 (0.19)

Table 6. Classification results with a LVQ2 network . Network training parameters: MSD : 200 epochs, goal: 0.01 and learning rate: 0.01; VV : 50 epochs, goal: 0.01 and learning rate: 0.005. Mean (Standard deviation) of 10 crossvalidations.

Feature extracted	#Features	#Hidden units	% Accuracy	Sensitivity	Specificity
MSD	24	10	83.0 (0.12)	0.74 (0.23)	0.92 (0.1)
VV	3611	10	77.0 (0.15)	0.76 (0.23)	0.78 (0.17)

The best accuracy result (Table 6) is 83% with the LVQ2, but this result is not far from the results of LVQ1 and PNN. Which is a very encouraging result, given that we have not removed critical subjects from the data collection: very mildly demented subjects who could end in a false positive diagnosis and . Regarding the usefulness of the features extracted, it is difficult to make an assessment, because some algorithms work better with VV than with MSD, and other have the inverse performance. Training and validation on MSD features is obviously more time efficient, and the best result corresponds to this feature extraction process.

4 Conclusions

In this work we have studied several ANN classifiers applied to classify MRI volumes of AD patients and normal subjects. The feature extraction processes is based on VBM analysis. After examining different designs for the SPM of the VBM we have found that the basic GLM design without covariates can detect subtle changes between AD patients and controls that lead to the construction of ANN classifiers with a discriminative accuracy of 83% in the best case as shown in table 6. A result of 83% of accuracy is really encouraging considering the number of subjects in the database. Improvements could be obtained using Adaptive Boosting including different types of ANNs and Support Vector Machines. The problem we have found is that the subjects wrongly classified maybe the most critical ones: old control subjects classified as AD (false positives) and subjects with a very early or mild dementia classified as normal (false negatives), exactly the ones which are the target in these studies that try to perform early detection of AD. Post-mortem confirmation data of AD diagnosed subjects could improve the results.

Further work may address the use of disease specific templates or other type of morphometric measures, such as Deformation-based Morphometry.

Acknowledgments

We thank the Washington University ADRC for making MRI data available.

References

1. http://www.fil.ion.ucl.ac.uk/spm/
2. Ashburner, J., Friston, K.J.: Voxel-based morphometry: The methods. Neuroimage 11(6), 805–821 (2000)
3. Busatto, G.F., Garrido, G.E.J., Almeida, O.P., Castro, C.C., Camargo, C.H.P., Cid, C.G., Buchpiguel, C.A., Furuie, S., Bottino, C.M.: A voxel-based morphometry study of temporal lobe gray matter reductions in alzheimer's disease. Neurobiology of Aging 24(2), 221–231 (2003)
4. Chen, S., Cowan, C.F.N., Grant, P.M.: Orthogonal least squares learning algorithm for radial basis function networks. IEEE Transactions on Neural Networks 2(2), 302–309 (1991)
5. Davatzikos, C., Fan, Y., Wu, X., Shen, D., Resnick, S.M.: Detection of prodromal alzheimer's disease via pattern classification of magnetic resonance imaging. Neurobiology of Aging 29(4), 514–523 (2008)
6. Fotenos, A.F., Snyder, A.Z., Girton, L.E., Morris, J.C., Buckner, R.L.: Normative estimates of cross-sectional and longitudinal brain volume decline in aging and AD. Neurology 64(6), 1032–1039 (2005)
7. Frisoni, G.B., Testa, C., Zorzan, A., Sabattoli, F., Beltramello, A., Soininen, H., Laakso, M.P.: Detection of grey matter loss in mild alzheimer's disease with voxel based morphometry. Journal of Neurology, Neurosurgery & Psychiatry 73(6), 657–664 (2002)

8. García-Sebastián, M., Savio, A., Graña, M., Villanúa, J.: On the use of morphometry based features for Alzheimer's disease detection on MRI. In: Omatu, S., Rocha, M.P., Bravo, J., Fernandez, F., Corchado, E., Bustillo, A., Corchado, J.M. (eds.) IWANN 2009. LNCS, vol. 5518, pp. 957–964. Springer, Heidelberg (2009)
9. Hagan, M.T., Demuth, H.B., Beale, M.H.: Neural Network Design, Har/Dsk edition. PWS Pub. Co. (December 1995)
10. Haykin, S.: Neural Networks: A Comprehensive Foundation, 2nd edn. Prentice Hall, Englewood Cliffs (1998)
11. Huang, C., Yan, B., Jiang, H., Wang, D.: Combining voxel-based morphometry with artifical neural network theory in the application research of diagnosing alzheimer's disease, May 2008, vol. 1, pp. 250–254 (2008)
12. Kloppel, S., Stonnington, C.M., Chu, C., Draganski, B., Scahill, R.I., Rohrer, J.D., Fox, N.C., Jack Jr., C.R., Ashburner, J., Frackowiak, R.S.J.: Automatic classification of MR scans in alzheimer's disease. Brain 131(3), 681 (2008)
13. Kohonen, T.: Self-organization and associative memory, 3rd edn. Springer-Verlag New York, Inc., New York (1989)
14. Lao, Z., Shen, D., Xue, Z., Karacali, B., Resnick, S.M., Davatzikos, C.: Morphological classification of brains via high-dimensional shape transformations and machine learning methods. Neuroimage 21(1), 46–57 (2004)
15. Liu, Y., Teverovskiy, L., Carmichael, O., Kikinis, R., Shenton, M., Carter, C.S., Stenger, V.A., Davis, S., Aizenstein, H., Becker, J.T.: Discriminative MR image feature analysis for automatic schizophrenia and alzheimer's disease classification. In: Barillot, C., Haynor, D.R., Hellier, P. (eds.) MICCAI 2004. LNCS, vol. 3216, pp. 393–401. Springer, Heidelberg (2004)
16. Marcus, D.S., Wang, T.H., Parker, J., Csernansky, J.G., Morris, J.C., Buckner, R.L.: Open access series of imaging studies (OASIS): cross-sectional MRI data in young, middle aged, nondemented, and demented older adults. Journal of Cognitive Neuroscience 19(9), 1498–1507 (2007)
17. Rumelhart, D.E., Hinton, G.E., Williams, R.J.: Learning internal representations by error propagation, pp. 318–362. MIT Press, Cambridge (1986)
18. Scahill, R.I., Schott, J.M., Stevens, J.M., Rossor, M.N., Fox, N.C.: Mapping the evolution of regional atrophy in alzheimer's disease: Unbiased analysis of fluid-registered serial MRI. Proceedings of the National Academy of Sciences 99(7), 4703–4707 (2002)
19. Somervuo, P., Kohonen, T.: Self-Organizing maps and learning vector quantization for feature sequences. Neural Process. Lett. 10(2), 151–159 (1999)
20. Specht, D.F.: Probabilistic neural networks. Neural Netw. 3(1), 109–118 (1990)

Neural classifiers for schizophrenia diagnostic support on diffusion imaging data

Alexandre Savio, Juliette Charpentier, Maite Termenón, Ann K. Shinn, Manuel Graña *

Abstract: Diagnostic support for psychiatric disorders is a very interesting goal because of the lack of biological markers with sufficient sensitivity and specificity in psychiatry. The approach consists of a feature extraction process based on the results of Pearson correlation of known measures of white matter integrity obtained from diffusion weighted images: fractional anisotropy (FA) and mean diffusivity (MD), followed by a classification step performed by statistical support vector machines (SVM), different implementations of artificial neural networks (ANN) and learn vector quantization (LVQ) classifiers. The most discriminant voxels were found in frontal and temporal white matter. A total of 100% classification accuracy was achieved in almost every case, although the features extracted from the FA data yielded the best results. The study has been performed on publicly available diffusion weighted images of 20 male subjects.

Key words: *DWI, Schizofrenia, Neural Classifiers, Fractional Anisotropy, Mean Diffusivity*

1. Introduction

There is growing research effort devoted to the development of automated diagnostic support tools that may help clinicians perform their work with greater accuracy and efficiency. In medicine, diseases are often diagnosed with the aid of biological markers, including laboratory tests and radiologic imaging. The process of diagnosis becomes more difficult, however, when dealing with psychiatric disorders, in which diagnosis relies primarily on the patient's self-report of symptoms and the presence or absence of characteristic behavioral signs. Schizophrenia is a disabling psychiatric disorder characterized by hallucinations, delusions, disordered thought/speech, disorganized behavior, emotional withdrawal, and functional decline [2]. Currently, diagnosis is made almost exclusively on subjective measures like self-report, observation, and clinical history.

A large number of magnetic resonance imaging (MRI) morphological studies have shown subtle brain abnormalities to be present in schizophrenia. Structural

*A. Savio, M. Termenón, M. Graña are with the Grupo de Inteligencia Computacional (GIC), Universidad del País Vasco, Spain
J. Charpentier is with the Institut Superieur de BioSciences de Paris (ISBS), ESIEE, Université Paris-Est, France
A.K. Shinn is with the McLean Hospital, Belmont, Massachusetts; Harvard Medical School, Boston, Massachusetts, US

studies have found enlargement of the lateral ventricles, particularly the temporal horn of the lateral ventricles [28];[28]; reduced volumes of medial temporal structures (hippocampus, amygdala, and parahippocampal gyrus) [4, 17, 29], superior temporal gyrus [17], prefrontal cortex [15, 32], and inferior parietal lobule[27, 14]; and reversal of normal left greater than right volume in male patients with schizophrenia [24, 12]. In 1984, Wernicke [35] proposed that schizophrenia might involve altered connectivity of distributed brain networks that are diverse in function and that work in concert to support various cognitive abilities and their constituent operations. Consistent with the "dysconnectivity hypothesis", studies have found correlations between prefrontal and temporal lobe volumes [36, 7] and disruptions of functional connectivity between frontal and temporal lobes in schizophrenia [23]. These findings strongly point to widespread problems of connectivity in schizophrenia.

Diffusion tensor imaging (DTI) is a MRI method that allows more direct investigation into the integrity of white matter (WM) fibers, and thus into the anatomical connectivity of different brain regions. DTI depends upon the motion of water molecules to provide structural information in vivo [25, 5], and yields measures like fractional anisotropy (FA) and mean diffusivity (MD). The most commonly demonstrated DTI abnormalities in schizophrenia are decreased FA in the uncinate fasciculus (a tract connecting temporal and frontal regions and involved in decision-making, emotions, and episodic memory), the cingulum bundle (a tract interconnecting limbic regions which involved in attention, emotions, and memory), and the arcuate fasciulus (a tract connecting language regions) [21]. Lower anisotropic diffusion within white matter may reflect loss of coherence of WM fiber tracts, to changes in the number and/or density of interconnecting fiber tracts, or to changes in myelination [19, 22, 1, 20].

The present paper will focus on the application of machine learning (ML) algorithms for the computer aided diagnosis (CAD) of schizophrenia, on the basis of feature vectors extracted from DTI measures of WM integrity, FA and MD. This feature extraction method is based on Pearson correlation, and is simpler than others found in the literature [13, 11]. These features will be the input for statistical SVM and artificial neural networks (ANN) classifiers. We found literature on the application of ML algorithms to the discrimination of schizophrenia patients from healthy subjects. A minimum recognition error of 17,8% using geometry features and FA of DTI from a database of 36 healthy subjects and 34 patients with schizophrenia was reported in [34]. A study of the effect of principal component analysis (PCA) and discriminant PCA (DPCA) was carried on FA volumes reaching a minimum one-leave-out validation classification error 20% using Fisher linear discriminant (FLD) in [9]. Good classification results were also obtained in structural MRI (sMRI) studies [37, 11].

Section 2. gives a summary of the classification algorithms used for this study. Section 3. describes the materials and methods in the study: characteristics of the subjects conforming the database for the study, the acquisition protocol, the preprocessing steps of the MRI and DTI volumes and the feature extraction process. Section 4. gives the results of our computational experiments. Section 5. gives our final comments and conclusions.

2. Neural Network and Statistical Classification Algorithms

We deal with two class classification problems, given a collection of training/testing input feature vectors $X = \{\mathbf{x}_i \in \mathbb{R}^n,\ i = 1, \ldots, l\}$ and the corresponding labels $\{y_i \in \{-1, 1\},\ i = 1, \ldots, l\}$, which sometimes can be better denoted in aggregated form as a binary vector $\mathbf{y} \in \{-1, 1\}^l$. The algorithms described below build some classifier systems based on this data. The simplest algorithm is the 1-nearest neighbor (1-NN) which involves no adaptation and uses all the training data samples. The classification rule is of the form:

$$c\left(\mathbf{x}\right) = y_{i^*} \text{ where } i^* = \arg \min_{i=1,\ldots,l} \left\{\|\mathbf{x} - \mathbf{x}_i\|\right\},$$

that is, the assigned class is that of the closest training vector. To validate their generalization power we use ten-fold cross-validation.

2.1 Support Vector Machines

The support vector machine (SVM) [33] approach to build a classifier system from the given data consists in solving the following optimization problem:

$$\min_{\mathbf{w},b,\boldsymbol{\xi}} \frac{1}{2}\mathbf{w}^T\mathbf{w} + C\sum_{i=1}^{l}\xi_i, \tag{1}$$

subject to

$$y_i(\mathbf{w}^T\phi(\mathbf{x}_i) + b) \geq (1 - \xi_i),\ \xi_i \geq 0,\ i = 1, 2, \ldots, n. \tag{2}$$

The minimization problem is solved via its dual optimization problem:

$$\min_{\alpha} \frac{1}{2}\boldsymbol{\alpha}^T Q\boldsymbol{\alpha} - \mathbf{e}^T\boldsymbol{\alpha}, \tag{3}$$

subject to

$$\mathbf{y}^T\boldsymbol{\alpha} = 0,\ 0 \leq \alpha_i \leq C,\ i = 1, \ldots, l. \tag{4}$$

Where $\mathbf{e}$ is the vector of all ones, $C > 0$ is the upper bound on the error, Q is an $l \times l$ positive semidefinite matrix, whose elements are given by the following expression:

$$Q_{ij} \equiv y_i y_j K(\mathbf{x}_i, \mathbf{x}_j), \tag{5}$$

where

$$K(\mathbf{x}_i, \mathbf{x}_j) \equiv \phi(\mathbf{x}_i)^T\phi(\mathbf{x}_j), \tag{6}$$

is the kernel function that describes the behavior of the support vectors. Here, training vectors $\mathbf{x}_i$ are mapped into a higher (maybe infinite) dimensional space by the function $\phi(\mathbf{x}_i)$. The decision function is:

$$sgn(\sum_{i=1}^{l} y_i \alpha_i K(\mathbf{x}_i, \mathbf{x}) + b). \tag{7}$$

The regularization parameter C is used to balance the model complexity and the training error. It was always set to 1 in this case study.

The chosen kernel function results in different kinds of SVM with different performance levels, and the choice of the appropriate kernel for a specific application is a difficult task. In this study we only needed to use a linear kernel, defined as:

$$K(\mathbf{x}_i, \mathbf{x}_j) = 1 + \mathbf{x}_i^T \mathbf{x}_j, \tag{8}$$

this kernel shows good performance for linearly separable data.

2.2 Backpropagation

Backward propagation of errors, or backpropagation (BP), [26, 16] is a non-linear generalization of the squared error gradient descent learning rule for updating the weights of artificial neurons in a single-layer perceptron, generalized to feed-forward networks, also called multi-Layer perceptron (MLP). Backpropagation requires that the activation function used by the artificial neurons (or "nodes") is differentiable with its derivative being a simple function of itself. The backpropagation of the error allows to compute the gradient of the error function relative to the hidden units. It is analytically derived using the chain rule of calculus. During on-line learning, the weights of the network are updated at each input data item presentation. We have used the resilient backpropagation, which uses only the derivative sign to perform the weight updating.

We restrict our presentation of BP to train the weights of the MLP for the current two class problem. Let the instantaneous error E_p be defined as:

$$E_p(\mathbf{w}) = \frac{1}{2}\left(y_p - z_K(\mathbf{x}_p)\right)^2, \tag{9}$$

where y_p is the p-th desired output y_p, and $z_K(\mathbf{x}_p)$ is the network output when the p-th training exemplar $\mathbf{x}_p$ is inputted to the MLP composed of K layers, whose weights are aggregated in the vector $\mathbf{w}$. The output of the j-th node in layer k is given by:

$$z_{k,j}(\mathbf{x}_p) = f\left(\sum_{i=0}^{N_{k-1}} w_{k,j,i} z_{k-1,i}(\mathbf{x}_p)\right), \tag{10}$$

where $z_{k,j}$ is the output of node j in layer k, N_k is the number of nodes in layer k, $w_{k,j,i}$ is the weight which connects the i-th node in layer $k-1$ to the j-th node in layer k, and $f(\cdot)$ is the sigmoid nonlinear function, which has a simple derivative:

$$f'(\alpha) = \frac{df(\alpha)}{d\alpha} = f(\alpha)\left(1 - f(\alpha)\right). \tag{11}$$

The convention is that $z_{0,j}(\mathbf{x}_p) = \mathbf{x}_{p,j}$. Let the total error E_T be defined as follows:

$$E_T(\mathbf{w}) = \sum_{p=1}^{l} E_p(\mathbf{w}), \tag{12}$$

where l is the cardinality of X. Note that E_T is a function of both the training set and the weights in the network. The backpropagation learning rule is defined as follows:

$$\Delta w(t) = -\eta \frac{\partial E_p(\mathbf{w})}{\partial w} + \alpha \Delta w(t-1), \tag{13}$$

where $0 < \eta < 1$, which is the learning rate, the momentum factor α is also a small positive number, and w represents any single weight in the network. In the above equation, $\Delta w(t)$ is the change in the weight computed at time t. The momentum term is sometimes used ($\alpha \neq 0$) to improve the smooth convergence of the algorithm. The algorithm defined by equation (13) is often termed as *instantaneous backpropagation* because it computes the gradient based on a single training vector. Another variation is *batch backpropagation*, which computes the weight update using the gradient based on the total error E_T.

To implement this algorithm we must give an expression for the partial derivative of E_p with respect to each weight in the network. For an arbitrary weight in layer k this can be written using the Chain Rule:

$$\frac{\partial E_p(\mathbf{w})}{\partial w_{k,j,j}} = \frac{\partial E_p(\mathbf{w})}{\partial z_{k,j}(\mathbf{x}_p)} \frac{\partial z_{k,j}(\mathbf{x}_p)}{\partial w_{k,j,i}}. \tag{14}$$

Because the derivative of the activation function follows equation 11, we get:

$$\frac{\partial z_{k,j}(\mathbf{x}_p)}{\partial w_{k,j,i}} = z_{k,j}(\mathbf{x}_p)\left(1 - z_{k,j}(\mathbf{x}_p)\right) z_{k-1,j}(\mathbf{x}_p), \tag{15}$$

and

$$\frac{\partial E_p(\mathbf{w})}{\partial z_{k,j}(\mathbf{x}_p)} = \sum_{m=1}^{N_{k+1}} \frac{\partial E_p(\mathbf{w})}{\partial z_{k+1,m}(\mathbf{x}_p)} z_{k+1,m}(\mathbf{x}_p)\left(1 - z_{k+1,m}(\mathbf{x}_p)\right) w_{k+1,m,j},$$

which at the output layer corresponds to the output error :

$$\frac{\partial E_p(\mathbf{w})}{\partial z_K(\mathbf{x}_p)} = z_L(\mathbf{x}_p) - y_p. \tag{16}$$

2.3 Radial Basis Function Networks

Radial basis function networks (RBF) [10] are a type of ANN that use radial basis functions as activation functions. RBFs consist of a two layer neural network, where each hidden unit implements a radial activated function. The output units compute a weighted sum of hidden unit outputs. Training consists of the unsupervised training of the hidden units followed by the supervised training of the output units weights. RBFs have their origin in the solution of a multivariate interpolation

problem [8]. Arbitrary function $g(\mathbf{x}) : \mathbb{R}^n \to \mathbb{R}$ can be approximated by a map defined by a RBF network with a single hidden layer of K units:

$$\hat{g}_{\boldsymbol{\theta}}(\mathbf{x}) = \sum_{j=1}^{K} w_j \phi(\sigma_j, \|\mathbf{x} - \mathbf{c}_j\|), \tag{17}$$

where $\boldsymbol{\theta}$ is the vector of RBF parameters including $w_j, \sigma_j \in \mathbb{R}$, and $\mathbf{c}_j \in \mathbb{R}^n$; let us denote $\mathbf{w} = (w_1, w_2, \ldots, w_p)^T$, then the vector of RBF parameters can be expressed as $\boldsymbol{\theta}^T = \left(\mathbf{w}^T, \sigma_1, \mathbf{c}_1^T, \ldots, \sigma_K, \mathbf{c}_K^T\right)$. Each RBF is defined by its center $\mathbf{c}_j \in \mathbb{R}^n$ and width $\sigma_j \in \mathbb{R}$, and the contribution of each RBF to the network output is weighted by w_j. The RBF function $\phi(\cdot)$ is a nonlinear function that monotonically decreases as $\mathbf{x}$ moves away from its center $\mathbf{c}_j$. The most common RBF used is the isotropic Gaussian:

$$\hat{g}_{\boldsymbol{\theta}}(\mathbf{x}) = \sum_{j=1}^{p} w_j \exp\left(-\frac{\|\mathbf{x} - \mathbf{c}_j\|^2}{2\sigma_j^2}\right).$$

The network can be thought as the composition of two functions $\hat{g}_{\boldsymbol{\theta}}(\mathbf{x}) = W \circ \Phi(\mathbf{x})$, the first one implemented by the RBF units $\Phi : \mathbb{R}^n \to \mathbb{R}^K$ performs a data space transformation which can be a dimensionality reduction or not, depending on whether $K > n$. The second function corresponds to a single layer linear Perceptron $W : \mathbb{R}^K \to \mathbb{R}$ giving the map of the RBF transformed data into the class labels. Training is accordingly decomposed into two phases. First a clustering algorithm is used to estimate the Gaussian RBF parameters (centers and variances). Afterwards, linear supervised training is used to estimate the weights from the hidden RBF to the output. In order to obtain a binary class label output, a hard limiter function is applied to the continuous output of the RBF network.

2.4 Probabilistic Neural Networks

A probabilistic neural network (PNN) [31] uses a kernel-based approximation to form an estimate of the probability density function of categories in a classification problem. In fact, it is a generalization of the Parzen windows distribution estimation, and a filtered version of the 1-NN classifier. The distance of the input feature vector $\mathbf{x}$ to the stored patterns is filtered by a RBF function. Let us denote the data sample partition as $X = X_1 \cup X_{-1}$, where $X_1 = \left\{\mathbf{x}_1^1, \ldots, \mathbf{x}_{n_1}^1\right\}$ and $X_1 = \left\{\mathbf{x}_1^{-1}, \ldots, \mathbf{x}_{n_{-1}}^{-1}\right\}$. That is, superscripts denote the class of the feature vector and $n_1 + n_{-1} = n$. Each pattern $\mathbf{x}_j^i$ of training data sample is interpreted as the weight of the j-th neuron of the i-th class. Therefore the response of the neuron is computed as the probability of the input feature vector according to a Normal distribution centered at the stored pattern:

$$\Phi_{i,j}(\mathbf{x}) = \frac{1}{(2\pi)^{n/2}\sigma^n} \exp\left[-\frac{\left\|\mathbf{x} - \mathbf{x}_j^i\right\|}{2\sigma^2}\right]. \tag{18}$$

Therefore the output of the neuron is inside $[0, 1]$. The tuning of a PNN network depends on selecting the optimal sigma value of the spread σ of the RBF functions,

which can be different for each class. In this paper an exhaustive search for the optimal spread value in the range (0, 1) for each training set has been done. The output of the PNN is an estimation of the likelihood of the input pattern $\mathbf{x}$ being from class $i \in \{-1, 1\}$ by averaging the output of all neurons that belong to the same class:

$$p_i(x) = \frac{1}{n_i} \sum_{j=1}^{n_i} \Phi_{i,j}(\mathbf{x}). \tag{19}$$

The decision rule based on the output of all the output layer neurons is simply:

$$\hat{y}(\mathbf{x}) = \arg\max_i \{p_i(\mathbf{x})\}, \quad i \in \{-1, 1\}, \tag{20}$$

where $\hat{y}(\mathbf{x})$ denotes the estimated class of the pattern $\mathbf{x}$. If the a priori probabilities for each class are the same, and the losses associated with making an incorrect decision for each class are the same, the decision layer unit classifies the pattern $\mathbf{x}$ in accordance with the optimal Bayes' rule.

2.5 Learning Vector Quantization Neural Network

Learning vector quantization (LVQ), as introduced by Kohonen [18], represents every class $c \in \{-1, 1\}$ by a set $W(c) = \{\mathbf{w}_i \in \mathbb{R}^n; i = 1, \ldots, N_c\}$ of weight vectors (prototypes) which tessellate the input feature space. Let us denote W the union of all prototypes, regardless of class. If we denote c_i the class the weight vector $\mathbf{w}_i \in W$ is associated with, the decision rule that classifies a feature vector $\mathbf{x}$ is as follows:

$$c(\mathbf{x}) = c_{i^*}$$

where

$$i^* = \arg\min_i \{\|\mathbf{x} - \mathbf{w}_i\|\}.$$

The training algorithm of LVQ aims at minimizing the classification error on the given training set, i.e., $E = \sum_j (y_j - c(\mathbf{x}_j))^2$, modifying the weight vectors on the presentation of input feature vectors. The heuristic weight updating rule is as follows:

$$\Delta\mathbf{w}_{i^*} = \begin{cases} \epsilon \cdot (\mathbf{x}_j - \mathbf{w}_{i^*}) & \text{if } c_{i^*} = y_j \\ -\epsilon \cdot (\mathbf{x}_j - \mathbf{w}_{i^*}) & \text{otherwise} \end{cases}, \tag{21}$$

that is, the input's closest weight is adapted either toward the input if their classes match, or away from it if not. This rule is highly unstable, therefore, the practical approach consists in performing an initial clustering of each class data samples to obtain an initial weight configuration using equation 21 to perform the fine tuning of the classification boundaries. This equation corresponds to a LVQ1 approach. The LVQ2 approach involves determining the two input vector's closest weights. They are moved toward or away the input according to the matching of their classes.

3. Materials and Methods

Structural MRI and DTI data from twenty men (aged 21-55 yr), ten patients and ten controls, from a publicly available database from the National Alliance for Medical Image Computing (NAMIC) [1] were the subjects of this study in this experiment. The imaging parameters and demographic information about the subjects can be obtained from the web site, we omit them for lack of space. A technical description of the feature extraction method and the data will be available [2], because many of the difficulties found have no place in an academic paper, but are important for the reproducibility of the results.

3.1 Scalar Features of Diffusion Tensors

In DTI, a diffusion tensor at a voxel is a 3×3 positive-definite symmetric matrix D, which can be represented by its decomposition as $D = \lambda_1 \mathbf{g}_1 \mathbf{g}_1^T + \lambda_2 \mathbf{g}_2 \mathbf{g}_2^T + \lambda_3 \mathbf{g}_3 \mathbf{g}_3^T$, where $\lambda_1 \geq \lambda_2 \geq \lambda_3$ and $\mathbf{g}_1$, $\mathbf{g}_2$, $\mathbf{g}_3$ are the eigenvalues and eigenvectors of D, respectively. Two scalar measures were extracted [6] from the voxels diffusion tensors: the mean diffusivity (MD) and the fractional anisotropy (FA). The first corresponds to the average eigenvalue:

$$MD = \frac{\mathrm{Tr}\,(D)}{3} = \frac{\lambda_1 + \lambda_2 + \lambda_3}{3}. \tag{22}$$

The FA measures the fraction of the magnitude of D that can be related to anisotropic diffusion in a mean-squared sense (i.e. the extent of deviation from isotropic diffusivity in all direction). Its magnitude is also rotationally invariant, and independent from sorting of the eigenvalues. The FA is calculated as follows:

$$FA = \sqrt{\frac{1}{2}} \frac{\sqrt{(\lambda_1 - \lambda_2)^2 + (\lambda_2 - \lambda_3)^2 + (\lambda_3 - \lambda_1)^2}}{\sqrt{\lambda_1^2 + \lambda_2^2 + \lambda_3^2}}. \tag{23}$$

Thus, isotropic diffusion is imaged as zero value and FA maximum value is one. Figure 1 show slices of FA and MD volumes of one study subject.

3.2 Image preprocessing

Feature extraction requires that the diffusion related data is spatially normalized, in order to compute the correlation measure and to extract the values of the feature vectors. Our starting point was the nonlinear registration [3] of the T1-weighted sMRI skull stripped volumes of each subject to the Montreal Neurological Institute (MNI152) standard template, using the ANTS[3] nonlinear elastic registration algorithm. For the elastic registration, a probabilistic correlation similarity metric was chosen with window radius 4 and gradient step length 1. The optimization has been performed over three resolutions with a maximum of 100 iterations at the coarsest level, 100 at the next coarsest and 10 at the full resolution. The optimization stops when either the distance between both images cannot be further minimized or the

[1] http://www.insight-journal.org/midas/collection/view/190?path_navigation=17
[2] http://www.ehu.es/ccwintco/index.php/GIC-experimental-databases
[3] http://www.picsl.upenn.edu/ANTS

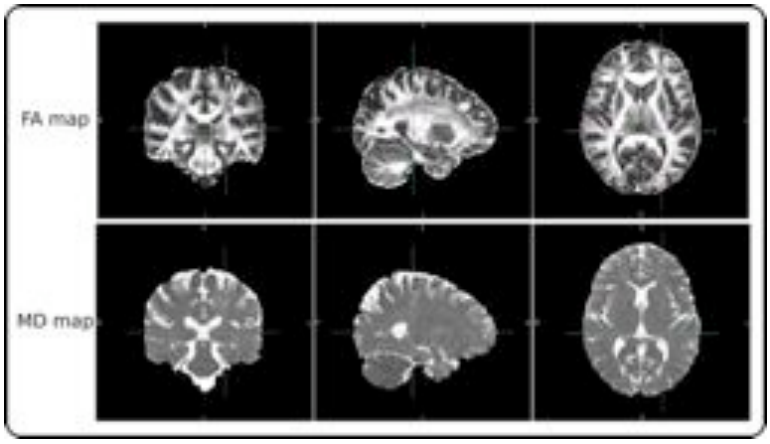

Figure 1 *FA and MD maps of one subject.*

maximum number of iterations is reached. We used a Gaussian regularization with sigma parameter value 3 which operates only on the deformation field and not on the similarity gradient. In addition, a previous histogram matching step has been performed. The deformation fields of this registration were used afterwards for the spatial deformation of the FA and MD volumes.

The DWI scans were already noise filtered and corrected for eddy currents and head motion by the group that originally acquired the scans. A brain mask was obtained for each DWI data volume to calculate the FA and MD maps of each subject [6]. The FA and MD maps were linearly registered to the sMRI skull stripped volumes [30] of each subject and then non-linearly registered to MNI applying the deformation fields obtained from the sMRI data nonlinear registration. All of the FA and MD volumes were then considered spatially normalized.

3.3 Feature extraction

Once the FA and MD maps were spatially normalized, we processed them independently. We considered each voxel site independently, forming a vector at the voxel site across all the subjects. Then we computed the Pearson correlation coefficient between this vector and the control variable with the labels (patient=1, control=-1). Thus we obtained for FA and MD data two independent volumes containing correlation values at each voxel. For each volume we estimated the empirical distribution of the absolute correlation values and determined a selection threshold corresponding to a percentile of this absolute correlation distribution. Voxel sites with absolute value of the correlation above this threshold were retained, and the feature vector for each subject was composed of the FA or MD values at these voxel sites. In table I we show the percentiles and the number of voxels selected for each feature vector.

Although the voxel sites selected to build the feature vectors (the feature mask) were localized in many different regions of the subject brains, we found that most were concentrated in regions of characteristic abnormalities found for schizophrenia

Database	Percentile	DT Measure	Number of voxels
A	99.990%	FA	241
		MD	241
B	99.992%	FA	193
		MD	193
C	99.995%	FA	121
		MD	121
D	99.997%	FA	72
		MD	72
E	99.999%	FA	24
		MD	24

Table I *Databases considered, percentile on the correlation distribution and size of the feature vectors.*

shown in the literature (see [19] for references). The features voxel locations [4] were different for FA and MD maps. In the case of FA, the selected voxels were localized mainly in parietal and temporal lobes, but also in the cerebellum and occipital lobe. More specifically, in WM we found discriminant voxel values in the cingulum bundle, superior and inferior longitudinal fasciculus and in the inferior fronto-occipital fasciculus. On the other hand, in the MD maps, the most discriminant voxel values were the ones localized in frontal and parietal lobes, more specifically thecingulum bundle, inferior fronto-occipital and longitudinal fasciculus, and superior longitudinal fasciculus.

3.4 Classifiers parameters

All classifiers were calculated with a maximum iteration number (epochs) of 100. For the 1-NN classifier, we used the nearest neighbor rule with euclidean distance. In the SVM algorithm, a linear kernel function was used as well as a sequential minimal optimization for the separating hyperplane method. For BPNN, the number of neurons in the hidden layer was 4, the learning rate was set to 0.05, tan-sigmoid transfer function, and training and learning functions were gradient descent with momentum. LVQ2 was trained with 2 hidden neurons, learning rate set to 0.01. The training function used for RBF was according to resilient backpropagation algorithm. In the case of PNN, random order incremental training was used. For the last three algorithms (BPNN, LVQ2 and RBF) zeros were set as initial input and layer delay conditions. These parameters have been selected after a sensitivity analysis.

We tested several cross-validation strategies, because the small database size may have an influence on the results obtained with each of these cross-validation processes. Cross-validation partitions were computed 40 times and we show average accuracy, sensitivity, and specificity for the 10-fold cross-validation procedure.

[4] This specification of the voxel locations were obtained with the "atlasquery" tool from FMRIB's FSL (http://www.fmrib.ox.ac.uk/fsl/) using the "MNI Structural Atlas" and the "JHU White-Matter Tractography Atlas".

Database		FA	MD
A	1-NN	1.00 (1.00-1.00)	1.00 (1.00-1.00)
	SVM	1.00 (1.00-1.00)	1.00 (1.00-1.00)
	BP	0.75 (0.67-1.00)	0.78 (0.69-1.00)
	RBF	0.98 (0.97-1.00)	1.00 (1.00-1.00)
	PNN	1.00 (1.00-1.00)	0.54 (0.54-0.54)
	LVQ2	1.00 (1.00-1.00)	1.00 (1.00-1.00)
B	1-NN	1.00 (1.00-1.00)	1.00 (1.00-1.00)
	SVM	1.00 (1.00-1.00)	1.00 (1.00-1.00)
	BP	0.75 (0.66-1.00)	0.78 (0.70-1.00)
	RBF	1.00 (1.00-1.00)	1.00 (1.00-1.00)
	PNN	1.00 (1.00-1.00)	0.52 (0.52-0.52)
	LVQ2	1.00 (1.00-1.00)	1.00 (1.00-1.00)
C	1-NN	1.00 (1.00-1.00)	1.00 (1.00-1.00)
	SVM	1.00 (1.00-1.00)	1.00 (1.00-1.00)
	BP	0.77 (0.68-1.00)	0.77 (0.68-1.00)
	RBF	1.00 (1.00-1.00)	1.00 (1.00-1.00)
	PNN	1.00 (1.00-1.00)	0.52 (0.52-0.52)
	LVQ2	1.00 (1.00-1.00)	1.00 (1.00-1.00)
D	1-NN	1.00 (1.00-1.00)	1.00 (1.00-1.00)
	SVM	1.00 (1.00-1.00)	1.00 (1.00-1.00)
	BP	0.77 (0.68-1.00)	0.77 (0.68-1.00)
	RBF	1.00 (1.00-1.00)	0.84 (0.79-0.90)
	PNN	0.99 (0.99-1.00)	0.55 (0.55-0.55)
	LVQ2	1.00 (1.00-1.00)	1.00 (1.00-1.00)
E	1-NN	0.94 (0.90-0.99)	1.00 (1.00-1.00)
	SVM	0.95 (0.90-1.00)	1.00 (1.00-1.00)
	BP	0.76 (0.67-1.00)	0.77 (0.68-1.00)
	RBF	0.92 (0.90-0.94)	0.89 (0.91-0.88)
	PNN	0.94 (0.90-0.99)	0.52 (0.52-0.52)
	LVQ2	0.97 (0.94-1.00)	1.00 (1.00-1.00)

Table II *10-fold cross-validation results. Accuracy (Sensitivity, Specificity)*

4. Results

The results are presented in table II. The most striking result is that we found optimal performance of almost all classifiers built from the provided feature vectors. The only exceptions were the results of PNN on MD data; tuning of the Gaussian kernel variance was more difficult than applying the training algorithm of other approaches . Also BP shows lower performance than the others. The second general result is that MD features seem to perform slightly better than FA features, disregarding the anomaly of PNN classifiers. In the experimental design we wanted to test if decreasing the size of the feature vectors had an impact on the classifiers performance. We found that performance was not affected down to the smallest feature vector (database E) where decreases in performance can be appreciated in all the classifiers for the FA data, while 1-NN, SVM and LVQ2 maintain their performance for MD data.

5. Conclusion

The goal of this paper was to test the hypothesis that classification algorithms constructed using statistical and Neural Network approaches can discriminate between schizophrenia patients and control subjects on the basis of features extracted from DTI data. The way to build the feature vectors has been the direct selection of voxels from the DTI-derived FA and MD scalar valued volumes that show a high correlation with the control variable that labels the subjects. The selected voxels roughly correspond to findings reported in the medical literature. Surprisingly, all the classifiers obtain near perfect results. Despite the simplicity of our feature extraction process, the results compare well with other results found in the literature [9, 34]. We think that appropriate pre-processing of the data is of paramount importance and can not be disregarded trusting that ensuing statistical or machine learning processes may cope with the errors introduced by lack of appropriate data normalization. Therefore, our main conclusion is that the proposed feature extraction is very effective in providing a good discrimination between schizophrenia patients that can easily be exploited by the classifier construction algorithms. The main limitation of this study is that the results come from a small database. Therefore, more extensive testing will be needed to confirm our conclusions. Nevertheless, we are making available [5] the actual data employed in the computational experiments to allow for independent validation of our results.

Acknowledgements

Thanks to the National Alliance for Medical Image Computing and the Brigham & Women's Hospital for making the database used for this study publicly available.

[5] http://www.ehu.es/ccwintco/index.php/GIC-experimental-databases

References

[1] N. Andreone, M. Tansella, R. Cerini, A. Versace, G. Rambaldelli, C. Perlini, N. Dusi, L. Pelizza, M. Balestrieri, C. Barbui, M. Nosè, A. Gasparini, and P. Brambilla. Cortical white-matter microstructure in schizophrenia. diffusion imaging study. *The British Journal of Psychiatry: The Journal of Mental Science*, 191:113–119, August 2007. PMID: 17666494.

[2] American Psychiatric Association. *DSM-IV-TR: Diagnostic and Statistical Manual of Mental Disorders (Diagnostic & Statistical Manual of Mental Disorders*. American Psychiatric Press Inc., 4th text revision edition, July 2000.

[3] B.B. Avants, C.L. Epstein, M. Grossman, and J.C. Gee. Symmetric diffeomorphic image registration with Cross-Correlation: evaluating automated labeling of elderly and neurodegenerative brain. *Medical image analysis*, 12(1):26–41, February 2008. PMID: 17659998 PMCID: 2276735.

[4] P.E. Barta, G.D. Pearlson, L.B. Brill, R. Royall, I.K. McGilchrist, A.E. Pulver, R.E. Powers, M.F. Casanova, A.Y. Tien, S. Frangou, and R.G. Petty. Planum temporale asymmetry reversal in schizophrenia: replication and relationship to gray matter abnormalities. *The American Journal of Psychiatry*, 154(5):661–667, May 1997. PMID: 9137122.

[5] P.J. Basser, J. Mattiello, and D. LeBihan. MR diffusion tensor spectroscopy and imaging. *Biophysical Journal*, 66(1):259–267, January 1994. PMID: 8130344 PMCID: 1275686.

[6] T.E.J. Behrens, M.W. Woolrich, M. Jenkinson, H. Johansen-Berg, R.G. Nunes, S. Clare, P.M. Matthews, J.M. Brady, and S.M. Smith. Characterization and propagation of uncertainty in diffusion-weighted MR imaging. *Magnetic Resonance in Medicine*, 50(5):1077–1088, 2003.

[7] A. Breier, R.W. Buchanan, A. Elkashef, R.C. Munson, B. Kirkpatrick, and F. Gellad. Brain morphology and schizophrenia: A magnetic resonance imaging study of limbic, prefrontal cortex, and caudate structures. *Archives of General Psychiatry*, 49(12):921–926, December 1992.

[8] D.S. Broomhead and D. Lowe. Multivariable functional interpolation and adaptive networks. *Complex Systems*, 2:321–355, 1988.

[9] A. Caprihan, G.D. Pearlson, and V.D. Calhoun. Application of principal component analysis to distinguish patients with schizophrenia from healthy controls based on fractional anisotropy measurements. *NeuroImage*, 42(2):675–682, August 2008.

[10] S. Chen, C.F.N. Cowan, and P.M. Grant. Orthogonal least squares learning algorithm for radial basis function networks. *IEEE Transactions on Neural Networks*, 2(2):302–309, 1991.

[11] Y. Fan, D. Shen, R.C. Gur, R.E. Gur, and Christos Davatzikos. COMPARE: classification of morphological patterns using adaptive regional elements. *IEEE Transactions on Medical Imaging*, 26(1):93–105, January 2007. PMID: 17243588.

[12] M. Frederikse, A. Lu, E. Aylward, P. Barta, T. Sharma, and G. Pearlson. Sex differences in inferior parietal lobule volume in schizophrenia. *The American Journal of Psychiatry*, 157(3):422–427, March 2000.

[13] M. García-Sebastián, A. Savio, M. Graña, and J. Villanúa. On the use of morphometry based features for alzheimer's disease detection on MRI. In *Proceedings of the 10th International Work-Conference on Artificial Neural Networks: Part I: Bio-Inspired Systems: Computational and Ambient Intelligence*, pages 957–964, Salamanca, Spain, 2009. Springer-Verlag.

[14] J.M. Goldstein, J.M. Goodman, L.J. Seidman, D.N. Kennedy, N. Makris, H. Lee, J. Tourville, V.S. Caviness, S.V. Faraone, and M.T. Tsuang. Cortical abnormalities in schizophrenia identified by structural magnetic resonance imaging. *Archives of General Psychiatry*, 56(6):537–547, June 1999.

[15] R.E. Gur, P.E. Cowell, A. Latshaw, B.I. Turetsky, R.I. Grossman, S.E. Arnold, W.B. Bilker, and R.C. Gur. Reduced dorsal and orbital prefrontal gray matter volumes in schizophrenia. *Archives of General Psychiatry*, 57(8):761–768, August 2000.

[16] S. Haykin. *Neural Networks: A Comprehensive Foundation*. Prentice Hall, 2 edition, July 1998.

[17] D.P. Holinger, M.E. Shenton, C.G. Wible, R. Donnino, R. Kikinis, F.A. Jolesz, and R.W. McCarley. Superior temporal gyrus volume abnormalities and thought disorder in Left-Handed schizophrenic men. *The American Journal of Psychiatry*, 156(11):1730–1735, November 1999.

[18] T. Kohonen. Learning vector quantization. In *The handbook of brain theory and neural networks*, pages 537–540. MIT Press, 1998.

[19] M. Kubicki, R. McCarley, C.-F. Westin, H-J Park, S. Maier, R. Kikinis, F.A. Jolesz, and M.E. Shenton. A review of diffusion tensor imaging studies in schizophrenia. *Journal of psychiatric research*, 41(1-2):15–30, 2007. PMID: 16023676 PMCID: 2768134.

[20] M. Kubicki, H. Park, C.-F. Westin, P.G. Nestor, R.V. Mulkern, S.E. Maier, M. Niznikiewicz, E.E. Connor, J.J. Levitt, M. Frumin, R. Kikinis, F.A. Jolesz, R.W. McCarley, and M.E. Shenton. DTI and MTR abnormalities in schizophrenia: Analysis of white matter integrity. *NeuroImage*, 26(4):1109–1118, July 2005. PMID: 15878290 PMCID: 2768051.

[21] M. Kubicki, C.F. Westin, R.W. McCarley, and M.E. Shenton. The application of DTI to investigate white matter abnormalities in schizophrenia. *Annals of the New York Academy of Sciences*, 1064(1):134–148, 2005.

[22] M. Kyriakopoulos, T. Bargiotas, G.J. Barker, and S. Frangou. Diffusion tensor imaging in schizophrenia. *European Psychiatry*, 23(4):255–273, June 2008.

[23] P.K. McGuire and C.D. Frith. Disordered functional connectivity in schizophrenia. *Psychological Medicine*, 26(4):663–667, July 1996. PMID: 8817700.

[24] M. Niznikiewicz, R. Donnino, R.W. McCarley, P.G. Nestor, D.V. Iosifescu, B.O'Donnell, J. Levitt, and M.E. Shenton. Abnormal angular gyrus asymmetry in schizophrenia. *The American Journal of Psychiatry*, 157(3):428–437, March 2000.

[25] C. Pierpaoli, P. Jezzard, P.J. Basser, A. Barnett, and G. Di Chiro. Diffusion tensor MR imaging of the human brain. *Radiology*, 201(3):637–648, December 1996. PMID: 8939209.

[26] D.E. Rumelhart, G.E. Hinton, and R.J. Williams. *Learning internal representations by error propagation*, pages 318–362. MIT Press, 1986.

[27] T.E. Schlaepfer, G.J. Harris, A.Y Tien, L.W. Peng, S. Lee, E.B. Federman, G.A. Chase, P.E. Barta, and G.D. Pearlson. Decreased regional cortical gray matter volume in schizophrenia. *The American Journal of Psychiatry*, 151(6):842–848, June 1994.

[28] M.E. Shenton, C.C. Dickey, M. Frumin, and R.W. McCarley. A review of MRI findings in schizophrenia. *Schizophrenia research*, 49(1-2):1–52, April 2001. PMID: 11343862 PMCID: 2812015.

[29] M.E. Shenton, R.Kikinis, F.A. Jolesz, S.D. Pollak, M. LeMay, C.G. Wible, H. Hokama, J. Martin, D. Metcalf, M. Coleman, and R.W. McCarley. Abnormalities of the left temporal lobe and thought disorder in schizophrenia. *New England Journal of Medicine*, 327(9):604–612, 1992.

[30] S.M. Smith, M. Jenkinson, M.W. Woolrich, C.F. Beckmann, T.E.J. Behrens, H.Johansen-Berg, P.R. Bannister, M. De Luca, I. Drobnjak, D.E. Flitney, R.K. Niazy, J. Saunders, J. Vickers, Y. Zhang, N. De Stefano, J.M. Brady, and P.M. Matthews. Advances in functional and structural MR image analysis and implementation as FSL. *NeuroImage*, 23(Supplement 1):S208–S219, 2004.

[31] D.F. Specht. Probabilistic neural networks. *Neural Networks*, 3(1):109–118, 1990.

[32] P.R. Szeszko, R.M. Bilder, T. Lencz, S. Pollack, J.M. Alvir, M. Ashtari, H. Wu, and J.A. Lieberman. Investigation of frontal lobe subregions in first-episode schizophrenia. *Psychiatry Research*, 90(1):1–15, February 1999. PMID: 10320207.

[33] V.N. Vapnik. *Statistical Learning Theory*. Wiley-Interscience, September 1998.

[34] P. Wang and R. Verma. On classifying Disease-Induced patterns in the brain using diffusion tensor images. In *Medical Image Computing and Computer-Assisted Intervention - MICCAI 2008*, pages 908–916. 2008.

[35] C. Wernicke. *Grundriss der Psychiatrie in klinischen Vorlesungen / von Carl Wernicke*. VDM Verlag Dr. Müller, Saarbrücken, 2007.

[36] C.G. Wible, M.E. Shenton, H. Hokama, R. Kikinis, F.A. Jolesz, D. Metcalf, and R.W. McCarley. Prefrontal cortex and schizophrenia: A quantitative magnetic resonance imaging study. *Archives of General Psychiatry*, 52(4):279–288, April 1995.

[37] U. Yoon, J.-M. Lee, K. Im, Y.-W. Shin, B.H. Cho, I.Y. Kim, J.S. Kwon, and S.I. Kim. Pattern classification using principal components of cortical thickness and its discriminative pattern in schizophrenia. *NeuroImage*, 34(4):1405–1415, February 2007.

Analisis preliminares para portar SPM v8 desde Matlab a Scilab

Maite Termenon Conde

Grupo de inteligencia Computacional

El software SPM (Statistical Parametric Mapping) es un software de amplia utilización en los campos de neuroimagen y neurociencias. Abarca el proceso de señales de Electroencefalografía (EEG), imágenes funcionales basadas en marcadores de isotopos radiactivos (PET y SPECT), imágenes de resonancia magnética nuclear estructural y funcional. En este breve trabajo hemos identificado los principales módulos computacionales de SPM para estudiar su portabilidad desde Matlab a Scilab. El interés de este cambio de lenguaje soporte es evidente puesto que Matlab es un software propietario de un costo elevado, mientras que Scilab es software gratuito y libre, al que se pueden realizar aportaciones y modificaciones publicas. Esta filosofía está en el marco del proyecto SOFLIMRI en el que se ha realizado este trabajo de análisis previo. En este informe recogemos los principales procesos que deberían ser transformados de Matlab a Scilab.

La filosofía básica de SPM es la realización sobre un conjunto de medidas espaciales consideradas como independientes de analisis linear multivariante seguido de tests estadísticos univariantes que contemplan la existencia de correlaciones espaciales para realizar correcciones sobre los umbrales de decisión de los tests. Esta modelo de proceso se aplica sistemáticamente a distintos tipos de datos. En este informe nos concentramos en tres tipos de datos neurofisiológicos: EEG, PET y fMRI, y en los procesos específicos asociados con ellos.

En primer lugar, la siguiente figura muestra en esquema las opciones y procesos dedicados a los datos de Electroencefalografía (EEG), que incluyen:

- Preproceso temporal incluyendo operaciones de conversión de los datos, filtrado temporal para la eliminación de ruido gausiano, promediado para la obtención de estimaciones robustas, la descomposición en épocas para el proceso de las repeticiones y su promediado, y rutinas específicas para la eliminación de artefactos de la señal, como la eliminación de los pulsos debidos al parpadeo. Se incluyen una miscelanea de operaciones como el

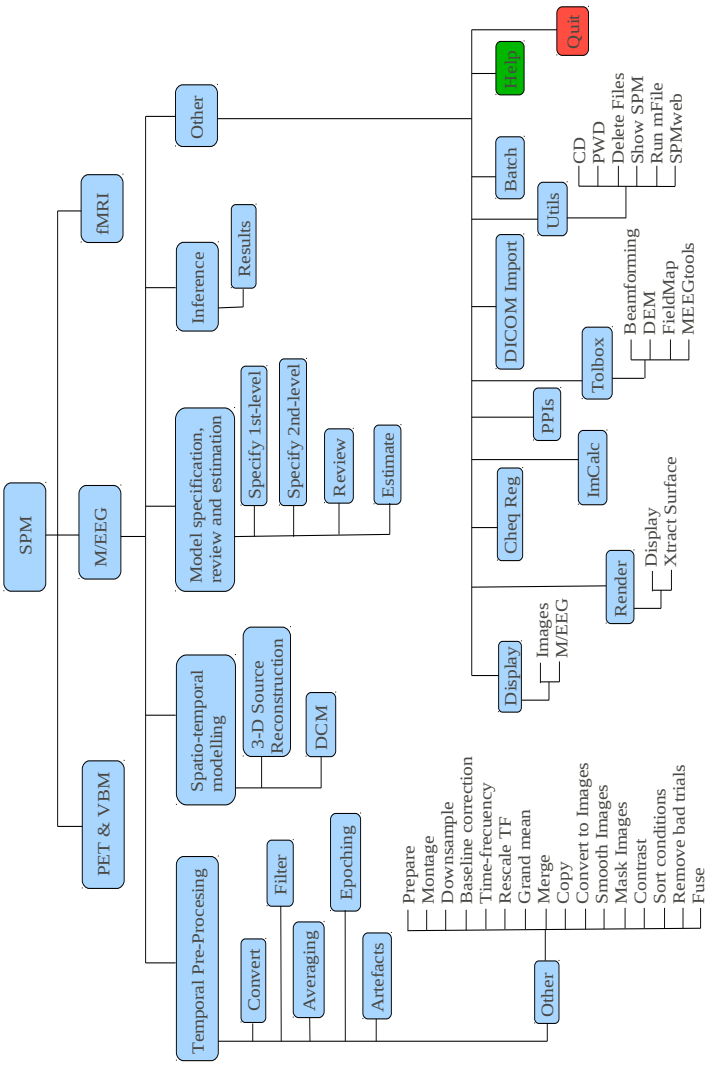

montaje de épocas para reconstruir la señal, facilidades para realizar el remuestreo (downsampling) de forma que es posible reducir la cantidad de información que se está manipulando, corrección de la tendencia, reescalado en el plano tiempo-frecuencia, la conversión a imágenes para la visualización, larealización de contrastes, el reordenamiento de las condiciones experimentales, la eliminación de trials incorrectos, etc.

- El modelado espacio-temporal para la reconstrucción de la fuentes en el espacio tridimensional, con el objeto de localizar las redes cerebrales subyacentes a la señal percibida. Se incluye en este aspecto la posibilidad de especificar modelos dinámicos causales (DCM) que especifican las causas e interrlaciones dinámicas entre elementos de las redes neuronales cerebrales
- La especificación de los modelos temporales de primer y segundo nivel con los procesos de estimación de parámetros asociados y las herramientas de revision de los resultados y datos.
- Los procesos de inferencia estadística a partir de los datos para la verificación de las hipótesis bajo test.

- Una colección de operaciones misceláneas de procesos de los datos.
    - Visualización de señales e imágenes
    - Renderización 3D de superficies
    - Cálculo de imágenes
    - Toolbox de formación de rayos, creación de mapas y otras herramientas
    - Importar datos DICOM
    - Utilidades genéricas para el manejo de ficheros y directorios
- Función de ayuda

La siguiente figura recoge el esquema de las operaciones y facilidades para el manejo de datos PET. PET es un tipo de imagen funcional que permite detectar los lugares donde se producen los procesos mentales asociados a tareas cognitivas. Es de utilidad para diagnóstico de enfermedades neurodegenerativas. En el mismo

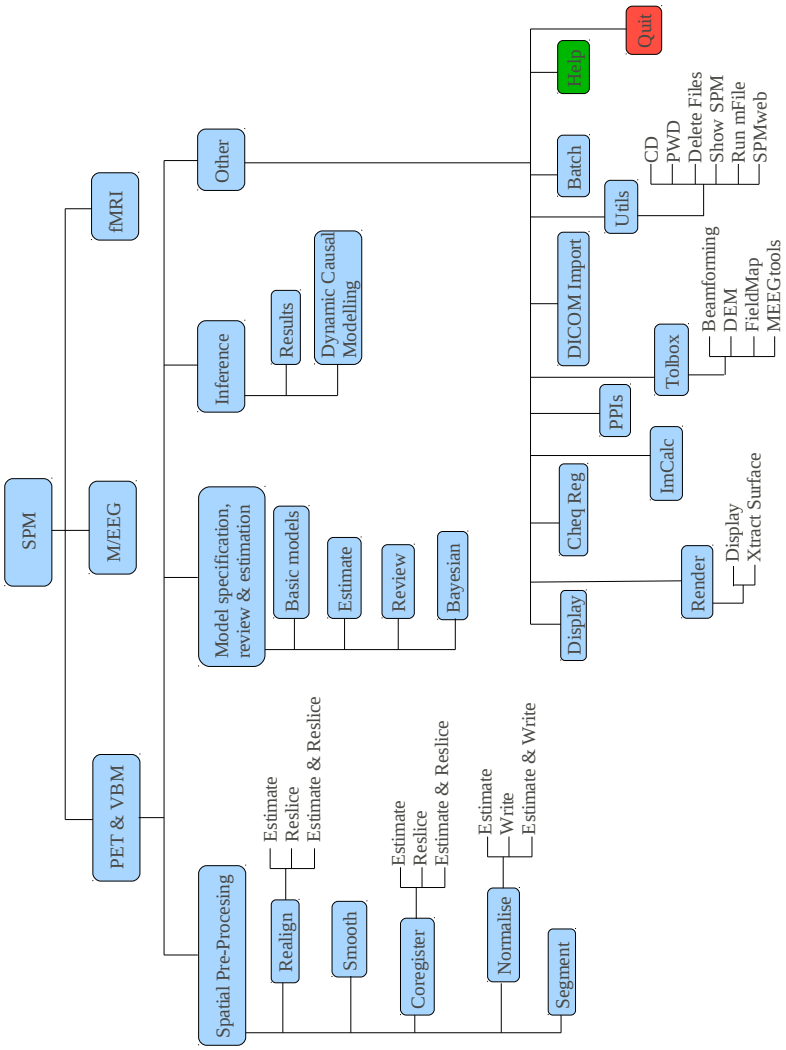

paquete se pueden realizar operaciones de comparación de volúmenes a nivel de voxel (VBM). Las operaciones incluidas son:

- Preproceso espacial, puesto que los datos son volúmenes correspondientes a diversos sujetos o al mismo sujeto en el tiempo, es necesario conseguir que estén solapados de forma que un voxel corresponda a la misma característica anatómica en todos los volúmenes.
    - Realineamiento que consiste en estimar la traslación y rotación que hace coincidir optimamente los volúmenes en su correspondiente anatomico y aplicarlo. Este proceso puede implicar cambios de resolución de los datos, cuando están tomados a distintas resoluciones o se comparan con un modelo que tiene resolución espacial distinta.
    - Suavizacion para disminuir el efecto de los cambios en las imágenes inducidos por el realineamiento
    - Corregistro: cuando tenemos diversas modalidades de datos y una de ellas es usada para calcular la normalización espacial. En este caso, la segunda modalidad usa sin más las transformaciones de la primera.
    - La normalización no lineal se aplica en algunos casos para obtener una más perfecta correspondencia anatómica, implica procesos no lineales de deformación espacial.
    - Procesos de segmentación para facilitar emparejamientos y la localización de los hallazgos.
- La especificación del modelo de regresion lineal para la detección de efectos sobre los datos. Se aplican de forma independiente a los voxeles a través de los individuos. El modelo utilizado el modelo lineal general. Incluye la posibilidad de especificar la variables y co-variables, realizar la estimación de los coeficientes lineales, asegurar la naturaleza gausiana de los datos e incluso aplicar procesos de inferencia bayesiana.
- Procesos de inferencia, permiten la revisión y se incluyen también modelos dinámicos causales para la estimación de causas dinámicas.
- Una colección de operaciones misceláneas de procesos de los datos.
    - Visualización de señales e imágenes
    - Renderización 3D de superficies
    - Cálculo de imágenes
    - Toolbox de formación de rayos, creación de mapas y otras herramientas
    - Importar datos DICOM
    - Utilidades genéricas para el manejo de ficheros y directorios
- Función de ayuda

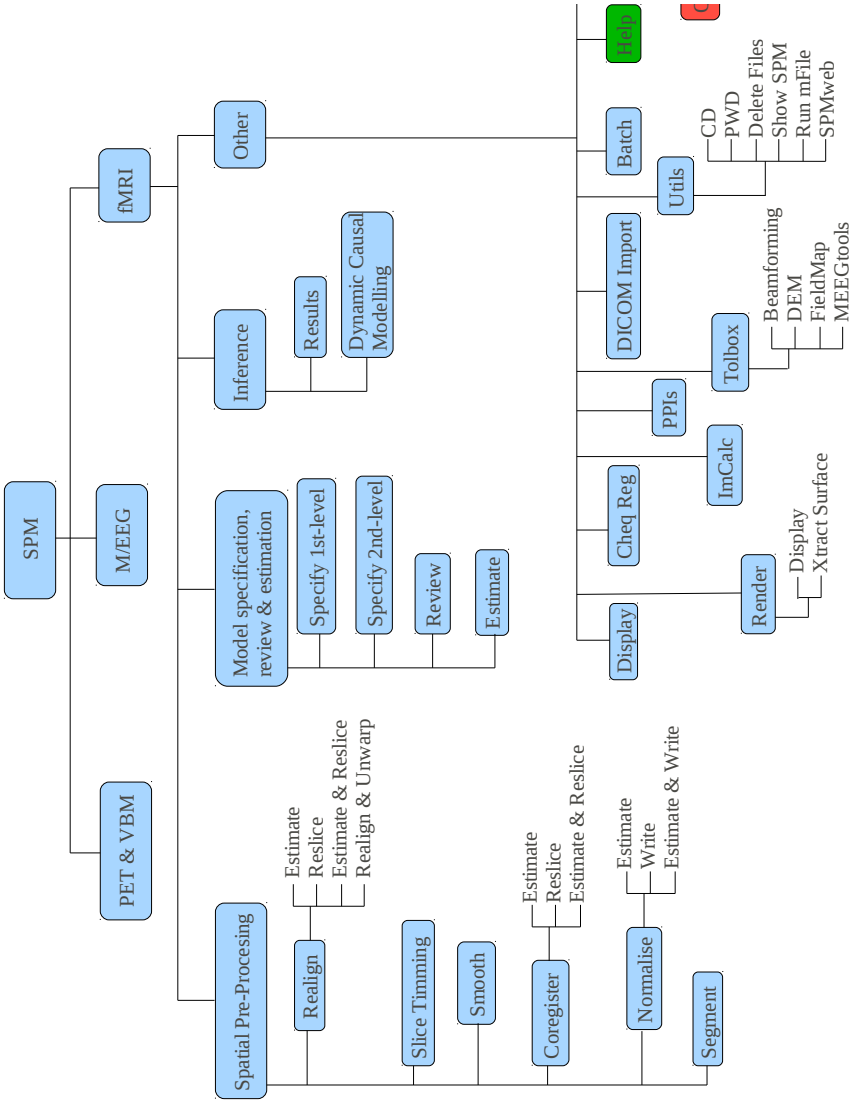

Finalmente, las operaciones que pueden aplicarse a los datos de resonancia magnética nuclear funcional, fMRI, se especifican en la figura. Incluyen la posibilidad de especificar e inferir procesos dinámicos temporales. Las operaciones incluidas son:

- Preproceso espacial, puesto que los datos son volúmenes correspondientes a diversos sujetos o al mismo sujeto en el tiempo, es necesario conseguir que estén solapados de forma que un voxel corresponda a la misma característica anatómica en todos los volúmenes.
    - Realineamiento que consiste en estimar la traslación y rotación que hace coincidir optimamente los volúmenes obtenidos en cada instante de tiempo con su correspondiente anatómico y aplicarlo. Se realizan dos procsos, uno de alineamiento intrínseco de la serie temporal para eliminar efectos de movimiento, y otro de registro cotra la imagen de resonancia magnética estructural. Este proceso puede implicar cambios de resolución de los datos, puesto que los datos estructurales están tomados a distintas resoluciones.
    - Suavizacion para disminuir el efecto de los cambios en las imágenes inducidos por el realineamiento
    - Corregistro: cuando tenemos diversas modalidades de datos y una de ellas es usada para calcular la normalización espacial. En este

caso, la segunda modalidad usa sin más las transformaciones de la primera.
    - La normalización no lineal se aplica en algunos casos para obtener una más perfecta correspondencia anatómica, implica procesos no lineales de deformación espacial.
    - Procesos de segmentación para facilitar emparejamientos y la localización de los hallazgos.
- La especificación del modelo de regresion lineal para la detección de efectos sobre los datos. Se aplican de forma independiente a los voxeles a través de los individuos. El modelo utilizado el modelo lineal general. Incluye la posibilidad de especificar la variables y co-variables, realizar la estimación de los coeficientes lineales, asegurar la naturaleza gausiana de los datos e incluso aplicar procesos de inferencia bayesiana.
- Procesos de inferencia, permiten la revisión y se incluyen también modelos dinámicos causales para la estimación de causas dinámicas. En este caso, los datos tienen precisamente un componente temporal claro, por lo que es evidente que pueden ser ajustados a las correspondientes series temporales.
- Una colección de operaciones misceláneas de procesos de los datos.
    - Visualización de señales e imágenes
    - Renderización 3D de superficies
    - Cálculo de imágenes
    - Toolbox de formación de rayos, creación de mapas y otras herramientas
    - Importar datos DICOM
    - Utilidades genéricas para el manejo de ficheros y directorios
- Función de ayuda